MULTIVARIATE FLEXIBLE METAL ORGANIC FRAMEWORKS: THE ROLE OF FUNCTIONALIZED LINKERS, HETEROGENEITY AND DEFECTS IN ADSORPTION PROCESSES

Dissertation

Stephanie Terruzzi

MULTIVARIATE FLEXIBLE METAL ORGANIC FRAMEWORKS: THE ROLE OF FUNCTIONALIZED LINKERS, HETEROGENEITY AND DEFECTS IN ADSORPTION PROCESSES

A thesis submitted for the degree of

Doctor of Philosophy

by Stephanie Terruzzi (student ID n° R12191)

June 2022

Supervisor: Prof. Valentina Colombo

Co-supervisor: Prof. Angelo Sironi

PhD coordinator: Prof. Dominique Roberto

XXXIV Ph. D. Cycle in Industrial Chemistry

A. A. 2020-2021

"There is something in such laws that takes the breath away. They are not discoveries or inventions of the human mind but exist independently of us. In a moment of clarity, one can at most discover that they are there and take them into account. Long before there were people on the earth, crystals were already growing in the earth's crust. On one day or another, a human being first came across such a sparkling morsel of regularity lying on the ground or hit one with his stone tool and it broke off and fell at his feet, and he picked it up and regarded it in his open hand, and he was amazed."

— MAURITS CORNELIS ESCHER —

Abstract

Metal-Organic Frameworks (MOFs) are a class of synthetic porous crystalline materials based on metal ions connected through spacing ligands. They possess interesting properties such as, high porosity, high concentration of metal centers, flexibility, *etc.*, which are difficult to find in conventional porous materials. As a result of these unique features, MOFs can maintain porous structures upon removal, inclusion, exchange, or reaction of a wide selection of molecular guests, making them useful for applications in selective gas adsorption/separation. Furthermore, a number of MOFs have the ability to respond to specific stimuli such as *host-guest* interactions, temperature or pressure change, light, *etc.* To date, most of the applications of these flexible MOFs is related to gas-storage and selective adsorption/separation, but it was soon recognized that the responsive properties of these materials have enormous potential in many areas, a really interesting example are NPs@MOFs composites which can be used to design novel "smart" heterogeneous catalysts capable of reversibly adapt to substrates and/or respond to regulating stimuli (*e.g.* reversible structural transitions upon adsorption of guest molecules).

The work within this thesis is divided into two parts. The first one focuses on the understanding of the *host-guest* interactions during adsorption processes in highly stable, rigid, porous metal-organic frameworks. of formula $Fe_2(BDP)_{3x}(BDP-NH_2)_{3(1-x)}$ (x = 0, 0.5, 1) with $H_2BDP-NH_2$ = 2-amino[1,4-bis(1H-pyrazol-4-yl)benzene]. Their investigation was performed through a multi-technique approach exploiting high-resolution powder X-ray diffraction (HR-PXRD), advanced gas adsorption measurements and Monte Carlo simulations. In particular, the *host-guest* interactions during CO_2 adsorption were studied via *in situ* HR-PXRD dosing CO_2 in certain pressure ranges at different temperatures and compared between functionalized and bare systems. Rietveld refinements of the diffraction data collected at each pressure point was used to understand the preferential adsorption sites occupied by the gaseous probe and the *host–guest* interactions, as well as the breathing behaviour, whose mechanism was not yet completely described in the literature. The metal ion and ligand functionalization modulate the sorption properties of these materials, enhancing their affinity to CO_2 molecules. Finally, new flexible, multivariate MOFs of general formula $Zn(BDP)_{0.5}(BDP-X)_{0.5}$ (X = NH_2 or NO_2) were synthesized. The deep characterization of the adsorption properties and the structural features of these materials will be crucial to understand the relation between the structural flexibility, functionalization degree and crystal size, with the gas adsorption and separation properties.

The second part of this thesis describes a family of pillar-layered MOFs of general formula $[M_2(fu-bdc)_2P]_n$ with $M^{2+} = Zn^{2+}$, fu-bdc^{2-} = diversely functionalised 1,4-benzenedicarboxylate) and how catalytically inert nanoparticles (silica NPs, 30 nm) can be embedded into the microporous ordered MOFs structures, obtaining hybrid materials where the NPs represent typically a meso-scale "defect" or "heterogeneity" to the system. In particular, the work was focused on the comparison between the plain MOFs and the new composite materials NPs@MOF. The parent $[Zn_2(bdc)_2(dabco)]_n$ is only weakly flexible, whereas the substituted frameworks $[Zn_2(fu-bdc)_2(dabco)]_n$ (with fu = DM, 2,5-bis(methoxy)-1,4-benzenedicarboxylate or BME, 2,5-bis(2-methoxyethoxy)-1,4-benzenedicarboxylate) contract significantly upon guest removal to a narrow pore (*np*) form and expand again (*lp* form) upon adsorption of DMF, EtOH, or CO_2, *etc.* In contrast, N_2 is hardly adsorbed and does not open the narrow pore form. These "breathing" dynamics are attributed to the dangling side chains present on the linkers, which interact with mobile guest molecules as well as with themselves and with the framework backbone. The samples were characterized by a variety of techniques: PXRD, FTIR, TGA, DSC, EFTEM-EDX, TEM tomography, UV-Vis and PL spectroscopy, standard N_2 (77 K) and CO_2 (195 K) gas adsorption experiments with the objective of understanding the connection between defects, disorder with flexibility. The *in-depth* and *in situ* structural and spectroscopic characterization carried out, especially gas adsorption and variable temperature PXRD experiments, revealed interesting differences in the flexible behaviour between the parent MOFs and the NPs@MOFs.

Chapter 1

METAL ORGANIC FRAMEWORKS
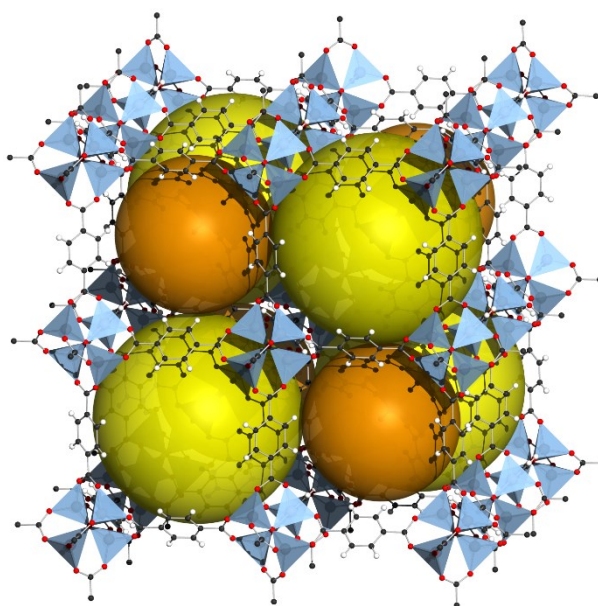
1.1 From Early Coordination Chemistry to 3D Coordination Polymers

Porous materials have always been interesting for scientists for their peculiar properties and many possible applications. Materials with porosity such as active carbons and zeolites are found in nature and have gained great economic importance during the years because they could be applied for industrial applications in many different areas.[1]

In 1893, A. Werner synthesised the complex $[Co(NH_3)_6]Cl_3$ complex and its analogues, proposing the right description for their structure with the metal centre octahedrally coordinated to the organic ligands.[2] However, these concepts couldn't have been completely proven without the progresses achieved in X-ray crystallography. For example, Prussian Blue ($Fe_4[Fe(CN)_6]_3$) was known since the 18th

century but its crystal structure was only clarified in 1977 and is still studied today.[3,4] Already in 1897 K. A. Hofmann and F. Z: Küspert coined the concept of *framework* related it to a molecular structure. The so-called Hofmann clathrate $[Ni(CN)_2(NH_3)](C_6H_6)$ was discovered in the same year[5] and its structure was explained only in the 1950s.[6] The next logical step was to link metal ions entirely through organic linkers to form the so-called coordination networks, the first members of this class of materials were reported by Saito and co-workers who linked Cu+ ions through bis(alkylnitrilo) units of different lengths to yield a series of crystalline materials with structures of varying dimensionality,[7–9] the key compound being $[Cu(ADI)_2](NO_3)$, which shows a 3D structure based on the diamond net (dia). The advances in the synthetic procedures and in the field of crystallography along the years, and consequent solution of the crystalline structures of these materials (Figure 1.1).[10]

These works laid the foundation for the subsequent development of important basic principles which inspired the recent advances in coordination chemistry. In the last decades many porous materials have been developed and a huge, important class of these materials is that of Porous Coordination Polymers (PCPs), this term was used for the first time in a publication in 1916.[11,12]
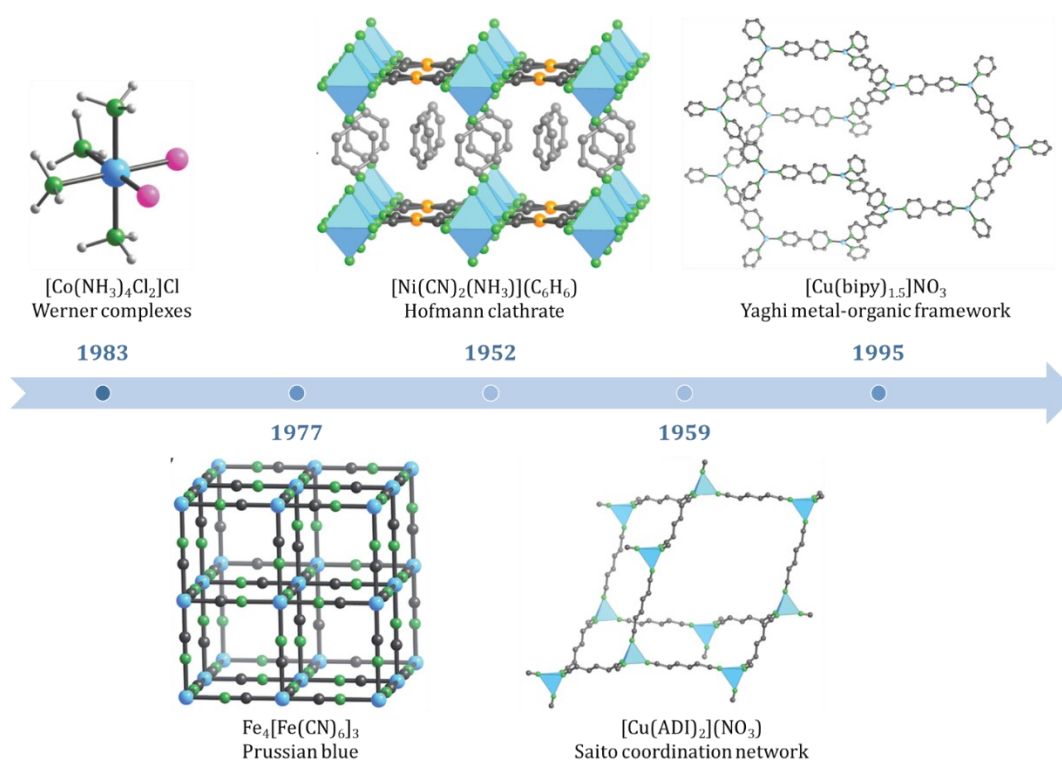
Figure 1.1 - Some examples in the development of coordination chemistry towards MOFs. 1983: *cis*-isomer for the octahedral Werner complex, colour code: Co, blue; N, green; Cl, pink; H, light grey. 1977: Prussian blue framework, colour code: C, black; N, green; metals, blue. 1952: Hofmann clathrate structure, colour code: Ni, blue and orange spheres; C, grey; N, green; benzene guest, light grey. 1959: 3D coordination network based on copper and adiponitrile, colour code: Ni, blue; C, grey; N, green. 1995: first definition of metal-organic framework represented by a 3D framework based on trigonal planar Cu(I) single metal nodes connected by linear bipyridine linkers, colour code: Cu, blue; C, grey; N, green. H atoms are omitted for clarity.

To avoid any misunderstanding, in 2013 the International Union of Pure and Applied Chemistry (IUPAC) gave a definition for the terms: coordination compound, polymer and network.[13]

⦿ *Coordination compound* is "[...] any compound that contains a coordination entity", which means that an ion or neutral molecule (the so-called entity) is surrounded by a group of atoms, the ligands.

⦿ *Coordination polymers* are an extension of coordination compounds into one, two or three dimensions. And they do not necessarily need to be crystalline.

⦿ *Coordination networks* are regarded as a subclass of coordination polymers possessing supplementary "[...] cross-links between two or more individual chains, loops or spiro-links [...]".

1.2 Metal-Organic Frameworks

In 1995 O. M. Yaghi adopted a term for a new type of porous material after the synthesis of a 3D-polymeric coordination compound of copper, $Cu(4,4'\text{-bipy})_{1.5}NO_3(H_2O)_{1.5}$, which consists of interpenetrated nets and is able to retain its structure even after removal of the guest solvent molecules in the framework.[14] This discovery was the beginning for a new and huge research field which developed very quickly in the following decades.

The problem is that the terminology coordination polymer and Metal Organic Framework (MOF) have often been used interchangeably, which is why the IUPAC proposed another definition to avoid any confusion: "A metal–organic framework, abbreviated to MOF, is a coordination network with organic ligands containing potential voids".[13] Thanks to this, MOFs can be clearly discerned from coordination polymers (or networks), even though being a subclass thereof, and they can alternatively be called porous coordination networks (or polymers), emphasising the intrinsic porosity of MOFs.[15]
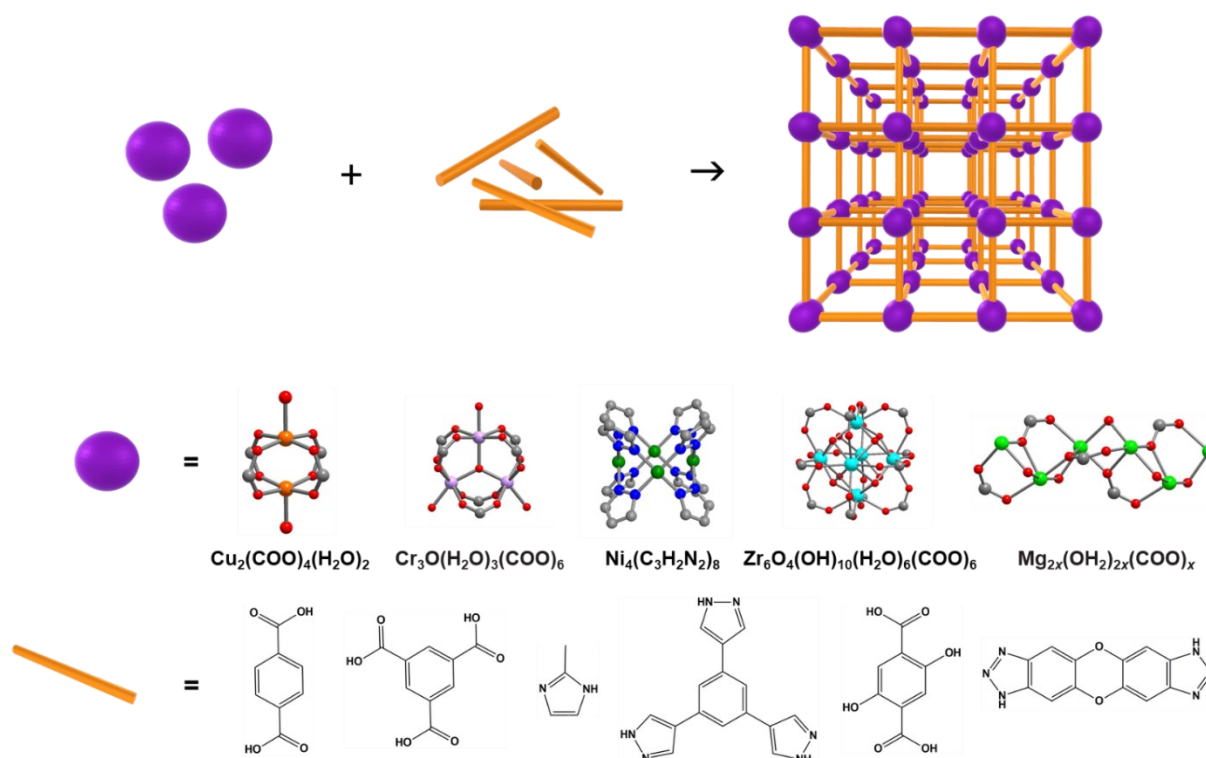
Figure 1.2 - Schematic representation for the formation of a metal organic framework with examples of inorganic SBUs (purple spheres) and organic linkers (orange rods).

Hence, metal organic frameworks are a class of porous crystalline materials containing metallic ions and organic ligands creating an infinite 3D open net accessible to guest molecules (Figure 1.2). Their structure is constituted by inorganic nodes, which can be simple metal ions in their coordination geometry (*e.g.* Fe(II)/(III), Al(III), Mg(II), Co(II), Cu(I)/(II), Zn(II) e Zr(IV)) or secondary building units (SBUs),[16] which are small metal clusters (*e.g.*, $Zn_4O(COO)_6$, $Cu_2(COO)_4(H_2O)_2$ or $Zr_6O_4(OH)_{10}(H_2O)_6(COO)_6$) (Figure 1.2). These units are linked together via strong coordination bonds they form to organic linkers (mono-, bi-, tri- and tetra-dentate being the most common types). These ligands can contain a variety of functional groups, such as simple nitriles, carboxylates, phosphonates, pyrazolate, imidazolate, or pyridyl groups. The organic linkers also have their own structure which can lead to a defined spatial arrangement. An interesting point is the possibility to tune the pore size of the framework by changing the length of the ligand and maintaining the same functionalities. Moreover, it is possible to tune the basicity/acidity of the framework introducing specific substituents/functional groups on the organic ligand without changing the fundamental structure of the framework.

The combination between organic linkers and metallic nodes (or SBUs) gives rise to a large number of different topologies.[17–19] In particular, with respect to the single metal ion, the SBUs contain both metal and non-metal atoms (typically oxygen and nitrogen), which offer the possibility to have a larger variety in terms of connectivity, functionalities and structures. The stability of the resulting MOF depends on

the strength of the bonds between metal ion and organic linker, that can vary from strong covalent bonds to labile van der Waals interactions.

Along the years, most of the transition metals have been used to synthesise the SBUs, from alkali metals to lanthanides and actinides. MOFs are different from the classic porous materials (*i.e.* active carbons and zeolites) for many aspects: they possess highly ordered tuneable porous structures, possible flexible and dynamic behaviour (induced by the interaction with guest molecules or other external stimuli) as well as a drastically larger modifiability by functionalisation of the organic ligands (*i.e.* the pores) leading to interesting catalytic and/or selective properties. Moreover, they can show magnetic, optic or electric properties thanks to the presence of the metal ions.

The seemingly infinite possibilities when assembling metal ions and organic ligands permits to design many different frameworks, each one unique and with specific properties. Indeed, in the last years the number of deposited crystal structures in the Cambridge Crystallographic Data Centre (CCDC) has grown exponentially (Figure 1.3). Today, the MOF subset included in the Cambridge Structural Database (CSD) counts 112.400 crystal structures.[20]
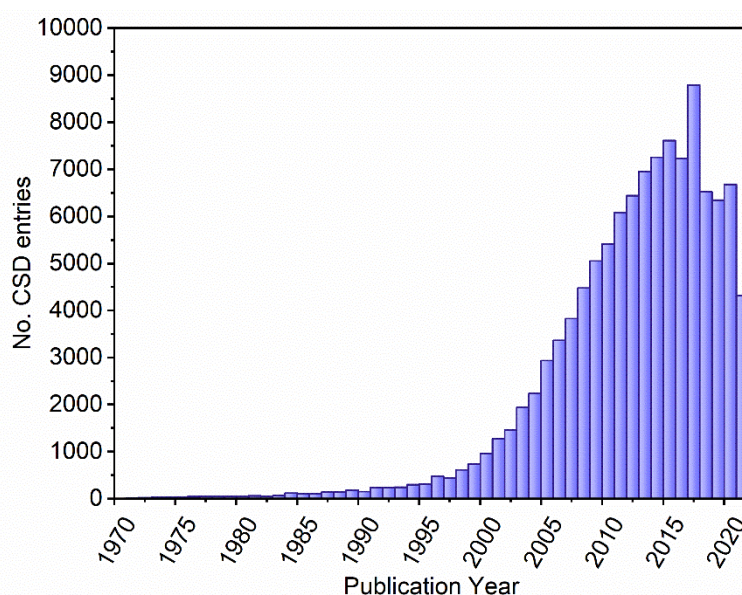
Figure 1.3 - Number of papers published over the period of time 1970 – present regarding Metal Organic Frameworks as main topic.

1.2.1 Design

As introduced in the previous paragraph, the building blocks of MOFs are metal ions and organic linkers, which confer specific topologies and properties to the final porous material. But there are many other parameters that need to be controlled (Figure 1.4) in order to obtain the desired product:

a) Synthetic methodology. MOFs are commonly obtained via hydro- or solvothermal reactions where the metal precursor, the linker and a suitable (often polar) solvent are mixed in a reaction vessel (for example in Teflon liners) under high temperature and pressure.[21-23] Else, it can be a classic reaction in a flask, or using microwaves, or an electrochemical synthesis, *etc.*

b) Templates. They are molecules that do not take part in the reaction but influence the crystal growth of the PCP. Examples are benzene, dimethylformamide (DMF), dimethylsulfoxide (DMSO), cyclohexane, *etc.*

c) Concentration of reagents. The ratio between the metal ion and the ligand and the concentration of the solvent are very important parameters; different frameworks can be obtained just changing for example the quantity of solvent used.

d) Metal salt. A wide range of metal salts can be chosen: acetate, nitrate, chloride, bromide, oxide, *etc.* To facilitate the formation of crystalline products lesser coordinative anions are preferred.

e) Temperature. Ranging from 77 K of liquid nitrogen to 194 K of dry ice and up over 473 K, the maximum temperature being the decomposition temperature of the organic linker. The use of Teflon liners permits to reach temperatures higher than the boiling point of the solvent used and this is particularly useful to try to isolate the thermodynamic stable phase and avoid kinetics driven products.

f) Acid or base. The control of the pH during the reaction is very important to permit the protonation/deprotonation of the organic ligands and to influence the time of the nucleation process.

Figure 1.4 - Important experimental parameters to be optimised to obtain the desired MOF.

g) Time. Reactions times vary widely, they can be very short (few seconds) or last for hours, days or even weeks.

h) Solvent. Depends on the type of synthesis, metal salt and organic ligands. Common solvents are water and some organic ones (methanol, ethanol, DMF, *etc.*); high boiling point solvents are often used (DEF, DMF. DMSO, *etc.*) since high temperatures are useful to break and form coordination bonds in the nucleation phase. Mixtures of solvents are also extensively used.

1.2.2 Generations

The as synthesised MOFs contain solvent molecules in their frameworks, which can be removed during the so-called activation process, where the material is put *in vacuo* and at elevated temperatures after the synthesis. It is interesting to note that many MOFs do not retain their permanent porosity after the removal of guest molecules, the solvent in this case.

Porous coordination polymers can be classified into first, second and third generation materials, these categories were proposed by S. Kitagawa in 1998[24] and are schematically depicted in Figure 1.5:

- ⦿ *First generation* MOFs lose their crystal order after removing the solvent molecules in the cavities, with irreversible collapse of the framework.

- ⦿ *Second generation* compounds do not collapse after removal of the guest molecules because they possess stable and robust frameworks, and they are able to re-adsorb these molecules without changing their morphology. Therefore, this kind of materials can be regarded as rigid.

- ⦿ *Third generation* compounds, also called *soft porous crystals*, possess a highly ordered network and structural stability but they are also very flexible and can perform (reversible) phases transformations. They have dynamic structures that change upon external stimuli, both chemical or physical, more details about this responsive behaviour are written in Chapter 4.1.[25,26]
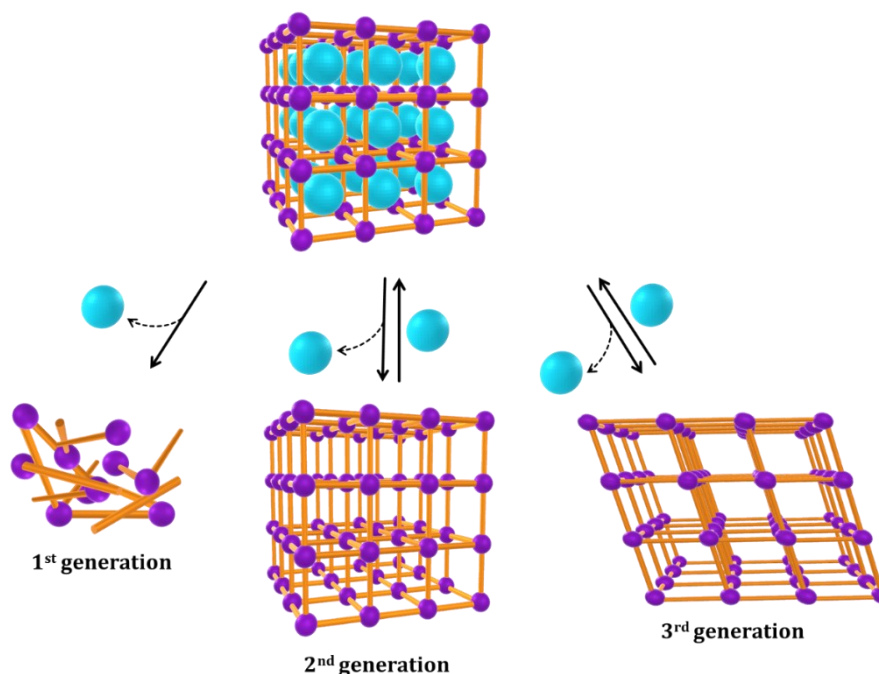
Figure 1.5 - Graphical representation of MOF generations as first classified by Kitagawa. Colour code: metal, purple spheres; linker, orange rods; guest, light blue spheres.

Recently, also the concept of the *fourth generation* porous materials have been introduced by S. Kitagawa,[27,28] which show capabilities that exceed the examples from the first three generations and can be used for advanced applications. These additional features are: (a) Hierarchy and hybrid ("double-H"), for example solid-liquid reversible phase transition caused by heating can be used to manipulate crystals and create membranes. (b) Anisotropy and asymmetry ("double-A"), hybridisation of MOFs with other materials can enhance and/or develop new properties.[29,30] (c) Disorder and defect (double-D), many examples have been recently discovered of crystal downsizing influencing the material's properties (Figure 1.6).[31,32]
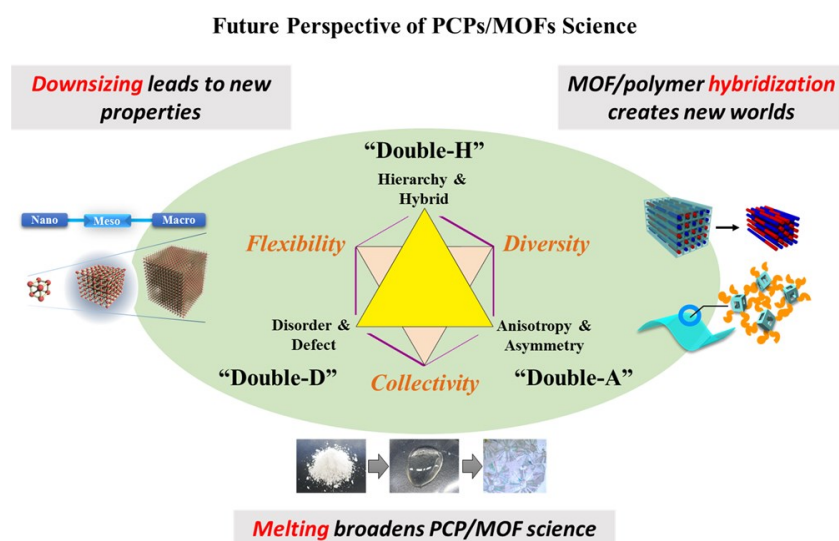
Figure 1.6 - Fourth generation MOFs possess different attributes that can lead to advanced porous materials.[28]

1.2.3 Classification of Porosity

MOFs are ordered materials characterised by an external surface area (outside the pores) and an internal one (surface of all pore walls) and they can be classified in terms of their pore size[33] in the context of physisorption:[34]

- ⊙ *Macroporous materials*, with pore widths exceeding 50 nm.
- ⊙ *Mesoporous materials*, with pore sizes between 2 nm and 50 nm.
- ⊙ *Microporous materials*, with pore widths smaller than 2 nm.

The majority of the PCPs are microporous or mesoporous because larger pores lead to less stable frameworks, which collapse more easily.

The total accessible internal volume is measured through gas adsorption measurements, *i.e.* by actually* filling the pores. The resulting adsorption isotherms were grouped into six types by IUPAC in 1985.[34]

However, along the years new types of isotherms have been recognised and an updated classification has been proposed in 2015. The various physisorption isotherms are depicted in Figure 1.7.[35]
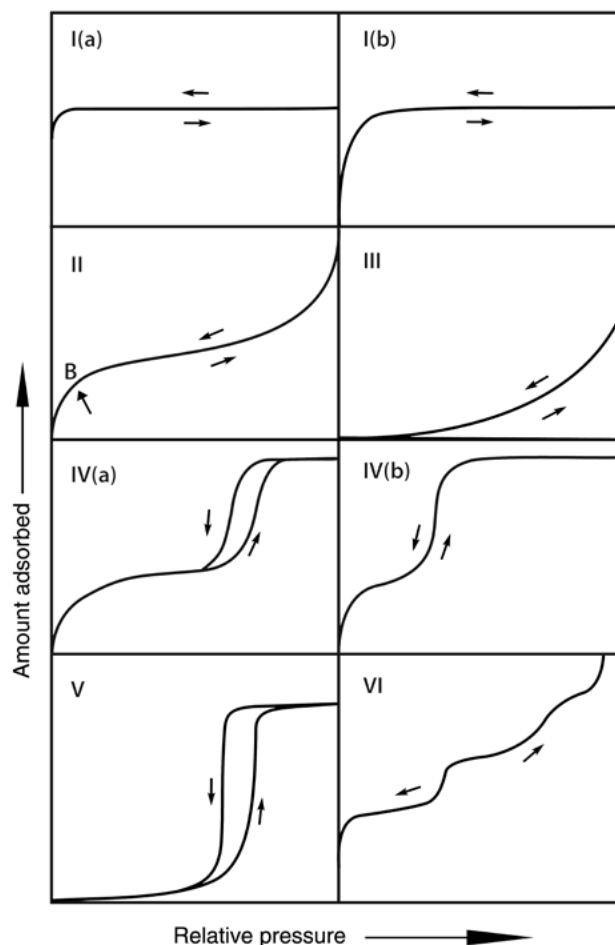
Figure 1.7 - Different types of sorption isotherms as classified by IUPAC (2015).[35]

Type I(a) isotherms are typical for microporous materials possessing mainly narrow micropores (<1 nm) and are characterised by a sharp increase in the adsorbed amount of gas at low relative pressures as the sole feature/invariance at higher pressures. *Type I(b)* isotherms are given by materials having a broader range of pore sizes (<<2.5 nm) but show essentially the same behaviour with simply a bigger magnitude in the initial increase. *Type II* (reversible) isotherms are found in nonporous or microporous adsorbents, where point B represents the beginning of the almost linear trend and normally corresponds to the end of monolayer coverage. For a *Type III* isotherm, there is no point B and therefore no monolayer formation. This means that the adsorbent-adsorbate interactions in the microporous or nonporous material are weak and that the adsorbed molecules are mainly accumulated on specific sites on the surface. *Type IV* isotherms are typical for mesoporous solids. The curve is characterised by an initial monolayer-multilayer adsorption on the mesopore walls, followed by pore condensation (when a gas condenses to a liquid-like phase in a pore at a lower pressure than the saturation pressure of the

liquid[36,37]), Eventually at larger pressures, there is a saturation plateau. In this case two different types of isotherms can be distinguished: *Type IVa* presents capillary condensation accompanied by hysteresis whereas *Type IVb* has the same shape but no hysteresis loop because mesopores have smaller widths. Both types are completely reversible. The *Type V* isotherm is similar to that of *Type III* in the low p/p_0 range, where the interactions are quite weak. Instead at higher relative pressure, molecular clustering is observed and then pore filling. *Type VI* isotherms indicate a reversible layer-by-layer adsorption type with steps, their height represents the adsorption capacity for each layer, while their shape varies according to the temperature and type of material.

Hysteresis loops generally represent capillary condensation and depend on adsorption metastability as well as network effects. In a pore network, the desorption branch is dependent on the size and spatial distribution of the pore necks. Therefore, useful information about the pore size can be retrieved.

There are six different types of hysteresis loops (Figure 1.8), which are closely related to specific features of the pores in the adsorbent. The main types are shown in Figure 1.8. *Types H1, H2(a), H3* and *H4* were already defined in the IUPAC report of 1985. *H2b* and *H5 Types* have been introduced later after additional findings.
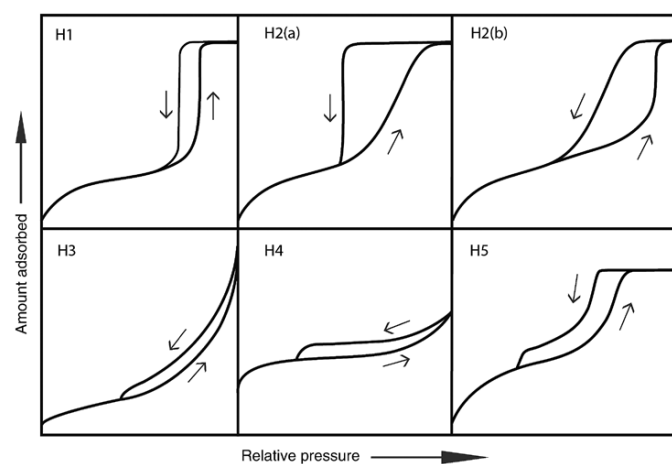
Figure 1.8 - Different shapes of hysteresis loops as classified by IUPAC (2015).[35]

A Type H1 hysteresis loop is observed in solids with a narrow range of uniform mesopores (*e.g.* templated silicas, mesoporous carbons). The narrow loop is caused by a delayed condensation during adsorption or when the width of the pore necks is similar to that of the pore/cavity size itself.[36]

Type H2 loops are found in more complex pore structures where the very steep desorption branch is for example related to pore-blocking/percolation in a narrow range of pore necks. For instance, *H2(a)* loops are given by silica gels, porous glasses as well as some ordered mesoporous materials; for *Type H2(b)* loops the situation is similar but the pore blocking is associated with larger pore necks.

Type H3 loop looks like a *Type II* isotherm for the adsorption branch and is found in non-rigid aggregates of plate-like particles (*e.g.* clays) where the macropores are not fully filled.

For *Type H4* loop the adsorption branch resembles both *Types I* and *II* isotherms, where the high uptake at low relative pressure is associated with micropores filling. This type of behaviour is often shown by zeolites or micro-mesoporous carbons.

The strange shape of *Type H5* loops is due to a distinctive form with pore structures containing both open and partially blocked mesopores.

1.2.4 Functionalisation and Modification

The various interesting traits described to this point render MOFs the perfect candidates for the design and fine-tuning of properties with the aim of obtaining specific physicochemical properties useful for a large number of possible applications (see Chapter 1.2.5 and Chapter 4.1.2). The key feature of MOFs is indeed the possibility to almost freely tune the internal pore surface by modifying the metal centre, the SBU geometry or the organic linker (geometry, number and type of functionalities). An enormous number of different topologies can be created thanks to the so-called concept of reticular chemistry, introduced by O. Yaghi.[16,38] For the functionalisation of the ligand, two main approaches are used: add a functionality to the organic linker prior to the synthesis of the MOF,[39–42] or implementing the functional group after the synthesis, *i.e.* post-synthetic modification approaches, which will be discussed more in detail in the next paragraph.[43]

Pre-synthetic functionalisation of the linker
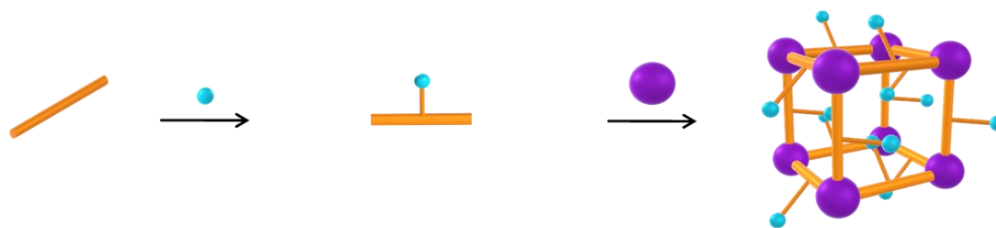
Post-synthetic deprotection
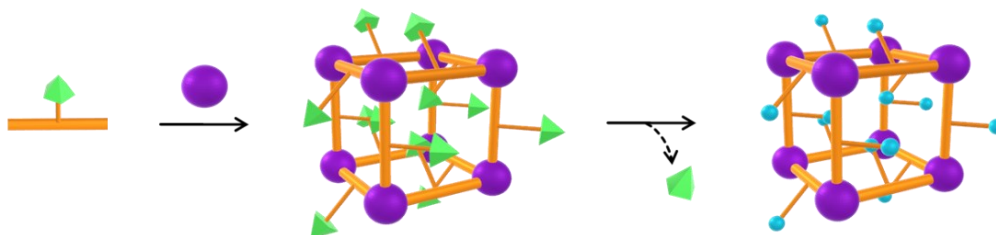
Post-synthetic exchange
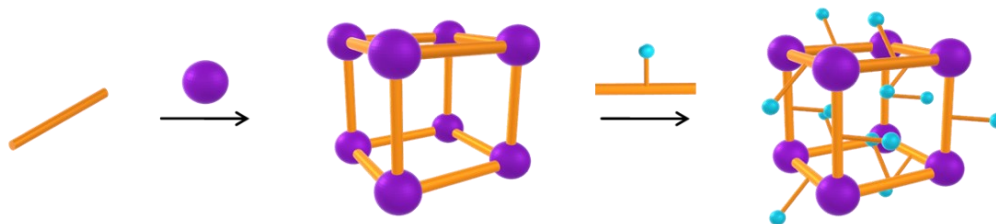
Creation of missing linker defects
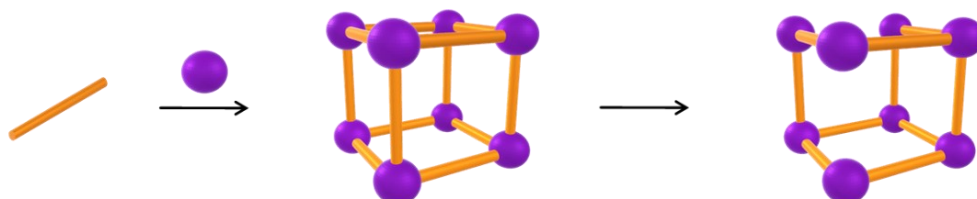
Encapsulation of NPs
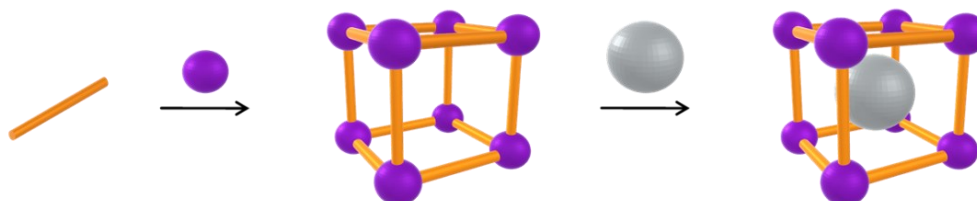
Figure 1.9 - Schematic representation of different kind of PSM to functionalise MOFs. Colour code: metal, purple spheres; linker, orange rods; functional groups, light blue spheres; protection group, green diamonds; nanoparticle, grey sphere.

When applying the first method (pre-synthetic functionalisation of the linker, Figure 1.9), it must be noted that in some cases the functionalisation of the organic ligand makes the synthesis of the MOF more difficult, if not impossible, because the introduction of new substituents may change the reaction conditions. Indeed, the chosen functional group could interfere by reacting with the metal ion or other reagents and possibly deviating the reaction towards a different product. Furthermore, the functional group could change the solubility and/or thermal stability of the ligand which would require modifications of the reaction parameters, for instance using modulators, different solvents, changing the temperature or time, *etc.*

An alternative to evade these problems is the post-synthetic modification (PSM) which is possible only if the material is robust enough to undergo a transformation without losing its structural integrity. Generally speaking, PSM refers to any change in the MOF structure after its formation. The advantages deriving from the PSM are: *a)* the possibility to include many different functional groups without considering eventual problems for the reaction conditions of the MOF; *b)* the purification and isolation of the modified products are easier because the functionalisation is made directly on the crystalline solids; *c)* the same MOF can be modified with different reagents leading to a large number of topologically identical materials but with different functionalities, thus different properties; *d)* the control on the type of substituent and the entity of the modification, permits the introduction of multiple functional groups in the same material and allows to effectively optimise its properties.

Depending on the type of modification, PSM can be carried out through different methodologies:

- ◉ *PSM of the spacing organic linker.* This is the case when the functional groups attached to the linker, also called tags, are subject to simple reactions like oxidation or esterification.[44–48] Another example is PSD, post-synthetic deprotection, where the organic linker is functionalised with a protective group prior to the synthesis of the MOF which is then eliminated post-synthetically.[49–51]

- ◉ *PSM of the SBU.* Solvent-assisted linker exchange (SALE or PSE, post-synthetic exchange) occurs when the synthesised MOF is put in a solution of the desired linker and a ligand exchange occurs without changing the framework topology, this method is highly useful when the direct synthesis with certain linkers is difficult.[52,53] Another example can be the oxidation or reduction of the metal centre of the SBU.[54]

- ◉ *Ionic interchange.* MOFs possessing an ionic charge usually have counterions in their frameworks to counterbalance the total charge; in the case of PSM, this cations or anions can be exchanged.[55,56]

- ◉ *Encapsulation of nanoparticles.* In the last years, many examples showed that incorporation of metal nanoparticles (MNPs) inside metal–organic frameworks is a promising strategy to design hybrid materials that can be used as catalysts. The encapsulation of NPs into MOFs shows many advantages, like reduction of NP aggregates, size control or stabilisation of the NPs confined into

the pores. In some cases, the catalytic activity of MNPs inside MOFs is even superior with respect to simple metal NPs.[57–59] This topic is explored more in detail in Chapter 4.1.4.

- ◉ *Creation of defects*. Defects can be defined as sites in the crystalline matrix in which the regular and periodic disposition of the atoms is lost because of the absence or dislocation of the atoms or ions. They can be classified in point defects (vacancies), line defects (dislocations), planar defects or bulk defects. When inspecting the location of these defects, they can be divided into internal or external (surface) defects. In certain cases, crystals as perfect as possible are necessary, for example in the optoelectronic field, On the other hand important properties of solids depend on the presence of defects (electronic, adsorption, catalytic, conductivity properties *etc.*). For this reason, the introduction of defects in the MOFs structures is a very interesting strategy to tune their chemical and physical properties. Defects are intrinsically present in every crystal, simply because "perfect crystals" meant as infinite repetition of identical groups of atoms in the space, do not exist. Real crystals always contain a variable quantity of structural defects (Figure 1.10). The simplest way to introduce defects into the crystalline structure of a MOF is via thermal activation. In fact, labile guest molecules, such as solvent molecules, coordinated usually to the metal centres, can be eliminated from the pores of the structure by simply heating the MOF. The result of this process is a porous material with free coordination sites (or open metal sites, OMS).[54,59,59,59–62] Other methodologies frequently used are the reaction with acids or bases or modification of the activation conditions.[44]
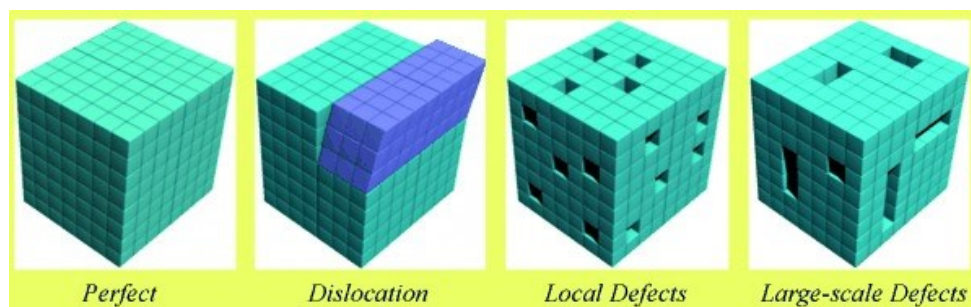
Figure 1.10 - Representation of an ideal crystal and of the most common defects found in crystals.[32]

A different approach to build differently functionalised MOFs is represented by the synthesis of single-phase materials with different ratios of components. This concept originally found in solid state chemistry, has been transposed to MOFs by S. Kitagawa[63] and O. Yaghi,[64] who created the concept of solid solutions, or multivariate, or mixed component MOFs. These can be characterised by different functionalised organic ligands, different SBUs,[65] the important thing being the coordination environment, connectivity and spatial arrangement of the SBUs and the linkers, which must be complementary (Figure 1.11). The advantage is that solid solutions can have advanced properties with

respect to single-component MOFs, thanks to the ability of modulating their composition, pore geometry and space and properties by simply changing the various building blocks.
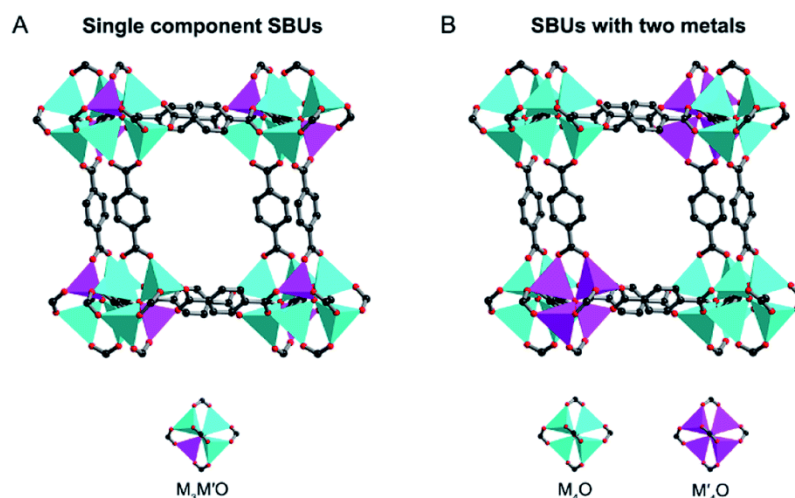
Figure 1.11 - Representation of an example of MOF solid solution featuring a framework with two different SBU with alternating distribution (C, black; O, red; M, green; M', violet).[65]

1.2.5 Applications

As mentioned above, the two classes most used of adsorbing materials for industrial applications (cracking in petroleum refining, removal of calcium from water, air purification, *etc.*) are zeolites and active carbons. Zeolites are natural porous solids whose name comes from the combination of two Greek words ζέω (zéō), to boil, and λίθος (líthos), stone, *i.e.* boiling stone, which stems from their property to free water entrapped in the pores when heated. Zeolites are a class of crystalline tectoaluminosilicate minerals discovered in 1756 by A. F. Cronstedt.[66] There are about 40 naturally occurring zeolites but many others have been synthesised in laboratory and around 200 different structures are known today.[67] A direct consequence of that was the research and synthesis of artificial porous materials possessing more advantages than the natural ones. Thanks to the control of the reaction conditions and engineering of specific and desired properties which lead to the synthesis of MOF-5 (as already discussed in the previous paragraph) and successive porous coordination polymers.

Thanks to their impressive features, which are unique among porous materials, MOFs have found place for numerous applications and industrial processes (Figure 1.12). Even some petrochemical companies have invested in their research and development, such as Chevron, Exxon Mobil Corp., BASF just to cite a few. Some MOFs are also commercially available, the most famous example being the Basolite® series, produced by BASF (*e.g.* Fe-BTC = iron 1,3,5-benzenetricarboxylate, ZIF-8 = 2-methylimidazole zinc salt; MIL-53(Al) = aluminum terephthalate).[68] Moreover, many start-ups that research and produce MOFs

are emerging with the aim of speeding up the thechnological transfer and the scale up process. Some examples are MOF Technologies, NuMat Technologies, NovoMOF, MOSAIC and Particular Materials.[69]

MOFs have been studied for a large variety of applications like gas adsorption and separation[1,70–73] catalysis,[73–76] environmental remediation,[77] biomedicine and drug delivery.[78] Furthermore, the possibility of designing thin-films or depositing MOFs on membranes and textiles, lead to the production of MOF-based sensors,[79] textile filters or membrane separators[80] that can for example be useful as protection against hazardous gases or chemical warfare agents.[81] MOFs are usually insulating materials with a low dielectric constant and can, therefore, be used in the field of microelectronics.[82] Recently, even MOFs with high ionic and/or protonic conductibility have been developed.[83]

Flexible MOFs have huge potential in gas storage and separation thanks to the ability of selectively switch to open or closed pore crystalline phases. Flexibility can also be exploited to design biomimetic dynamic systems capable of capturing and releasing guest molecules.[25,84]

Overall, the most studied field for MOF applications remains gas adsorption and separation. Thanks to the modulation of pore dimension as well as shape and different types of host-guest interactions, they can be used as high capacity reservoirs for gases (H_2 and CH_4) but also for industrial gas separations, like ethylene/ethane, propylene/propane, acetylene/carbon dioxide, propine/propylene; hydrocarbon separation, capture and separation of CO_2, N_2, O_2, CO and many more.[85,86]
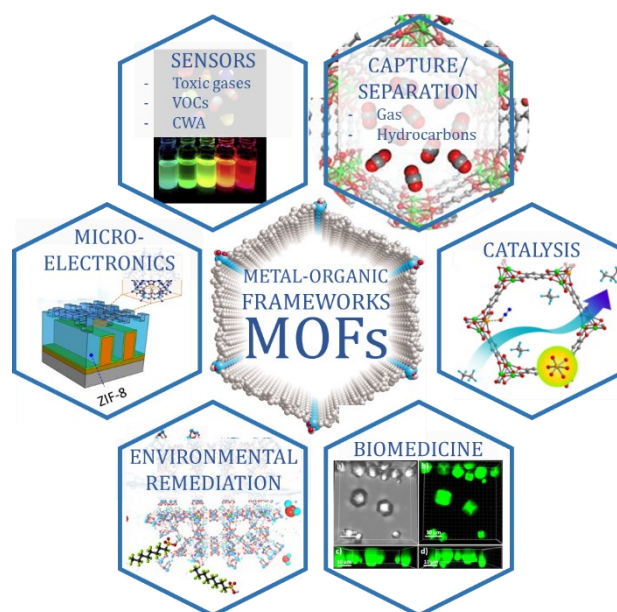
Figure 1.12 - Examples of MOFs' applications.

1.3 Conclusions

The developments in the area of reticular chemistry, *i.e.* the possibility to control the pore structure, accessibility of functional sites and coordinatively unsaturated metal atoms as well as the feasibility to introduce post-synthetic modifications and defects, offer abundant possibilities to be explored within the MOF field.

The best way to characterise MOFs is via crystallographic studies (*in situ* and *operando*) as they give a detailed description of the crystalline structures, adsorption phenomena and correlating property-structure relations such as gas adsorption, thermal stability experiments.

MOFs are becoming increasingly important among porous materials. The design as well as development of more advanced and smarter systems will be the key to mitigate, and maybe resolve, energetic and environmental challenges of our time. This has even been recognized by the IUPAC which has recently put MOFs among the best ten sustainable innovations.[87]

Chapter 2

CO₂ ADSORPTION TO FACE GLOBAL WARMING

2.1 Global Warming and Possible Solutions

The Intergovernmental Panel on Climate Change (IPCC), formed in 1988 by the World Meteorological Organization and the Environmental Plan of the United Nations, produced several reports in which the necessity to plan urgent actions for the climate change caused by greenhouse gases emissions has been made clear. The increase of the CO_2 emissions in the atmosphere during the last decades is due to the dependency of the society on fossil fuels for the generation of energy. In addition to that, other greenhouse gases concentrations in the atmosphere, such as CO_2, CH_4, NO_x and SO_2, are the highest at least of the last 800.000 years according to IPCC fifth assessment report.[88] Global temperatures have been consistently increasing since since 1860 when the industrial revolution began, and the emissions started growing exponentially.

The Paris agreement, constituted in agreement between nearly every nation in the world (192 Countries plus the European Union), sets the objective to limit the increase of CO_2 emissions to less than 2 °C by the year 2100, in order to mitigate the global temperature rise.[89] Another factor that makes the situation even more delicate is the continuous growth of the world's population. Assuming a constant rate, this could bring the global warming to dangerous levels in a range of 4-5 °C and would in fact be a disaster from the climate point of view.

Greenhouse gas emissions by economic sectors

Electricity and heat production 25%
AFOLU 24%
Buildings 6.4%
Transport 14%
Industry 21%
Other energy 9.6%

Total: 49 Gt CO_2-eq (2010)

Energy 1.4%
Industry 11%
Transport 0.3%
Buildings 12%
AFOLU 0.87%

Figure 2.1 - Total anthropogenic GHG emissions (gigatons of CO_2 equivalent per year) from economic sectors in 2010; large point sources and distributed ones are equally responsible for GHG emissions.[90]

A recent report of 2018 regarding the methods for global greenhouse gases (GHG) mitigation,[90] identifies and lists the main sources of carbon dioxide emissions divided by economic sector for the year 2010 (Figure 2.1), these are divided into different categories which are concentrated sources (steel, cement industries, chemical production, *etc.*), distributed sources (transport, heating, *etc.*) as well as the AFOLU category (agriculture, forestry and other land use) which is responsible for a considerable part of emissions.

IPCC experts project a cumulative need of negative CO_2 emissions of 100 to 1000 Gt between now and 2100 based on today's emissions, which are 35-40 Gt/y[91] which corresponds to the reduction of the concentration of CO_2 from the current 415 ppm[92] to below 400 ppm, ideally. This represents a huge scientific challenge.

Until now the technological options to decrease the CO_2 emission in the atmosphere are *a)* to raise the conversion and/or use efficiency of energy; *b)* to increase the use of renewable sources (biofuels, wind energy, *etc.*) or nuclear energy; *c)* to use technologies for the CO_2 capture and storage (CCS). There is an unavoidable component represented by processes that cannot be fully decarbonized yet, such as the cement and steel production. However, there are also negative emission technologies (NET), such as agriculture forestry and changing the way of land usage to try to store more CO_2 underground. None of the described technologies alone can solve the CO_2 emission problem but the CCS seems to be the most promising option. In 2002 the United Nations first defined CCS as the stable capture and storage of carbon emitted in the form of CO_2 for all energetic systems, since then several CCS-related EU projects have been funded and in 2009 the EU Directive on geological storage of CO_2 was published (Figure 2.2).[93] CCS consists in the segregation of CO_2 produced by industries and relative energy sources, its
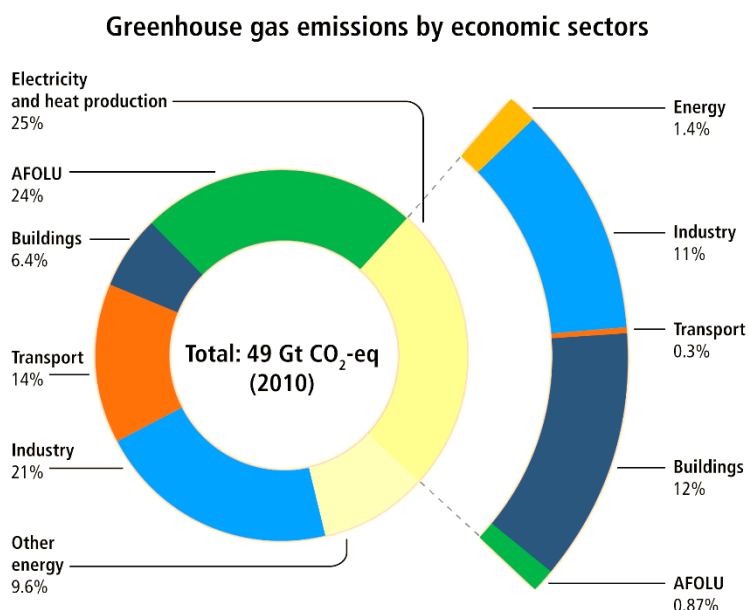
transportation through gas pipelines or ships and its successive long-term deposition in geological formations at more than 1000 metres of depth, in oceans or in the form of inorganic carbonates.
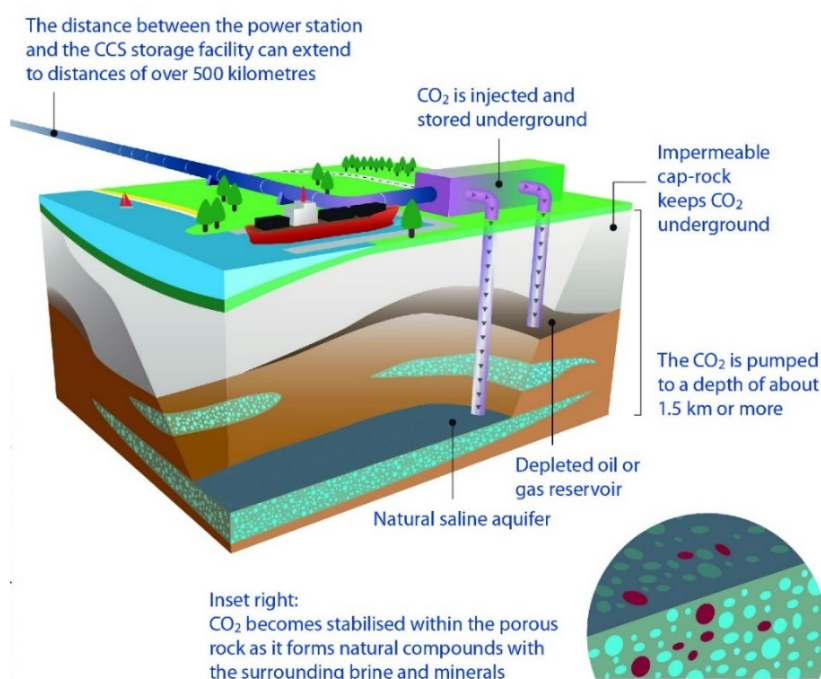
Figure 2.2 - Schematic representation of the CCS process; source: European Commission, DG TREN.

Actual capture of CO_2 is the most expensive step of all the CCS process, which is why it is important to develop new capture systems with low energy and economic impact in order to reduce the overall cost. There are three main approaches to apply CCS: post-combustion capture,[94] pre-combustion[95] capture and direct air capture (DAC).[96] The first two methods are more relevant to the concentrated sources.

⊙ *Post-combustion capture* is suitable for most large point sources, such as which include coal- and gas-fired power plants as well as heavy industry (steel, cement, glass, chemicals) where the CO_2 concentration in the flue gases ranges between 4 and 25% (for gas fired power plants and for steel industry, respectively) together with other species: N_2, CO, H_2O, O_2, H_2, H_2S, NO_x, SO_x. Retrofitting at atmospheric pressure is possible, it means putting a device on top of a chimney to strip the CO_2.

⊙ *Pre-combustion capture* involves the production of syngas (CO + H_2) from fuel reforming, followed by water-gas shift reaction to give CO_2 and H_2. At this point CO_2 is removed from the gas mixture while H_2 is used as fuel with the only final byproduct being water. In this case the carbon dioxide concentration in the stream is 15-25 % together with H_2. The process occurs at pressures between 18-28 bar. Retrofitting is not possible, thus the total cost is higher.

⊙ *DAC* is more suitable for distributed sources, where the CO_2 is captured directly from the air, and if coupled with permanent storage enables negative emissions. The main advantage of this method is that it is not geographically constrained in contrast to the two aforementioned methods. However, the very low concentration of CO_2 in air (0.04 % together with N_2, O_2, H_2O, Ar) represents a big challenge because materials capable of strongly binding diluted CO_2 at atmospheric pressure are very difficult to design.

The chemistry of CO_2 sorbents is a very wide area of research. The and the major categories are liquid absorbents, inorganic porous crystalline solids, porous crystalline solids, polymer-based sorbents, metal oxides as well as porous carbon materials. An overview is given in Table 2.1.[97]

Table 2.1 - Principal CO_2 sorbents divided into categories.

Solid sorbents	*Inorganic porous crystalline solids*	Porous silica (MCM-41, SBA-15), porous alumina, porous aluminosilicate (13X, ZSM-5)
	Porous crystalline solids	Metal-organic frameworks (MOFs), zeolite-imidazolate frameworks (ZIFs), covalent organic frameworks (COFs)
	Polymer-based	Porous organic polymers (POPs), conjugated microporous polymers (CMPs), polymers of intrinsic microporosity (PIMs)
	Metal oxides	Chemical looping
	Porous carbon materials	Activated carbons, activated carbon fibers, ordered porous carbons, nanocarbon graphene
Liquid sorbents	*Aqueous absorbents*	Monoethanolamine (MEA), diethanolamine (DEA), Selexol, *etc.*
	Anhydrous absorbents	Ionic liquids (conventional task-specific, reversible CO_2-triggered switchable solvents), nanoparticle organic hybrid materials
Other approaches	*Membrane separation, hydrate-based separation, cryogenic distillation*	

2.1.1 Liquid Sorbents

The state-of-the-art process for post-combustion capture is amine scrubbing,[98,99] where a 20-30 wt% aqueous monoethanolamine (MEA) is usually employed as the absorbent. The amine acts as a nucleophile which binds the Lewis acid CO_2 at its positively charged carbon atom. This produces carbamates when primary and secondary amines are involved, or hydrogen carbonates, in case of the presence of water (Figure 2.3, left). When tertiary amines are used, water is needed for a reaction to occur and carbonates of tertiary ammonium ions are formed.
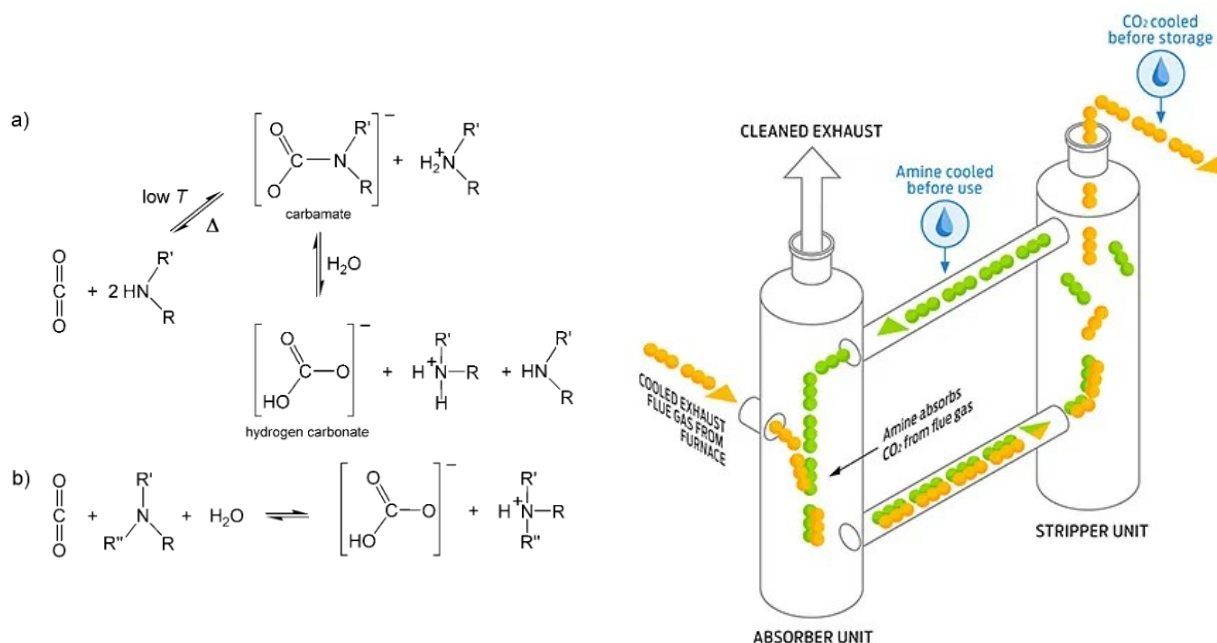
Figure 2.3 - Reaction schemes for the chemical absorption of CO_2 by a) primary or secondary and b) tertiary amines (left).[99] Scheme for amine scrubbing process units (right).

Industrially, this is carried out as a cyclic operation: within the absorber unit a stream of CO_2 is brought into contact with a counterflow of MEA which chemically absorbs the CO_2 by the reaction described above. The CO_2-enriched amine stream has to be transferred to a stripper. In the stripper the temperature is increased in order to regenerate the amine and give it a pure stream of CO_2. The main advantages of this process are the low cost and the high CO_2 working capacity. However, this involves also certain problems. On one hand cleavage of the carbon-nitrogen bond requires high temperatures and a large part of the energy produced by the power plant, which leads to higher energy costs; on the other hand, the toxicity and corrosiveness of amines pose challenges in terms of construction of plants which must withstand these reagents.

2.1.2 Solid Sorbents

In the case of solid sorbents CO_2 is adsorbed, *i.e.* bound, to the huge surface of the material, both external and internal. Examples include porous materials such as zeolites, porous carbons, mesoporous silica, MOFs or Covalent-Organic Frameworks (COFs) which offer a wide range of unique features. However, to utilize them in a commercially viable process, important conditions have to be met to render them an efficient sorbent:[100]

- *high working capacity*, *i.e.* what can be recovered at each cycle (>2 mmol CO_2 per gram of sorbent);
- *recyclability* for at least 1000 cycles;
- *selectivity*, or the ability to absorb CO_2 selectively over other gases, especially N_2;
- *stability* towards temperature (>150 °C), mechanical stress, water, chemicals (H_2S, SO_x, NO_x, HCl, NaOH) as well as the other components found in the respective flue gas;
- *low cost*, ideally less than $ USD 50 per kilogram for the process (sorbent cost <$ 10 per kilogram);
- *fast kinetics* for adsorption and desorption in order to perform more cycles in the unit of time (>1 mmol $(g \times min)^{-1}$).
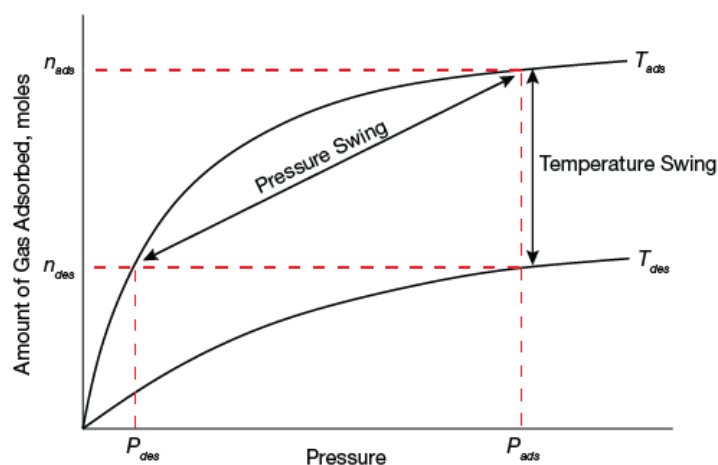
Figure 2.4 - Representation of pressure-swing and temperature-swing cycles in PSA and TSA (n = equilibrium amount adsorbed, P = pressure). Sorbents' working capacity depends on the shape of their isotherm.

In contrast to amines where only temperature swing gas adsorption (TSA) is possible, solid sorbents can also be regenerated by pressure swing gas adsorption (PSA). Figure 2.4 gives a schematic representation of these processes with two isotherms corresponding to adsorption (top, T_{ads}) and desorption (bottom, T_{des}) temperature. Increasing the pressure increases the quantity of CO_2 bound on the surface of the material and once the saturation is reached, hence, regeneration is needed. The working capacity in each case is given by $n_{ads}–n_{des}$. Decreasing the pressure down to that of desorption

(P_{des}), or respectively increasing T_{des} in TSA, the working capacity is increased again and the sorbent regenerated.[101]

With regard to the selectivity in the capture process, nitrogen represents the main competitor for adsorption from flue gas. The key to achieving effective separation are the different properties of these two gases. CO_2 and N_2 differ in terms of quadrupolar moment, polarizability, and kinetic diameter.[102,103] Both molecules are nonpolar molecules and have a quadrupolar moment. However, in the case of CO_2 this is caused by the positive charge on the carbon and the negative charge on the oxygen atoms respectively whereas in N_2 the lone pairs on both atoms produce small negative charges on both ends of the molecule. This causes larger charge imbalances for CO_2 as well as an electron cloud that can be deformed more easily. This plays a crucial role for the interaction with inner surfaces of the solid sorbents. An additional important parameter which is different for both molecules is the kinetic diameter, which is slightly smaller for CO_2 (3.3 Å versus 3.6 Å of N_2). An example for that is the exploitation of diffusion limitation, *i.e.* the ability to discriminate these molecules not simply based on thermodynamics or strength of interactions with the surface, but rather on a kinetic basis or even by physically sieving them.

To characterize and quantify the strength of the interaction of the material's surface with CO_2 requires conclusive parameters. One of these is the enthalpy of adsorption, which is negative because adsorption is an exothermic process. In literature the concept of heat of adsorption (Q_{st}) is used more frequently, even though the only difference is the inversion of its sign to positive.
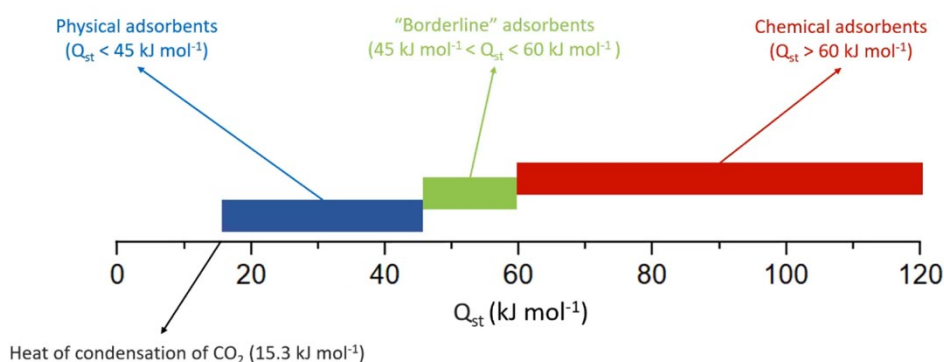
Figure 2.5 - Classification of solid sorbents according to the strength of the interaction between adsorbate and surface given in terms of heat (or enthalpy) of adsorption (Q_{st}).

Physical adsorbents show weak non-covalent interactions with a Q_{st} of less than 45 kJ/mol. In contrast, chemical adsorbents usually form covalent bonds with the surface resulting in a Q_{st} of more than 60 kJ/mol. An intermediate zone with 45 kJ/mol < Q_{st} < 60 kJ/mol includes adsorbents with either very strong physisorption or weak chemisorption. The requirement for utilizing a material for CCS is a Q_{st} of

at least 15.3 kJ/mol, which corresponds to the heat of condensation of CO_2, *i.e.* the interaction energy of CO_2 with itself (Figure 2.5).

The most studied solid sorbents for CO_2 capture of the last years include active carbons, zeolites and MOFs. Active carbons can adsorb large quantities of CO_2 at room temperature, while zeolites possess fast adsorption kinetics, and the entire process requires little energy. One example of a commercially available and heavily used molecular sieve is zeolite NaX (or 13X, Figure 2.6).[104] It is a microporous, cheap synthetic aluminosilicate with faujasite type structure (FAU) which has two different types of pores (7.4 and 11 Å pore diameter), and extra-framework sodium cations to compensate the excess negative charge of the framework. These cations are the main adsorption sites for the quadrupolar CO_2 molecules. However, the use of these materials is limited because they can only perform physisorption and the CO_2/N_2 separation factor is generally low.[105,106] For this reason, porous coordination polymers present a material to obtain CO_2 capture with high selectivity and low energy demand.[107–109]

Zeolite NaX (or 13X)

$Na_7[Al_7Si_{17}O_{48}]\cdot 32H_2O$
Pore size = 11, 17 Å
BET = 330-726 m^2/g

Q_{st} = 40 KJ/mol
CO_2:N_2 selectivity = 150
18/25 mixture, 296 K, 1 bar
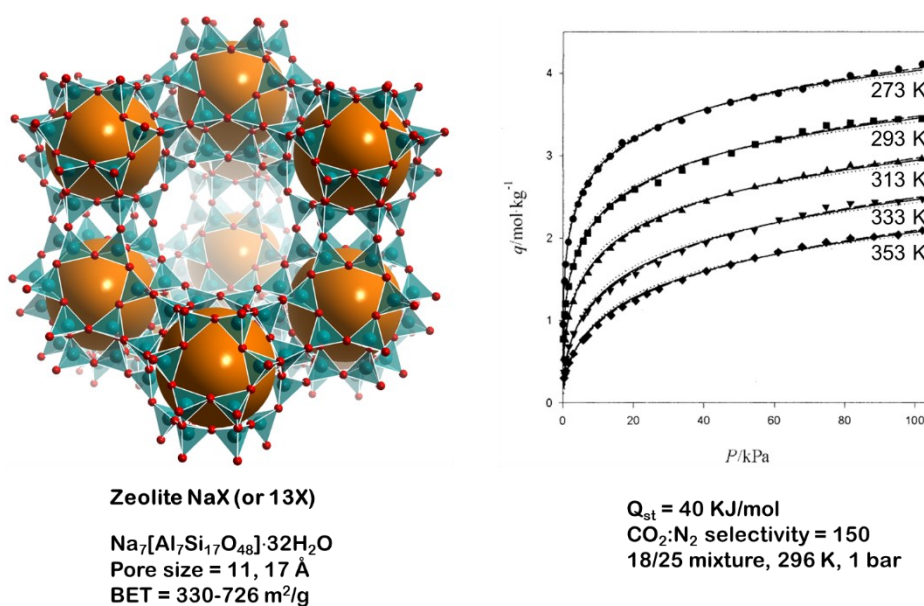
Figure 2.6 - Crystal structure of zeolite 13X (faujasite type), orange spheres represent void space in the sodalite cages (left). Experimental isotherms for CO_2 adsorption for zeolite 13X at various temperatures (right).[104]

2.2 MOFs as CO₂ Adsorbents

MOFs are suitable candidates for CO_2 capture[110] because of the possibility to manipulate decisive properties applying the methods which have been described in Chapter 1.2.4.[111–113] This involves the modulation of pore size and shape, tuning of the interactions between adsorbate/adsorbent, modification of the thermodynamic and kinetic equilibria and consequently the selectivity towards a

particular gas (Table 2.2). MOFs can exhibit a wide range of adsorption mechanisms with carbon dioxide interacting with specific binding sites of the pores through weak forces. The process can be tuned by exploiting the quadrupole moment of carbon dioxide and thus modifying different possible sites of adsorption: *a*) open metal sites,[113] *b*) Lewis basic sites,[114] c) polar functional groups;[115–118] or specific features of the framework: *d*) pore size,[119] *e*) flexibility,[120]) hydrophobicity.[121]

The complex adsorption phenomena shown by many MOFs, which in some cases have not been observed previously in other solid sorbents, need an accurate description in order to improve and develop materials suitable for industrial applications to overcome current problems (Table 2.2). This can be achieved by a combination of advanced experimental and computational methods is such as diffraction methods, X-ray absorption spectroscopy, vibrational spectroscopy, solid state NMR spectroscopy, gas sorption analysis, adsorption thermodynamics or quantum mechanical calculations. In fact, a detailed understanding of adsorption mechanisms can help developing better sorbents for CO_2 capture (and other gas separation as well).[121–123]

Table 2.2 - Advantages and drawbacks of MOFs as CO_2 sorbents.

PROs	CONs
I. (Often) higher CO_2 adsorption capacity and CO_2/N_2 separation than zeolites	I. (Often) low hydrolytic stability
II. Fine tuning of pore size/shape and physicochemical properties to maximize interaction with CO_2	II. In many water-stable MOFs, H_2O preferentially occupies the same adsorption sites of CO_2
III. Improved working capacity and selectivity through structural rearrangements induced by CO_2 adsorption	III. Low CO_2/N_2 selectivity due to high N_2 adsorption (many MOFs are too porous)
	IV. Expensive cost of production

The research group of O. M. Yaghi was the first to synthesise a MOF that could be used for the capture of CO_2.[124] Their publication demonstrated that MOF-177 [$Zn_4O(btb)_2$] (H_3btb = 1,3,5-tris(4-carboxyphenyl); BET surface area = 4508 m^2/g), has a greater adsorption capacity than one of the most used zeolites (13X) and commercial active carbon MAXSORB (Figure 2.7) which justifies the expectations that are made for the research of gas adsorption of MOFs.
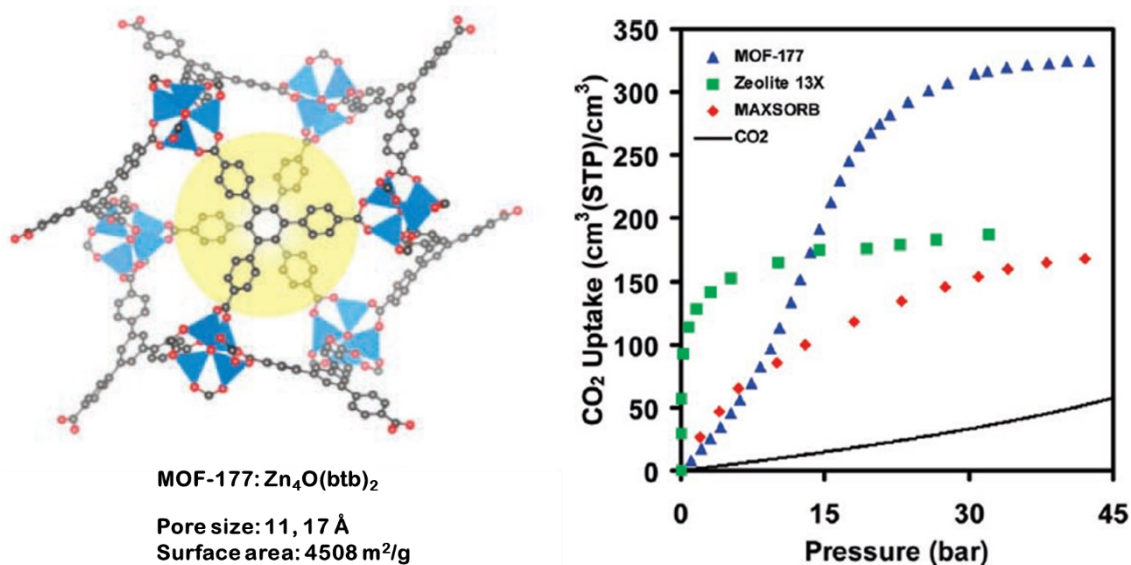
Figure 2.7 - Three-dimensional structure of MOF-177 (Left); comparison of the CO_2 adsorption capture between MOF-177, zeolite 13X and the active carbon MAXSORB (right).[124]

Many other publications about MOFs for CO_2 capture have followed MOF-177.[121,125–127] CALF-20 (Zn_2(1,2,4-triazolate)$_2$(oxalate)), for instance, is an innovative material that has found success in an industrial pilot-scale carbon capture project.[128] This MOF is based on Zn^{2+}, 1,2,4-triazole and oxalic acid and is used to capture the CO_2 produced by a cement factory. Pilot scale tests have been performed using simulated cement kiln off gas (17% CO_2, 10% O_2, 5% H_2O, balanced N_2) which have proved that this material is exceptionally stable and retains its separation performance over hundreds of temperature swings and adsorption cycles.

2.3 Conclusions

To cope with global warming, two different, but complementary, paths can be pursued: investing and researching in the field of green energies; or alternatively, developing more efficient technologies for greenhouse gases capture and sequestration/utilization. Among the proposed approaches to reduce the CO_2 and limit the temperature rise, carbon capture and storage (CCS) and negative emissions technologies (NET), are the most promising ones.

Even though MEA aqueous solutions are one of the most used methods for CO_2 adsorption their regeneration trough high temperature and related energy consuming sets limits for their economical profitably. Solid sorbents such as activated carbons, zeolites and mesoporous silica show some potential as substitutes of amine solutions but suffer from disadvantages such as poor gas selectivity or capacity and high cost of production. In contrast, metal-organic frameworks represent a class of innovative materials that could solve these problems. Many MOFs can be industrially attractive as sorbents, because they possess high thermal and chemical stability, and they can afford multiple cycles of adsorption and recovery. Indeed, a large number of articles which demonstrate the enormous potential of this class of compounds have been published. Thanks to the possibility of modulating MOFs structures by choosing within a vast library of building units (metal ions/clusters and organic linkers), together with their high specific surface area, these porous materials can be suitably modified to obtain specific properties. Additionally, the possibility to modulate pore size and shape, to decorate the pore walls with functional groups and to insert defects, allows the preparation of superior materials with customized adsorption capacity and selectivity.

The comprehension of the fundamental aspects behind the interactions between guest gas molecules and MOF framework, the development of new feasible operating conditions in industrial environment as well as the improvement of selective gas adsorption, material stability, recyclability and production cost, are all crucial fields in which significant progress has been made in the last decades and metal-organic frameworks represent promising candidates.

Chapter 3

AZOLATE-BASED MOFS
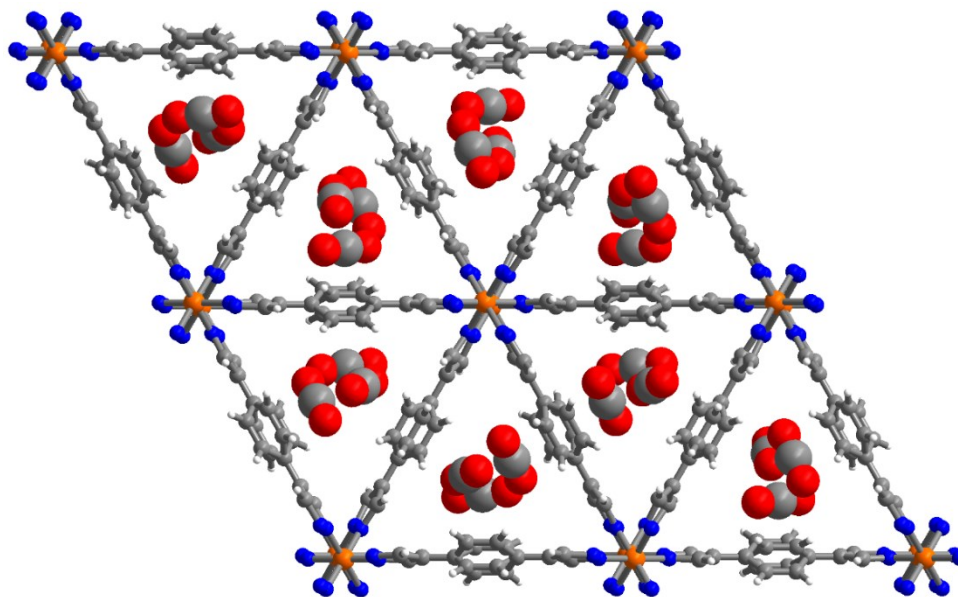
3.1 Enhancing the Stability of MOFs

The chemical and mechanical robustness of MOFs is a fundamental feature for their development in catalysis and all other applications in which harsh working conditions are needed. The robustness of metal-organic frameworks can be generally described as the ability to preserve their structural integrity upon exposure to diverse external stimuli, such as, temperature, pressure, mechanical stress, vacuum, *etc.* The stability of MOFs is indeed correlated to their intrinsic structure, in particular to the metal-ligand bond forming the network, which is the weakest bond in the system. Actually, MOFs can be considered porous crystalline *metastable* materials, in fact, after activation, the solvent is removed from the framework leaving behind a large accessible surface area, generating a metastable material if compared to the dense (solvated) phase. A material is defined metastable when it is only kinetically stable, in other words, there is an activation barrier before it collapses. Therefore, designing a material with higher stability means finding ways to increase this activation energy. A way to increase MOFs' stability is of course the variation of the building blocks which constitute the 3D framework. It has been

demonstrated for instance that the stability of some MOFs decreases with increasing length of the organic linker: this causes the enlargement of the pores size (*e.g.* UiO-66 series,[129] SUMOF-7 series[130]) and the consequent instability of the framework. The cause for this must be searched in kinetic factors, like the rigidity of the ligand, coordination number, interpenetration, and so on.[131,132]

The concept of MOF stability has been focusing on different aspects during the last years, indeed in the early stages when the first porous MOF (MOF-5[133]) was synthesised, the interest was mainly on the thermal and mechanical stability.[134–136] Later, the focus shifted towards the understanding of framework collapse in air and humid conditions.[136] Nowadays, the great advances in characterisation techniques and crystallography in general, allowed the development of new methods of crystal growth and design of advanced porous materials possessing extraordinary stability and interesting properties which lead to industrial applications and commercialisation (see Chapter 1.2.5).

3.1.1 Synthetic Methodologies to Improve the Chemical Stability

In order to enhance the chemical stability of MOFs, two main types of approaches can be followed: *de novo* synthesis of new stable MOFs or improving the stability of existing ones. There are many ways to improve MOFs' stability *via de novo* synthesis:

- ⊙ *Using high-valent metal ions*, according to HSAB principle, high-valent metals with high charge density (hard acids) (Zr^{4+}, Cr^{3+}, Al^{3+}, Fe^{3+}, *etc.*) preferentially coordinate O donor ligands (hard bases) (Figure 3.1), under the same coordination environment, resulting in good chemical stability and strong bonds; additionally, thanks to the low pK_a of carboxylate linkers the metal ion gains some acidic stability. For example, G. Férey and co-workers synthesised the so-called MIL-101(Cr) based on Cr^{3+} ions and carboxylate linkers, which is highly resistant to acids (HCl, pH = 0 and pH = 4) and bases (NaOH, pH = 12) and stable in aqueous solutions of pH = 0–12 for 2 months.[137,138]

- ⊙ *Using low-valent metal ions,* which can be considered as soft acids (Zn^{2+}, Co^{2+}, Ni^{2+}, Fe^{2+}, and Ag^+, *etc.*), together with N-donor ligands (soft bases) (for example azoles, Scheme 3.1) result in highly stable MOFs. The high pK_a of azoles and the strong coordination bonds make these materials resistant in basic solutions (Figure 3.1). But the formation of single crystals is more difficult due to the strong coordination bonds perturbating the continuous self-exchange of metal ions and ligands in the solution helping the crystal growth. A renown example is represented by (ZIF)-8, which is based on four-coordinated Zn^{2+} ions connected through imidazolate linkers to form a zeolite-type framework highly stable in aqueous environment,[139,140] and even in alkaline conditions (8 M aqueous NaOH solution for 24 h at 100 °C). Another impressive example is $Ni_3(BTP)_2$, where Ni^{2+} ions are bound to the pyrazolate ligand H_3BTP (1,3,5-tris(1H-pyrazol-4-yl)benzene (H_3BTPP) Figure 3.5) to build an ultra-stable framework. It can withstand extreme

acid and basic environments, such as boiling aqueous solutions of pH 2 to 14 for a prolonged period of time (2 weeks).[141]
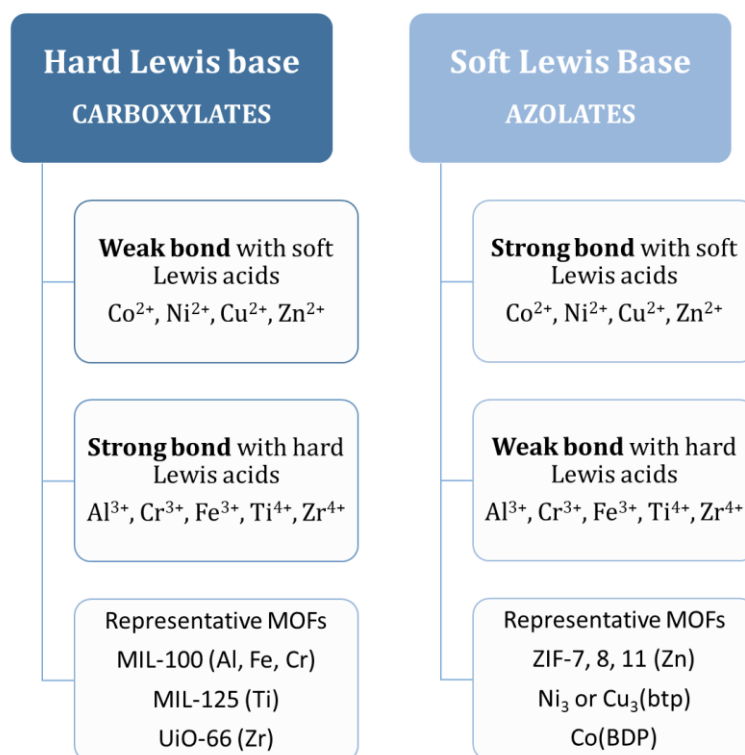
Figure 3.1 - Key points for HSAB theory for the construction of stable MOFs.

- ⊙ *Building mixed-metal MOFs* is a strategy that has shown to produce MOFs with enhanced stability compared to the single-metal counterparts in many cases. The principle lies in the substitution of existing metal ions with others that are more inert. As an example, partially replacing Zn^{2+} with Ni^{2+} ions in MOF-5 to give the Ni-doped material, results in a higher hydrolytic stability.[142]
- ⊙ *Mixing azolate and carboxylate ligands*, the weak coordination interaction obtained between low-valent metal ions and carboxylates results in single crystals of good quality but often fragile, on the other hand high-valent metal ions with the same type of linkers (or low-valent metal ions with azolate linkers) tend to produce microcrystalline powders, preventing single crystal X-ray diffraction studies. In such cases, the use of organic ligands containing both azolate and carboxylate groups can help with this contradiction and yield MOFs' single crystals which are at the same time highly stable and large enough for structure determination. For example, Montoro *et al.* successfully modified MOF-5 by replacing the carboxylate ligand (bdc^{2-}) with an azole containing carboxylic acid ligand (3,5-dimethyl-4-carboxypyrazole, $H_2dmcapz$). The final material has shown to be stable in water and other organic boiling solvents, thanks to the stronger Zn-N bonds, as opposite to the parent MOF-5 which is moisture-sensitive.[143]

- *Using hydrophobic linkers* can help weakening the affinity of MOFs to water (*i.e.* humid conditions); the hydrophobic water repellent functional groups are added on the organic linker and can help protecting the weak coordination bonds around the metal clusters, thus enhancing the MOF stability in water.[144]

- *Introducing stabilizing pillars* into the channels of frameworks possessing very large pores and/or surface areas improves the robustness of the overall network.[145]

- *Creating an interpenetrated framework* avoids the instability caused by excessive free spaces of large porous frameworks. Interpenetration, also called framework catenation, consists in the interweaving or entanglement of two or more independent and identical frameworks in the same MOF structure.[146]

Some methodologies for the post-synthetic modification of MOFs have already been discussed in Chapter 1.2.4, here is reported a comprehensive list of methods useful to improve the chemical stability of existing MOFs:

- *Post-synthetic exchange (PSE)*, including metal-ion metathesis, linker exchange, replacement of the counterions, etc., in order to increase the bond strength or modify the water resistance of the framework without alter it.[147]

- *Post-synthetic modification (PSM)* can modify the pore environment by introducing specific functional groups on the organic linker, and for example improving the material's water stability.[43,148]

- *Hydrophobic surface treatment* becomes useful when the adsorption capacity of a MOF is greatly reduced by the occupation of the channels by dangling functional groups; in this regard, an exterior protective surface avoids the entrance of water molecules into the framework but preserves the internal surface area.[149]

- *Composites* synthesis thanks to the high porosity and compatibility of MOFs which allows for their hybridization with other materials such as polymers, nanoparticles, graphite oxide, carbon nanotubes, *etc*.[150-156] These hybrid materials have combined properties derived from the basic components, which often result in new functions like hydrolytic stability, enhanced mechanical properties and so on.[157]

P. J. Miller *et al.* recently tested the resistance towards a variety of reagents and environments commonly used in organometallic synthesis:[158] *a*) air and solvent stability, placing the desolvated MOFs in an oven at 120 – 180 °C in air for 24h. *b*) Brønsted acids and bases, acids (H^+) typically react with MOFs via protonation of the ligands and consequent rupture of the framework; bases, especially nucleophilic aqueous hydroxide (OH^-), can cause displacement of the linkers leading to M–OH and M–O species.[159] *c*) Electrophiles, such as alkyl halides, halogens and isocyanates (*e.g.* MeCOCl, Me$_3$SiCl, SO$_2$Cl$_2$, Me$_2$SO$_4$), react similarly to the previously described acids with the anionic ligands. *d*) Nucleophiles, such as the corrosive gases H$_2$S and NH$_3$, or solutions of nBuNH$_2$, PhMgBr, TBAF in THF (1.0 M), have been

previously shown to degrade several MOFs[160–162] and their study is of particular importance because many nucleophiles are present in industrial environments (H_2S, NH_3) and most synthetic procedures. *e*) Reductants have been poorly studied in relation to the stability of PCPs, so they have chosen the single-electron reductant samarium iodide (SmI_2) and the strongly reducing solution of $LiBH_4$ in THF (1.0 M) to test the chosen frameworks. *f*) Oxidants, such as O_2 and Cl_2, can oxidise linkers or metal centres;[163,164] in this study different 1.0 M solutions in CH_2Cl_2 (*e.g.* I_2, Br_2, pyridinium cholorochromate (PCC)) have been chosen to perform the stability tests.

They systematically studied the robustness of 17 stable MOFs, which can be divided into three main categories: carboxylate-, salicylate- and azolate-based materials. Specifically, they analysed the XRPD patterns comparing the full width at half-maximum (FWHM) of reflections in order to check the MOF degradation after subjecting the materials to the indicated conditions for 24 hours. The only materials excluded from this study are those that are known to be sensitive to moisture.

Table 3.1 - Representation of stability results as "heat map" as a function of reagent category and MOF. The blue colours mean little-to-no degradation while red colours indicate that significant degradation occurred; the values represent the score from 0 to 1, with 1 indicating 0% change in FWHM.[158]

MOF	Air (2)	Acids (3)	Bases (4)	Nucleophiles (5)	Electrophiles (4)	Oxidants (4)	Reductants (2)
MIL-100 (Fe)	0.91	0.84	0.23	0.63	0.58	0.90	0.00
MIL-100 (Cr)	0.90	0.94	0.24	0.75	0.94	0.94	0.91
MOF-808	0.98	0.88	0.08	0.73	0.93	0.91	0.12
UiO-66	0.97	0.64	0.24	0.74	0.92	0.93	0.31
UiO-67	0.86	0.00	0.00	0.35	0.28	0.35	0.17
PCN-128	0.93	0.00	0.00	0.16	0.46	0.20	0.00
MOF-74 (Mg)	0.46	0.00	0.62	0.89	0.26	0.33	0.81
MOF-74 (Ni)	0.14	0.60	0.69	0.88	0.69	0.81	0.46
Ni$_2$(*m*-dobdc)	0.50	0.64	0.71	0.90	0.63	0.48	0.89
Mg$_2$(dobpdc)	0.93	0.00	0.25	0.47	0.25	0.23	0.78
Mg$_2$(dotpdc)	0.97	0.00	0.22	0.70	0.24	0.43	0.96
ZIF-8	0.95	0.22	0.63	0.78	0.46	0.35	0.82
Ni$_2$Cl$_2$(btdd)	0.96	0.88	0.57	0.95	0.71	0.48	0.00
Ni$_3$(btp)$_2$	0.99	0.61	0.81	0.89	0.42	0.38	0.56
Zn(bdp)	0.97	0.09	0.49	0.45	0.27	0.42	0.39
Ni(bdp)	0.99	0.16	0.33	0.64	0.40	0.28	0.49
Fe$_2$(bdp)$_3$	0.96	0.97	0.93	0.96	0.91	0.73	0.92

$0 \leq S < 0.20$	$0.20 \leq S < 0.40$	$0.40 \leq S < 0.60$	$0.60 \leq S < 0.80$	$0.80 \leq S \leq 1.00$

As shown in Table 3.1, to produce a stability ranking of the MOFs presented in this study, the authors have created a scoring system with values from 0 to 1, where the complete loss of crystallinity (or > 100% change in FWHM) is indicated by a score of 0, while 0% change in FWHM is 1. The study has revealed that the MIL-100(Cr), MOF-808, MOF-74(Ni) and $Fe_2(BDP)_3$ possess the most stable frameworks under the variety of reaction conditions proposed. In particular, $Fe_2(BDP)_3$ has shown unprecedented stability and its crystallinity can be retained under a variety of extreme conditions. As

XRPD analysis alone is not enough to ensure complete structural stability, its robustness has been further evaluated within the same study and also by our research group[165] (see Chapter 3.5.1), *via* IR spectroscopy, gas adsorption measurements, scanning electron microscopy (SEM) experiments, and so on, have revealed minimal changes, confirming the remarkable robustness of this MOF. Therefore, $Fe_2(BDP)_3$ and its solid solutions or pore-expanded analogues,[166] are promising for the development of heterogeneous catalysts, reagents for applications in organic synthesis and industrial applications in general.

In conclusion, the chemical, mechanical and thermal stability of MOFs is an essential feature when dealing with industrial applications, in this regard, many studies have been performed to discover new porous materials that can stand various environments, such as humid air, acid and basic media, extreme temperatures and pressures, water, *etc.*

It is important to note that during the first years of research made on MOFs, industrial applications were in part prevented by some key factors, such as thermal and chemical stability, production costs, environmental impact of solvothermal reactions, which are often performed with toxic and expensive solvents like *N,N*-dimethylformamide (DMF). These drawbacks have been overcome in two different ways: *a)* applying the HSAB theory (hard-soft acid-base)[167,168] to MOF synthesis in order to tune the stability of the desired materials; *b)* optimising synthesis and scale-up reactions based on the principles of "green chemistry".**[169]**

Furthermore, the main advantage of N-donor ligands with respect to carboxylate ligands (O-donor) is the higher stability of the resulting porous materials because of the greater strength of the M-N coordination bond, depending on the basicity of the N-donor groups. For this reason, an increasing number of robust azolate-based MOFs has been published in the last years in the topic of practical applications. The drawback is represented by the formation of products as polycrystalline powders which prevent structural determination from single crystal X-ray diffraction. In the next sections, a more detailed overview of N-donor linkers, with a special focus on pyrazolates, is presented.

3.2 N-donor Organic Linkers: Azoles

Azoles are part of a large class of heterocyclic compounds constituted by five-membered rings in which there is at least a nitrogen atom and one other non-carbon atom (*e.g.* nitrogen, sulphur, or oxygen) as part of the ring.[170,171] They include the heterocyclic rings in Figure 3.2.

This class of heterocyclic molecules is largely used because of its occurrence in natural compounds with biological activity (*e.g.* cardiovascular, anti-inflammatory, antidiabetic agents)[172,173] and their employment in coordination chemistry is gaining more and more importance as it can be seen by the

huge variety of PCPs capable of a wide range of applications,[174] from gas storage and separation to heterogeneous catalysis. Azoles are aromatic molecules in which one of the heteroatoms shares two of its valence electrons with the ring. The majority are basic molecules (azolinium cation is the protonated form), even though azoles can be acidic because they can be deprotonated using a base obtaining the corresponding azolate anion. When deprotonated the pyrrolic nitrogen is negatively charged and can coordinate metal ions, so in the form of azolate anions the basicity of the donor sites increases. They can also act as neutral ligands possessing n-1 coordination sites (with n = number of N atoms) using all valence electrons on the nitrogen atom.
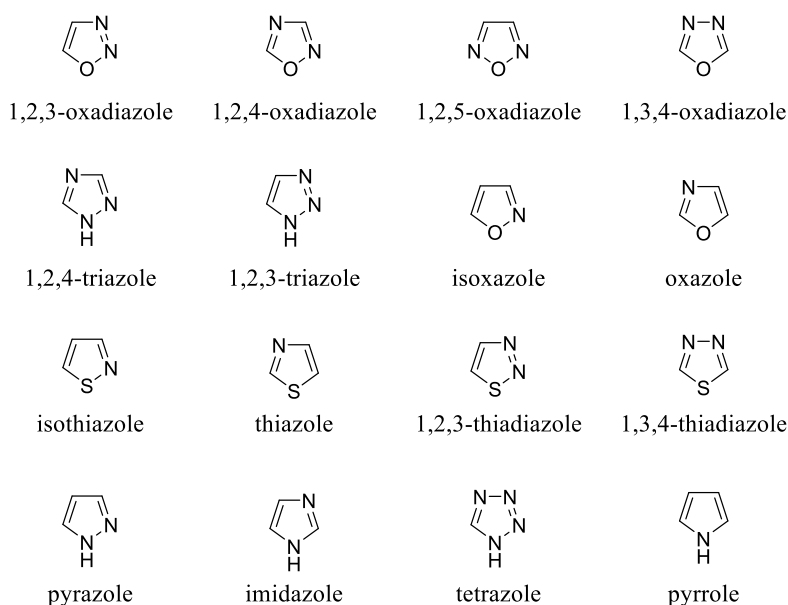
Figure 3.2 - Examples of azole heterocyclic rings.

The nitrogen atom is electron-withdrawing, therefore the higher the number of N atoms, the higher the acidity of the azolate ring. Indeed, it has been observed that azolate-based linkers result in more robust MOFs compared to carboxylate-based ones.[174] In Figure 3.3 the main members of the azolate family are listed, together with their respective pK$_a$ values. It is known that for pyrazolate- and imidazolate-based MOFs, the resulting stability is higher rather than for triazolate- and tetrazolate-based ones. This observation can be correlated to the pK$_a$ value for the deprotonation of the N–H bond, which follow the trend pK$_a$ = 19.8 (pyrazole) > 18.6 (imidazole) > 13.9 (triazole) > 8.2 (tetrazole),[175] indeed resulting in a strong metal-nitrogen bond after deprotonation and, as a consequence, in more stable materials. The disadvantage linked to the strength of the M–L bond lies in the difficulty of growing single crystals for azolate-based MOFs, due to fast precipitation of microcrystalline powders. But this is not always the case, for example, suitable single crystals for XRD analysis of many imidazolate-based MOFs have been easily obtained (*e.g.* ZIF-8[176]).

	pyrazole	imidazole	triazole	tetrazole
pK$_a$	19.8	18.6	13.9	8.2
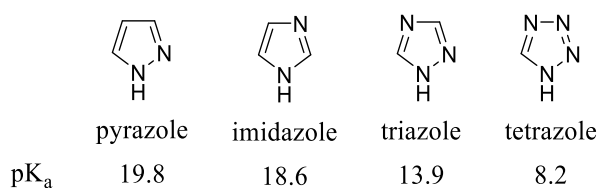
Figure 3.3 - Azole heterocyclic rings and corresponding values of pK$_a$ in dimethyl sulfoxide at 25 °C.

3.2.1 Pyrazoles

Among the simplest azoles containing two nitrogen atoms, pyrazoles are a very common ligand used in coordination chemistry.[177–180] Simple 1H-pyrazoles have a Lewis acid pyrrolic N–H group at N(1), and a Lewis basic pyridine N-donor at N(2), directly adjacent to each other. Therefore, electronically, these heterocycles are both σ-donor and π-acceptor ligands and, as per their steric and electronic features, they are planar and non-bulky ligands. Pyrazoles have attracted considerable interest mainly because their conjugate bases, pyrazolates (obtained by deprotonation of the N(1)–H bond with a base), have been found to bind metals in a variety of coordination modes and, as already anticipated, are also robust bridging ligands (Figure 3.4). The most common coordination modes of the pyrazolate anion are the

mono-dentate mode (κ^1); the exo-bidentate (κ^1:κ^1-μ) and the endo-bidentate (κ^2) ones. In the exo-bidentate coordination mode, pyrazolate ligands have a strong tendency to act as bridges between two metal centers, with a rather small bridging angle (~72°), which results in a metal-metal distance of 3.5 - 4.7 Å (depending on the ion radius). If simple pyrazolate rings are used in coordination chemistry, the structural motifs arising are usually monomers, clusters or low dimensionality polymers.[181–184]

Similar to the relation between traditional coordination compounds and coordination polymers, the collection coordination compounds found in the literature for simple 1H-pyrazoles, can be imagined serving as SBUs for the construction of higher dimensional networks through the use of polytopic pyrazolate-based ligands. As a matter of fact, polytopic pyrazolate-based ligands have been designed during the years and coupled to late transition metal ions to obtain highly porous and stable MOFs. The design of many organic linkers with different aromatic spacers, or bearing various donor sites, exemplifies the "reticular chemistry" approach that requires the use of small building units to direct the assembly of ordered networks. In order
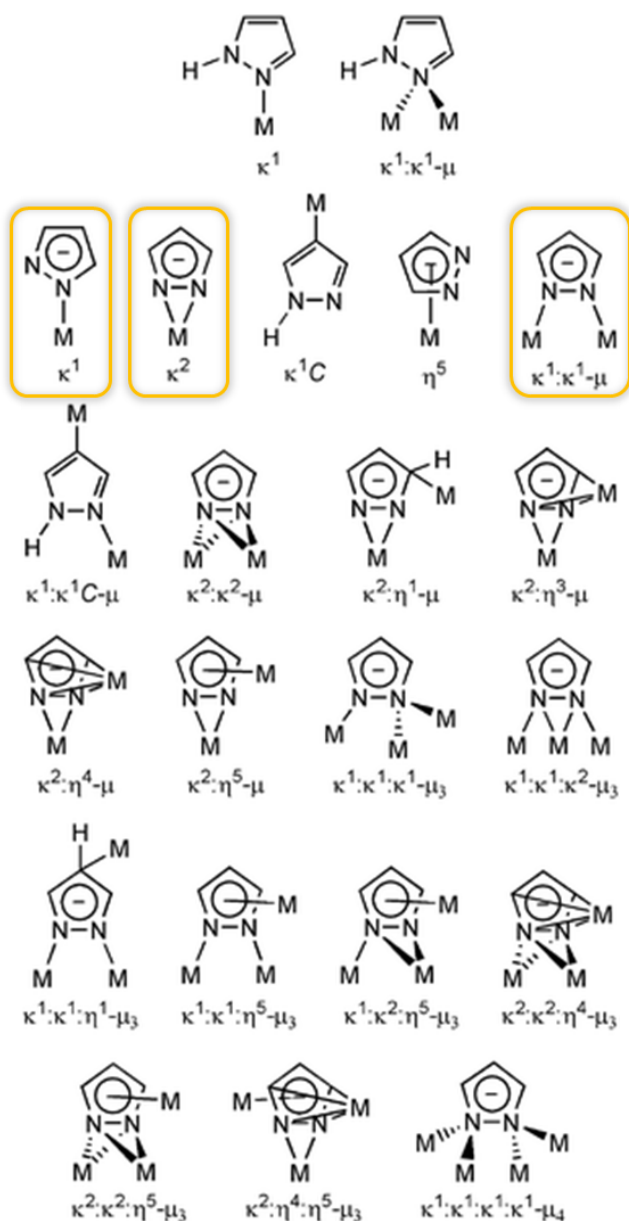
Figure 3.4 - Coordination modes for the pyrazolate anion. The most common ones found in coordination chemistry are highlighted in yellow.

to design 3D MOF structures, the choice of the metal ion and the pyrazolate-based linker is fundamental, in particular the dimensionality of the structure can be increased making use of polytopic pyrazolate-based linkers, capable of bonding two or more metal ions. Some examples are reported in Figure 3.5. and the simplest one is obtained through the condensation of two pyrazolate rings on the C4 atom to form the bitopic 4,4'-bis(pyrazole) (H_2BPZ).[185] Following the concept of reticular chemistry, the length of the linker has been increased through the use of aromatic rings as spacers between the pyrazoles. This strategy is well represented by the linkers 1,4-bis(pyrazol-4-yl)benzene (1,4-H_2BDP),[186] 4,4'-bis(1H-pyrazol-4-yl)biphenyl (H_2PBP)[187] and the bis(N-(3,5-dimethyl-1H-pyrazol-4-yl))naphtalenetetracarboxylic-dianhydride (H_2NDI-H).[188]
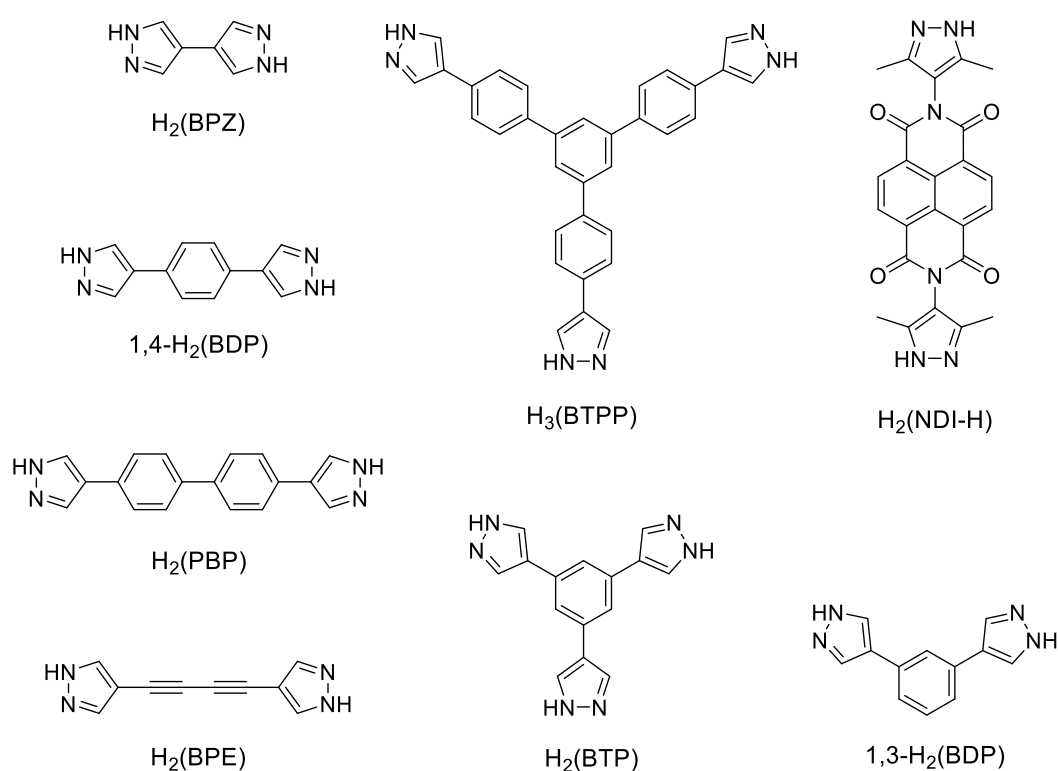
Figure 3.5 - Some examples of poly(pyrazole) linkers reported in the literature: H_2BPZ = 4,4'-bis(pyrazole),[185] 1,4-H_2BDP = 1,4-bis(pyrazol-4-yl)benzene, [186] H_2PBP = 4,4'-bis(1H-pyrazol-4-yl)biphenyl,[187] H_2BPE = 4,4'-buta-1,3-diyne-1,4-diylbis(1H-pyrazole),[189] H_3BTPP = 1,3,5-tris((1Hpyrazol-4-yl)phenyl)benzene,[188] H_3BTP = 1,3,5-tris(1H-pyrazol-4-yl)benzene,[186] H_2NDI-H = bis(N-(3,5-dimethyl-1H-pyrazol-4-yl))naphtalenetetracarboxylic-dianhydride,[188] 1,3-H_2BDP = 1,3-bis(pyrazol-4-yl)benzene.[190]

In addition to purely pyrazolate-based ligands, there is a considerable range of hetero-functional linkers such as carboxylate-, tetrazolate-, imidazolate-, pyridine-pyrazolate ones.[186,188,190,191] The combination of different functionalities allows to obtain more versatile materials possessing specific properties. For instance, MOFs based on mixed carboxylate–pyrazolate linkers are more sensitive to water in

comparison to those purely constituted by pyrazolate linkers, which usually show high stability in humid conditions.[189] In this regard, it is anticipated here that the scale-up and improvement of the synthetic route for a new mixed pyrazolate/carboxylate-based linker has been developed in our research group (Figure 3.6). The desired product has been obtained pure and in decent yield and it will be used for the construction of highly stable and flexible MOFs in the future.
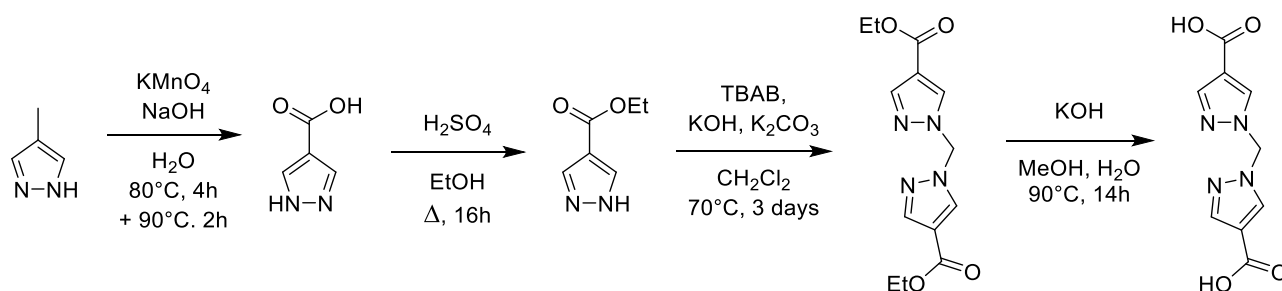
Figure 3.6 - Synthetic path for the new carboxylate/pyrazolate-based ligand.

3.3 Pyrazolate-based MOFs

Among the dinitrogen linkers, pyrazoles have been widely used in the synthesis of MOFs. Even though, only in recent years, materials containing this type of linker have become progressively more common; possible reasons include difficulty in the deprotonation of the ligand together with the very short bridging length, which cause the formation of highly insoluble and microcrystalline products. Nevertheless, pyrazolate ligands can impart very interesting properties to the desired products, which will be discussed in the next paragraph. For this reason, they are becoming more and more common in the MOF field. Indeed, in the Cambridge Structural Database (CSD) MOF subset (today it counts 112,400 reported structures), the difference in number of published papers between carboxylate- and pyrazolate-based MOFs is enormous: 45,403 (for O-based) versus 764 (for N-based) reported structures. But the latter category has been developing quite fast in the last years (Figure 3.7) thanks to various factors, among which
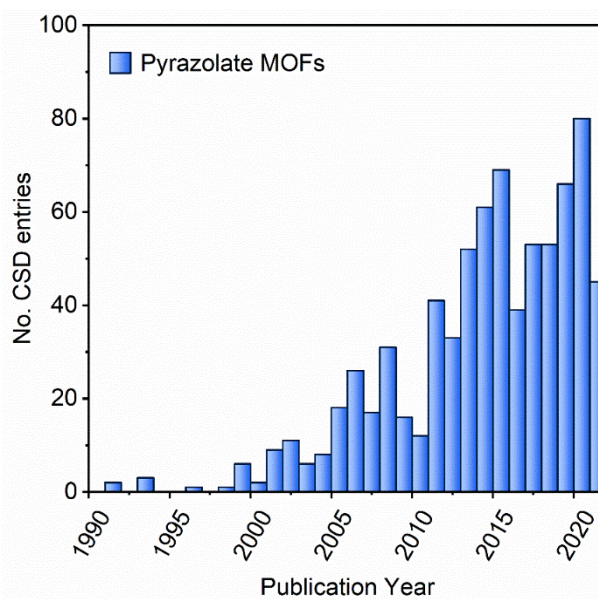
Figure 3.7 - Graphical summary of the number of publications containing pyrazolate-based MOFs over the period 1990-2022.

the development of more sophisticated characterisation techniques and the ability to synthesise more variate and complex organic linkers.

The most common SBUs observed in pyrazolate based MOFs are depicted in Figure 3.8: (*a*) octahedral [$M_4(m_4-O)(m-pz)_6$], (*b*) cubic [$M_8(m_4-OH)_6(m-pz)_{12}$], (*c*) triangular [$M_3(m_3-O)(m-pz)_3(H_2O)_3$]$^+$, (*d*) double zigzag chain with square-planar metal ions, (*e*) double zig-zag chain with tetrahedral metal ions and (*f*) triple zig-zag chain with octahedral metal ions.[192]

As anticipated, these SBUs recall the coordination chemistry of simple pyrazoles, and have been used to build 3D porous coordination polymers exploiting polypyrazolate linkers, like the ones shown in Figure 3.5 (Chapter 3.2). In metal-organic frameworks chemistry, the first most prominent example of metal-pyrazolate frameworks is probably the one published by J. Long and co-workers and called [Co(BDP)]

(H$_2$BDP = 1,4-bis(pyrazol-4-yl)benzene). This MOF can be seen as an extension of Co(pz)$_2$ chains by the long, coplanar ligand H$_2$BDP (Figure 3.9, left).[193] Using the same linker, but exploiting different metal geometries, MOFs possessing various pore geometries can be obtained. For example, using the octahedral geometry typical of Fe^{3+} metal ions, the rigid 3D framework Fe$_2$(BDP)$_3$ is obtained. In this MOF triple zigzag chains of Fe^{3+} metal ions and pyrazolate rings in their *exo*-bidentate mode are found (Figure 3.8f) and forms triangular channels rather than the square ones observed for [Co(BDP)]. According to XRPD data, Fe$_2$(BDP)$_3$ has a remarkable chemical and thermal stability.[194] A more detailed description of this MOF can be found in Chapter 3.4-5.
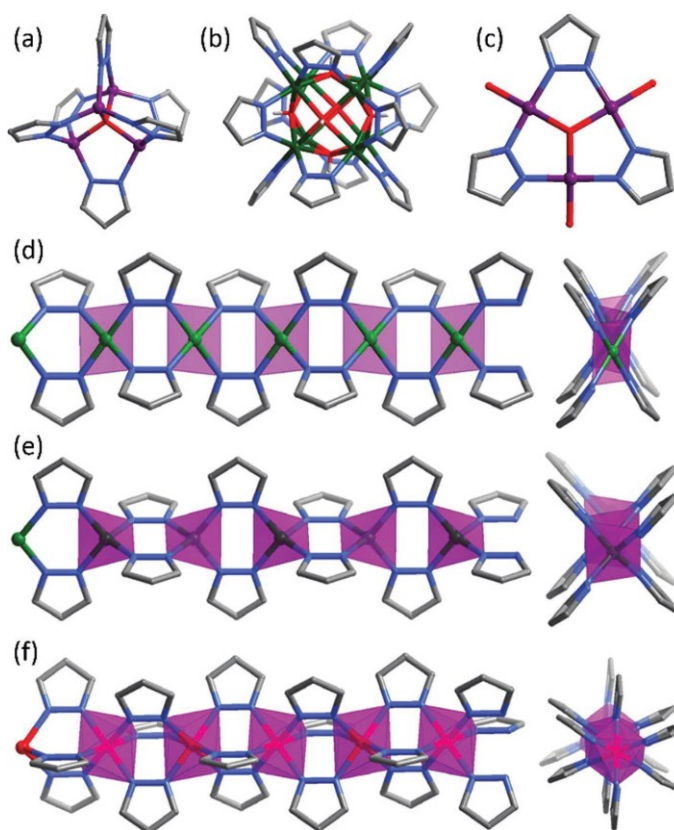
Figure 3.8 - Structural representation for the most common SBUs based on bidentate coordinated pyrazolates.[192] Colour code: O, red; N, blue; C, grey; other colours, different metal ions. The hydrogen atoms are omitted for clarity.
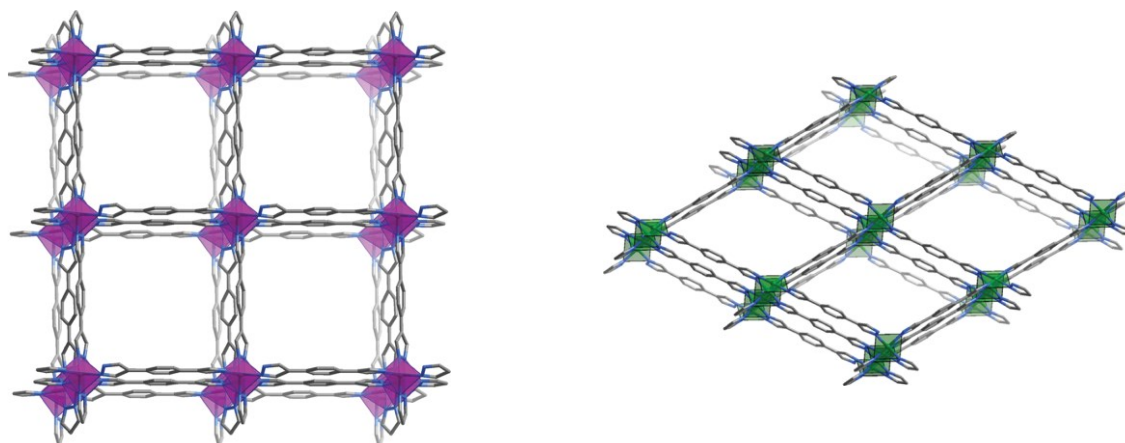
Figure 3.9 - Structure of [Co(BDP)] in its most expanded configuration (left); structure of [Ni(BDP)] in its contracted configuration. Colour code: Co, purple octahedron; Ni, green rhombi; O, red; N, blue; C, grey. Hydrogen atoms are omitted for clarity.

[Ni(BDP)] is another important example of pyrazolate-based MOF possessing, in this case, square planar Ni^{2+} ions. S. Galli and co-workers reported in 2010 the synthesis and *ab initio* XRPD structural determination of [Ni(BDP)], together with its capability of removing harmful organic vapours, even in the presence of humidity (Figure 3.9, right).[186]

Exploiting the similarity between pyrazolate and carboxylate derivatives, it is possible to replace or combine these two types of linkers in the same framework; for example, L. Hou *et al.* partially substituted the benzenedicarboxylate spacer in $[Zn_4O(bdc)_3]$ (MOF-5) with bpz^{2-} and obtained the isoreticular framework $[Zn_4O(bpz)_2(bdc)]$.[195] Complete replacement of all dicarboxylates with bipyrazolates in the same system was achieved by M. Tonigold and co-workers using a long ligand, 1,4-bis[(3,5-dimethyl)-pyrazol-4-yl]benzene.[196] Cubic octanuclear Ni-based SBUs have been reported for another highly porous Ni-based MOF, $[Ni_8(\mu^4\text{-}OH)_4(\mu^4\text{-}OH_2)_2(PBP)_6]$ (H_2PBP = 4,4'-bis(1H-pyrazol-4-yl)biphenyl, Figure 3.5) with a Langmuir surface area over 1700 m^2/g. This MOF is indeed based on long linear bis-pyrazolate ligands and octanuclear SBUs of formula $[Ni_8(\mu^4\text{-}OH)_6(pz)_{12}]^{2-}$.[197]

It is nowadays known that the possible practical application in gas separation or capture processes does not depend exclusively on the adsorption properties of the materials, but also on their chemical and thermal stability in environmental conditions, their use in continuous cycles (lifetime), on the costs of production and the feasibility of their synthesis from an engineering point of view. Moreover, water stability is an important factor because MOFs are handled most of the time in air (*i.e.* humid conditions), making their stability toward water an unavoidable feature. Indeed, a high adsorption capacity, a good selectivity, a favourable adsorption kinetic, a good regenerability and a high thermal stability are the desired properties for a material that will be promising for gas separation and air purification.

The constantly increasing preoccupation for the environment has promoted research in many fields in order to limit the consequences of climate change. This is also true for the MOF field, in which many

research groups decided to design and analyse innovative porous materials for the capture and separation of greenhouse gases, such as CO_2. In this regard, one of the first materials synthesised for this purpose was [Cu(hoxonic)(bpy)$_{0.5}$]·1.5H_2O, capable of selectively capturing CO_2 in gas mixtures of CO_2/CH_4.[198] Another example is HKUST-1 which, thanks to post-synthetic modification, gained a higher adsorption and selectivity towards CO_2 also in humid conditions.[198] J. A. R. Navarro and co-workers focused on the construction of MOFs based on N-heterocyclic ligands, possessing strong M–L bonds, which showed great performances for gas separation,[199] capture of toxic volatile organic compounds (VOCs)[189] and catalysis.[200] For instance, the isoreticular series [Ni$_8$(OH)$_4$(H_2O)$_2$(L)$_6$]$_n$ based on L = functionalized linear bis-pyrazolate based linker is noteworthy, these MOFs possess high stability and permanent porosity, moreover, some of them have also high hydrophobicity, and thanks to these characteristics these materials are useful in the capture of diethyl sulfide (DES), also in extreme humidity conditions (80% relative humidity).[186]

In the last years, a longstanding collaboration between the research groups of J. A. R. Navarro of the University of Granada, N. Masciocchi of the University of Insubria and V. Colombo of the University of Milan, contributed to the development and the structural characterisation of a pyrazolate-based MOF family. For this purpose, many different pyrazolate-based ligands have been synthesised. Coupling these linkers with metal ions from the first series of transition metals, they have obtained a highly robust series of PCPs useful for gas adsorption and separation, VOCs capture and catalysis. The research topic evolved with the objective of optimising the selectivity of the materials in gas separation experiments, in this regard, the proposed method was to functionalise the channels of the synthesised MOFs introducing particular functional groups on the organic spacing ligands, in order to enhance the specific interactions with guest molecules. Indeed, they performed the pre-synthetic modification of H_2BDP introducing various tags on position 2 on the aromatic ring, obtaining an isoreticular series of MOFs of general formula: M(BDP-X) with M = Ni^{2+}, Zn^{2+} and X = NO_2, NH_2, OH, SO_3H (Figure 3.10). It has been demonstrated that the functionalisation of the framework with these polar groups enhances the selectivity resolution of mixture of polar/nonpolar gases (*e.g.* N_2/CO_2 or CH_4/CO_2),[199] as well as the capture capacity towards harmful volatile organic compounds, such as thiophene or DES.[186]
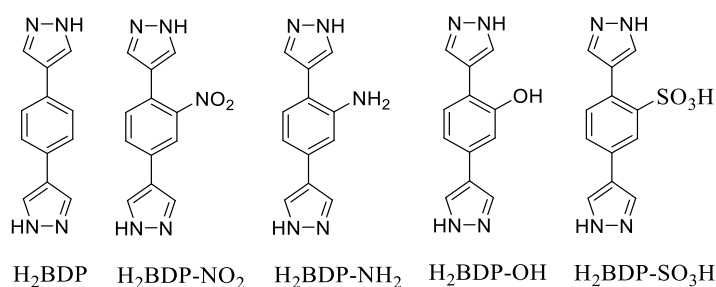
Figure 3.10 - Functionalised linkers derived from 1,4-*di(*1H-pyrazol-4-*yl)*benzene (H_2BDP).

3.4 Robust MOFs for Gas Adsorption Applications

As discussed earlier, azolate MOFs comprehend a vast family of frameworks possessing high stability. Pyrazolate-based ones particularly show excellent hydrothermal resistance thanks to the strong M-N coordination bond.[141,158,185,194] Considering all the information given in the previous chapters, the key aspect of this work has been the development of strategies for studying and developing new pyrazolate-based porous materials[186,199,201,202] but also tuning properties of other interesting known MOFs in order to improve their adsorption capacity of towards the capture of the greenhouse gas CO_2. Indeed, the objective of this work focuses on the synthesis and full characterisation of highly stable MOFs, based on various pyrazolate linear linkers and different metal ions. In particular, the aim is to understand the correlations between the crystal structure and the macroscopic properties, focusing on CO_2 gas adsorption and separation. Then, study the effects of linker substitution on the gas adsorption capacity and test the robustness of the synthesised porous materials. Indeed, a deep insight into the chemical, physical and mechanical stability of the structures will be fundamental to better understand the gas adsorption properties.

On the basis of previous studies on pyrazolate-based MOFs and the great stability shown by this family of materials (recalling for example the isoreticular series M(BDP-X) described in Chapter 3.3), the focus of the first part of this PhD project will be on three pyrazoles, namely H_2BDP (1,4-bis(pyrazol-4-yl)benzene) and their functionalised versions with a nitro or amino group attached to the benzene ring: $H_2BDP-NO_2$ and $H_2BDP-NH_2$ (Scheme 3.9), which have been used for the preparation of two isostructural series of porous MOFs of formula $Fe_2(BDP)_{3x}(BDP-NH_2)_{3(1-x)}$ (x = 0, 0.5, 1) and $Zn(BDP)_{0.5}(BDP-X)_{0.5}$ (X = NH_2 or NO_2) based on Fe(III) and Zn(II) ions, respectively, which generally result in stable frameworks of easy handling in air. The results obtained for the iron-based MOF series is presented in Chapter 3.5, whereas preliminary data on the zinc-based ones can be found in Chapter 3.7.

The three organic ligands have been synthesised according to reported procedures. The H_2BDP ligand was prepared trough a Vilsmeier-Haack formylation reaction with *p*-phenylendiacetic acid and $POCl_3$/DMF, followed by quenching in water and metathesis with $NaClO_4$, giving the intermediate which is isolated as bis(perchlorate) vinamidium salt. The successive heterocyclisation with hydrazine leads to the desired ligand in good yield.[182,203,204] The $H_2BDP-NO_2$ ligand was obtained introducing on the 2-position of the benzene ring of H_2BDP a nitro group through a simple nitration reaction, using a mixture of sulphuric acid and nitric acid.[205] The $H_2BDP-NH_2$ was synthesised from $H_2BDP-NO_2$ via reduction of the nitro group with Pd/C (10%).[206] The three iron-based MOFs, $Fe_2(BDP)_3$, $Fe_2(BDP-NH_2)_3$ and $Fe_2(BDP)_{1.5}(BDP-NH_2)_{1.5}$, have been synthetized according to a synthetic procedure previously reported in the literature by Herm *et al.* in 2013.[194] For the

H_2BDP $H_2BDP-NO_2$ $H_2BDP-NH_2$

Figure 3.11 - Pyrazole based ligands used for the synthesis of the MOFs presented in this Thesis.

multivariate MOF two previously prepared solutions containing the organic linkers in DMF are put together and shortly stirred prior to solvothermal reaction. The samples have been then accurately washed following the same procedure: three times in DMSO at 100 °C, three times in DMF at 100 °C, three times in CH_2Cl_2 at room temperature for 8 h (total time > 72 h); finally, they have been and thermally activated at 180 °C for 24 hours under vacuum. An important note is that, among the synthesised PCPs, $Fe_2(BDP-NH_2)_3$ and $Fe_2(BDP)_{1.5}(BDP-NH_2)_{1.5}$ are new and not yet published. The complete synthetic methodologies and preliminary analytical characterization can be found in Chapter 3.5 (additional details can be read also in the Experimental section Chapter 6.2-3). The exceptional robustness of $Fe_2(BDP)_3$ has been widely studied,[158,194,207] however an extensive study of the structural modifications during the CO_2 adsorption process has never been done. Indeed, in this work *in situ* high resolution powder X-ray diffraction (HR-XRPD) on the already reported $Fe_2(BDP)_3$ in comparison with the preliminary results obtained for the novel amino tagged and the multivariate MOF counterparts, have been performed together with a range of other analytical techniques. With the aim of comparing and understand the correlations between the crystal structures and the macroscopic properties, with a particular focus on gas adsorption and separation.

Pyrazolate-containing MOFs often precipitate as microcrystalline powders and for the products obtained in this work is no exception. However, the impossibility to grow single crystals did not prevented structural investigations, since X-ray powder diffraction (XRPD) allowed to disclose otherwise non-accessible crystallographic features.[208]

The long-term goal will be the design of MOFs capable of withstanding extreme conditions for possible practical industrial applications as gas capture systems for flue-gas.[209–211]

An overview on the general characteristics of the MOFs studied in this thesis is given in Table 3.2. Please note that a more detailed description of these materials has been given in the next sections.

Table 3.2 - Overview of the Fe(III) pyrazolate-based MOFs studied in this thesis.

	$Fe_2(BDP)_3$	**$Fe_2(BDP-NH_2)_3$**	**$Fe_2(BDP)_{1.5}(BDP-NH_2)_{1.5}$**
Composition	M = Fe^{3+} L = BDP^{2-}	M = Fe^{3+} L = $BDP-NH_2^{2-}$	M = Fe^{3+} L = BDP^{2-} + $BDP-NH_2^{2-}$
Space group	*Fddd* (orthorhombic)	*Fddd* (orthorhombic)	*Fddd* (orthorhombic)
Main properties	Highly robust, rigid framework, triangular channels		

3.5 Results and Discussion

3.5.1 Crystal Structure, Chemical and Thermal Stability

The isostructural nature of $Fe_2(BDP)_3$,[194] $Fe_2(BDP-NH_2)_3$ and $Fe_2(BDP)_{1.5}(BDP-NH_2)_{1.5}$ has been confirmed by XRPD (Figure 3.12a). Indeed, these MOFs present the same structural features, they crystallize in the orthorhombic space group *Fddd* and their crystal structure consists of one-dimensional μ^2-pyrazolate-bridged chains of octahedral iron(III) nodes, which run along the crystallographic *a*-axis (Figure 3.12b), connected in three dimensions by the BDP^{2-} linkers, to yield rigid frameworks with triangular 1-dimensional channels (Figure 3.12c). Additional details regarding Le Bail refinements and the resulting unit cell parameters for each MOF can be found in the Experimental Section (Chapter 6.3.2).
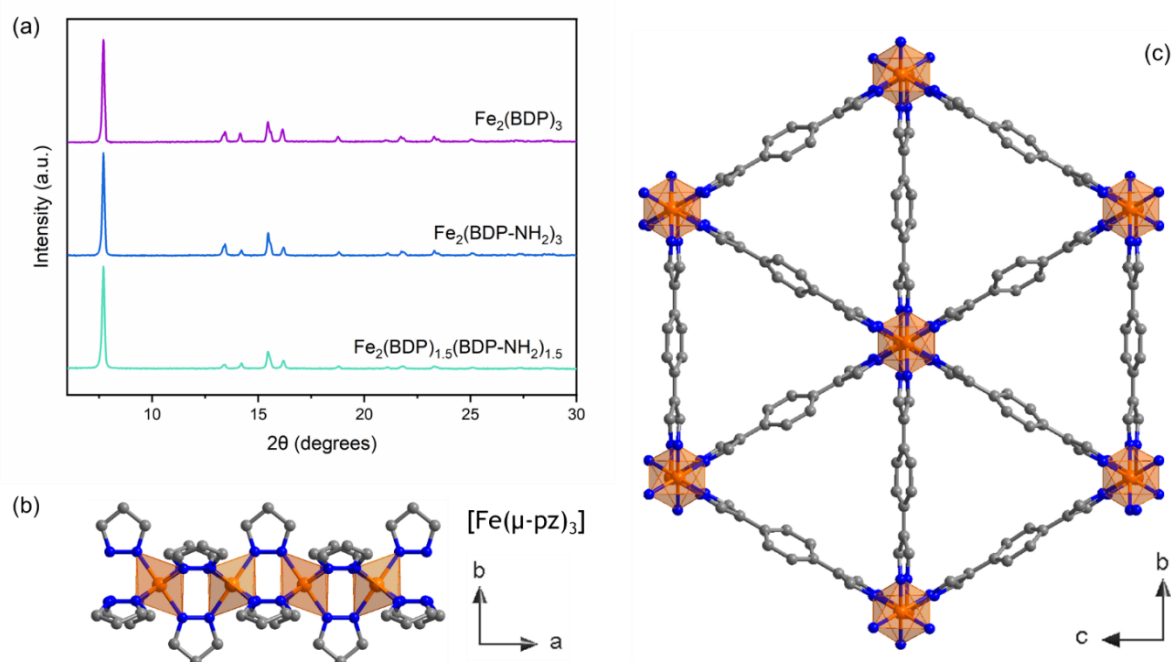
Figure 3.12 - a) XRPD patterns for the isostructural MOFs of the series $Fe_2(BDP)_{3x}(BDP-NH_2)_{3(1-x)}$ (x = 0, 0.5, 1), the comparison between the diffraction patterns of the parent material and those of the tagged MOFs demonstrates the formation of pure, topologically equivalent, phases. b) Representation of a portion of a μ^2-pyrazolate-bridged chain of octahedral Fe(III) ions and c) the MOF crystal structure viewed along the [100] crystallographic direction. H atoms and functional groups on the BDP^{2-} linker are omitted for clarity.

The effective presence of the functional tags on the organic linkers was probed by FTIR. Comparison between the IR spectra of the parent $Fe_2(BDP)_3$ and the tagged/multivariate MOFs shows differences in the spectra of the latter, with typical signals form the absorption modes of the NH_2 functional group, further confirming the effective functionalization of the pore surfaces of each MOF. The experimental Chapter 6.3.3 provides a complete description of the IR spectroscopy characterization.

$Fe_2(BDP)_3$ has been recently recognized as one of the more stable MOFs reported so far.[158] Its high thermal and chemical stability, already demonstrated for other pyrazolate-based MOFs,[132,209,212] can be related to the strong Fe^{3+}–N bonds and the highly connected crystal structure. This material shows excellent hydrolytic stability and no relevant loss of crystallinity in presence of acids, bases, nucleophiles, electrophiles, oxidants and reductants. For example, it has been shown that it is one of the few azolate frameworks able to survive submersion for 24 hours in MeOCl and SO_2Cl_2/CH_2Cl_2 (1.0 M), which are strong electrophiles reagents, despite the nucleophilic N-based linkers. It is also exceptionally stable towards strong oxidants, such as Br_2, but also reductants, such as $LiBH_4$ solution, and other extreme conditions. For comparison, $Fe_2(BDP-NH_2)_3$ has been also tested under harsh conditions. The crystalline powder has been suspended in aqueous solutions of HCl (pH = 2) and NaOH (pH = 14) for a prolonged period of time (21 days); the crystallinity has been checked via XRPD and the results show no crystalline phase transition, nor decomposition of the framework.

Comparing this MOF with very similar others possessing the same crystal structure, such as $Fe_2(BPEB)_3$,[166,209] $Fe(BPEB-F1)_3$, $Fe(BPEB-F2)_3$ and $Fe(BPEB-F4)_3$ (H_2BPEB = 1,4-bis(1H-pyrazol-4-ylethynyl)benzene, with an increasing number of fluorine atoms on the central p-phenylene ring: BPEB-F1, BPEB-F2, BPEB-F4), a significant difference in decomposition temperatures can be observed, $Fe_2(BPEB)_3$ and derivatives start to decompose in the range 300-415 °C,[212] while $Fe_2(BDP)_3$ at 450 °C. Moreover, when $Fe_2(BPEB)_3$ is exposed to water vapours, one of the components of flue gas, hydrolysis takes place.[209] Also the thermal stability of $Fe_2(BDP-NH_2)_3$ has been evaluated by VT-XRPD and simultaneous TG/DSC analyses and compared to that of the parent MOF (see Experimental Sections Chapter 6.3.4 and Chapter 6.3.5). The results demonstrate the high thermal stability of the framework, even in the presence of substituents on the organic linkers. The highest decomposition temperature being observed for the not-substituted MOF: 430 < T_d < 450 °C. In the TG curves of the as-synthesized forms of all measured materials, each weight loss step that occurs below the decomposition temperature can be assigned to the removal of the occluded guest molecules.

Moreover, $Fe_2(BDP)_3$ can stand controlled reductive insertion of cations to access mixed-valence $Fe^{2+/3+}$ MOFs.[207,213] Considering the relevance of the thermal and chemical stability of MOFs when industrial applications are sought,[168] particularly for CO_2 separation processes, we decided to complement the available data on the chemical stability with the characterization of the thermal properties, performing a variable-temperature powder X-ray diffraction (VT-XRPD) experiment, up to thermal decomposition (Figure 6.8, Experimental Section), coupled to a simultaneous thermal analysis (Figure 6.6, Experimental Section). As shown by thermogravimetric analysis and VT-XRPD, $Fe_2(BDP)_3$ is stable up to 450 °C without undergoing any phase transition during the desolvation process.[194] In the VT-XRPD experiment, starting from 400 °C and up to decomposition, only a slow loss of crystallinity is observed. A parametric whole powder pattern refinement has been performed on the data collected in the temperature range 30-310 °C. This data treatment unveiled that the unit cell

volume undergoes a limited increase by 0.3%, mainly due to the slight enlargement of the *a*-axis, which is strictly related to the distance between the Fe^{3+} centres, thus confirming the rigid nature of the framework.

3.5.2 Adsorption Properties

$Fe_2(BDP)_3$ shows a good BET surface area of 1230 m^2/g (26.1% of the room temperature unit cell volume) when tested with N_2 at -196 °C.[194] The comparison of this literature value with that characterizing our samples confirmed the quality of our material (Figure 6.10). To characterize $Fe_2(BDP)_3$ as CO_2 scavenger material, both conventional single component adsorption isotherms and advanced dynamic experiments (breakthrough curve measurements) were used. The adsorption properties with regard to CO_2 have been evaluated at four different temperatures, namely at -78, 0, 10 and 25 °C (Figure 3.13a and Figure 6.10 in the Experimental Section). $Fe_2(BDP)_3$ adsorbs 13.29 mmol/g of CO_2 at P_{CO2} = 0.95 bar and T = -78°C, 5.19 mmol/g of CO_2 at P_{CO2} = 1 bar and T = 0 °C, 4.37 mmol/g of CO_2 at P_{CO2} = 0.86 bar and T = 10 °C and 3.52 mmol/g of CO_2 at P_{CO2} = 1 bar and T = 25 °C. This study enabled us to calculate the isosteric heat of adsorption (Q_{st}) and to evaluate the interaction strength between the adsorbate and the $Fe_2(BDP)_3$ pore surface. The calculation was performed based on the Clausius-Clapeyron equation [Eq.(1),[214]] derived from the gas sorption isotherms obtained at 0, 10 and 25 °C. The calculated Q_{st} values (Figure 3.13b) are given in Table 6.2 (see Experimental Section).

$$Q_{st} = -R[\Delta(lnP)/\Delta(1/T)]_N \quad \text{Eq. (1)}$$

Notably, the absolute values of Q_{st} monotonically increase with increasing guest loading. This is an unusual behaviour for a porous material which might be indicative of cooperative adsorption which might be related to favourable *guest-guest* and/or adaptative nature of 1-D channels in $Fe_2(BDP)_3$.

Only few other MOFs with 1-dimensional triangular channels are reported in the literature,[166,215–217] their CO_2 capacity, when studied, was compared to that of $Fe_2(BDP)_3$. Table 3.3 collects the textural parameters and the CO_2 adsorption capacity of these MOFs. $Fe_2(BDP)_3$ outperforms all the other reported MOFs in terms of CO_2 capacity except for its parents $Fe_2(BPEB)_3$,[166,209] Fe-PF1, Fe-PF2 and FePF4.[212] This occurrence can be ascribed to the shorter ligand hence the lower porosity of $Fe_2(BDP)_3$. Nonetheless, despite the slightly lower CO_2 adsorption capacity, 13.3 mmol/g instead of 13.4, 15.3, 15.2 and 14.8 mmol/g. at -78 °C and 1 bar for $Fe_2(BDP)_3$, $Fe_2(BPEB)_3$,[166,209] Fe-PF1, Fe-PF2 and FePF4 respectively,[212] the shorter BDP^{2-} ligand of $Fe_2(BDP)_3$ increases the thermal and chemical stability of the MOF, as highlighted above. Indeed, all the reported Fe^{3+} bis-pyrazolate MOFs start to decompose in the range 300 – 415 °C,[166,209,212] versus the value of 450 °C of $Fe_2(BDP)_3$. Moreover, when $Fe_2(BPEB)_3$ is exposed to water vapours, one of the components of flue gas, hydrolysis takes place.[209]

Table 3.3 - Comparison of the CO_2 adsorption capacity of $Fe_2(BDP)_3$ in respect to other MOFs with 1-dimensional triangular channels.

MOF	25 °C 1 bar			0 °C 1 bar			-78 °C 1 bar			Ref.
	cm³/g (STP)	wt%	mmol/g	cm³/g (STP)	wt%	mmol/g	cm³/g (STP)	wt%	mmol/g	
Fe₂(BDP)₃	76.1	15.4	3.5	112.7	22.9	5.2	298.0	58.5	13.3*	*This work*
Fe₂(BPEB)₃	-	-	-	105	20.6	-	300		13.4	[166,209]
Fe-PF1	-	12.3	2.8	113.5	22.4	5.1	342.9	-	15.3	[212]
Fe-PF2	69.6	14	3.1	138.2	27.3	6.2	340.7	-	15.2	[212]
Fe-PF4	-	14.1	3.2	118.8	23.3	5.3	331.7	-	14.8	[212]
[Er(DMTDC)₁.₅(H₂O)₂] (DMF)₀.₅(H₂O)₀.₅	36.9	-	1.65	50.4	-	2.25	-	-	-	[215]
Sc₂(BDC)₃	-	-	-	-	-	2.3	-	-	6	[217,218]
Sc₂(BDC-NH₂)₃	-	-	-	-	-	3.1	-	-	4.98	[218]
Sc₂(BDC-NO₂)₃	-	-	-	-	-	1.1	-	-	3	[218]
{[Yb(BTB)(H₂O)] (MeOH)₂(H₂O)}ₙ	60	-	-	92	-	-	-	-	-	[219]

* 0.95 bar

N_2 adsorption isotherms at 0 and 25 °C allowed us to calculate the CO_2/N_2 (15:85) ideal adsorption solution theory (IAST) selectivity[220] with partition coefficient α_{CO_2/N_2} = 23, 22 at 0 and 25 °C, respectively for a mixture of N_2:CO_2 (in 85:15 v/v *ratio*).

In the case of bulk gases separation, dynamic breakthrough experiments are more reliable than single component isotherms. To assess the actual CO_2 adsorption capacity and selectivity over interferents, a mixture of N_2:CO_2 (in 85:15 v/v *ratio* to simulate the flue gases emitted by a power plant) was passed through a column packed with $Fe_2(BDP)_3$ at different temperatures (T = 0/30/50/80 °C). At the essayed experimental conditions, the strongest interactions of the material take place with the quadrupolar CO_2 molecule, which is efficiently sequestrated, while N_2 is not retained, see Figure 3.13c. As expected, the CO_2 retention time and, consequently, the adsorption capacity are inversely proportional to the acquisition temperature, passing from 1.46 mmol/g of MOF at 0 °C to 0.35 mmol/g at 80 °C (see Experimental Section, Table 6.3). $Fe_2(BDP)_3$ recyclability was then evaluated by means of iterative adsorption-desorption cycles. At T = 30 °C, the MOF can undergo at least 11 cycles with no performance loss (Figure 3.13c-d and Table 6.5 in the Experimental Section) and no evidence of loss of crystallinity as shown by XRPD evidence as shown in Figure 3.14.
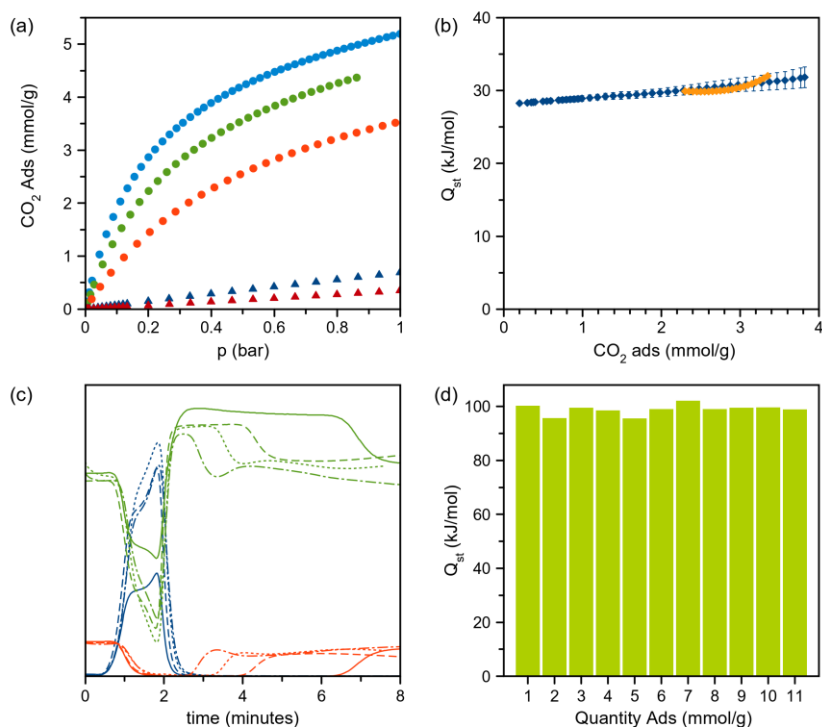
Figure 3.13 - a) CO_2 adsorption isotherms for $Fe_2(BDP)_3$ at T = 0 (light blue circles), 10 (green circles) and 25 ℃ (red circles) and N_2 adsorption isotherms at T = 0 (blue triangles) and 25 °C (dark red triangles). (b) Comparison between the isosteric heats of adsorption (Q_{st}) as a function of the CO_2 uptake for $Fe_2(BDP)_3$ calculated from adsorption isotherms (blue diamond) and retrieved from the HR-XRPD experiment (orange diamonds). (c) Graphical output of the breakthrough curves measured at T = 0 °C (solid line), 30 °C (dashed line), 50 °C (dotted line) and 80 °C (dash-dotted line). Colour code: He blue trace, N_2 green trace and CO_2 red trace. (d) Percentage variation of the CO_2 adsorption capacity of $Fe_2(BDP)_3$ over 11 consecutive cycles with respect to cycle 1.
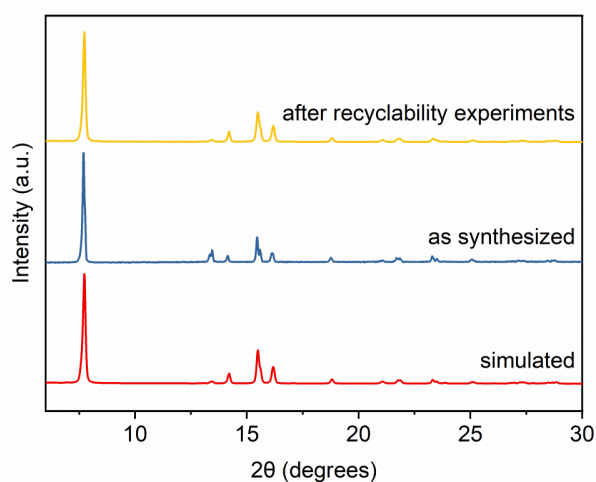
Figure 3.14 - Crystallinity comparison before (blue trace) and after breakthrough and recyclability experiments (yellow trace) by means of XRPD.

To investigate how different functionalities on the same ligand can affect the trends of stability and adsorption properties, the porosity of the isomorphous amino-tagged counterpart $Fe_2(BDP-NH_2)_3$ has been investigated by means of static adsorption experiments (N_2 at 77 K and CO_2 at 195 K), as well as dynamic ones through breakthrough experiments (Figure 3.15 and Figure 6.10 in the Experimental Section). As disclosed by XRPD, the amino-tagged MOF does not lose crystallinity or shows phase transitions after being probed with N_2 or CO_2 despite the presence of the functional group on the linker.

The decrease in BET surface area for the iron(III) tagged framework (339.5 m²/g), as compared to the parent $Fe_2(BDP)_3$ structure, follows the V/Z trend and can be largely ascribed to both the reduced free space available and an increased weight of the MOF after the introduction of substituents on the organic linker. The CO_2 isotherm collected at 195 K for the tagged framework (Figure 3.15a) shows that the introduction of the amino group results in a general increase of the steep of the adsorption isotherm in the low pressure region, which can be associated to an increase of the *host-guest* interactions and to a contraction of the pore size. Indeed, the presence of NH_2 substituents improves the formation of H-bonding interactions with the quadrupolar CO_2 molecules. These results are further supported by dynamic gas adsorption experiments (*i.e.* breakthrough curves, Figure 3.15b). To test CO_2 adsorption capacity and selectivity over interferents, the same experimental conditions for the parent MOF were used (binary mixture of N_2:CO_2 in 85:15 v/v *ratio* at T = T = 0/30/50/80 °C). Framework functionalization plays an important role also in this separation; comparing the obtained results, it can be seen that $Fe_2(BDP-NH_2)_3$ outperforms $Fe_2(BDP)_3$ in the studied conditions. In fact, the quantities of CO_2 retained at 50 °C, which is the typical condition of flue gas emission from a fossil fuel power plant, are 0.53 and 0.78 mmol/g for $Fe_2(BDP)_3$ and $Fe_2(BDP-NH_2)_3$, respectively (CO_2 retention times and quantities for all the temperatures essayed can be found in the Experimental Section, Table 6.4).
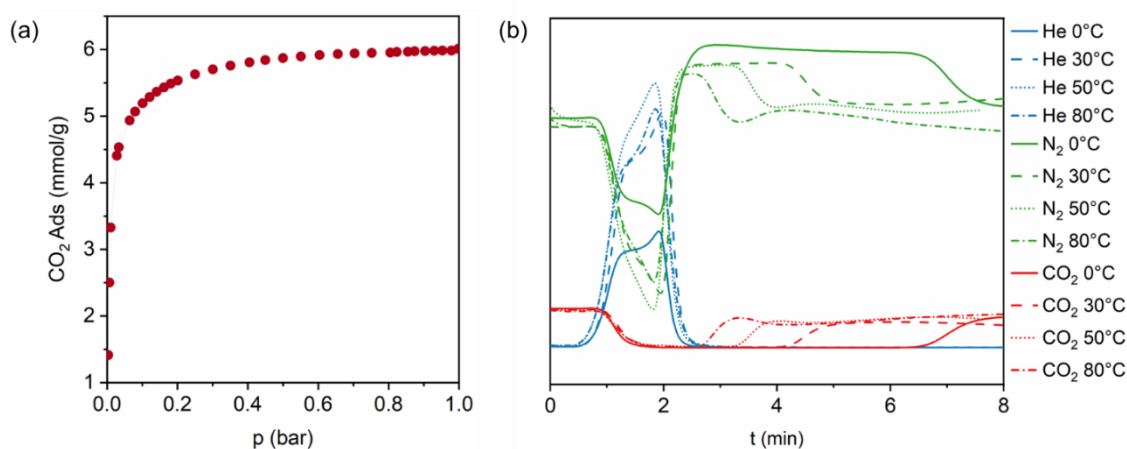
Figure 3.15 - a) CO_2 (195 K) adsorption isotherm for $Fe_2(BDP-NH_2)_3$; b) graphical output of the breakthrough curves measured for $Fe_2(BDP-NH_2)_3$ at different temperatures (T = 0 °C solid line, T = 30 °C dashed line, T = 50 °C dotted line and T = 80 °C dash-dotted line). Colour code: He blue trace, N_2 green trace and CO_2 red trace.

3.5.3 *In Situ* High-resolution Powder X-ray Diffraction

Unit cell parameters variation as a function of CO_2 loading

The complete activation of $Fe_2(BDP)_3$ was checked *via* TGA (see Figure 6.6 in the Experimental Section) before the synchrotron experiment and confirmed by a Rietveld refinement on the data acquired at 0 bar of CO_2 and 0 °C (see Experimental Section, Figure 6.14, top). Whole powder pattern refinements[221] were performed on each powder pattern acquired at 0 and 25 °C in the CO_2 pressure range of 0–8 bar (see Figure 3.16a for the HR-XRPD data acquired at 0 °C, and Figure 6.12b for the HR-XRPD data at 25 °C). The values of the unit cell parameters and of the figure of merit of the refinements are reported in Table 6.6 and Table 6.8 of the Experimental Section, while Figure 6.13 (see Experimental Section) shows the graphical result of a refinement as a representative example. Looking at the variation of the unit cell parameters, the framework shows a rigid response to the CO_2 pressure stimuli. Namely, a unit cell volume contraction between 0 and 1 bar of CO_2 ($\Delta V/V_0$ ~0.04% at T = 0 °C and $\Delta V/V_0$ < 0.05% at T = 25 °C) is followed by a slight increase ($\Delta V/V_0$ = 0.26% at T = 0 °C and $\Delta V/V_0$ = 0.16% at T = 25 °C) as shown in Figure 3.16b and Figure 6.17 of the Experimental Section. This initial unit cell volume shrinkage can be ascribed to the insurgence of favourable *host-guest* interactions at low pressure that may explain for the observed Q_{st} increase (see above); then, to accommodate an increasing number of CO_2 molecules, the framework slightly opens. The crystallographic *a*-axis, along which the iron(III) ions run, plays a main role in the described phenomena: at 0 °C, this axis undergoes a decrease by ~0.02% between 0 and 1 bar, followed by a slight increment of ~0.17% at 8 bar of CO_2. On the contrary, the *b*- and *c*-axis increase by only ~0.05% at 8 bar. At 25 °C, the unit cell parameters variation follows the same trend but with even less pronounced changes, with a total increase of ~0.09% for the *a*-axis at 8 bar. The rigidity of the framework can be related to the peculiar geometry of the 1-dimensional triangular channels, together with the metal ions chains, which run parallel to the [100] direction, and the nature of the ligand. Indeed, the μ^2-pyrazolate ring bridges two metal ions at a rather short distance (3.5 - 4.7 Å),[194,209] limiting more pronounced structural deformations.
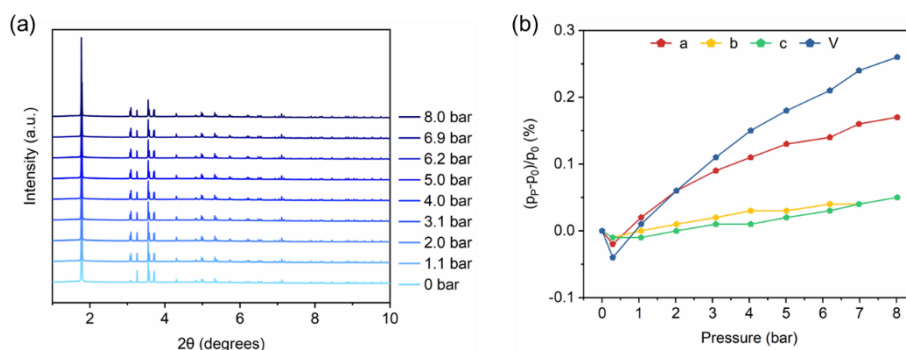
Figure 3.16 - a) HR-XRPD patterns acquired at 0 °C and variable CO_2 pressure. b) Relative percentage variation of the unit cell parameters (p_P) at 0 °C with respect to the values at p_{CO2} = 0 bar (p_0).

For $Fe_2(BDP-NH_2)_3$ and $Fe_2(BDP)_{1.5}(BDP-NH_2)_{1.5}$ HR-XRPD data treatment is currently ongoing and here are presented the preliminary results deriving from structureless diffraction pattern profile fitting which were performed *via* Le Bail method on each powder pattern acquired at 0 and 25 °C in the CO_2 pressure range of 0–26 bar (see Figure 6.19 for the HR-XRPD data acquired at 0 and 25 °C in the Experimental Section). The values of the unit cell parameters and of the figure of merit of the refinements are reported in the Experimental Section in Table 6.16 and Table 6.17 for $Fe_2(BDP-NH_2)_3$, while Figure 6.20 show the graphical results of Le Bail refinements at selected pressure values at 0 and 25 °C as representative examples. Looking at the variation of the unit cell parameters at 0 °C for both amino-tagged MOFs (Figure 3.17), the rigid nature of the framework upon CO_2 increasing pressure is once again confirmed. Indeed, the unit cell parameters variation follows the same trend of the parent $Fe_2(BDP)_3$ MOF but with a slightly more pronounced unit cell volume contraction between 0 and 4 bar of CO_2 (at T = 0 °C and p = 2 bar, $\Delta V/V_0$ = -0.07% for $Fe_2(BDP-NH_2)_3$; at T = 0 °C and p = 2 bar, $\Delta V/V_0$ = -0.12% for $Fe_2(BDP)_{1.5}(BDP-NH_2)_{1.5}$). The crystallographic *a*-axis, along which the iron(III) ions run, presents again a higher variation compared to *b*- and *c*-axes: at 0 °C, this axis undergoes a decrease by ~0.05% between 0 and 4 bar, followed by a slight increment of ~0.44% at 26 bar of CO_2 for $Fe_2(BDP-NH_2)_3$ (to compare with $Fe_2(BDP)_3$, the increase at 8 bar is of ~0.26%). Whereas for the multivariate MOF, at 0 °C the *a*-axis decreases by ~0.09% between 0 and 4 bar, followed by a slight increment of ~0.25% at 26 bar of CO_2 (to compare with $Fe_2(BDP)_3$, the increase at 8 bar is of ~0.12%). Overall, the most pronounced unit cell parameters variation can be attributed to the NH_2-tagged MOF. On the contrary, the *b*- and *c*-axes change is even less marked for the functionalised MOFs, only ~0.04% and ~0.02% at 8 bar for $Fe_2(BDP-NH_2)_3$ and $Fe_2(BDP)_{1.5}(BDP-NH_2)_{1.5}$, respectively. At 25 °C, the unit cell parameters variation for $Fe_2(BDP-NH_2)_3$ follows the same trend but with even less pronounced changes (Figure 6.21).
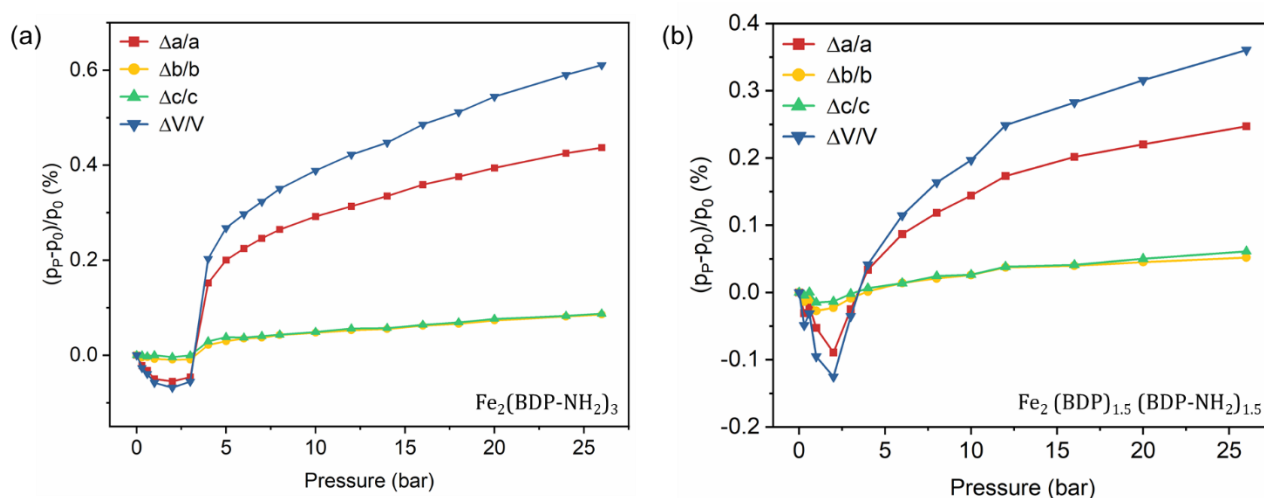
Figure 3.17 – Relative percentage variation of the unit cell parameters (p_P) at 0 °C with respect to the values at p_{CO2} = 0 bar (p_0) for $Fe_2(BDP-NH_2)_3$ (a) and $Fe_2(BDP)_{1.5}(BDP-NH_2)_{1.5}$ (b).

Location of the CO_2 adsorption sites and structural parameters depending on CO_2 loading

To localise the CO_2 primary adsorption sites and quantify the amount of gas adsorbed, Rietveld refinements were successfully performed on the HR-XRPD data of $Fe_2(BDP)_3$. Three primary adsorption sites with different occupancy were identified in the range 0-8 bar and 0/25 °C. Hence, three crystallographically independent CO_2 molecules were modelled inside the triangular channels, namely: CO_2-1, CO_2-2 and CO_2-3, see Figure 3.18a. The three adsorption sites are present at all the studied pressures and temperatures; only a slight variation in the orientation of the guest molecules were observed during CO_2 loading. Two different types of host-guest interactions were found: side-on interactions for CO_2-1 and CO_2-3, where both the oxygens interact with the carbons of the central ring of the ligand (C_{ligand}–O_{CO2} = 2.3 - 2.8 Å)-, whereas CO_2-2 interacts with the carbons of the ligand central ring in an end-on mode with only one oxygen (C_{ligand}–O_{CO2} = 2.3 - 2.8 Å). Interestingly, both at 0 and 25 °C, the applied CO_2 pressure affected the rotation and the disorder of the central ring of one of the two crystallographically independent ligands (see Figure 3.18c and Table 6.10, Table 6.11 in the Experimental Section). This occurrence can be explained by the described O_{guest}–C_{host} interactions. The amount of CO_2 adsorbed increases applying higher pressure and is inversely proportional to the adsorption temperature, as expected. The occupancies of CO_2-1, CO_2-2 and CO_2-3 as a function of the applied pressure are reported in Figure 6.15, Figure 6.16 and Table 6.14, Table 6.15 in the Experimental Section. The CO_2 occupancies obtained by Rietveld refinements, where then used to reconstruct the CO_2 adsorption isotherms up to 8 bar both at 0 and 25 °C (Figure 3.18b). $Fe_2(BDP)_3$ adsorbs 3.4 and 2.7 mmol/g of CO_2 at 0 and 25 °C and 1 bar, values which are slightly lower if compared to the CO_2 adsorption isotherms, and up to 4.2 and 3.7 mmol/g at 0 °C and 25 °C and 8 bar, respectively. The Freundlich-Langmuir model[214] was successfully applied to the experimental isotherm built from Rietveld refinements data in the range 0-8 bar at 0 and 25 °C (Figure 3.18b). Finally, the modelled CO_2 isotherms (T = 0 and 25 °C) were used to calculate the Q_{st} and the resulting values compared to the ones retrieved from conventional adsorption isotherms.
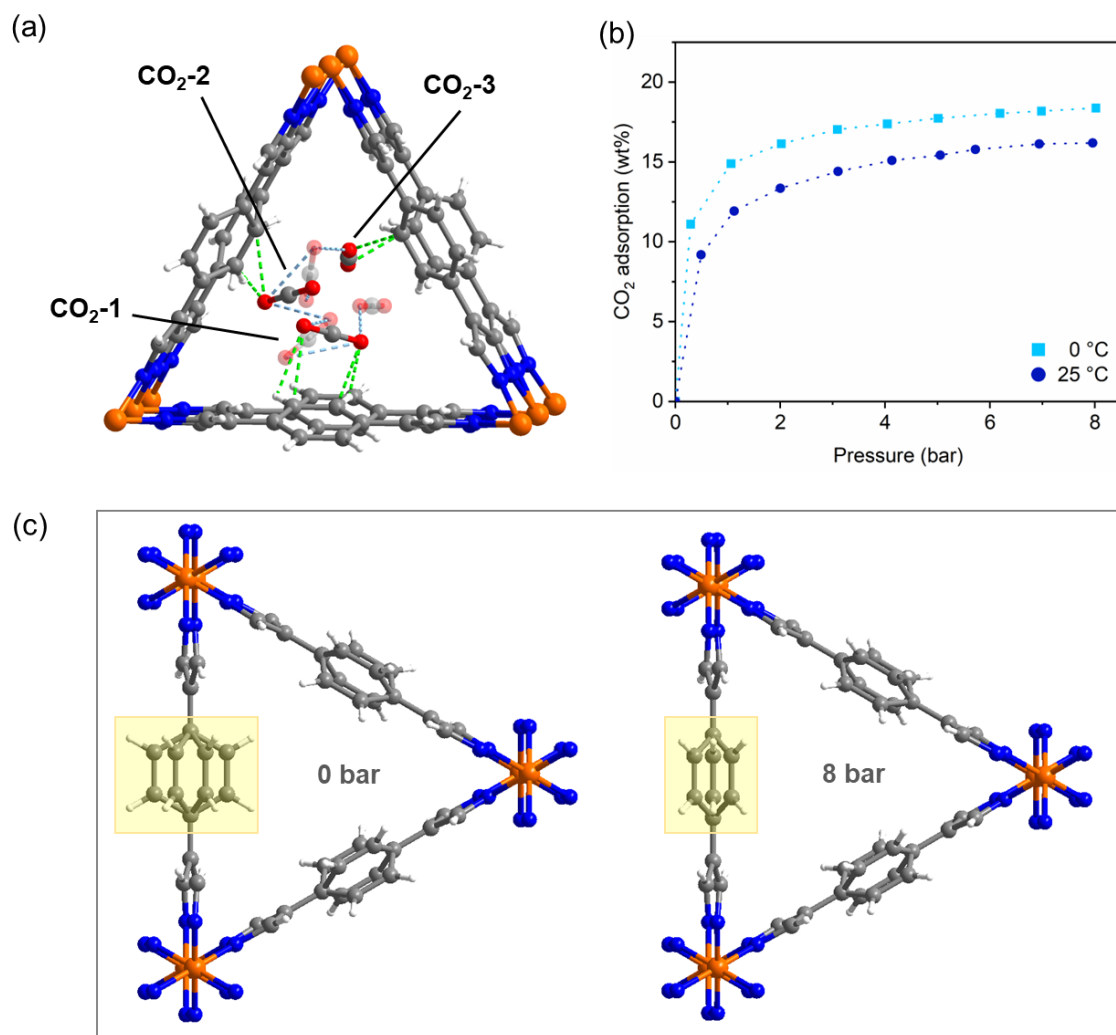
Figure 3.18 - a) Position of the three independent CO_2 molecules, together with the main *host-guest* interactions (green dashed lines), obtained from the Rietveld refinement at 0 °C and p_{CO2} = 1 bar; the central ring of the ligands has been ordered for clarity. b) Quantity of CO_2 adsorbed at T = 0 and 295°C as resulting from the Rietveld refinements. c) Torsion variation of the benzene ring of the ¼ ligand before and after CO_2 loading.

3.5.4 Monte Carlo Simulations

The use of computational methods can help in understanding the adsorption process at the atomic level, thus complementing experimental observations.[222] The CO_2 adsorption isotherms at 0 and 25 °C were simulated in the range 0-8 bar, using Materials Studio 6.0 (MS6.0),[223] and compared to the experimental ones (p_{CO2} = 0 - 1 bar) and those retrieved from HR-XRPD data treatment (p_{CO2} = 0 - 8 bar), see Figure 3.19a. The results of the simulation are in good agreement with the experimental ones in the range 0-2 bar, while at higher CO_2 pressures they overestimate the experimental ones This occurrence could be related to the (experimentally observed) orientational disorder affecting the central ring of the ligands, that is not taken into account during the simulation. Figure 3.19b-c shows the centre of mass of the calculated CO_2 adsorption sites and the main host-guest interactions at 0 °C. All the configurations can

be found in the Experimental Section in Figure 6.25, Figure 6.26. The simulations confirmed the experimental data, the carbon dioxide molecules interact with the walls of the triangular channels in two different ways, namely by using: *a*) both the oxygens in side-on mode, as interactions in the range 2.10-3.3 Å with the carbon atoms of the phenyl ring of the ligand, or *b*) only one oxygen, in an end-mode (2.7 Å). These two different configurations are in good agreement with what experimentally observed for the couple CO_2-1/CO_2-3 and CO_2-2, based on the HR-XRPD experiment.
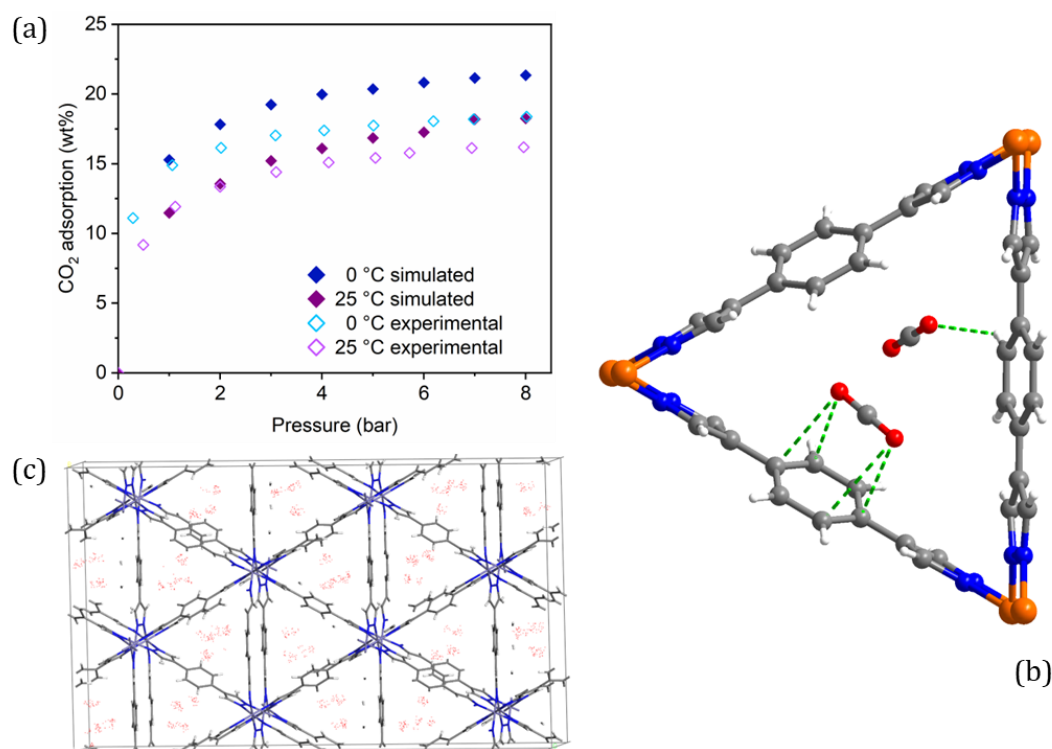
Figure 3.19 - a) Comparison of the simulated and experimental from HR-XRPD CO_2 adsorption isotherms at 0 and 25 °C. b) Representation of the main *host-guest* interactions retrieved from the molecular simulation. c) Representation of the centre of mass probability density of the CO_2 molecules per unit cell of $Fe_2(BDP)_3$ viewed approximately along the [100] direction, as determined from a Monte Carlo simulation at 0 °C.

3.6 Conclusions

As already discussed in Chapter 2, new and effective methods to cope with global warming must be developed rather quickly. Two different, but complementary, promising solutions are represented by progresses in the field of green energies and developing more efficient novel materials and technologies for the sequestration/utilization of greenhouse gases. Metal-organic frameworks proved to be good candidates for CO_2 capture and storage. In particular, azolate-based MOFs are attractive for this kind of applications thanks to their high thermal and chemical stability. Among the large family of these N-donor based ligands, pyrazoles represent an appealing subcategory for crystal engineering because they can create particularly strong and directional bonds with metal ions or even act as bridging linkers, all of this leads to (potentially) high chemical and thermal inertness and the creation of many different SBUs.

The isostructural bis(pyrazolate)-based MOFs described, namely $Fe_2(BDP)_3$, $Fe_2(BDP-NH_2)_3$ and $Fe_2(BDP)_{1.5}(BDP-NH_2)_{1.5}$, have been successfully obtained as pure microcrystalline powders. The amino functionalities have been introduced on the organic linker to tune pore size and adsorption capacity and selectivity toward specific guests. The solid-state characterization of these materials and the good BET surface area values obtained, confirmed their robustness and suitability for CO_2 capture and separation. In particular, $Fe_2(BDP)_3$ has been studied in both static and dynamic conditions, through adsorption isotherms and breakthrough curves, respectively. It has shown the capacity of performing multiple cycles of gas adsorption and recovery and unexpectedly, the CO_2 adsorption process proceeds with an increase of the isosteric enthalpy of adsorption.

In situ high-resolution XRPD measurements, aimed to get information on the CO_2 adsorption properties of the selected MOFs, have been performed at ESRF collecting the data at different temperatures while varying the applied CO_2 gas pressure. Overall, the multi-technique approach presented, provided key information to better understand the CO_2-host interactions, thus disclosing the chemical and structural features making $Fe_2(BDP)_3$ suitable as CO_2 scavenger.[118,212]

Preliminary results on the tagged and multivariate MOFs demonstrate a remarkable thermal stability, decomposing, in air, above 430 °C, while maintaining their functionality. Single component adsorption isotherms and gas separation experiments, *i.e.* breakthrough curve measurements, allowed rationalisation of the effect of linker functionalization on the adsorption capacity and selectivity towards CO_2. This resulted greatly improved for $Fe_2(BDP-NH_2)_3$ when using a mixture of apolar gases (*i.e.* N_2/CO_2 mixture) thanks to the introduction of polar tags.

Such first relevant results may contribute to the design and development of MOFs applicable to a extensive range of industrial applications and outperforming traditional porous materials (*e.g.* zeolites, activated carbons).

3.7 Multivariate Flexible (Bis)pyrazolate-MOFs – *Preliminary Results*

Our research group, in collaboration with the one of J. A. R. Navarro of the University of Granada (Spain), accomplished the synthesis of new flexible, multivariate MOFs of general formula $M(BDP)_{0.5}(BDP-X)_{0.5}$, with $M = Zn^{2+}$, H_2BDP = 1,4-bis(1H-pyrazol-4-yl)benzene and X = -NH$_2$ or -NO$_2$, according to what reported in the literature. The organic linkers were obtained from already known procedures as well as the MOFs,[203–206] which were isolated in the form of air-stable polycrystalline powders in solvothermal conditions. Initial characterization of the multivariate MOFs revealed the flexible nature of their frameworks, as shown by comparison of the XRPD patterns for the as synthesised and solvent reinfiltrated materials (see Experimental Section, Figure 6.27, Figure 6.28). Indeed, the difference between the patterns in terms of peak positions and intensities is probably due to slightly different framework structures, one being more open than the other. Solvent release triggers a certain degree of flexibility, this is particularly evident when looking at the shifted position of the first diffraction peak for both MOFs; while some peaks can still be related to those shown by the solvated counterparts, other ones are completely new. Further proof for this dynamic behaviour will be given after performing Le Bail refinements on XRPD data and static adsorption measurements (N$_2$, 77K).

The deep characterization of the adsorption properties and the structural features of these materials will be crucial to understand the relation between the structural flexibility, functionalization degree and crystal size, with the gas adsorption and separation properties.

Chapter 4

FLEXIBLE MOFS
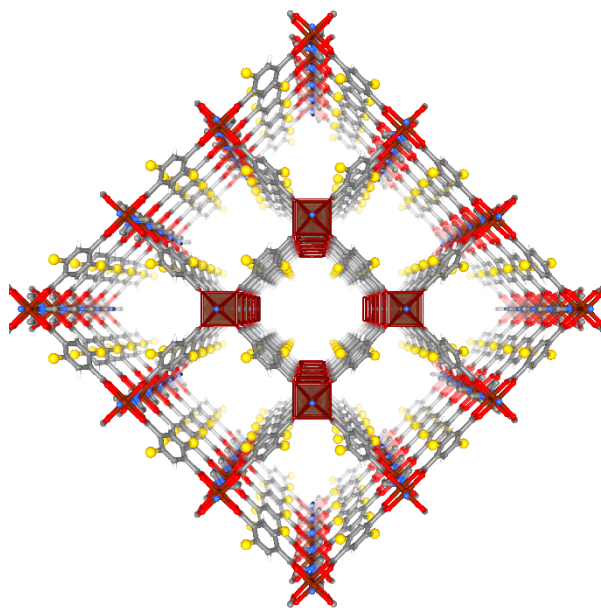
4.1 Overview of Soft Porous Coordination Polymers

MOFs can undergo structural changes when the solvent is removed after the synthesis. This applies to 3rd generation MOFs (Chapter 1.2.2) which display large scale dynamic behaviour in the presence or absence of guest molecules. This subclass of MOFs is described with the broad term "flexibility".[140,224–226] In Figure 4.1, a historical overview regarding flexible metal organic framework is depicted.
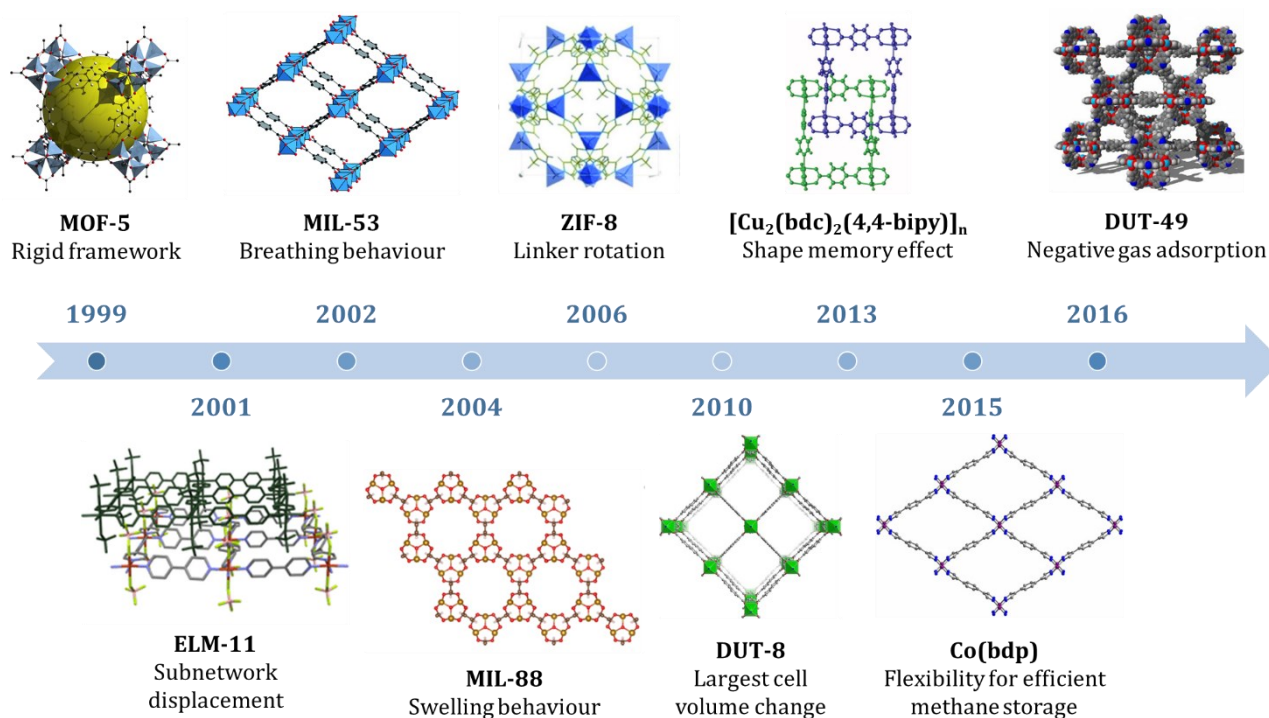
Figure 4.1 - Historical timeline depicting the first porous material defined as MOF and selected examples of flexible MOFs developed in the last years.

Important first milestones in this area are MOF-5 ($Zn_4O(BDC)_3$ with BDC^{2-} = 1,4-benzodicarboxylate)[133] and HKUST-1 (Cu_2BTC_3 with BTC^{3-} = *1*,3,5-benzenetricarboxylate),[227] developed in 1999. HKUST-1 is still greatly studied, among other reasons, because it is industrially produced by BASF under the commercial name of Basolite® C300.[228] The first flexible MOF appeared not much later, in 2001, and it is called ELM-11 ($Cu(4,4'$-bipyridine$)_2(BF_4)_2$),[229,230] which stands for elastic layered material, and showed the so-called gating effect upon increasing gas pressure.[231,232] Its framework contains Cu(II) ions and bipyridine linkers which form a structure with square lattice (sql) topology. The crystal structure also contains BF_4^- anions (Figure 4.2, green tetrahedron) that counterbalance the metal ion charges; they are located at the top and bottom of each 4.4 layer and this way cause the switching mechanism: in the closed pore (*cp*) phase, there is a very small distance between the two layers and the BF_4^- anions which leads to a blockage of the pores. Once a gas is adsorbed the layers expand and lead to a structure with open pores (*op*). This process was already discovered by D. Li and K. Kaneko in 2001,[231] even though at that time they did not fully understand the structure of ELM-11. In Figure 4.2 the original adsorption isotherms from their paper are reported. From the shape of the isotherms the prototypical gating process is clearly visible which involves no uptake at low pressure. Only at a certain, higher pressure, the so-called gate pressure, a sudden opening of the network including a huge gas uptake is observed.
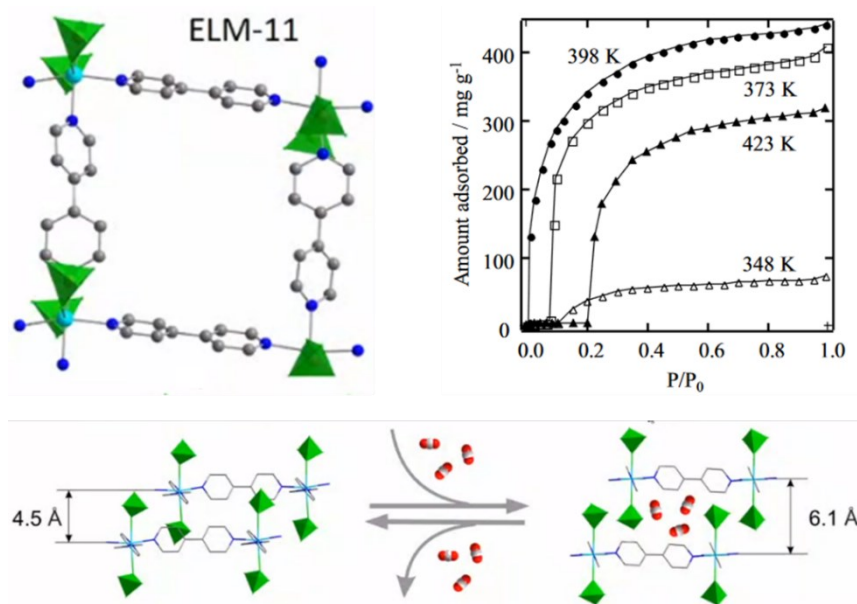
Figure 4.2 - Crystal structure of ELM-11 (left) and its N_2 adsorption isotherms at different temperatures (right).[231] The stacked layers of the 4.4. move with respect to each other to accommodate guest molecules. Colour code: Cu, light blue; N, blue; C, grey; BF_4^-, green tetrahedron; O, red.

Soon after, G. Férey and co-workers synthesised the so-called breathing or swelling MOFs, which show huge volume changes. The most famous representatives examples are MIL-88 ($Fe_3O(CH_3OH)_3(1,3-$ benzenedicarboxylate)$_3$)[233] and MIL-53 (Fe(OH)(BDC))[232,234] which is another successful example of commercially produced MOF (Basolite® A100).[233] In 2006, the new class of zeolitic imidazolate frameworks (ZIFs) was developed.[235] Also, these compounds exposed to have a small degree of flexibility, caused by bending motions of the linker. In 2008, S. Kaskel *et al.* developed the prototypical gating MOF family called DUT.[236] These materials belong to the class of pillared-layer MOFs of the type M_2L_2P (for a detailed description of this kind of structure see Chapter 4.2.1), possessing binuclear paddle-wheel units built by divalent metal ions M^{2+} and anionic dicarboxylate linkers L^{2-}, together with a neutral nitrogen containing pillar P.[237] They have become well-known in the last years for their intrinsic responsiveness.[238] A remarkable discovery of S. Kitagawa that followed in 2013 is the shape memory effect. This demonstrates that not only the solid-state structure, but also the particle size, plays an important role in the flexibility of MOFs.[239–241] A good example for this interesting phenomenon is DUT-8(Ni) ($Ni_2(2,6$-ndc)$_2$(dabco) with 2,6-ndc^{2-} = 2,6-naphthalenedicarboxylate, dabco = 1,4-diazabicyclo[2.2.2]octane), which is flexible or rigid depending on the particle size. If it is small (200-500 nm), the system is rigid and shows a *Type I* adsorption isotherm (N_2 at 77 K). Crystals with a particle size ranging from 20 to 100 μm instead are flexible and show a typical gating adsorption isotherm. Remarkably, there is no significant difference in the chemical composition and the pore structure is the same, the only difference is the crystal size.[239,242–244] Furthermore, DUT-8(Ni) is interesting for gas separation because it only opens its pores when exposed to carbon dioxide, however, not in the presence

of methane. In contrast, the rigid DUT-8(Ni) allows the access of both of CH_4 and CO_2 (with a preferential adsorption for CO_2 because of a stronger interaction with the host), as NMR measurements has demonstrated.[245] Also the reverse effect of this phenomenon has been observed, *i.e.* the transition flexible to non-flexible upon crystallite downsizing of the MOF family [Cu_2(fu-bdc)$_2$(dabco)] (fu = DE = 2,5-diethoxy and BME = 2,5-bis(2-methoxyethoxy)) discovered by R. Fischer and co-workers.[246] Then in 2015, J. Long *et al.* discovered that both at low and high pressure certain MOFs can show breathing behaviour which lead to advantages for gas storage applications. In particular the Co(BDP) (with BDP $^{2-}$ = 1,4-bis(pyrazol-4-yl)benzene) system showed relevant advances for hydrogen and methane storage applications.[247] In the following year S. Kaskel *et al.* published an article describing a rather counterintuitive phenomenon, called negative gas adsorption (NGA). This was observed with MOF DUT-49 (Cu_2(bbcdc) with bbcdc^{4-} = 9,9'-([1,1'-biphenyl]-4,4'-diyl)bis(9H-carbazole-3,6-dicarboxylate))[248] and comprises the desorption of guest molecules (methane and *n*-butane in this case) during pressure increase in a defined temperature and pressure range. The reason is a contraction to a closed pore (*cp*) phase with lower volume because it is energetically favourable. With increasing guest pressure instead, the material adsorbs more of the guest molecules and reverts to its open pore (*op*) form.

Even though a variety of flexible MOFs has been discovered ever since the advent of the field of flexibility, their behaviour is still not fully understood leaving open questions even after 20 years of research. This is mainly due to the difficult access of advanced characterization techniques needed to monitor the structural changes and transformations *in situ* as a response to guest stimuli.
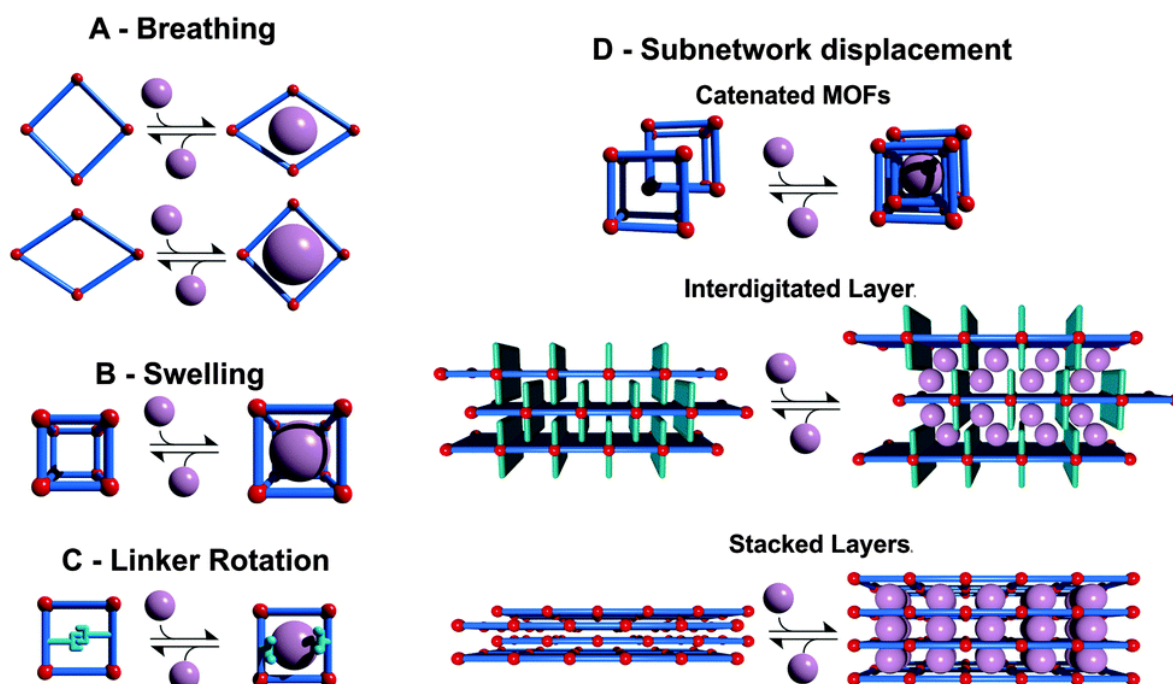
Figure 4.3 - Schematic representation of the various flexibility mechanisms found in MOFs.[246] Colour code: metal node, red; linker, blue; guest molecule, pink.

Most flexibility mechanisms, which are based on the structural changes as response to a certain external stimulus, have been clarified. They can be divided into four categories which are shown in Figure 4.3.[246] These include simpler mechanisms such as:

- *Swelling* (Figure 4.3, B), which describes the enlargement of the unit cell volume upon adsorption of guest molecules. For example, the MIL-88 series $[M_3O(L)_3(H_2O)]_2$ with $M^{3+} = Cr^{3+}$, Fe^{3+}; L = fumaric acid, 2,6-naphthalenedicarboxylate, 4,4'-biphenyldicarboxylate and functionalised (fu-)bdc derivatives; fu = F-, Cl-, Br-, OH-, *etc.*)[137,249,250] can show a considerable enlargement of the unit cell volume in the range of 60-230% depending on the type of linker and guest.

- *Linker rotation* (Figure 4.3, C), which is enabled by the spatial freedom and the high porosity of these materials. The rotational mobility of the linker can be categorised in three groups: complete rotation, partial rotation and side group rotation. It occurs for example when molecules with a larger kinetic diameter than the pore size of the framework are adsorbed as observed for ZIF-8 (zeolitic imidazolate framework, $Zn(mIm)_2$ with $mIm^- = 2$-methylimidazolate).[251–253]

Instead, more complex mechanisms are for example:

- *Subnetwork displacement* (Figure 4.3, D), which occurs in MOFs possessing interpenetrated frameworks that are not connected by covalent bonds but only weak van der Waals interactions and therefore can show some minor structural transformation after intrusion of (gas) guest molecules. These so-called subnets can drift, relocate, or shift.[254–256] In two dimensional materials another phenomenon can be observed, which is the swelling of the stacked layers as they expand after inclusion of guest molecules.

- *Breathing* (Figure 4.3, A; Figure 4.4), which is a (reversible) phase transition between two crystalline phases, a narrow or closed pore (*np* or *cp*) form to an open or large pore (*op* or *lp*) one. During this mechanism the open network first contracts and expands again then at higher pressure, resembling a lung showing a breathing behaviour. The result is a change in the unit cell volume and of the crystallographic space group which can be very large. Plenty of examples can be found in the literature (*e.g.* MIL-53 family[234,257,258], M(BDP) with $M^{2+} = Co^{2+}$, Fe^{2+},[247,259] DUT-8[260,261]).

- *Gating* (Figure 4.4) is similar to the breathing behaviour, and together are the most common dynamic modes shown by flexible MOFs. An effective way to distinguish between these two behaviours is performing gas sorption experiments, which allows to highlight the different modifications of the framework upon pressure variation by observing the isotherms' shape (Figure 4.4). When following the *gating* effect on an isotherm (like the one shown for ELM-11, Figure 4.2), no uptake at low pressure is observed and this region corresponds to the so-called closed pore (*cp*) phase. After introduction of gas molecules, the open pore phase (*op*) is formed

once the gate pressure, characteristic for each material, is reached. This is accompanied by a sudden and large uptake of gas. This switching phenomenon arises because there are coupled phase transitions: the uptake of gas and then the desorption, whose branch of the isotherm is shifted to lower pressure and is accompanied by the network closure. This is therefore a one-step transformation (Figure 4.4, left). The typical isotherm observed for breathing MOFs shows a transformation from a large pore (*lp*) which then contracts to a narrow pore (*np*) form and then re-opens. The hysteresis occurs in a higher-pressure range, which is why there is a steep uptake and followed by a bending of the isotherm, and then another hysteresis. all these processes represent the re-opening of the structure to the large pore form. This behaviour has been extensively studied and demonstrated on MIL-53, one of the most famous examples of a breathing system (Figure 4.4, right).[258]
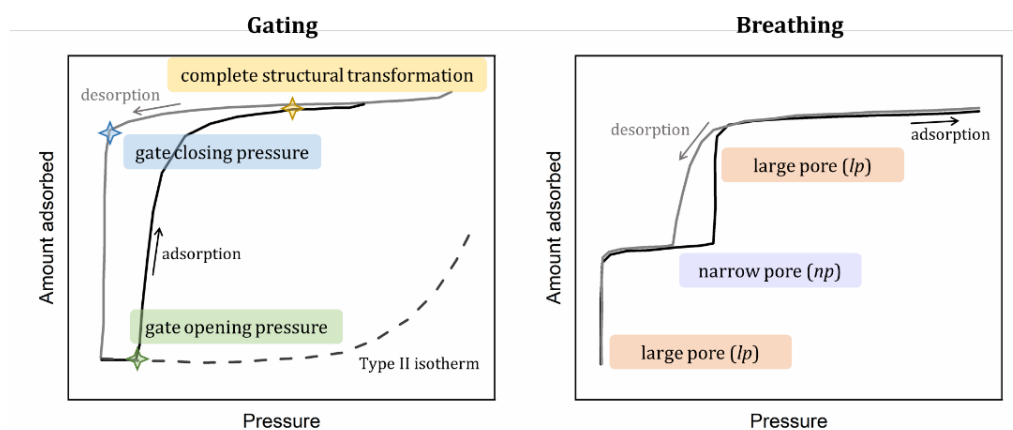
Figure 4.4 - Schematic representation of sorption isotherms for gating (left) and breathing (right) mechanisms.

4.1.1 Experimental Methods to Investigate Flexibility in MOFs

Understanding the flexible behaviour of MOFs is important because it is fundamental to completely understand the consequences in properties and performance of the responsive materials, especially regarding adsorption and diffusion of gas molecules.[25,246,262] Which is also the major research topic of this thesis. However, it is a very difficult task that often needs to be addressed by a multi-technique approach where advanced and/or customised *in situ* analytical techniques are combined with theoretical simulations. Here are listed the most used characterisation methods for a better comprehension of the structural dynamics in flexible MOFs:

- ⊙ *In situ powder X-ray diffraction* (XRPD) is widely used for the study of flexible MOFs, the main advantage comes from the possibility of accurately monitoring crystalline phases evolution, as structural transitions commonly occur with significant changes in the lattice parameters and cell volume.[263] Furthermore, combining for example the XRPD set-up with a gas handling system, the diffraction data can be acquired on the activated sample under controlled temperature

and/or pressure conditions, in order to monitor the changes before, during and after the phase transition(s).[218,264,265] To collect high quality data, high intensity synchrotron radiation is required,[218,266–268] even though comparable experiments are also possible with laboratory set-up in many cases. Likewise, *in situ* neutron powder diffraction can be used to study pore-dependent dynamics upon gas adsorption and it is particularly useful when dealing with light atom adsorbates.[269–271] *In situ* single crystal XRD experiments are also possible but less common due to the crystals' short-life during structural transformations under various conditions and to the fact that they cannot always be grown.[272] A possible solution to this problem could be electron diffraction whose development has been quite fast and promising in the last years;[273,274] nevertheless, its availability and feasibility are still very small.

⊙ *Gas sorption analysis* can be used as first indication to recognise that a MOF is flexible in a fast and usually easy way. Normally, for a typical microporous material a *Type I* isotherm is expected. In contrast, in the case of flexible behaviour there is always some degree of hysteresis in the isotherm which leads to a unique and irregular shaped (sigmoidal) Langmuir *Type IVa* isotherm. These materials usually adsorb a low quantity of gas before a phase change occurs. The latter is visible as one (or more) steps in the isotherm related to one (or more) phase change(s) that correspond to the "opening" of the MOF pores. All these changes only happen at critical pressure points (see Chapter 1.2.3).

⊙ *Thermogravimetry analysis* (TGA) and *differential scanning calorimetry* (DSC) are useful methods to monitor and estimate the energy changes during a structural transformation in a flexible MOF[275] upon heating or guest release. Endothermic signals in DSC often indicate the presence of a breathing effect in a flexible framework, from which the desorption enthalpy corresponding to the removal of water can be calculated.[276]

⊙ *Infrared* (IR) or *Raman spectroscopy* represent valid tools to understand the flexible behaviour of MOFs at the molecular level, providing structural fingerprints of the different phases before and after phase transitions.[277,278] The appropriate IR range useful to study dynamic structural transitions is represented by the far-IR region, which contains significant variations in the vibrational spectra necessary to study the properties of flexible motions. However, there are several challenges, for example it is difficult to collect a high-quality spectrum in this region, another difficulty is the identification of low-frequency modes which do not originate from known characteristic vibrations of specific functional groups.[277]

⊙ *^{129}Xe nuclear magnetic resonance* (^{129}Xe-NMR) exploits the change in chemical shift, line width, chemical shift anisotropy and longitudinal relaxation time of Xe when it is adsorbed by a flexible MOF, in fact its chemical shift heavily depends on the pore surface, size and shape of the host MOF.[279–281] *In situ* NMR is a powerful technique which, combined for example with XRPD, provides important information about *host–guest* interactions in flexible MOFs. To date, the limited number of studies described in the literature uses ^{129}Xe and $^{13}CO_2$ as a probe for the

experiment.[282,283] A major drawback is that NMR is a non-selective technique and MOFs are often obtained in mixtures with other crystalline or amorphous phases which are covered in the analysis as well. Less common is the use of solid-state NMR in this area of research.[284]

⦿ *Transmission electron microscopy* (TEM) is an effective method to directly observe and study the molecular rearrangement of MOF nanocrystals. These types of structural transformations can be achieved by temperature variation or adsorption of solvents on the crystallite.[285]

⦿ *X-ray absorption spectroscopy* (XAS) allows the determination of the local structure of the metal cluster, which is crucial for understanding specific properties of MOFs.[286–288] Thanks to XAS is straightforward to obtain detailed information about the coordination geometry, oxidation state and bond angles of the metal centre in the framework during gas adsorption (represented for example by breathing or gating effects).[289] In particular, i*n situ* extended X-ray absorption fine structure (EXAFS) coupled with XRPD is widely used to study flexible MOFs during hydration and dehydration processes.[286,290]

⦿ *In situ liquid-phase atomic force microscopy* (AFM) is a powerful tool to observe the responsiveness of MOF surfaces with a lattice resolution. It differentiates from electron microscopy techniques (*e.g.* TEM and SEM) because AFM enables the direct observation of crystalline surfaces in a "live" mode.[291]

Both thermodynamic studies and molecular modelling are often applied in combination with the characterisation techniques described, this allows a deeper understanding of MOFs structural dynamics. Classical simulations, such as grand canonical Monte Carlo (GCMC) or density functional theory (DFT) calculations, are among the most used methods. Although the understanding of the structural features behind these phenomena can be challenging, it is of great importance when trying to better control the chemical design and tuning of the properties of flexible MOFs, for example the possibility to systematically adjust the shape of the isotherms when dealing with industrial gas adsorption applications.

4.1.2 Applications of Flexible MOFs

The study and understanding of flexible behaviour in MOFs influence the development of really interesting potential applications (Figure 4.5), some of them are unique of these materials while in other cases they outperformed the rigid analogues. Flexible frameworks are promising for gas adsorption application, because they can have enhanced selectivity, high usable storage capacities, and reduced thermal management requirements.[13,84,292,293] The flexible MOF Co(BDP), for instance, is outperforming all rigid analogues in terms of CH_4 storage because it can desorb CH_4 from the pores below its threshold pressure and shows an excellent CO_2/CH_4 separation capacity thanks to a size exclusion mechanism.[120] There are other examples of applications outside the topic of gas adsorption and separation, such as

selective recognition of small molecules thanks to a change in a particular physical property (optical, magnetic, electrical, *etc.*),[294,295] drug delivery,[296] chemical sensing.[297] Additionally, some MOF composites are used as gas threshold sensors, allowing for example the recognition of specific concentration levels of toxic volatile compounds[298] whereas other flexible MOFs are good shock absorbers or even actuators.[299]
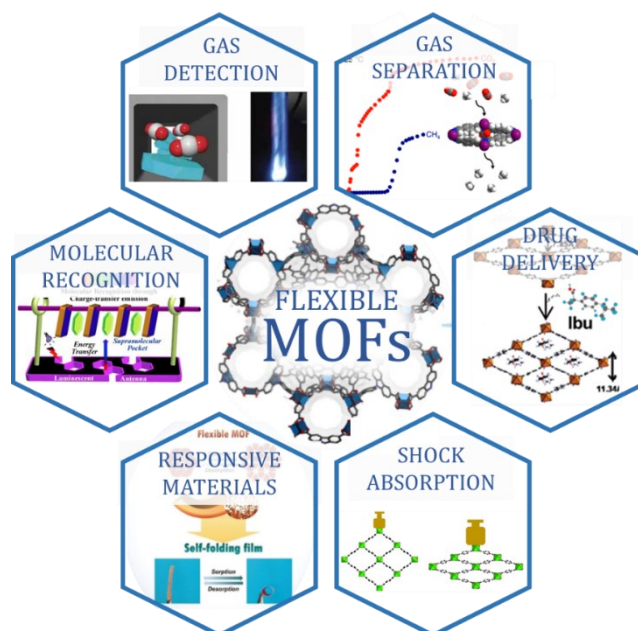
Figure 4.5 - Example of potential applications for flexible MOFs.

4.1.3 Flexible MOFs for Catalysis

Most of the work done in search of applications for flexible MOFs is related to gas-storage and selective adsorption/separation and the corresponding sensing properties of these materials.[246,300,301] Only recently it was noticed that also catalytically active materials can benefit from the interesting properties of flexible MOFs, which could be used as novel "smart" heterogeneous catalysts, able to (reversibly) respond and adapt to specific external stimuli. Indeed, the embedding of a catalytic component within the flexible MOF structure could lead to switchable reversible catalysts. The catalytic element is here regarded as a defect site in the crystalline framework of the chosen flexible MOF. Most studies have focused on the confinement of nanoparticles in MOFs but ignored their structural flexibility (Table 4.1). Nevertheless, a few interesting examples about this complex topic can be found in literature. For example, the flexible composite catalyst Pt@ZIF-8 ($Zn(mIM)_2$) by Q. Kuang and co-authors has been developed for the hydrogenation of cinnamaldehyde, showing high selectivity for cinnamic alcohol with the confinement effect of the aperture.[302] Another example is from the paper by H. C. Zhou and co-authors where a flexible Zr-MOF, namely PCN-700 series, has been designed for the realization of switchable catalysis in cycloaddition reactions of CO_2 with epoxides, exploiting the breathing behaviour of the system.[295]

Table 4.1 - Some references as example regarding the embedding of NPs into both rigid and flexible MOFs.

Catalitically inert nanoparticles				
Reference	**NP type**	**NP size**	**MOF**	**Encapsulation method**
[303]	NP@mSiO$_2$	44 nm	ZIF-8	Selective nucleation and MOF growth on the surface of NP@mSiO$_2$ nanostructures
[304]	SiO$_2$-NH$_2$ SiO$_2$-COOH SiO$_2$-OH	167 nm 197 nm 153 nm	MOF-5	Solvothermal growth of MOF-5 in the presence of SiO$_2$ NPs
[305]	SiO$_2$ SiO$_2$-NH$_2$	200 nm	MOF-5	Solvothermal growth of MOF-5 in the presence of SiO$_2$ NPs
[306]	SiO$_2$	70 nm	ZIF-8	Growth of a MOF shell around the pre-formed NPs
[307]	PS	180 nm	ZIF-8	*"Bottle-around-the-ship"* strategy
[308]	PS-COOH	>>5 nm	ZIF-8	*"Bottle-around-the-ship"* strategy
[309]	Au@SiO$_2$	142 nm	ZIF-8	*"Bottle-around-the-ship"* strategy
[310]	PS-COOH	0.87 μm	ZIF-8	Growth of a MOF shell around the pre-formed MNPs
Metal nanoparticles				
Reference	**NP type**	**NP size**	**MOF**	**Encapsulation method**
[311]	Pd	2.1 nm	UiO-67	Pre-synthetic linker functionalization approach, followed by reduction
[312]	Pt	3.3–13 nm	UiO-66 ZIF-8	*In situ* encapsulation followed by calcination at high temperature
[302]	Pt	4.5 nm	ZIF-8 ZIF-71	Impregnation-reduction process
[313]	Au/Ag	40–80 nm	ZIF-8	MOF shell growth around the pre-formed MNPs
[314]	Pd	3.0 nm	UiO-67	Ligand design prior to MOF assembly
[315]	Pd	1.5 nm	UiO-66	One step
[316]	Pd	4.8 nm	ZIF-8	Mechanochemical approach
[317]	Au	< 3nm	MIL-101	Impregnation-reduction process
[318]	ZrO$_2$	< 5 nm	MIL-101	Double solvents method
[319]	Ag$_3$O$_4$	20 nm	MIL-53(Fe)	Precipitation
[320]	Pt-Co	1.7 nm	UiO-66	One step or impregnation
[321]	In$_2$S$_3$	2.5 nm	MIL-101	Double solvents method
[322]	Au	2 nm	Zn$_{14}$(L)$_6$(O)$_2$(H$_2$O)$_3$	Centrifugation
[323]	Pt Ni	10–15 nm < 5 nm	MIL-101	Rotary chemical evaporation method
[324]	Pd	2.4 nm	MIL-101	Double solvents method coupled with reduction
[325]	AuNi	1.8 nm	MIL-101	Double solvents method

With the objective of obtaining switchable reversible catalysts, the species that can be embedded in the framework can be of two types: catalytically active guests (*e.g.* metal catalyst complexes, metal clusters, surfactant stabilized metal NP) and catalytically inert guests (*e.g.* polystyrene nanobeads, silica nanoparticles). In particular the latter can be regarded as a meso-scale "defect" or "heterogeneity" in the framework. Indeed, an important fact to take into account when trying to understand the flexible behaviour of MOFs, is that they are particularly prone to various forms of defects and related disorder (missing linkers and nodes, modified nodes, correlated defects, *etc.*)[326] and that the mechanical properties are related to the defect concentration and type. Thus, their flexible behaviour depends not only on the size and shape of the crystallites, but also on the "defectiveness" of the structure. The contribution of disorder becomes even more relevant in the case of functionalised linkers and multivariate (*i.e.* mixed-ligand or multicomponent) MOFs. However, the theoretical comprehension of particle size effects, defects, influence of substituted linkers, presence of guest molecules and their interrelationship within flexible MOFs is still at an early stage. T. D. Bennett and co-authors proposed an analysis about the complex correlation of these properties in a pioneering article (Figure 4.6).[327]
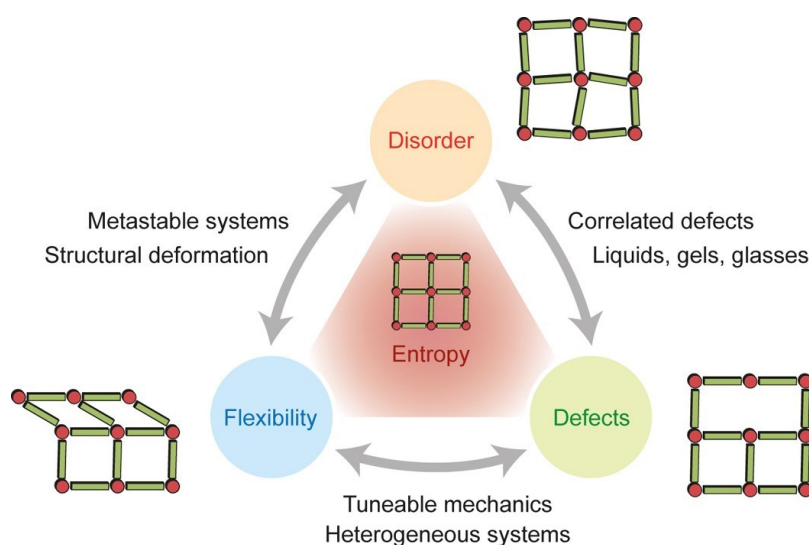
Figure 4.6 - Illustration of the interplay between the intertwined concepts of flexibility, defects and disorder in metal–organic frameworks, highlighting some of the phenomena that emerge from their combination.[327]

The long-term vision will be the design of "switchable-lock" catalysts. In other words, catalytic functionalised MOFs that are capable of selectively converting a specific molecule under a controlled stimulus of a gate-opening molecule. It would for example be interesting to obtain a higher adsorption of a molecule A in the presence of B and thus an enhanced formation of P_A over P_B if an external stimulus is applied.

4.1.4 Synthetic Strategies for Integration of NPs into MOFs

It is well known that the size and morphology of NPs are important parameters which greatly affect their catalytic performance. However, it is difficult to precisely control the size and dispersion and retain the ideal morphology of NPs during the actual synthesis of NPs@MOF composite catalysts. Therefore, several preparation methods for embedding (metal) NPs into MOFs have been developed[57–59,328,329] and can be generally classified into four main strategy groups:

1) The *"ship-in-a-bottle"* strategy is a two-steps process in which the corresponding precursors are dispersed inside the MOF pores followed by the formation of the NPs by *in situ* self-assembly. Several different methods have been applied for this:

   ⊙ *Chemical vapor deposition* (CVD), the method first used for that, is carried out exposing the activated MOF to vapours of the volatile metal precursor, in order to diffuse it into the MOF framework at a certain temperature under static vacuum. Utilizing UV irradiation and/or reactive gases, the NPs are integrated inside the MOF. This is a solvent-free process based on the high volatility of most organometallic compounds at high temperatures.[330,331]

   ⊙ *Solution impregnation* is a simple method where MOF crystals are immersed in a solution of the metal precursors. The capillary pressure facilitates these to enter the interior voids of the MOFs spontaneously. Subsequently, the metal precursors are reduced to NPs.[332,333]

   ⊙ *Double-solvent approach* (DSA) is an effective methodology for immobilizing NPs inside the MOF pores and avoiding their aggregation on the outer surface of the MOF. First a low-boiling-point organic solvent is used to disperse the MOF powder while a second one, usually a really small volume of aqueous solution of the metal precursor, is added to the suspension. The metal precursor is absorbed in the MOF cavities owing to the capillary force arising from hydrophilicity of the inner surface of the MOF. Tiny NPs are finally obtained by reduction of the metal precursor and confined into the framework.[334]

   ⊙ *Solid grinding* is another simple method where a specific ratio between the amounts of metal precursor and pre-activated MOFs are ground mechanochemically. The organometallic precursors sublimate during grinding and diffuse into the MOF pores. This is followed by the reduction of the metal precursor at an appropriate temperature to yield the NPs.[335]

2) The *"Bottle-around-a-ship"* is a strategy, which involves *in situ* construction of MOF around the dispersed NPs by the following methods:

   ⊙ The *surfactant-assisted encapsulation* is done using surfactant-capped NPs. Their surface is functionalized with polyvinylpyrrolidone (PVP), which acts as a surfactant both to stabilize and to regulate the size and shape of the NPs. They are then dispersed and enclosed into the MOF crystals.[307]

- ◉ The *sacrificial template method* is useful to obtain core–shell structural materials or porous materials. A typical procedure starts with coating of the pre-synthesized NPs with a template layer, in order to grow a MOF shell outside, then the template layer is selectively eliminated.[309,336]

- ◉ The *template protection–sacrifice method* is characterised by four steps. First one is the synthesis of the NPs, followed by growth of a silica shell around them; later there is an *in-situ* formation of MOF crystals around the coated NPs (like for the "bottle-around-a-ship" method), and finally selective etching of the silica layer is made. SiO_2 serves as a protector against the metal NPs oxidation, as a sacrificial template and also as a generator of hollow space between the NPs and the MOF shell.[337]

3) The *step-by-step* strategy is mainly used for the synthesis of sandwich-like structures (MOFs/MNPs/MOFs).[338] To achieve these composite catalysts, the first step is the synthesis of the MOF crystals, then pre-synthesized NPs are assembled on the surface of the MOF core by physical adsorption or electrostatic interaction, and finally a MOF layer is grown out of the core–shell component obtained previously.

4) The *one-step synthesis* consists in the direct mixing of all the precursors for the NPs and also for the MOF, in the appropriate reaction mixture (usually PVP and dimethylformamide (DMF) are the most common media for the synthesis of metal NPs and MOFs respectively) to obtain the core–shell structure.[339]

4.2 Stimuli-responsive MOFs

Flexible Metal Organic Framework are also known by the term *stimuli-responsive* MOFs. To better understand the responsiveness shown by these materials, a distinction between dynamic and static behaviour must be defined first. Dynamic behaviour is defined by response of the material to a certain external stimulus (temperature, gas pressure, light, *etc.*)[340–342] with a considerable structural change, such as a phase transition to another crystalline phase,[234,247,260,343,344] amorphization (*i.e.* loss of long-range order),[345–347] or switching of a flexible functionality on the linker. On the other hand, static responsiveness occurs without structural variations of the framework, but instead considers the *host-guest* interactions, for example when showing adsorption towards a specific guest thanks to the size, polarity or shape of the pores.[85,348–351] Important to note is that responsive behaviour is not always reversible.[352,353] Both behaviours are well-known and deeply studied today, yet only a small fraction of MOFs can be defined as stimuli-responsive among the plethora of MOFs reported so far (112,400 reported structures in the CSD, Figure 1.3).[20]

The most relevant definition for flexible MOFs was established by S. Kitagawa, who describes them as "[…] porous solids that possess both a highly ordered network and structural transformability. They are bistable or multi-stable crystalline materials with long-range structural ordering, a reversible transformability between states, and permanent porosity. The term permanent porosity means that at least one crystal phase possess space that can be occupied by guest molecules, so that the framework exhibits reproducible guest adsorption."[25] This definition, however, is very narrow and does not include other types of flexibility. Flexible MOFs, which are often alternatively called soft-porous crystals, can be divided into two general classes:

⊙ *Class a* materials, with intrinsic responsiveness, which undergo structural changes without the need of guest molecules, but (reversibly) respond to other stimuli such as temperature, pressure, light, electric or magnetic fields *etc*. (Reversible) crystalline to amorphous transitions can also be allocated to this group. The series of so-called fu-MLPs, $[M_2(fu-L)_2(dabco)]$ ($M^{2+} =$ Zn^{2+}, Cu^{2+}, Co^{2+}, Ni^{2+}; L = linker (*e.g.* bdc^{2-}), P = pillar (*e.g.* dabco = diazabicyclo[2.2.2]octane)), introduced by R. Fischer and co-workers[343] is a good example for this category. The responsiveness is introduced by inserting flexible side chains on the linker (fu-L) and which causes large volumetric expansion these materials (breathing behaviour) when varying the temperature and/or the gas pressure.[354]

⊙ *Class b* materials, which possess intrinsic mechanical responsiveness based on host/guest interactions (adsorption/desorption). The promising possible applications of flexible MOFs in current industrial challenges for gas adsorption (*e.g.* hydrogen[355,356] and carbon dioxide[357,358]) and separation (*e.g.* olefines *vs.* paraffins from hydrocarbon mixtures[359]) stem from the interesting properties of these systems, such as intrinsic porosity, reversible uptake of guest molecules, or the possibility to tune the selectivity. Exploiting dynamic responsiveness for this kind of applications is still difficult, and in fact more studies in this direction are known for static-responsive MOFs. For example, introducing functional groups in the bdc^{2-} linker of the Zr-based MOF UiO-66 ($Zr_6O_4(OH)_4(bdc)_6$) revealed an increased CO_2 uptake when using small, polar substituents such as $-NH_2$, $-NO_2$ or $-OH$, whereas the N_2 uptake is more affected by the molar mass and size of the linker.[360,361]

4.2.1 Pillared-layer MOFs

The aforementioned fu-MLPs series is a member of the pillared-layer MOF family that can be described with the general formula M_2L_2P. It consists of binuclear paddle-wheels based on divalent metal ions (M(II)) and linear anionic dicarboxylate linkers (L^{2-}, *e.g.* trans-1,4-cyclohexanedicarboxylate, 1,4-benzenedicarboxylicate, or 2,5-functionalised-1,4-benzenedicarboxylate) as well as the pillar (P, *e.g.* diazabicyclo[2.2.2]octane, 4,4'-bipyridine) which is a neutral nitrogen linker.[237,362] In particular, the

pillared-layer MOFs based on functionalised bdc^{2-} linkers (denoted from now on as fu-bdc^{2-}) and dabco molecules, the pillars, have been intensively studied in the research group of. R. Fischer over the last years. These materials are characterised by intrinsic responsiveness, *i.e.* breathing phenomena.[343] Interestingly, the parent MOF of this family, $Zn_2(bdc)_2dabco$, has been initially considered a 2nd generation framework. Only successive studies revealed that it shows a dynamic response dependent on the nature of the guest, which leads to a deformation of the network in the presence of N,N-dimethylformamide (DMF) or benzene (Figure 4.7).[363] Later works showed that also the presence of alcohols (methanol, ethanol, isopropanol) in the framework can lead to expansion and shrinking phenomena.[364]
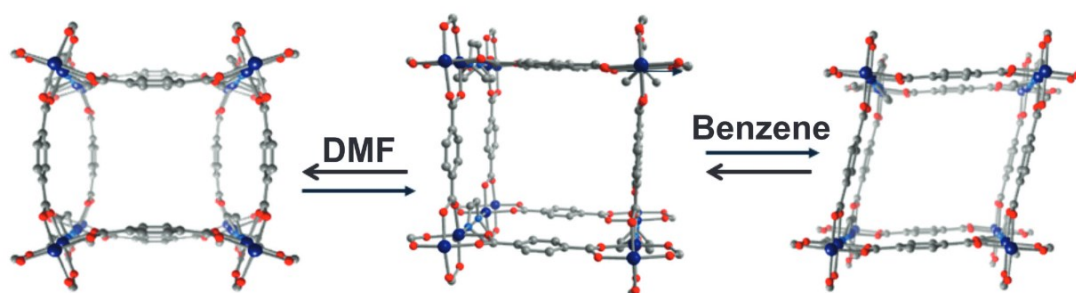

Figure 4.7 - Graphical representation of the as synthesised $Zn_2(bdc)_2dabco$ framework (centre), distorted upon impregnation with DMF (left) and benzene (right). Colour code: Zn, blue; O, red; C, grey; H atoms are omitted for clarity.[246]

The discovery of a new type of flexibility in this MOF family was an important breakthrough. S. Cohen and co-workers changed the functionalisation of the bdc^{2-} linker for the MOF $Zn_2(NH_2\text{-bdc})_2dabco$ (NH_2-bdc^{2-} = 2-amino-1,4-benzenedicarboxylate) *via* PSM by treating with linear alkyl anhydrides of different chain length which converted the NH_2 groups to the corresponding amide. The modified MOF retains its crystallinity and microporosity and gains a breathing behaviour from an *op* to a *cp* phase upon guest removal.[46] For pillared-layer MOFs this was the first time, researchers observed that the presence of flexible side chains pointing inside the framework pores induces a breathing-type behaviour. Bringing forward the same line of research, S. Henke *et al.* synthesised a new series of pillared-layer MOFs of the general formula $[M_2(fu\text{-bdc})_2P]$ with M^{2+} = Zn^{2+}, fu-bdc^{2-} = vast library of pendant alkyl ether functionalised benzenedicarboxylate linkers (Figure 4.8) and P (pillar) = dabco or bipy.
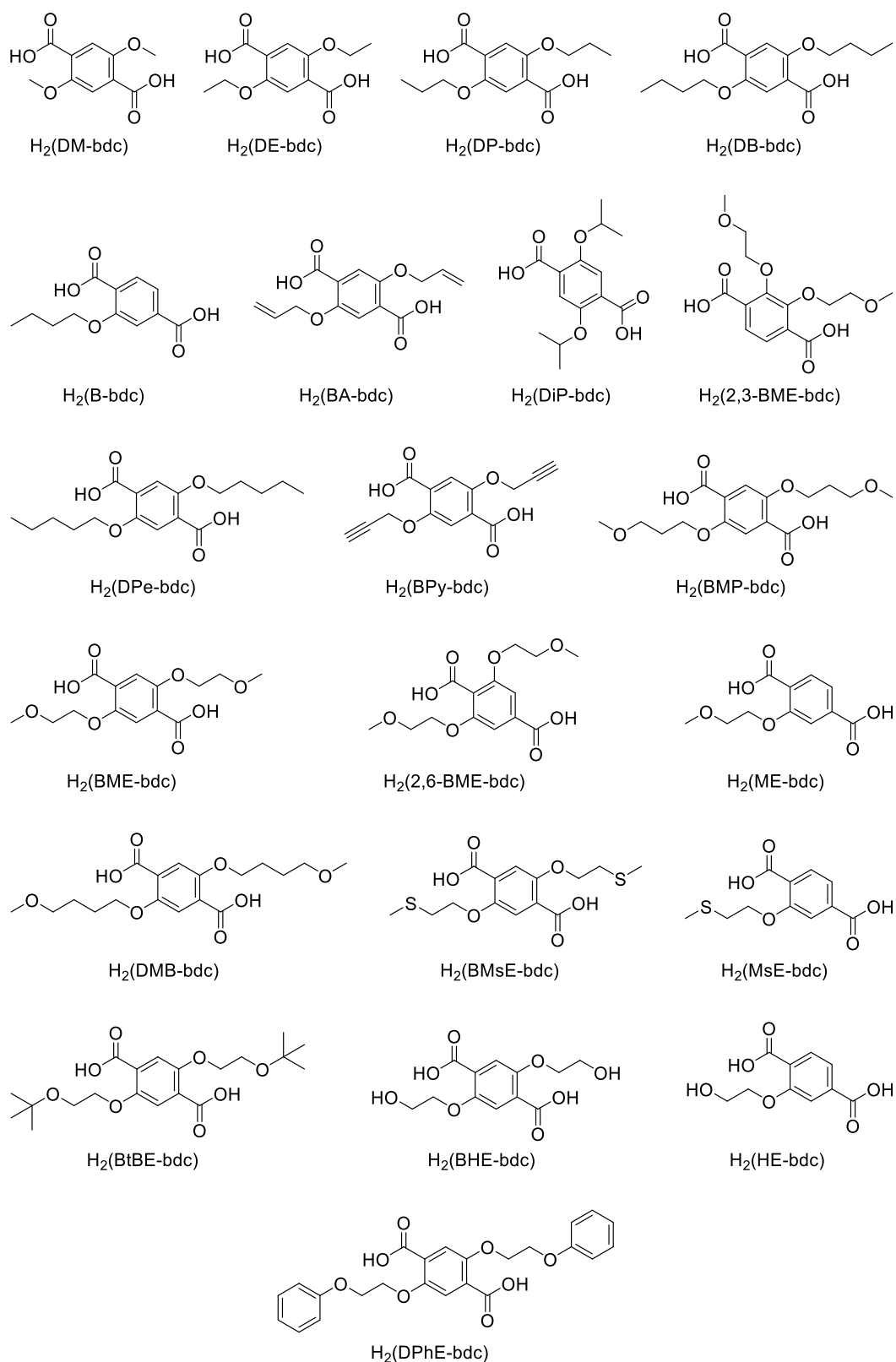
Figure 4.8 - Library of H$_2$(fu-bdc) linkers having various linear alkoxy groups with different chain lengths and degree of saturation.

These MOFs respond to various stimuli such as temperature, pressure, *host-guest* interactions and solvent removal after the synthesis, showing a phase transition from an *op* to a *np* phase. The degree of flexibility and responsiveness depend on both the choice of metal centre and the linker, in particular its functionalisation. Interestingly, the degree of structural phase transition decreases with longer side chains and flexibility is completely lost when the alkoxy chain length exceeds five carbon atoms. This is caused by the steric hindrance present in the pores and the resultant difficulty of the contraction of the framework.[343] As an example, the crystal structure of the flexible pillar-layered MOF Zn_2(BME-bdc)$_2$dabco (with BME-bdc^{2-} = 2,5-bis(2-methoxyethoxy)-1,4-benzenedicarboxylate; side chain length = 5 atoms including C and O) in shown in Figure 4.9.[41,343,365]
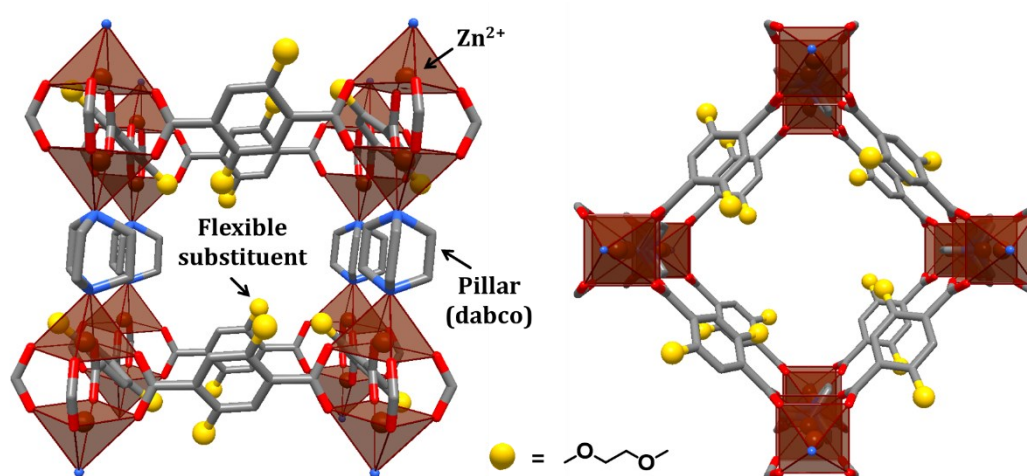

Figure 4.9 - Crystal structure of Zn_2(BME-bdc)$_2$dabco determined by single-crystal X-ray diffraction. View along the [110] direction (left) and view along the [001] direction (right). The flexible side chains on linker could not be included in the structural model due to the high degree of disorder and are here represented as yellow spheres. Colour code: Zn coordination polyhedra, brown; O, red; N, blue; C, grey.[343]

The MOF Zn_2(BME-bdc)$_2$dabco has been thoroughly studied in the group of R. Fischer.[42,343,354,366–369] It crystallises in the monoclinic space group *C2/m* and the SBU is constituted by paddle-wheels built from binuclear units where Zn^{2+} is bridged by four carboxylates of four linkers to form a 2D square planar grid of {Zn_2bdc$_2$} motifs. The pillars link these grids to form a 3D framework, which presents a rhombic pattern instead of a square one seen by the parent MOF Zn_2(bdc)$_2$dabco. Zn_2(BME-bdc)$_2$dabco is non-porous towards N_2 but has a good sequestration capacity for CO_2 thanks to the polar functional groups on the linkers which can be seen as molecular gates that open when reaching a certain threshold pressure (P ≈ 0.2 GPa). The CO_2 sorption isotherm is characterised by steps and a hysteresis loop, distinctive for breathing MOFs. The framework contraction is enthalpically favoured, while the opening is entropically driven. The transformation between *op* and *np* phases has also been observed upon solvent removal via thermal activation and re-solvation with DMF (Figure 4.10).[343]
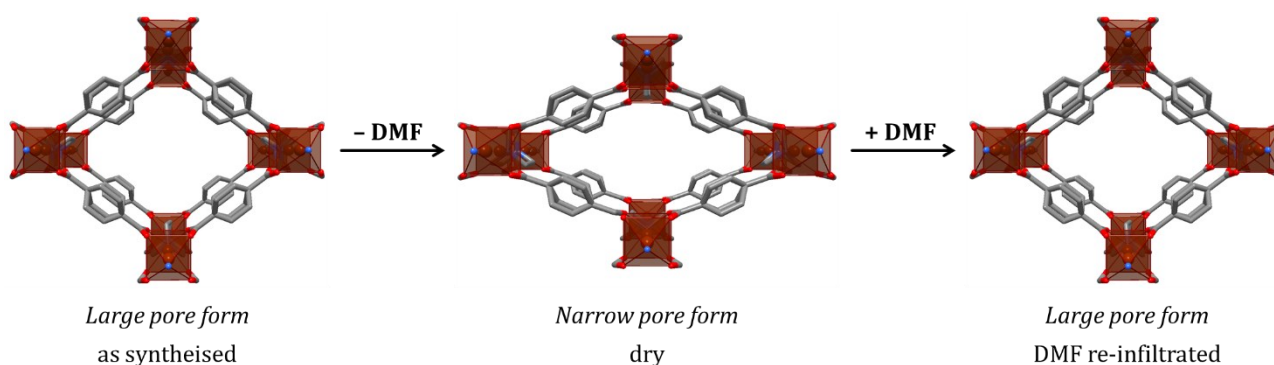
Large pore form
as syntheised

Narrow pore form
dry

Large pore form
DMF re-infiltrated

Figure 4.10 - Visualisation of the pore aperture along the crystallographic c-axis. The *as*-synthesised *lp* form of Zn$_2$(BME-bdc)$_2$dabco transforms to the dry *np* form upon guest removal. Soaking the dry MOF in DMF gives the re-infiltrated *lp* form, which has nearly the same structure as the initial one. The 2-methoxyethoxy side chains are omitted for clarity. Colour code: Zn coordination polyhedra, brown; O, red; N, blue; C, grey.[343]

4.3 Implementing Defects, Disorder and Guests into Flexible MOFs

The objective of this work focuses on the encapsulation of nanoparticles (NPs) without catalytic function in order to effectively study the correlation between mesoscopic defects in selected flexible MOFs and their properties. The work is based on the comparison of the parent pillared-layer MOFs with the corresponding composite materials indicated with the term NPs@MOFs (or SiO$_2$@MOF in this study). The focus lies on the structural heterogeneity and disorder obtained after inclusion of catalytically inert NPs (silica or polystyrene) and the consequent creation of meso-scale defects in the framework. Not only the encapsulated NPs but also the presence of flexible (disordered) side chains at the linker backbone can be regarded as "defects" or more precisely as elements of disorder to the system. Many other aspects worth understanding are also investigated, such as the effects of the length and functionalisation of the linker side chains on the pore volume, dipolar interactions arising from the use of different alkoxy side chains on the organic ligands, or the degree of heterogeneity of the system due to mixed fu-bdc^{2-} or nanoparticle encapsulation. Moreover, the use of big NPs (30 nm) larger than the MOF pores is linked to one of the objectives of this work, *i.e.* the implementation of mesoscopic defects and understanding of the correlation between flexibility, defects and disorder.

An overview on the general characteristics of the MOFs studied in this thesis is given in Table 4.2.

Table 4.2 - Overview of the fu-MLP MOFs studied in this thesis.

	$Zn_2(bdc)_2(dabco)$	$Zn_2(DM\text{-}bdc)_2(dabco)$	$Zn_2(BME\text{-}bdc)_2(dabco)$
Composition	$M = Zn^{2+}$ $L = bdc^{2-}$ $P = dabco$	$M = Zn^{2+}$ $L = DM\text{-}bdc^{2-}$ $P = dabco$	$M = Zn^{2+}$ $L = BME\text{-}bdc^{2-}$ $P = dabco$
Space group	lp ⇨ *I4/mcm* np ⇨ *P4/mmm*	lp ⇨ *P4/nbm* np ⇨ *unknown*	lp ⇨ *C2/m* np ⇨ *C2/m*
Structure	Pillar-layered	Pillar-layered	Pillar-layered
Flexibility	*Dynamic* Small deformation in the presence of solvents	*Dynamic* Breathing under variable pressure	*Dynamic* Breathing under variable temperature and pressure

* bdc^{2-} = benzenedicarboxylate; DM = dimethoxy; BME = bis-(2-methoxyethoxy)

Next, the synthesised hybrid systems NPs@MOF were aimed to be characterised by a range of techniques:

⦿ Routine methods to check the composition and crystalline phase purity (XRPD, IR, EA) as well as thermal stability (TGA).

⦿ Imaging techniques and specific spectroscopy experiments to locate the nanoparticles (EFTEM, TEM tomography, UV-Vis and PL spectroscopy).

⦿ Specific analyses to understand variations in the flexible behaviour upon variable temperature (thermoresponsivity) (VT-XRPD, DSC/TGA, cyclic DSC) and variable gas pressure (single component sorption isotherms) in order to assess the effects of the mesoscopic defects introduced with the silica nanoparticles.

To summarize, the new hybrid systems NPs@MOF can be viewed as composite materials where the NP represents a mesoscopic defect in the network and since the thermodynamics of the flexible behaviour of MOFs is related to entropy, the understanding of defects and disorder is fundamental when designing and modelling their responsive behaviour while aiming for applications.

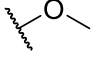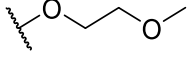The long-term vision will be the design of "switchable-lock" catalysts. In other words, catalytic fu-MLPs that are capable of selectively converting a specific molecule under a controlled stimulus of a gate-opening molecule. It would for example be interesting to obtain a higher adsorption of a molecule A in the presence of B and thus an enhanced formation of P_A over P_B if an external stimulus is applied.

4.4 Results and Discussion

4.4.1 Organic Components, Flexible MOFs and NPs@flexbile MOFs Synthesis

The flexible functionalised pillared-layer MOFs of formula $[M_2(fu\text{-}bdc)_2P]_n$ with $M^{2+} = Zn^{2+}$, $fu\text{-}bdc^{2-}$ = existing linker library (Table 4.3) and P = dabco, have been selected for this work.

Table 4.3 - Functionalised benzenedicarboxylate linkers used.

fu	–H		
Acronym	H_2bdc^{2-}	$DM\text{-}bdc^{2-}$	$BME\text{-}bdc^{2-}$
Name	1,4-benzenedicarboxylate	2,5-bis(methoxy)-1,4-benzenedicarboxylate	2,5-bis(2-methoxyethoxy)-1,4-benzenedicarboxylate

The synthesis of the chosen flexible MOFs follows the known protocols and consists in a solvothermal reaction in which a mixture of $Zn(NO_3)_2 \cdot 4H_2O$, $H_2(fu\text{-}bdc)$ and dabco (molar ratio 2:2:1) in DMF is heated in a closed screw jar to 120 °C for 48 h to yield small colourless crystals with composition $\{[Zn_2(bdc)_2(dabco)]_n \cdot (DMF)_x\}$ and light beige crystalline powders with composition $\{[Zn_2(DM\text{-}, BME\text{-}bdc)_2(dabco)]_n \cdot (DMF)_x\}$ (Figure 4.11).[343] Alkoxy-functionalized linkers, namely $H_2(DM\text{-}bdc)$ and $H_2(BME\text{-}bdc)$, were prepared by use of Williamson ether synthesis starting from 2,5-dihydroxy-terephthalic acid dimethyl ester and the corresponding *n*-bromoalkane according to the literature.[343]
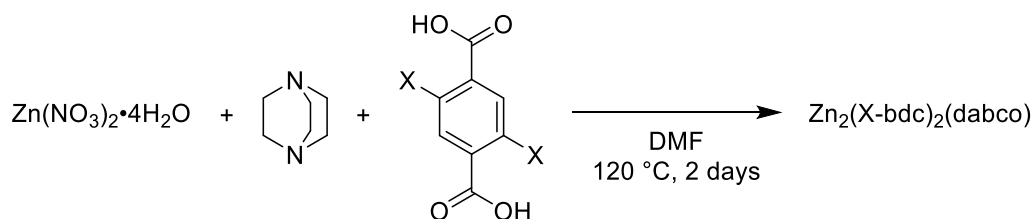
Figure 4.11 - General synthetic procedure for the plain MOFs $\{[Zn_2(fu\text{-}bdc)_2(dabco)]_n \cdot (DMF)_x\}$ from $Zn(NO_3)_2 \cdot 4H_2O$, dabco and $H_2(fu\text{-}bdc)$.

The selection of nanoparticles (NPs) without catalytic function for the implementation of mesoscopic defects into $[M_2(fu\text{-}bdc)_2P]$ consists of fluorescent silica nanospheres (Table 4.4). The choice of fluorescent nanoparticles arises from the need to detect them after the embedding into the framework. The large dimension of the NPs should allow the implementation of mesoscopic defects into the MOF framework. In fact, the NPs size is larger than the MOF pores, 30 and ~15 nm, respectively. Finally, the

idea of using functionalized NPs with surfactants should allow a better dispersibility in solvents, but also provides a core to grow the MOF shell outside.

Table 4.4 - Catalytically inert NPs chosen for the encapsulation process.

Material	Type	Size (nm)	Solvent	Quantity (mL)	Loading (calc.)
SiO$_2$	fluorescent, suspension (25 mg/mL), red	30	water	0.100 - 0.500	1 – 3.3 %
SiO$_2$-COOH	fluorescent, suspension (25 mg/mL), red	30	water	0.100	

For the encapsulation of the NPs, different synthetic routes have been tried with changing the main reaction parameters (solvent, temperature, time, heating method, nanoparticle loading) multiple times. Finally, the most promising results were obtained using the *"bottle-around-the-ship"* strategy. The general method is a solvothermal reaction in which a mixture of Zn(NO$_3$)$_2$·4H$_2$O, fu-bdc^{2-} and dabco (molar ratio 2:2:1) together with the SiO$_2$ NPs in DMF is heated in a closed screw jar to 120 °C for 48 h to yield a white crystalline powder for {SiO$_2$@[Zn$_2$(bdc)$_2$(dabco)]$_n$·(DMF)$_x$} and light beige crystalline powders for {SiO$_2$@[Zn$_2$(DM-, BME-bdc)$_2$(dabco)]$_n$·(DMF)$_x$} composite materials, where the NPs should be coated by a MOF shell (Figure 4.12). Interestingly, the syntheses for the pristine MOFs, as well as for the corresponding composite materials SiO$_2$@MOFs, have worked even running the reaction at room temperature.
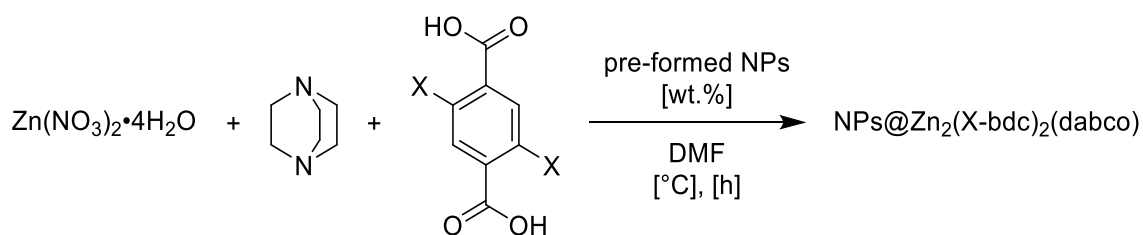
Figure 4.12 - General synthetic procedure of composite MOF materials {SiO$_2$@[Zn$_2$(fu-bdc)$_2$(dabco)]$_n$·(DMF)$_x$} from Zn(NO$_3$)$_2$·4H$_2$O, dabco, H$_2$(fu-bdc) and pre-formed silica nanoparticles.

The as synthetised samples (*as*) have been washed in DMF and CHCl$_3$ and/or CH$_2$Cl$_2$ and then activated *in vacuo* at elevated temperature to yield the guest-free (*dry*) MOFs under the following conditions: *a*) simple thermal activation (*act*) has been achieved heating to 120 °C for 2 hours and 80 °C overnight with subsequent storage of the sample in air, whereas *b*) complete framework evacuation (*dry*) has been obtained keeping the sample at 150 °C for 2 hours and 80 °C for 48 hours with subsequent storage of under inert atmosphere.

The products obtained after many synthetic trials have been checked through X-ray powder diffraction analysis (see Chapter 4.4.2) and an overview of all synthesised materials is given in Table 4.5. It was observed that the synthesis in the presence of pre-formed silica nanoparticles was never successful for the parent MOF $Zn_2(bdc)_2(dabco)$ (Figure 4.13a). A possible reason could be that it is possible to incorporate the NPs only in fully flexible frameworks, instead this MOF shows only a slight degree of flexibility.[246] On the contrary, all reactions were successful when working with DM-bdc[2-] linker containing MOFs (Figure 4.13b). Regarding the last sample, $Zn_2(BME-bdc)_2(dabco)$, only the encapsulation of SiO_2-COOH did not work. In fact, the desired crystalline phase was obtained, but from XRPD analysis additional peaks are detectable (Figure 4.13c).

The presence of the substituents on the linkers has been confirmed by elemental analysis and infrared spectroscopy (see Experimental Section, Figure 6.31).

Table 4.5 - Overview of the components and NPs used for the synthesis of pillared-layer MOFs, tick marks indicate the successfully obtained MOFs.

		Plain		With SiO_2		With SiO_2-COOH	
Metal	*Pillar*	*Ligand*	*Success*	*Ligand*	*Success*	*Ligand*	*Success*
		H_2bdc	✓	H_2bdc	✗	H_2bdc	✗
Zn^{2+}	dabco	DM-bdc	✓	DM-bdc	✓	DM-bdc	✓
		BME-bdc	✓	BME-bdc	✓	BME-bdc	✗

4.4.2 X-Ray Powder Diffraction Analysis

The as synthesised compounds yield only crystalline powders. Their purity as well as identity (cell metrics and space group) have been confirmed by XRPD analysis using a Le Bail fitting and comparison with the ones found in literature obtained from single crystal XRD, finally confirmed via Le Bail fitting. The obtained data clearly show that the plain MOFs and NPs@MOFs are isostructural. The obtained unit cell parameters for the as synthesised and dry crystalline phases are summarised in Table 6.21 of the Experimental Section and compared with literature data (Table 6.20).[354,363,37041371] Graphical output for all the Le Bail analyses performed is given in Figure 6.32.

On the reported powder patterns the chemical formulas on the right indicate the type of MOF and the synthetic conditions and/or post-synthetic treatment. In the case of $Zn_2(BME-bdc)_2(dabco)$ the pattern for the as synthesised material is not equivalent to the simulated one. This is due to the treatment applied to the MOF before XRPD analysis, which included washing with $CHCl_3$ prior to thermal activation. This results in a change of position of some diffraction peaks and the obtained powder pattern is the known one for the *dry* form (closed pore phase). In particular, some of the reflections are

shifted to higher 2θ values and this indicates a contraction of the framework (*op* to *cp* transition) when the solvent is removed. This interesting behaviour was already observed by S. Henke *et al.*[365] (Figure 4.13c). Re-infiltration with DMF leads to the initial op phase as determined by XRPD.

In the powder pattern of $Zn_2(DM\text{-}bdc)_2(dabco)$, small additional peaks are possible which been excluded from the Le Bail refinements because they represent the already partly desolvated structure.
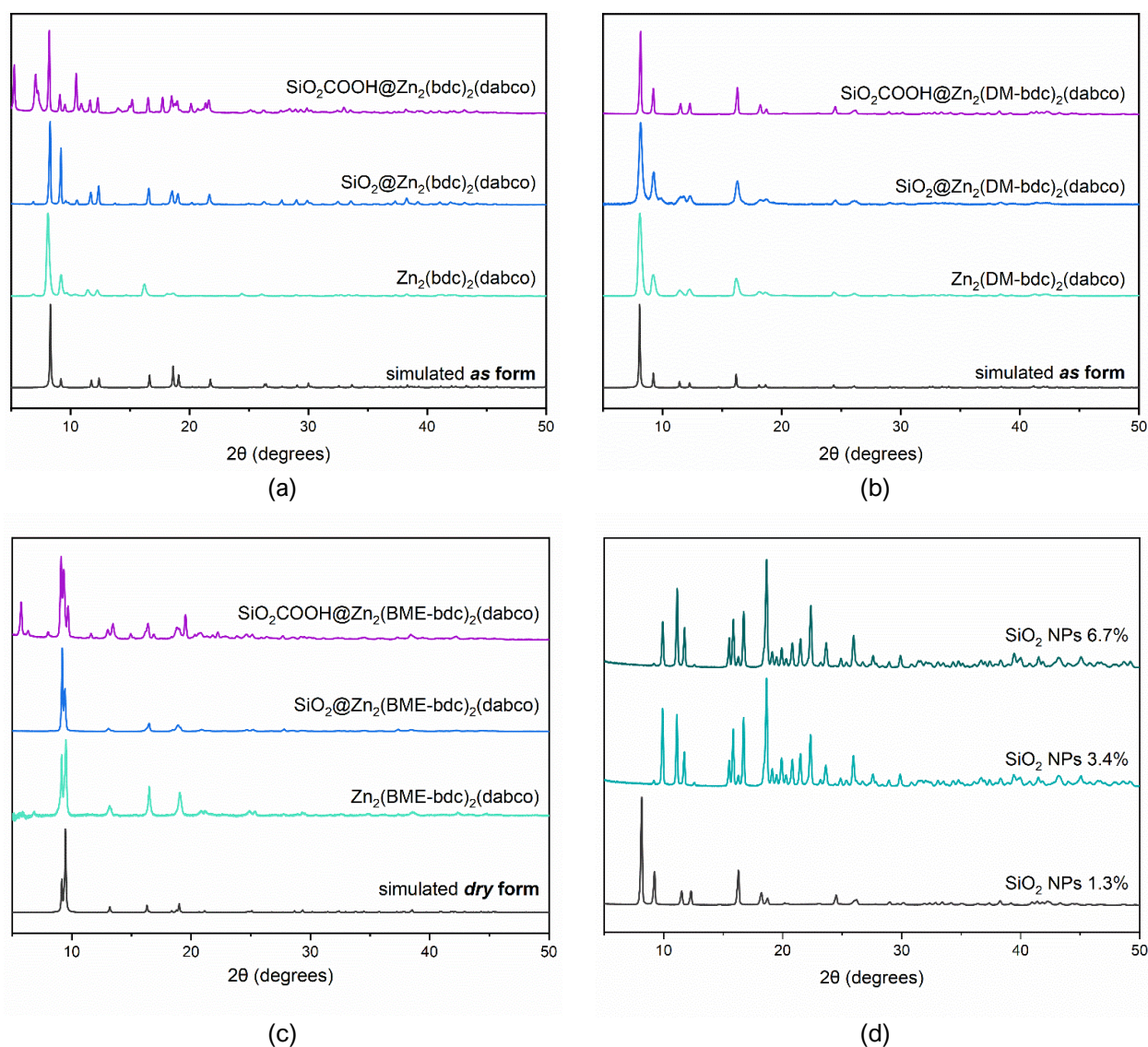
Figure 4.13 - XRPD patterns of the synthesised MOFs compared to simulated ones from single crystal XRD for (a) $Zn_2(bdc)_2(dabco)$, (b) $Zn_2(DM\text{-}bdc)_2(dabco)$ and (c) $Zn_2(BME\text{-}bdc)_2(dabco)$. (d) XRPD patterns of $SiO_2@Zn_2(bdc)_2(dabco)$ upon increasing nanoparticles loading.

As mentioned before, for $Zn_2(bdc)_2(dabco)$ only the plain MOFs is obtained and not the NPs embedded one (Figure 4.13a), and the crystalline phase matches the one reported in literature as confirmed by the results of the Le Bail fitting (see Experimental Section, Table 6.21). For $Zn_2(DM\text{-}bdc)_2(dabco)$ comparison of the experimental XRPD patterns with the simulated one derived from single crystal data,

81

reveals the good products obtained at different synthetic conditions (Figure 4.13b), but Le Bail fittings resulted particularly difficult to perform in the case of the activated materials because of the broadening of the peaks and a drastic loss of intensity. In fact, for the activated form (*cp* phase) of this MOF no unit cell parameters obtained from single crystal data can be found and XRPD analysis is impossible due to the major loss of crystallinity.[343] This interesting phenomenon resembling amorphization is better described in Chapter 4.4.3. SiO$_2$-COOH@Zn$_2$(BME-bdc)$_2$(dabco) could not be synthesised in a pure crystalline form. Although the desired product is obtained, additional peaks originating from an unknown crystalline phase(s) can be observed (Figure 4.13c) and no cell reported in literature could be successfully indexed with the experimental ones. This MOF, however, shows an interesting behaviour since the as synthesised powder presents the diffraction signals typical of the *dry* material; the difference between *as* and *dry* forms can be seen from the first signal at 6.8 2θ degrees, whose intensity is almost reduced to zero for the *dry* sample. This means that just for the BME-bdc^{2-} containing MOF, evacuation of the solvent molecules from the pores (and resultant transformation from a large to a narrow pore phase) is fast and can occur without thermal activation under vacuum.

After thermal activation, a general decrease of peaks' intensity is observed for all MOFs, especially in the case of Zn$_2$(DM-bdc)$_2$(dabco).

Embedding higher quantities of NPs (see Table 4.4) results in a complex mixture of crystalline phases, in fact encapsulation of around 0.100 mL (25 mg/mL) of nanoparticle suspension (1.3%) results in the correct product, NPs loadings ≥0.250 mL (3.4%) do not lead to the desired composite material (Figure 4.13d).

Since the all attempts for the encapsulation of the NPs into Zn$_2$(bdc)$_2$(dabco) failed, only the flexible MOFs containing DM-bdc and BME-bdc linkers will be considered for the successive analyses and compared to their respective NPs@MOFs.

4.4.3 Crystalline to Amorphous Reversible Transition

Among the MOFs studied in this work, Zn$_2$(DM-bdc)$_2$(dabco) and also SiO$_2$@Zn$_2$(DM-bdc)$_2$(dabco) were discovered to be structurally responsive upon removal of solvent from the framework. Indeed, the solvated MOFs possess a highly crystalline structure, whereas the empty network gives rise to a disordered crystalline phase where the loss of long-range order results in an (almost) amorphous XRPD pattern. Amorphization and partial collapse of the framework is observed even in the case of storage under inert atmosphere (glove box). The significant loss of crystallinity occurs when all adsorbed water molecules are removed from the framework, this happens over long periods of time (months) if the sample is left in air, otherwise is a much faster process when the MOF is thermally activated, this is not observed for the BME-bdc^{2-} containing MOF (Figure 4.14).
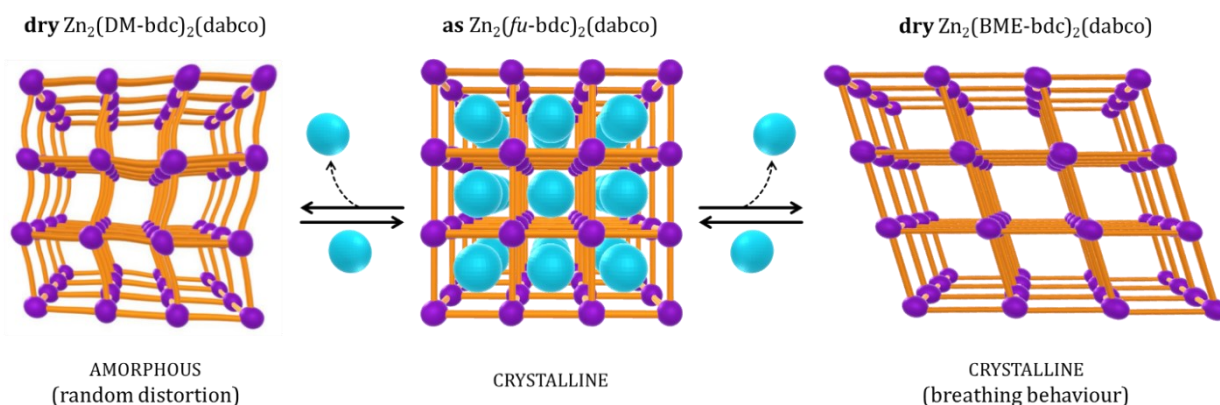
Figure 4.14 - Graphical representation of the different guest-responsive structural behaviour for Zn_2(DM-bdc)$_2$(dabco) (left) and Zn_2(BME-bdc)$_2$(dabco) (right).

Flexible MOFs which can transition between crystalline and amorphous phases are still poorly studied because of the difficulty in characterising their disordered nature, but this behaviour has been reported for other few MOFs structures.[345,346,372] This "amorphization" process is completely reversible and depends on the degree so solvent present in the MOF pores. In fact, upon impregnation of the "amorphous" material with appropriate solvents the framework yields the infiltrated composites DMF@Zn_2(DM-bdc)$_2$(dabco) which returns to the starting op form, as determined by XRPD. In the case of Zn_2(DM-bdc)$_2$(dabco), the return to the crystalline phase is quite fast (less than 1 hour) when DMF is added, instead nothing happens if the solvent used is CH_2Cl_2. In addition, two different re-solvation methods have been tried, *i.e.* stirring the MOF in DMF at room temperature for some hours and simply dropping a small quantity of solvent on the powder already prepared on the sample holder to be measured via XRPD. As shown in Figure 4.15, the crystallinity is again fully obtained in both cases.

This phenomenon can be better described as a loss of long-range order in the crystal structure. The structural analysis for the dry form of this MOF is challenging since the activated material cannot be analysed by routine X-ray diffraction methods. Furthermore, no unit cell parameters for the activated crystalline phase (*cp* form) of Zn_2(DM-bdc)$_2$(dabco) can be found in the literature. Additional experiments are being performed to comprehend this interesting phenomenon and more details can be found in Chapter 4.6.
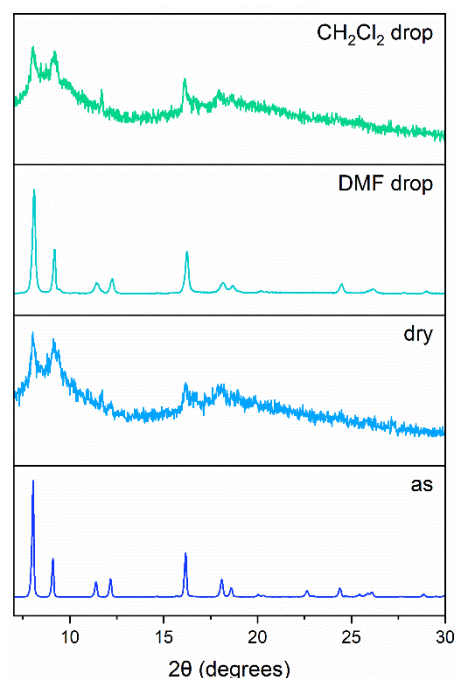

Figure 4.15 - PXRD patterns of the as-synthesised, dried, DMF and CH_2Cl_2 reinfiltrated forms of Zn_2(DM-bdc)$_2$(dabco).

4.4.4 UV-Vis and Photoluminescence Measurements

To check the presence of the fluorescent silica-NPs, Ultraviolet-Visible (UV-Vis) and photoluminescence (PL) spectroscopy have been chosen as preliminary detection tools to measure absorption and emission respectively. The measurements have been performed on solid samples. One can see from Figure 4.16 that the fluorescence signal is still present for different treatments on the composite materials, *i.e.* multiple washing procedures with $CHCl_3$ and CH_2Cl_2 and thermal activation at 150 °C for 2 hours and 80 °C for 48 hours. Because the pristine MOF is not fluorescent, the observation of the signal confirms the presence of the NPs in the new composite materials. However, no conclusion about the location (on the surface or inside the pores) can be done yet. The variation in intensity of the signals is not related to the concentration of NPs and it is only due to different instrumental parameters for the various experiments performed. In fact, no quantitative analysis has been made during these measurements. The results for $SiO_2@Zn_2(BME\text{-}bdc)_2(dabco)$ can be found in the Experimental Section, Figure 6.34.

Notably, fluorescence has been detected also in the solution where the reaction has been performed, meaning that not all the NPs have been encapsulated in the framework.
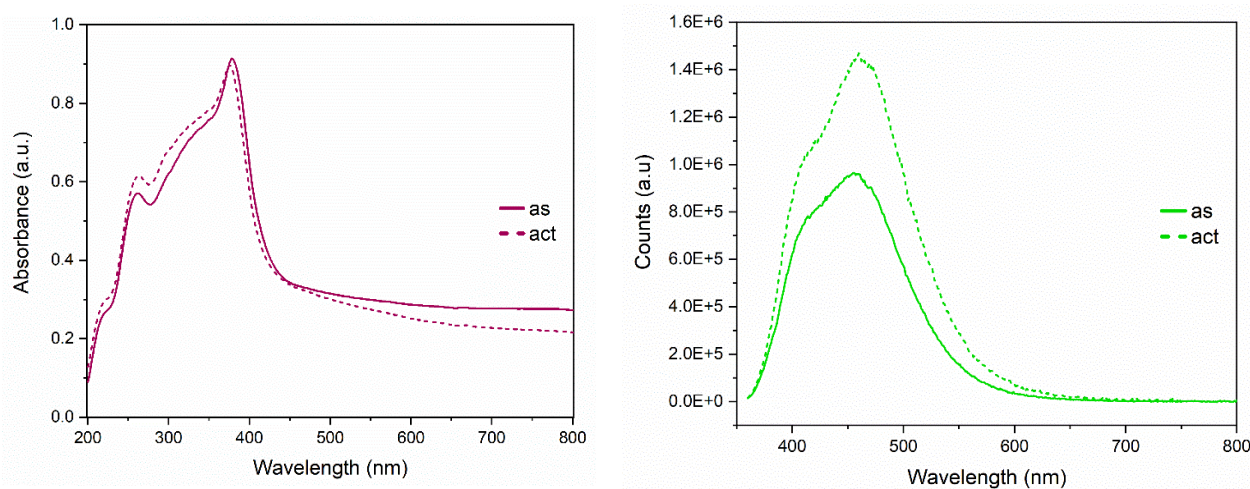
Figure 4.16 - Results for UV-Vis (left) and PL (right) measurements for $SiO_2@Zn_2(DM\text{-}bdc)_2(dabco)$, in each plot the as synthesised material is compared to the washed and activated one.

4.4.5 Energy-Filtered TEM-EDX

Energy filtered transmission electron microscopy (EFTEM) has been chosen as complementary technique to better understand whether the nanoparticles are present and furthermore to locate them. Indeed, the location of the silica NPs has been the major challenge in this work, because routine techniques for the detection of NPs such as TEM is not capable of identify them because light atoms (*i.e.* silicon) scatter electrons weakly and are difficult to detect. For this reason, EF-TEM has been chosen as

a more suitable technique for this type of composite materials, first of all it is suited to determine the distribution of lighter chemical elements (for this same reason each analysis has been coupled with energy-dispersive X-ray analysis (EDX) which has been successful in showing the light Si atoms contained in the NPs). Moreover, specimen damage is reduced, as MOFs' frameworks are quite sensible to high energy electron beams.

Since TEM can only give information about a single layer of a crystal and therefore gives no information of the bulk material, TEM *tomography* was performed on a sample of $SiO_2@Zn_2(DM-bdc)_2(dabco)$ in addition to EFTEM. The resulting set of images has not enough quality to clearly see inside the crystal, this is probably due to radiation damage that affected the surface of the crystallite, in fact this kind of measurement requires long acquisition times.

From all collected EFTEM images (Figure 4.17 and Figure 6.35 in the Experimental Section), an irregular distribution can be observed. Some crystals contain many nanoparticles while others contain less. Overall, the silica NPs are mainly located near and attached to the surface of the crystallites resulting from stable interactions, indeed some NPs aggregates can be seen. In some images in particular the interaction can be seen quite well where the silica NPs exhibit a deformation from the original sphere morphology, especially those sitting on the edges of the crystal which show the major degree of aggregation (see Experimental Section, Figure 6.35a).
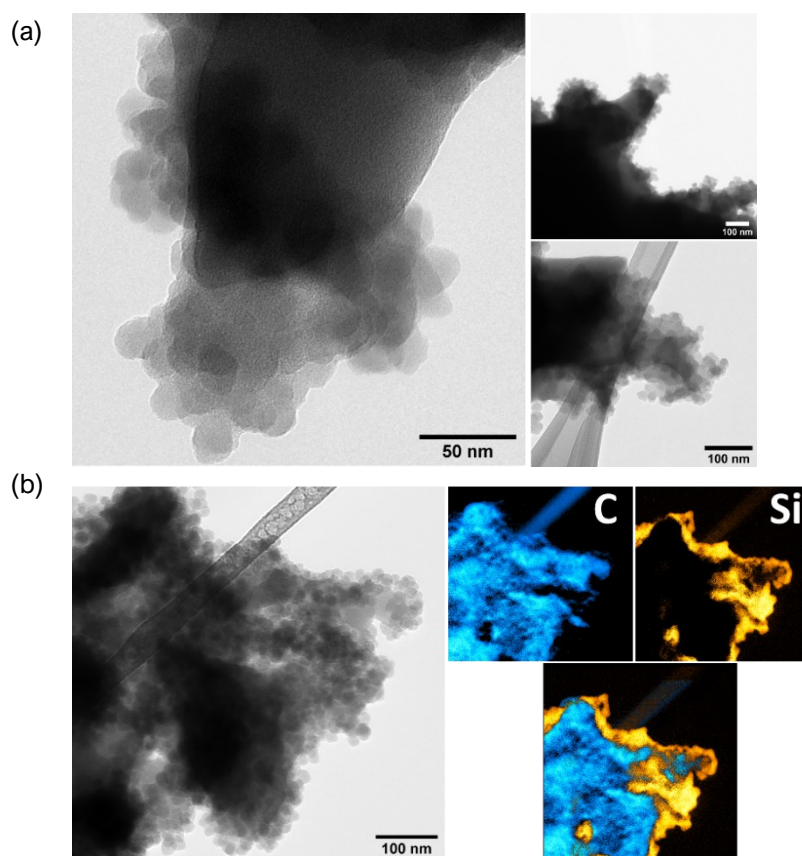

Figure 4.17 - EFTEM images for two different crystals of $SiO_2@Zn_2(DM-bdc)_2(dabco)$ (a), together with EDX images showing the distribution of lighter elements Si and C.

4.4.6 Gas Sorption

Pure component sorption isotherms of N_2 at 77 K and CO_2 at 195 K have been measured for Zn_2(X-bdc)$_2$(dabco) (with X = DM-bdc, BME-bdc) and the corresponding composite materials SiO_2@MOFs to verify if the breathing behaviour triggered by gas pressure is true also for the MOFs containing the NPs.

According to the literature,[42,370] N_2 is hardly adsorbed by these materials due to a gating of the pores caused by the pendant substituents on the linker. However, from the isotherms recorded in this work on different samples of both pristine and NP-embedded MOFs, in some cases a significant uptake is present in the range between 5 and 28 cm^3/g at standard temperature and pressure (STP). With the highest uptake of ~28 cm^3/g STP at P/P_0 = 0.96 measured for a single batch of SiO_2@Zn_2(DM-bdc)$_2$(dabco) (Figure 4.20). In general, for N_2 adsorption the known issue of very difficult activation can be observed in most of the presented isotherms, which is why the desorption curve lies below the adsorption one; this occurs because the residual gas is removed only during the measurement. As a general conclusion, a trend cannot be easily given while comparing pristine and hybrid materials N_2 isotherms.

The CO_2 sorption isotherms are shown in Figure 4.18 and Figure 4.19 (see also Experimental Section, Figure 6.36). One can clearly see that the overall uptake usually gets smaller with increasing chain length on the linker. This can be explained by the lower steric demand of the dimethoxy (DM) side chain compared to the longer 2-methoxyethoxy (BME) one, which should result in a larger pore space in the *lp* form.[370] Contrarily to expectations, Zn_2(DM-bdc)$_2$(dabco) adsorbs less amounts of CO_2 then the BME-analogue. The reason could be the aforementioned loss of long-range order in the framework (partial amorphization). Hence, the results gathered for this MOF should be handled with care.

The pristine Zn_2(DM-bdc)$_2$(dabco) shows a small hysteresis with a consistent gap between adsorption and desorption. This means that even the small amount of CO_2 that actually enter the pores are strongly kinetically hindered in its desorption and that there is a strong diffusion limit. Furthermore, the isotherm does not present any steps in contrast to what is reported in the literature.[370] The respective couple of NPs@MOFs exhibit a similar behaviour but with a lower uptake of CO_2 (Figure 4.18).

One batch of SiO_2@Zn_2(DM-bdc)$_2$(dabco) presented a different picture. It not only retained the hysteresis typical for flexible MOFs possessing two pore states, but also showed a two-step uptake under the same conditions. Furthermore, the narrow pore-large pore (*np-lp*) transition was well defined. In addition, this is the same sample with the unexpected high N_2 uptake introduced previously (Figure 4.20).

In general, the gas adsorption uptake trend for the DM-bdc containing materials is not regular which is probably due to the differences in the samples depending on the different synthetic approaches, washing and activation procedures. Indeed, the macroscopic bulk properties of flexible MOFs (*e.g.* the gate-opening pressure) also depend on the size and shape of the MOF crystallites. Additionally,

interfacial effects and surface barriers during guest uptake and release are important factors.[240,373] This could be the reason for the diversity of gas adsorption values obtained in the experiments. Nevertheless, it was commonly observed, that the gas uptake for the NPs@MOF systems is lower.

Zn_2(BME-bdc)$_2$(dabco) displayed a two-stepped CO_2 isotherm typical for flexible MOFs possessing two different pore states. This is true also for the NP-embedded MOF where also the *np-lp* transition is well defined. The CO_2 adsorption capacity values retrieved from experimental data for this MOF reaches 121.8 cm^3/g, which is slightly lower with respect to the parent MOF (P_{CO2} = 134.5 cm^3/g). In the relative pressure range of circa 0.0 – 0.18 bar the isotherm shows a *Type I* behaviour. At P/P_0 = 0.19 the transition starts and rapidly reaches the full *op* phase above P/P_0 = 0.25. The desorption branch starts at P/P_0 = 0.095 and occurs at lower pressure creating the expected hysteresis loop. The degree of contraction of the *np* state, the shape and shift of the stepped CO_2 sorption isotherm is not much different from the parent MOF Zn_2(BME-bdc)$_2$(dabco) (Figure 4.19).

For both sets of MOFs the selectivity towards CO_2 was demonstrated whereas N_2 did not show any significant adsorption. The reason for this is the quadrupole moment of the carbon dioxide molecule, which can interact with the flexible substituents on the linkers and therefore enter the framework triggering the structural transition.
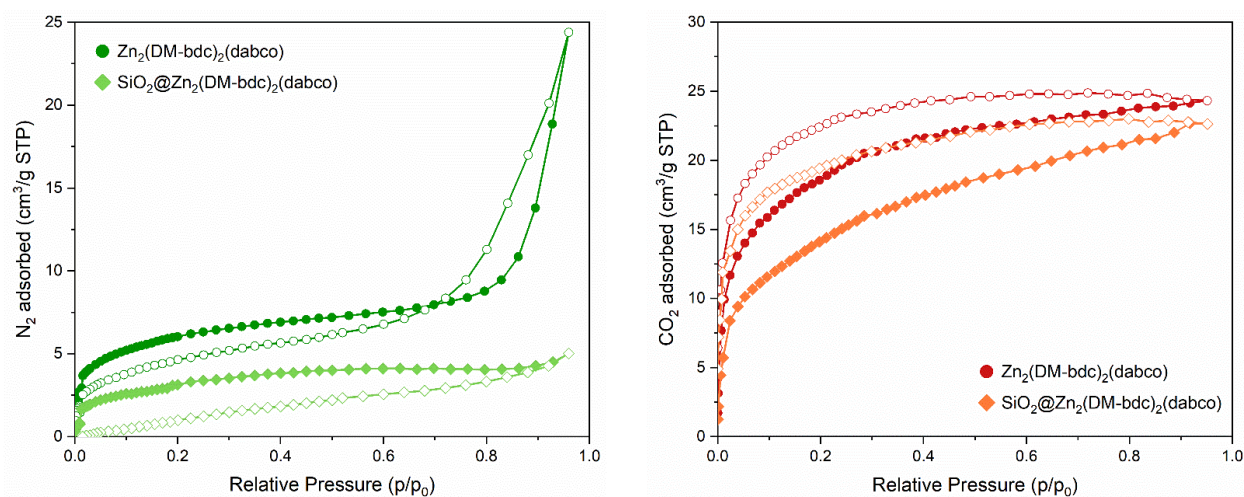
Figure 4.18 - Comparison of N_2 (left) and CO_2 (right) sorption isotherms for Zn_2(DM-bdc)$_2$(dabco) (circles) and SiO_2@Zn_2(DM-bdc)$_2$(dabco) (squares). The adsorption and desorption branches are represented with solid and open symbols respectively.
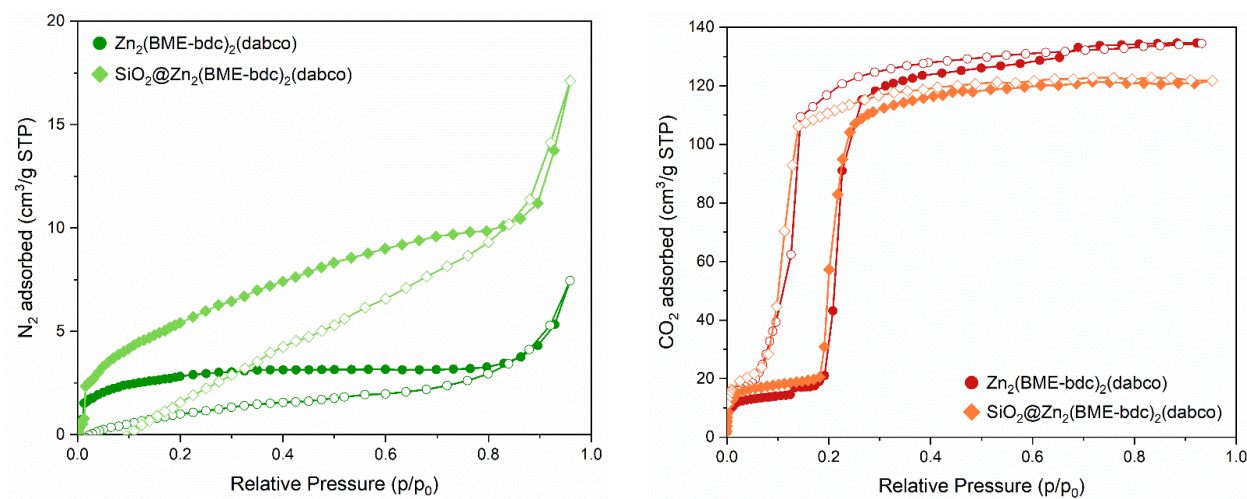
Figure 4.19 - Comparison of N_2 (left) and CO_2 (right) sorption isotherms for $Zn_2(BME-bdc)_2(dabco)$ (circles) and $SiO_2@Zn_2(BME-bdc)_2(dabco)$ (squares). The adsorption and desorption branches are represented with solid and open symbols respectively.
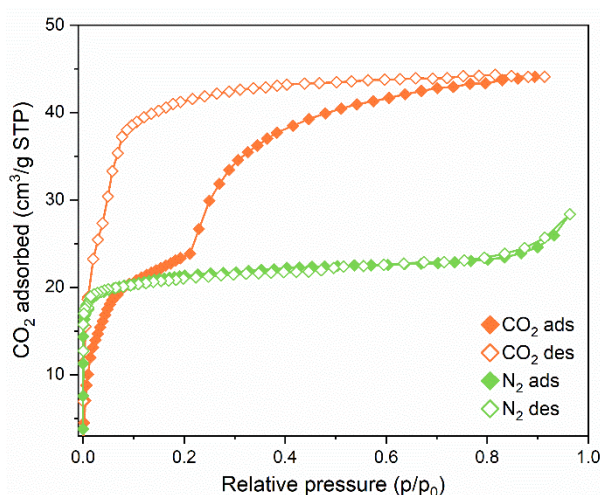
Figure 4.20 - Comparison of N_2 (green) and CO_2 (orange) sorption isotherms for the batch of $SiO_2@Zn_2(DM-bdc)_2(dabco)$ exhibiting unusually higher uptake values for N_2 and a stepped isotherm for CO_2. The adsorption and desorption branches are represented with solid and open symbols respectively.

4.4.7 TG and DSC Analysis

Thermogravimetric analysis (TGA) has been performed to monitor the sample activation and to check the stability of the composite materials $SiO_2@MOFs$ compared to pristine ones (Figure 4.21 and in the Experimental Section, Figure 6.37, Figure 6.38 and Figure 6.40).

The assessment of thermoresponsivity has been checked through differential scanning calorimetry (DSC) experiments and the reversibility of the transition has been tested via cyclic DSC measurements (Figure 4.22 and in the Experimental Section, Figure 6.39 and Figure 6.40) which is useful to give

information about the flexibility and phase transition properties. DSC analysis has been performed in the temperature range of 30 – 800 °C with a step of 10 °C/min, while cyclic DSC from –150 or 0 to 230 °C with a step 10 °C/min (1½ cycles: heat/cool/heat). All experiments have been done on the same sample for each type of MOF but over the course of different days, which explains the different solvent amounts in the frameworks.

As shown in Figure 6.39 (see Experimental Section), $Zn_2(DM\text{-}bdc)_2(dabco)$ is not flexible upon variable temperature,[370] indeed from simultaneous TG/DSC analysis and cyclic DSC experiments no endothermic event can be seen in the studied temperature range.

On the other hand, for both $Zn_2(BME\text{-}bdc)_2(dabco)$ the NPs embedded counterpart, TG/DSC analyses of the guest-free materials show an endothermic event. The flexible behaviour of the pristine MOF was already known[41,343,354] and it is confirmed also for $SiO_2@Zn_2(BME\text{-}bdc)_2(dabco)$. The endothermic signal lies at 219.9 °C for the plain MOF and instead at lower temperature for the NPs@MOF, 209.9 °C (Figure 4.21). Cyclic DSC measurements conducted on the same samples indicate that the phase transition is reversible and that for $Zn_2(BME\text{-}bdc)_2(dabco)$ two adjacent events at 220.6 and 224.7 °C contribute to the endothermic transition when heating, whereas three events are observed during cooling (at 226.8, 210.5 and 197.3 °C). In contrast, for the NP-embedded sample there are fewer events with just one endothermic one at 200.2 °C when heating and two different events at 205.9 and 170.0 °C when going down with temperature. The presence of multiple adjacent events during both heating and cooling, may be explained by the presence of different types of crystallites (dimension, defects, *etc.*) which cause slightly different transition temperatures. In general, it can be observed that all endothermic events occur at lower temperature for $SiO_2@Zn_2(BME\text{-}bdc)_2(dabco)$ (Figure 4.22).

TG analysis reveals that the incorporation of NPs results in a slight decrease of thermal stability, for both DM-bdc and BME-bdc containing systems: decomposition $T_{MOF} \sim 277$ °C > $T_{NPs@MOF}$ 270 °C for $Zn_2(DM\text{-}bdc)_2(dabco)$; decomposition $T_{MOF} \sim 289$ °C > $T_{NPs@MOF}$ 283 °C for $Zn_2(BME\text{-}bdc)_2(dabco)$ (see Experimental Section, Table 6.22).

As previously observed for pillar-layered MOFs,[370] TG analyses reveal that increasing the length of the linker side chain results in an enhanced thermal stability, with $Zn_2(BME\text{-}bdc)_2(dabco)$ being the most thermally stable framework, while $Zn_2(DM\text{-}bdc)_2(dabco)$ decomposes at lower temperature. The same trend can be recognised for the corresponding composite materials.
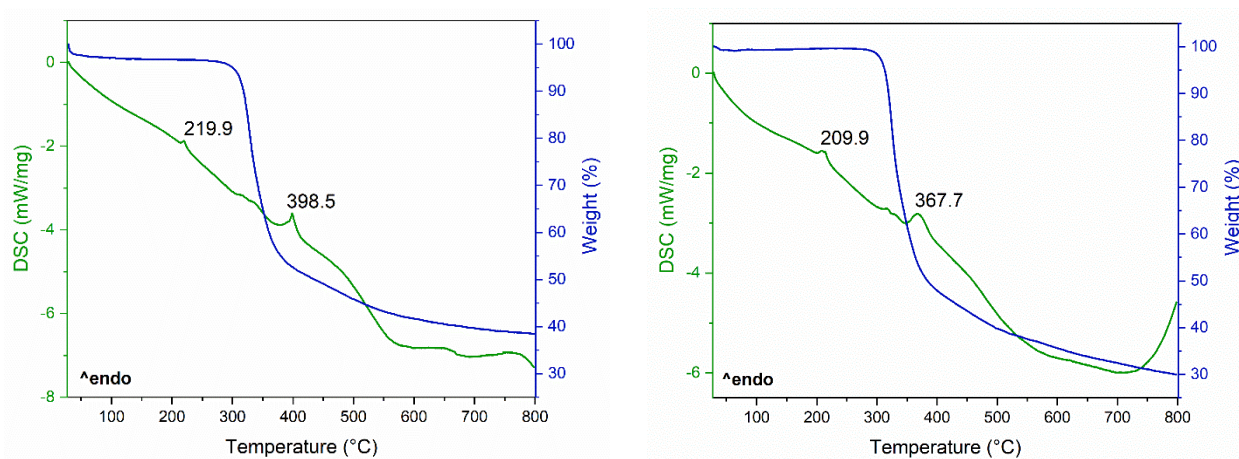
Figure 4.21 - Simultaneous TG-DSC analysis for pristine $Zn_2(BME\text{-}bdc)_2(dabco)$ (left) and for $SiO_2@Zn_2(BME\text{-}bdc)_2(dabco)$ (right) (heating rate 10 °C/min).
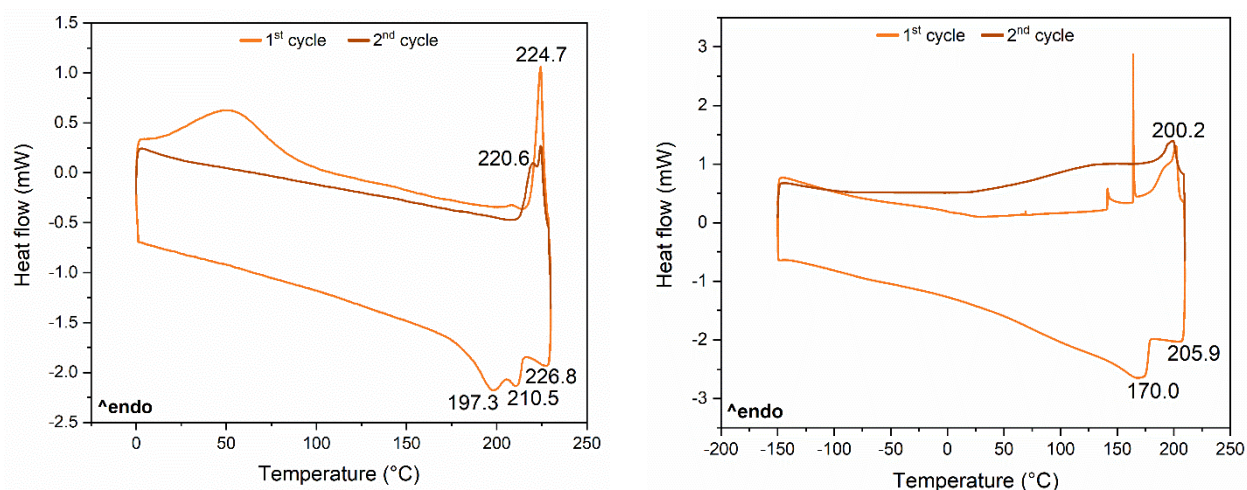
Figure 4.22 - Cyclic DSC experiments for prisitine $Zn_2(BME\text{-}bdc)_2(dabco)$ (left) and for $SiO_2@Zn_2(BME\text{-}bdc)_2(dabco)$ (right) (heating rate 10 °C/min). The spike signal visible at 165 °C is due to an instrumental problem and does not depend on the structural phase transition of the system.

4.4.8 Variable-temperature X-ray Powder Diffraction Analysis

Variable temperature X-ray powder diffraction (VT-XRPD) studies have been performed on activated samples of $Zn_2(DM\text{-}bdc)_2(dabco)$ and $SiO_2@Zn_2(BME\text{-}bdc)_2(dabco)$ to test the thermal stability and the presence of temperature induced flexibility and compare the results with the parent MOFs.

The chosen temperature ranges are 30 to 300 °C for heating and 280 to 30 °C for cooling, with 20 °C steps. Here are reported the results after data treatment on the diffraction patterns collected on Bruker D8 instrument (Bragg-Brentano geometry, no inert atmosphere) (Figure 4.23 and Figure 4.25). In the Experimental Section in Figure 6.41, the 2D-plots for the VT-XRPD experiments performed using another instrumental setup are reported.

Zn$_2$(DM-bdc)$_2$(dabco)

The DM-bdc^{2-} containing MOF is not flexible under variable temperature and additionally it loses most of its crystallinity upon heating (Figure 4.23). Therefore, the dried phase which is formed at high temperature cannot be studied by routine VT-XRPD. A more detailed description for this behaviour can be found in Chapter 4.6.
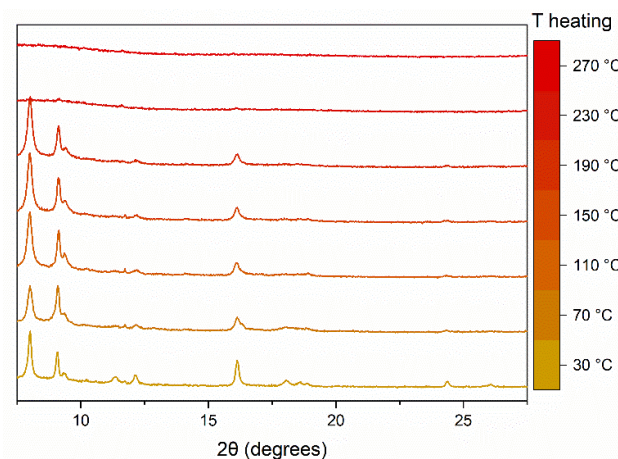
Figure 4.23 - VT-XRPD experiment for Zn$_2$(DM-bdc)$_2$(dabco) showing the loss of crystallinity upon heating.

Zn$_2$(BME-bdc)$_2$(dabco)

The flexible behaviour which already reported in the literature is confirmed for the plain Zn$_2$(BME-bdc)$_2$(dabco) (Figure 4.24).[354] It is retained also for the SiO$_2$@MOF which shows however a more gradual crystal phase transition when cooling (Figure 4.25, bottom) as already proven by TG and cyclic DSC analyses.

Figure 4.24 - Schematic representation of the guest and temperature dependent structural changes for Zn$_2$(BME-bdc)$_2$(dabco).

From the diffraction patterns the change in the peak positions as well as the transition from narrow pore (*np*) to large pore (*lp*) form starts at around 190 °C and is complete at 290 °C, including the presence of an intermediate medium pore form (*ip*). The inverse exothermic process occurs at a slightly lower temperature, giving rise to a small hysteresis, and goes from 290 to 100 °C before reaching the complete *np* form at around 60 °C. For the NPs embedded material the same trend is observed but with different temperature thresholds: the crystalline phase transition starts at 150 °C and ends at 280 °C with the *op* form. The inverse process is slower in this case and results in a slightly larger temperature hysteresis (Figure 4.27), from 230 to 80 °C but never completely reaching the full *np* form.

On all diffraction patterns, Le Bail fittings have been performed in order to retrieve the unit cell parameters at each temperature measured. The graphical and numerical results are reported in the Experimental Sections in Figure 6.42, Figure 6.43 and Table 6.23, Table 6.24. To note that in the temperature range from circa 150 to 270 °C (heating) and from circa 240 to 80 °C (cooling) both, the *np* and the *lp* form, are present. However, all data presented in Table 6.23, Table 6.24 have been obtained *via* single-phase fits choosing the majority crystalline phase. Plotting the unit cell parameters variation (Figure 4.26), it can be observed that the cell parameters *a* and *b* change continuously when increasing the temperature, whereas *c* and β remain almost constant.

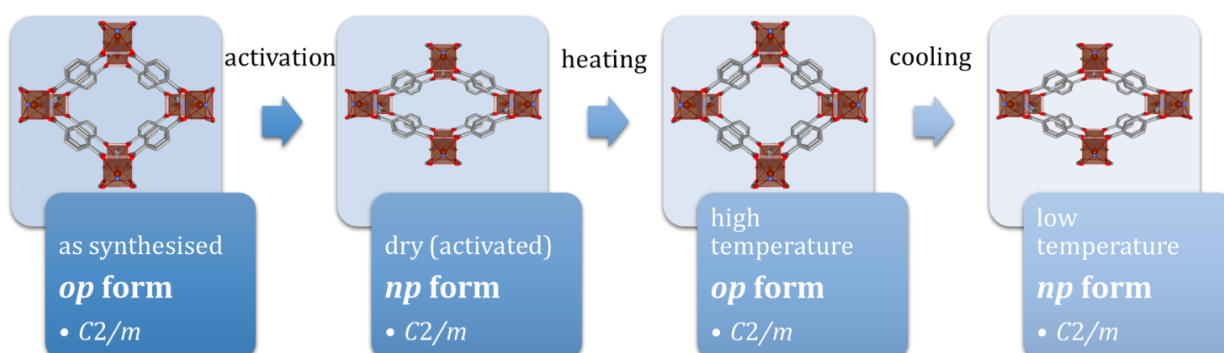From analysis of the diffraction patterns, it can be seen that reflections of the (00*l*) family do not shift. When the temperature raises the (110) reflection decrease in intensity and a new reflection at $2\theta = 8.11°$ emerges, which is the (110) reflection relative to the *op* phase. As soon as the (110) reflection of the *np* phase completely disappears and the new one of the *op* phase appears, the crystalline phase transition is complete and occurs at 290 °C for $Zn_2(BME\text{-}bdc)_2(dabco)$, at 280 °C for $SiO_2@Zn_2(BME\text{-}bdc)_2(dabco)$. On the cooling branch a small hysteresis is visible, which is in accordance with the DSC data Figure 4.27. When the temperature is again at 30 °C, both materials return to the same initial *np* form; the main difference between the plain MOF and the NPs@MOF is that for the composite system, the phase transition is slower and the *np* form is not fully reached when cooling to room temperature, indeed the (001) reflection at $2\theta = 9.37°$ never disappears even if its intensity is really small at low temperatures. Furthermore, the hysteric behaviour is shifted to lower temperatures and the trend is slower on the cooling branch.
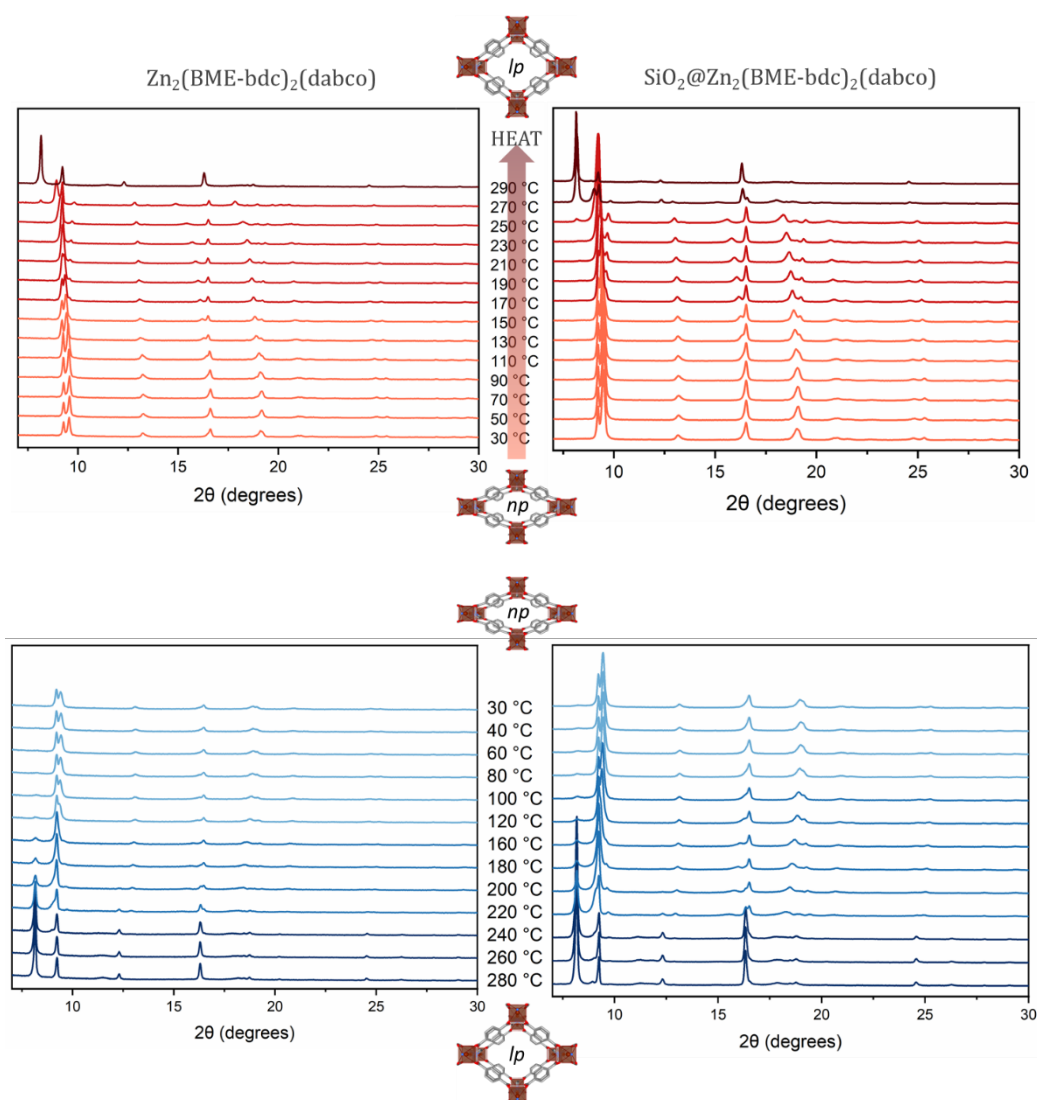
Figure 4.25 - VT-XRPD experiment for Zn$_2$(BME-bdc)$_2$(dabco) and SiO$_2$@Zn$_2$(BME-bdc)$_2$(dabco) showing the crystalline phase transition upon heating (top) and cooling (bottom) (step size 20 °C).
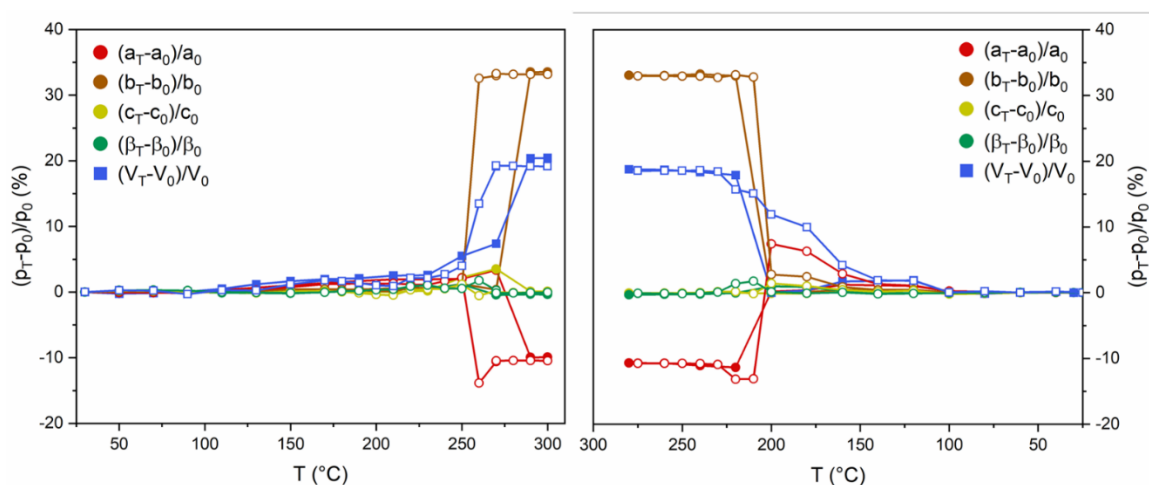
Figure 4.26 - Unit cell parameters and volume variation upon heating (left) and cooling (right) derived from VT-XRPD data for the plain Zn$_2$(BME-bdc)$_2$(dabco) (full symbols) and for NPs@MOF (open symbols).
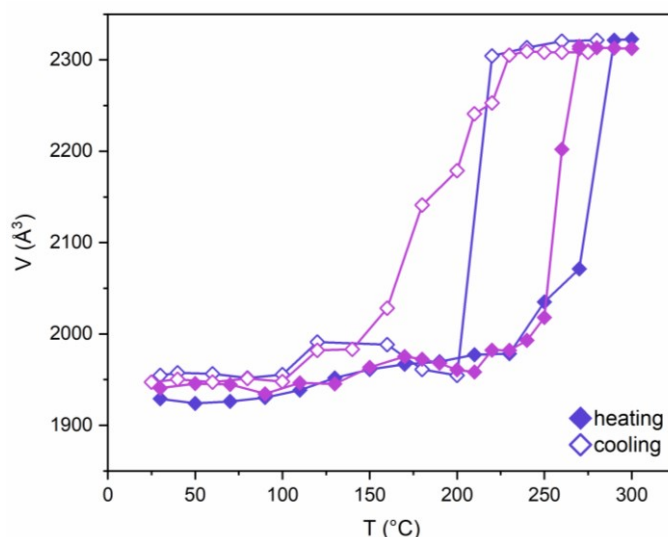
Figure 4.27 - Variation of volume with temperature for Zn_2(BME-bdc)$_2$(dabco) (purple) and SiO_2@Zn_2(BME-bdc)$_2$(dabco) (pink). Data points of the heating and cooling branches are represented as solid and open symbols respectively.

In conclusion, for Zn_2(BME-bdc)$_2$(dabco) and SiO_2@Zn_2(BME-bdc)$_2$(dabco) two different kind of stimuli, guest adsorption and heat, can trigger the structural transitions. This occurs in each of responsive MOF studied and shows a contraction of the 2D rhombic [Zn_2L_2] motif orthogonal to the crystallographic *c*-axis.

The investigations for Zn_2(DM-bdc)$_2$(dabco) and SiO_2@Zn_2(DM-bdc)$_2$(dabco) confirm that the flexibility initiated upon heating depends on the chain length of the substituents. If the side chains are short (chain length shorter than five non-hydrogen atoms) the MOFs remain in the *np* form upon heating.[354] On the contrary, if the side chains are longer, like in BME-dbc^{2-}, the steric hindrance present in the pores is enough to allow the contraction of the framework.[343]

4.5 Conclusions

The results presented in this chapter show how the responsive behaviour of pillared layer-based MOFs of the type {[Zn_2(bdc)$_2$(dabco)]$_n$·(DMF)$_x$} can be changed by addition of catalytically inert nanoparticles larger than the MOF pores. The synthesis was successful for both DM-bdc^{2-} and BME-bdc^{2-} containing MOFs and their composite materials NPs@MOF. Interestingly, these same MOFs could be obtained even at room temperature following the same synthetic path. In contrast to that, for the less flexible parent framework Zn_2(bdc)$_2$(dabco), several trials have been made without obtaining the NP-embedded material. Interestingly, the amount of nanoparticles used during the synthesis has been shown to affect

its outcome. In fact, only a small quantity of NPs (~1.3%) needs to be added to the system in order to obtain the desired crystalline phase.

The presence of the nanoparticles in the material after the encapsulation has been confirmed by UV-Vis and fluorescence spectroscopy. Indeed, a strong fluorescence signal coming from the silica NPs has been detected even after different treatments on the MOF crystallites (*i.e.* washing in different solvents or thermal activation under vacuum). To determine the position of the NPs, EFTEM-EDX and TEM tomography were used and showed that these are mainly located near the surface of the crystallites.

This has a critical influence also on the gas sorption properties. In fact, the CO_2 adsorption is slightly lower for both composite materials, which means that the NPs may partially block the entry of the gas molecules into the framework.

Interestingly, the response to guest molecules is different between the two studied MOFs. Upon guest removal the framework contracts and a change from an open-pore to a narrow-pore form is observed for $Zn_2(BME-bdc)_2(dabco)$ and its composite. Instead $Zn_2(DM-bdc)_2(dabco)$ reversibly loses its long-range crystalline order upon evacuation as proven by XRPD analysis performed on the dry and DMF reinfiltrated powder. Further studies on this particular behaviour are currently in progress.

The difference between the two systems is based on the length of the flexible substituents on the linker. Once a critical temperature is reached, the thermal energy is sufficient to overcome the attractive intra-framework interactions which leads to the *lp* form in the case of $Zn_2(BME-bdc)_2(dabco)$, where larger pore space is needed to accommodate the longer alkoxy chains. Instead, it was confirmed that for shorter ethoxy substituents (DM-bdc), there is no transformation between *np* to *lp* form.

The remarkable breathing behaviour in response to adsorbed guest molecules is retained for $SiO_2@Zn_2(BME-bdc)_2(dabco)$, as proven by variable-temperature XRPD, DSC and gas sorption experiments. Therefore, both BME-bdc^{2-} containing MOFs can not only reversibly switch between narrow- and open-pore structures upon gas adsorption, but also in response to temperature. The thermal expansion and contraction observed during VT-XRPD, indicate that the framework is reversibly flexible, and also that the transition is slower during cooling. Furthermore, the data presented for $SiO_2@Zn_2(BME-bdc)_2(dabco)$ show that the presence of the NPs has an impact on its breathing mechanism, resulting in a larger thermal driven hysteresis.

Such thermo-responsive properties are promising for several applications which are usually not associated to porous materials (*e.g.* heat storage, heat transfer). Even though the fundamental understanding of dynamic responsiveness is still at its early stages, the results presented serve as a significant step in this direction and further investigations on this topic will lead to a deeper understanding of the underlying basic properties and phenomena, which is essential to develop and design advanced materials.

4.6 "Frustrated" Flexibility in MOFs – *Preliminary Results*

In recent years, a small but growing group of so-called amorphous MOFs (*a*MOFs) is gaining the interest of the scientific community. They are characterised by the same basic building blocks and connectivity as crystalline MOFs but they lack long-range periodic order. Their identification is a challenging task because the XRPD patterns consist of broad peaks and sometimes, they appear completely amorphous. It is highly probable that many *a*MOFs have not been yet recognised and therefore not studied. In Table 4.6. various examples of *a*MOFs are reported.

Table 4.6 - List of some reported *a*MOFs together with their composition, synthetic condition and space group for the crystal phase.

Name	Composition§	Amorphization method	Space group*	Ref.
ZIF-1	$Zn(Im)_2$	Ball milling or high temperature	$P2_1/n$	[374,375]
ZIF-3	$Zn(Im)_2$	Ball milling or high temperature	$P4_2/mnm$	[374,375]
ZIF-4	$Zn(Im)_2$	Ball milling or high temperature or pressure	$Pbca$	[374,375]
ZIF-8	$Zn(mIm)_2$	Ball milling or pressure	$I43m$	[376,377]
ZIF-69	$Zn(mIm)(cbIm)$	Ball milling	$P6_3/mmc$	[376]
$Zn(ICA)_2$	$Zn(ICA)_2$	Direct preparation	-	[378]
Ni(II) bisimidazolate	$Ni(Im)_2$	High temperature	$P2_1/a$	[379]
Pd(II) bisimidazolate	$Pd(Im)_2$	High temperature	$Pnca$	[379]
Pt(II) bisimidazolate	$Pt(Im)_2$	High temperature	$P2_1/c$	[379]
Cu(II) bisimidazolate	$Cu(Im)_2$	High temperature	$P1$	[379]
MOF-5	$Zn_4O(bdc)_3$	Pressure or electrical discharge	$Fm3m$	[345,380, 381]
$Zn_4O(BME-bdc)_3$	$Zn_4O(BME-bdc)_3$	Solvent removal	$Pm-3m$	[382]
MOF-177	$Zn_4O(btb)_2$	Compression	$P31c$	[383]

§ Im = imidazolate ($C_3H_3N_2^-$); mIm = 2-methylimidazolate ($C_4H_5N_3^-$); cbIm = 5-chlorobenzenimidazolate ($C_7H_4N_2Cl^-$); ICA = imidazolate-2-carboxaldehyde ($C_4H_3N_2O^-$); bdc = benzene-1,4-dicarboxylate ($C_8H_3O_4^{2-}$); btb = 1,3,5-tris(4'-carboxyphenyl)benzene ($C_{21}H_{15}O_6^{3-}$); TPT = 2,4,6-tris(4-pyridyl)triazine ($C_{18}H_{12}N_6$); BTC = 1,3,5-benzenetricarboxylate ($C_9H_3O_6^{3-}$); H2BDP-NH2 = 2-amino[1,4-bis(1H-pyrazol-4-yl)benzene] ($C_{12}H_9N_5^{2-}$); DM-bdc = 2,5-bis(methoxy)-1,4-benzenedicarboxylate ($C_{10}H_8O_6^{2-}$); BME-bdc = 2,5-bis(2-methoxyethoxy)-1,4-benzenedicarboxylate ($C_{14}H_{16}O_8^{2-}$); L = 2,2'-diethoxy-1,1'-binaphthyl-6,6'-bis(4-vinylpyridine); CDC = trans-1,4-cyclohexanedicarboxylicacid ($C_8H_{10}O_4^{2-}$); dipn = N,N-di(3-aminopropyl)-amine (($NH_2CH_2CH_2CH_2)_2NH$); pdt = 2,3-pyrazinedithiolate ($C_4H_2N_2S_2^{2-}$); 4-peia = N-(2-pyridin-4-yl-ethyl)-isonicotinamide ($C_{13}H_{13}N_3O$).

Zn(CN)$_2$	Zn(CN)$_2$	Pressure or X-ray exposure	P43m	[384]
[ZnX$_2$]$_3$(TPT)$_2$	[ZnX$_2$]$_3$(TPT)$_2$ with X=I, Br, Cl	High temperature	C2/c	[385,386]
Fe$_3$O(BTC)$_2$F·H$_2$O	Fe$_3$O(BTC)$_2$F·H$_2$O	Direct preparation (aerogel)	-	[387]
Zn(BDP-X)	Zn(BDP-X) with X = NH$_2$, OH, NO$_2$	Solvent removal	Cccm	[199]
Zn$_2$(DM-bdc)$_2$ (dabco)	Zn$_2$(DM-bdc)$_2$ (dabco)	Solvent removal and high temperature	P4/nbm	[41]
Cd(L)(ClO$_4$)$_2$	[Cd(L)(ClO$_4$)$_2$]·11EtOH· 6H$_2$O	Solvent removal	P6222	[333]
ZrCDC	Zr$_6$O$_4$(OH)$_4$(CDC)$_6$	Solvent removal	I4/mmm	[388]
[Ni(dipn)]$_2$[Ni(dipn)-(H$_2$O)][Fe(CN)$_6$]$_2$	[Ni(dipn)]$_2$[Ni(dipn)-(H$_2$O)][Fe(CN)$_6$]$_2$·11H$_2$O	Solvent removal	C2/c	[389]
Cu[Cu(pdt)$_2$]	Cu[Cu(pdt)$_2$]	High temperature	P4$_2$/mmc	[390]
[Co(NCS)$_2$(4-peia)$_2$]·4Me$_2$CO	[Co(NCS)$_2$(4-peia)$_2$]·4Me$_2$CO	Solvent removal	P2$_1$/c	[391]

* for the crystal phase

Many of the first *a*MOFs investigated are part of the ZIF (zeolitic imidazolate framework) family or contain an imidazolate linker. The few examples reported in literature are obtained through different methods and show various types of behaviour, ranging from complete loss of structural order to presence of partial crystallinity. The most common conditions to apply stress to the crystalline frameworks and consequently obtain a disordered MOF are: high temperature, pressure, mechanical compression, solvent removal and electrical discharge.

*a*MOFs can be characterised taking advantage of the presence of diffuse scattering, since it contains important information about two-atom interactions, therefore pair distribution function (PDF) analysis can give a map of short- and medium-range order distances between atoms, if the composition of the system is known beforehand. Other useful techniques are IR and Raman spectroscopy, that can be used to identify functional groups and to help understanding short-range ordering.[380,383]

Applications of *a*MOFs

Crystalline to amorphous transitions may have interesting potential application, for example to reversibly store gas exploiting pressure-induced amorphization. ZIFs have been used for adsorbing harmful guest molecules and then collapsing to trap them inside the framework; T. D. Bennett and co-workers have shown that ZIF-8 can retain the radioactive I$_2$ (a nuclear fission by-product is the isotope

[129]I) inside its framework by irreversible pressure or ball milling induced amorphization.[376,377] Reversibility of such phenomenon could be promising for biomedical applications, where the *a*MOF needs to have the ability to enclose the guest and then release it slowly and uniformly. Partial loss of structural order may be useful when adjusting these characteristics. Another application could be optically active glassy materials which can be developed by inclusion of chiral molecules together with, for example, rare earth salts during solvothermal synthesis and before thermal (or pressure, compression, *etc.*) induced amorphization.

As already stated, the one major obstruction to the use of *a*MOFs is the problem of their recognition and characterisation. Distinguishing between effective "amorphous" MOFs and those who simply lose their structural integrity upon effect of an external stimulus may be complex but understanding the behaviour behind this "amorphization" is fundamental in order to gain deeper insight into the properties of these porous materials and be able to synthesise advanced functional materials.

The Case of $Zn_2(DM\text{-}bdc)_2(dabco)$

The crystalline-to-amorphous transition in $Zn_2(DM\text{-}bdc)_2(dabco)$ is reversible and can be triggered by tuning the presence or absence of polar guest molecules in the framework. This means that upon heating and re-infiltration with solvents the MOF reversibly switches between amorphous and crystalline phases, respectively.

As already seen for other MOF families (*e.g.* MOF-5[345]) and explained specifically for pillar-layered Zn based MOFs in Chapter 4.2, the parent framework $Zn_2(bdc)_2(dabco)$ can be regarded as rigid upon varying the gas pressure,[363] but gains flexibility when different types of functionalities are added to the organic linker, as in the case of the currently analysed material.[370] Since the parent MOF retains its crystallinity under various treatments and stimuli, the origin of the amorphization process may be found in the presence of the flexible methoxy groups, which upon solvent removal may coordinate to the zinc centres and, together with weaker dispersion interactions between near organic linkers, could induce a random distortion of the paddle-wheel units leading to a vast deprivation in long-range translational order. Indeed, the distorted MOF phase has the same topology (same connectivity and pattern) as the as synthesised system but lacks long-range crystalline order. Additionally, this kind of guest-responsive amorphization behaviour is sensible to the bulkiness and type of the functionalisation. As for $Zn_2(BME\text{-}bdc)_2(dabco)$ such a drastic change in the XRPD pattern upon heating, and consequent desolvation of the framework, cannot be seen. Nevertheless, a decrease in intensity of the diffraction peaks can be observed also in this last case, indicating the possibility of a similar structural transition when the network is evacuated (Figure 4.28).
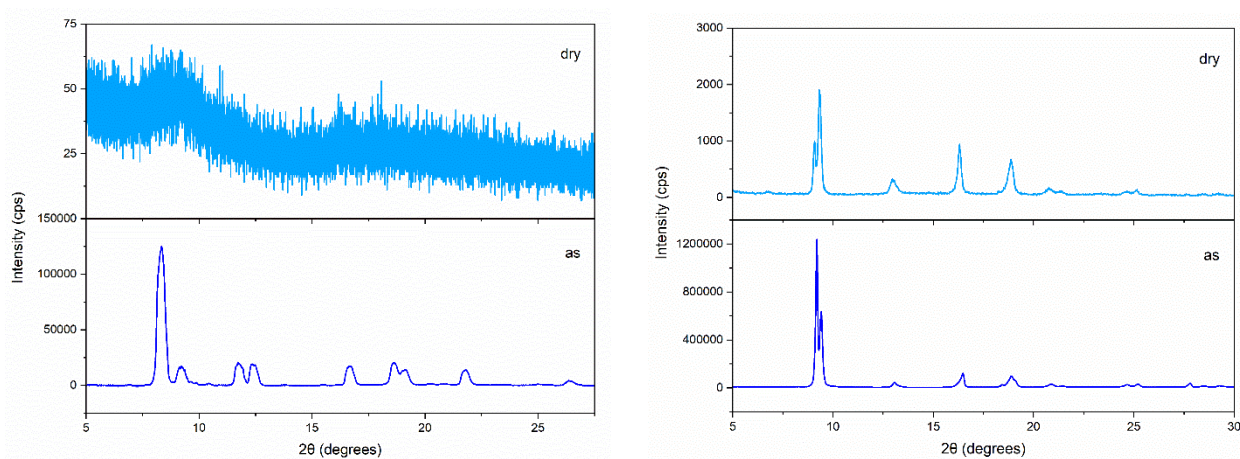
Figure 4.28 - XRPD patterns for as synthesised and dry $Zn_2(DM\text{-}bdc)_2(dabco)$ (left) and $Zn_2(BME\text{-}bdc)_2(dabco)$ (right).

The gas sorption properties of $Zn_2(DM\text{-}bdc)_2(dabco)$ have been analysed (Chapter 4.4.6). From CO_2 gas sorption measurements the total gas uptake was lower compared to other MOFs from the same family.[370] This may be caused by the disorder of the framework of the dry MOF that partially blocks the pores to the guest molecules. However, the flexibility of the system is confirmed by the *Type I* CO_2 sorption isotherm (recorded at 195 K), which presents a hysteresis loop. In an attempt to shed light on the mechanism behind the "amorphization" process of $Zn_2(DM\text{-}bdc)_2(dabco)$, a high resolution *in situ* X-ray diffraction study in dependence of the CO_2 pressure was performed at the high-resolution powder diffraction beamline (ID22) of the European Synchrotron Radiation Facility (ESRF). XRPD patterns have been recorded at 0 °C during adsorption in the pressure range from 0 to 35 bar (λ = 0.35425850).

Contrary to expectations, the framework did not open at high pressure, as shown by the diffraction patterns collected (Figure 4.29), and no further analysis could be done in this direction. Nevertheless, high-resolution X-ray total scattering studies for the dry MOF have been performed during the same time spent at ID22 beamline and data treatment is still ongoing. Furthermore, new experiments on the same sample are in progress, including X-ray absorption spectroscopy coupled with XRPD (XAS/XRPD), solid state NMR, IR spectroscopy, molecular dynamics simulations.
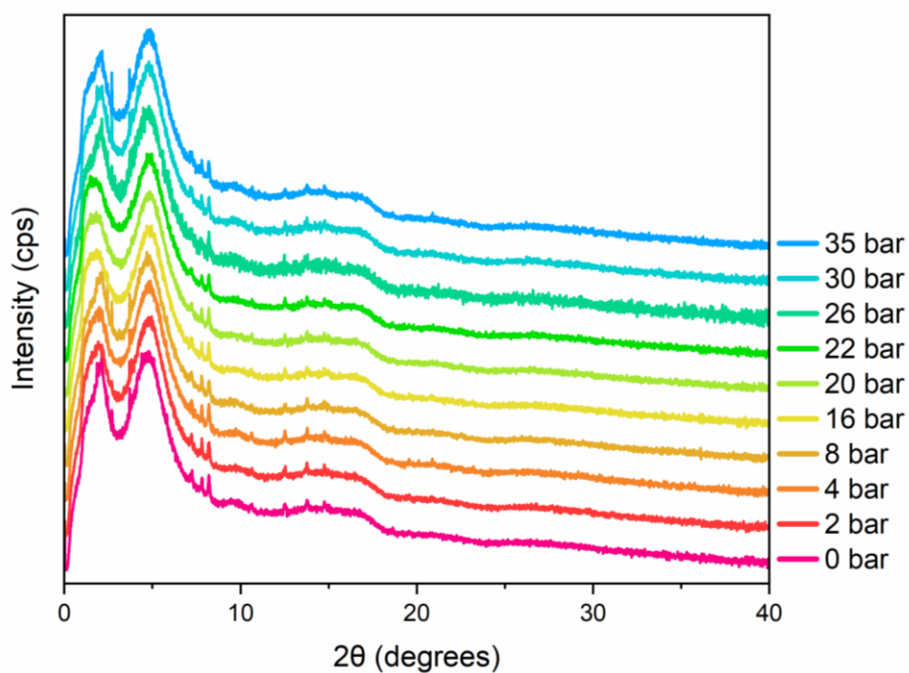
Figure 4.29 - XRPD patterns of dry $Zn_2(DM\text{-}bdc)_2(dabco)$ measured at variable CO_2 pressure between 0 and 35 bar at 0 °C.

In conclusion, the non-flexibility of $Zn_2(DM\text{-}bdc)_2(dabco)$ under variable temperature has been confirmed (as determined by DSC experiments) and that the non-crystalline dry phase can fully recover its ordered structure when specific solvent molecules (DMF) are introduced into the framework. This means that the amorphization mechanism is not an irreversible collapse of the framework but may originate from weak intra-molecular interactions, mainly between the alkoxy chains on the organic linkers and the framework backbone, which result in a loss of long-range order of the global structure.

Chapter 5

SUMMARY AND OUTLOOK
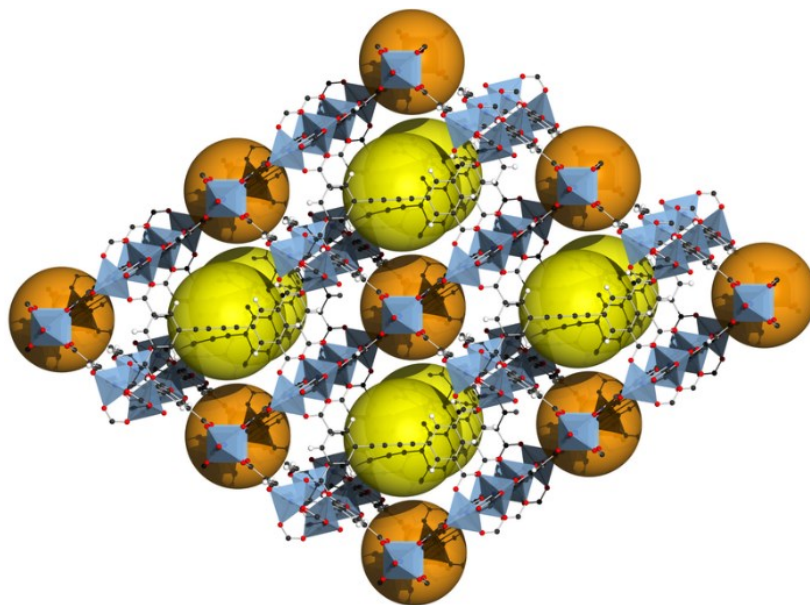
5.1 Elucidation of Adsorption Processes in Azolate-based MOFs through *In Situ* X-ray Powder Diffraction Experiments

The first part of this PhD thesis project focuses on the understanding of structural features in the solid-state matter, particularly in highly stable, porous, metal-organic frameworks. Their crystallographic properties have been rationalized via *non-ambient* diffraction techniques, such as variable gas-pressure and variable temperature single-crystal and powder X-ray diffraction both at laboratory- and large-scale facilities. In particular, the CO_2 adsorption properties of different MOFs of formula $Fe_2(BDP)_{3x}(BDP-NH_2)_{3(1-x)}$ (x = 0, 0.5, 1) with $H_2BDP-NH_2$ = 2-amino[1,4-bis(1H-pyrazol-4-yl)benzene],[209] have been investigated through *in situ* high-resolution powder X-ray diffraction (HR-PXRD) experiments, which were carried out at different temperatures dosing CO_2 in certain pressure ranges. The metal ion and ligand functionalization modulate the sorption properties of these materials, enhancing their affinity to

CO_2 molecules. $Fe_2(BDP-NH_2)_3$ and its parent MOF $Fe_2(BDP)_3$ possess robust, rigid frameworks. Additionally, a mixed-ligand MOF, namely $Fe_2(BDP)_{1.5}(BDP-NH_2)_{1.5}$, was synthesised, characterised and compared with the fully functionalised and bare systems. Rietveld refinements of the diffraction data collected at each pressure point is used to understand the preferential adsorption sites occupied by the gaseous probe and the *host–guest* interactions, as well as the breathing behaviour, whose mechanism is not yet completely described in the literature.

Fe_2BDP_3, $Fe_2(BDP-NH_2)_3$ and $Fe_2(BDP)_{1.5}(BDP-NH_2)_{1.5}$ are isostructural MOFs which crystallise in the orthorhombic space group *Fddd* and possess 1D triangular channels running along the [001] direction, composed of 1D chains of pyrazolate-bridged Fe^{3+} octahedra. Static and dynamic gas adsorption experiments showed that these materials can selectively adsorb CO_2 over N_2 and that the CO_2 adsorption-recovery process can be repeated multiple times. Taking care of these evidence, *in situ* HR-PXRD experiments were carried out at the European Synchrotron Radiation Facility (ESRF)[392] with the following experimental conditions: at 0 and 25 °C in the CO_2 pressure range of 0–8 bar for Fe_2BDP_3, 0–26 bar for $Fe_2(BDP-NH_2)_3$ and $Fe_2(BDP)_{1.5}(BDP-NH_2)_{1.5}$. For each pattern, variation of unit cell parameters at increasing gas pressure were obtained through structure-less Le Bail refinements.[393] Later on, *ab initio* XRPD structure solution on each crystal phase was used to retrieve the full description of the structural parameters at each pressure point. Location of the CO_2 molecules into the channels were found by means of the simulated annealing approach,[394] followed by Rietveld refinement,[395] both implemented in TOPAS Academic software.[396] The multi-technique approach presented and the good quality of the diffraction data, resulted in good and interesting results for all the three MOFs studied and provided key information towards the deeper understanding of the *guest-guest* and *guest-framework* interactions during the whole adsorption process, thus disclosing the chemical and structural features of these porous materials and their suitability as CO_2 scavenger.

New flexible, multivariate, MOFs of general formula $M(BDP)_{0.5}(BDP-X)_{0.5}$, with M = Zn^{2+}, H_2BDP-X= 1,4-bis(1H-pyrazol-4-yl)benzene and X = -NH_2 or -NO_2, have been recently synthesized in collaboration with the research group of J. A. R. Navarro of the University of Granada (Spain). Currently, a deep characterization of the sorption properties and the structural features of these materials is being performed and will be crucial to understand the relation between the structural flexibility, functionalization degree and crystal size, with the gas adsorption and separation properties. The results obtained are also relevant in driving the research field towards the design and synthesis of superior materials, useful in industrially relevant gas storage and gas separation applications.

5.2 NP@MOFs: the Role of Functionalised Linkers, Heterogeneity and Defects

A family of functionalised pillared-layer MOFs of general formula $[M_2(fu\text{-}bdc)_2P]$ with $M^{2+} = Zn^{2+}$, $fu\text{-}bdc^{2-}$ = functionalised benzenedicarboxylate linkers and P = dabco, has been studied along the years by the research group of R. Fischer at the Technical University of Munich in order to tune their responsive properties. Different metal centres and a library of functionalized bdc^{2-} type linkers, which bear alkoxy groups of varying chain length with diverse functionalities and polarity as side chains, have been used by the group.[343,367,370]

Only recently, it was recognized that the flexible properties of MOFs may have a positive effect on catalytic applications, other than the more classical ones such as gas-storage, selective adsorption/separation or sensing.[246,300,301] The catalytic property can be introduced by embedding in the frameworks: *a)* catalytically active guests ^{cat}G (*e.g.* metal catalyst complexes, surfactant stabilized metal NP); *b)* polystyrene nanobeeds (PS) or silica nanospheres (SI) as catalytically inert yet mesoscopic defect generating components ^{def}G.

To this aim, the work presented in the second part of this PhD thesis was carried out at the TUM in collaboration with R. Fischer's research group and the following flexible MOFs have been selected: $[M_2(fu\text{-}bdc)_2P]$ with $M^{2+} = Zn^{2+}$; $fu\text{-}bdc^{2-}$ = functionalized 1,4-benzenedicarboxylate (fu = H, DM (methoxy) or BME (2-methoxyethoxy)) and P = dabco. In particular, the work was focused on the comparison between the parent MOFs fu-MLP with ^{def}G@fu-MLP systems, where G refers to non-catalytic fluorescent silica nanoparticles (30 nm). The parent MOF, namely $[Zn_2(fu\text{-}bdc)_2(dabco)]_n$, is indeed only weakly flexible;[363] however, the substituted frameworks contract drastically upon guest removal to a narrow pore form and expand again upon adsorption of DMF, EtOH, or CO_2, *etc.*. In contrast, N_2 is hardly adsorbed and does not open the narrow pore form. These "breathing" dynamics are attributed to the dangling side chains present on the linkers, which interact with mobile guest molecules as well as with themselves and with the framework backbone.[42] The goal is to establish switchable catalysts based on flexible MOF support matrices and to understand how the incorporation of nanoparticles will affect MOFs' flexibility, defectiveness and long-range order.

The samples were characterized by a variety of techniques: PXRD, FTIR, TGA, DSC, EFTEM-EDX, TEM tomography, UV-Vis and PL spectroscopy, standard N_2 (77 K) and CO_2 (195 K) gas sorption experiments. The major challenge has been locating the NPs in the composite materials, for this purpose specific experiments have been performed: EFETEM-EDX, useful to detect light chemical elements, and TEM tomography. Results have shown that most of the NPs are not embedded in the framework but are strongly interacting with the surface of the crystals. This has generated interesting differences in the flexible behaviour between the parent MOFs and the NPs@MOFs upon incorporation of guest gas

molecules and variable temperature, as proven by the *in-depth* and *in situ* structural and spectroscopic characterization carried out and especially gas sorption and variable temperature XRPD experiments.

This project is in its early stages and a lot of work has still to be done, for example a different type or size of nanoparticle can be used, or alternative flexible MOFs can be chosen, *e.g.* not pillar-layered ones. The long-term vision of this very recent project is to design catalytic fu-MLPs, by embedding catalytically active guests catG, which allow a selective triggering of the conversion of a target molecule by a controlled stimulus of a gate-opening molecule. This function will be the basis of switchable "gate-lock" MOF catalysts.[302]

Chapter 6

EXPERIMENTAL SECTION
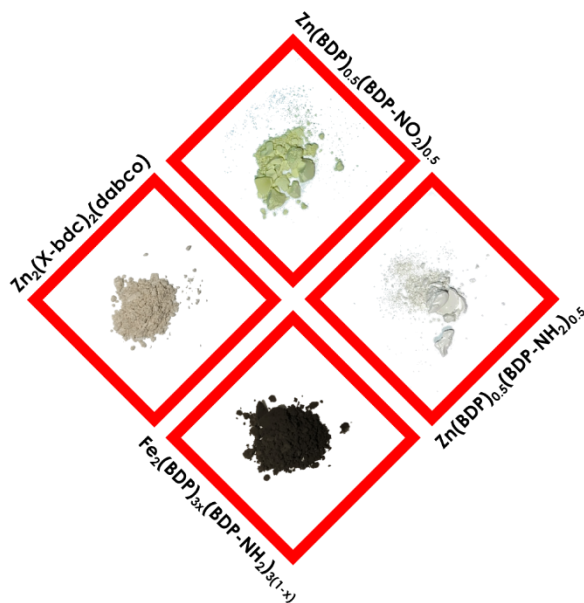
6.1 Materials and Methods

All solvents were dried and distilled under nitrogen by standard procedures prior to use. Unless otherwise specified, the reagents were obtained from commercial suppliers and used as received. Fluorescent silica nanoparticles were obtained commercially via Micromod Partikeltechnologie GmbH.[397]

Differential scanning calorimetry (DSC) and **thermogravimetric analysis** (TGA) were carried out simultaneously on a NETZSCH STA 409 PC/PG (University of Insubria) and a NETZSCH STA 449 F5 Jupiter (Technical University of Munich). For this, about 10 mg of sample, were weighed exactly to the fifth decimal digit, placed on an alumina pan and heated under a nitrogen flow (40 mL/min). The heating ramp used was 10 °C/min. Cyclic DSC experiments were performed on a TA Instruments DSC Q2000 (Technical University of Munich). Each sample was inserted in a sealed alumina crucible and measured

in air, using a heating ramp of 10 °C/min. One complete heating-cooling cycle and an additional heating cycle was performed, for a total of 1½ cycles in the temperature range of -150 – 230 °C.

Elemental analyses (EA) to determine of the quantity of carbon, hydrogen and nitrogen contained in the synthesised organic linkers and MOFs were performed on a Perkin-Elmer 2400 instrument (University of Milan).

Energy-filtered transmission electron microscopy (EFTEM) images were recorded on a ZEISS LIBRA200FE (LabCAT Istem, CNR-SCITEC) equipped with a 200 kV Schottky Field Emission electron gun, Kohler type (4 lenses) illumination, a HR objective lens (f = 1.7 mm, C_s = 1.2 mm, C_c = 1.2 mm) and a 2k × 2k SS-CCD detector, with the objective of observing the morphological and structural details of MOFs' crystallites and the nanoparticles with sub-nanometre resolution (point resolution = 0.24 nm). Additionally, the in-column Omega spectrometer and the Oxford EDS/**EDX** system provided a complementary tool to investigate the location of NPs and the chemical composition of the studied composite NPs@MOF materials. Tomographic reconstruction of the three-dimensional shape of the specimen was also possible, rotating the crystal of an amount of 2 degrees in both directions during the measurement.

Fluorescence spectra of solid samples were obtained on a FS5 Spectrofluorometer from Edinburgh Instruments (Technical University of Munich). As light source, a 150 W CW ozone-free xenon arc lamp was used and a Czerny–Turner design monochromator with a dual grating turret. The detector used was a Photomultiplier R928P with a spectral coverage of 200 nm–900 nm.

Gas sorption studies for $Fe_2(BDP)_{3x}(BDP-NH_2)_{3(1-x)}$ (x = 0, 0.5, 1) were performed on a Micromeritics Tristar III instrument (University of Granada). N_2 sorption measurements were carried out at -196 °C from 0 up to 1 bar, while CO_2 sorption measurements were carried out at -78, 0, 10 and 25 °C in the same pressure range. Sample activation was achieved through thermal activation at 120 °C for 12 h under high vacuum (~10^{-6} mbar). Additional CO_2 sorption measurements were obtained on an ASAP 2020 Micromeritics (LabCAT, CNR-SCITEC) at 25 °C from 0 up to 1 bar. Adsorption data for $Zn_2(bdc-X)_2(dabco)$ were carried out on a 3Flex Physisorption from Micromeritics Instrument Corp. (Technical University of Munich) and processed using the 3Flex Software Version 5.01 by Micromeritics Instrument Corp. The activated samples were transferred into pre-weighed sample tubes and capped with Micromeritics CheckSeals. Subsequently, they were activated again at 80 °C for 72 hours under dynamic vacuum of ~10^{-3} mbar using a SmartVac Prep by Micromeritics Instrument Corp. to ensure absence of unwanted adsorbates and identical pre-measurement states of all samples. The mass of the adsorbent was then recorded, generally in the range of 80-100 mg. A liquid nitrogen bath was used for measurements at -196 °C and a dry ice cooling bath was used for measurements at -78 °C.

Breakthrough curve experiments were carried out packing the adsorbent into a stainless-steel column of 152 mm length and 4 mm diameter (~0.5 g), through which a gas mixture of composition

$N_2:CO_2$ = 85:15 v/v was flowed at different temperatures (T = 0, 30, 50, 80 °C, total gas flux 20 mL/min). The relative gas mixture composition exiting the column was monitored with a PFEIFFER VACOON mass spectrometer (University of Granada) to detect the corresponding ion peaks at 4 (He), 28 (N_2) and 44 (CO_2) m/z value. Prior to the first measurement, the material was activated overnight at 80 °C under He flow (20 mL/min) and for 4 hours at 150 °C under He flow (20 mL/min) Successive activation procedures between measurements at different temperatures were performed at 120 °C under He flow (20 mL/min) for 20 min. The complete reactivation was monitored through a mass spectrometer.

IR spectra (ATR-IR) were acquired over the range of 4000–500 cm^{-1} in attenuated total reflectance (ATR) on a diamond crystal by means of a Perkin-Elmer Paragon 1000 spectrometer (University of Milan) and a PerkinElmer Frontier spectrometer (Technical University of Munich). All products have been measured without any dispersing media.

Monte-Carlo simulations were performed to study the interactions between the CO_2 molecules and the framework of $Fe_2(BDP)_3$ employing the Materials Studio 6.0 (MS6.0) software from Accelrys, Inc.[223] The Adsorption Locator module in MS6.0 was employed to construct the simulated systems and run the Monte-Carlo (MC) simulation. The Sorption module was used to perform CO_2 adsorption isotherm simulations at 0 °C and 25 °C.

Nuclear magnetic resonance (^1H NMR) spectra were recorded for the synthesised pyrazolate-based organic ligands (H_2BDP-X) on a Bruker spectrometer 300Mhz (University of Milan). For the H_2bdc-X series of linkers was employed a Bruker AV400 (400MHz) (Technical University of Munich) equipped with an autosampler. All measurements were recorded at T = 25 °C. DMSO-d_6 was used as solvent. Chemical shifts δ are given in ppm relatively to TMS and are referenced with MestreNova[398] to DMSO-d_6 as an internal standard.

UV/Visible spectra (UV/Vis) were obtained on an Agilent, Cary 60, UV-Vis Spectrophotometer and on a UV-3600 Plus from SHIMADZU for solid samples (Technical University of Munich), at a wavelength range of 200 nm–800 nm. In the case of solid-state UV-visible spectroscopy the sample was placed between two quartz microscope plates from Alfa Aesar and measured at room temperature.

X-ray powder diffraction (XRPD) data for qualitative analysis were acquired in the 2θ range of 3–35°, with a step of 0.02° and a time per step of 1 s, with the following procedure: gently ground powders of $Fe_2(BDP)_{3x}(BDP$-$NH_2)_{3(1-x)}$ (x = 0, 0.5, 1) were deposited in the 2 mm deep hollow of a quartz zero-background plate. Diffraction experiments were performed using Cu-K-alpha radiation (λ = 1.5418 Å) on a vertical-scan Bruker AXS D8 Advance diffractometer (University of Milan) in θ:θ mode, equipped with a Goebel Mirror and a Bruker Lynxeye linear Position Sensitive Detector, with the following optics: primary and secondary Soller slits, 2.3° and 2.5°, respectively; divergence slit, 0.1°; receiving slit, 2.82°. Generator setting: 40 kV, 40 mA. The nominal resolution for the present set-up is 0.08° 2θ (FWHM of the α_1 component) for the LaB_6 peak at about 21.3° (2θ).

The XRPDs of the as synthesized samples of $Zn_2(bdc-X)_2(dabco)$ were measured using Bragg-Brentano geometry with silicon wafer plates on a Rigaku Benchtop MiniFlex 600-C with a D/teX Ultra 1-D silicon strip detector (Technical University of Munich). X-ray Cu K-alpha radiation with generator settings of 40 kV voltage and 15 mA current were used. The activated samples instead were filled in borosilicate glass capillaries (diameter = 0.5 mm) in a glovebox under Argon atmosphere and measured in Debye-Scherrer geometry on a PANalytical Empyrean diffractometer equipped with a PANalytical PIXcel 1D detector (PASS) (Technical University of Munich). X-ray Cu K-alpha radiation with generator settings of 45 kV voltage and 40 mA current were used for the measurements. Whole powder pattern refinements were carried out adopting the Le Bail[221] and Pawley[393] methods, as implemented in TOPAS-Academic version 6,[396,399] using, as the starting point, the unit cell parameters already reported in the literature for the various studied MOFs.

Variable-temperature powder X-ray diffraction (VT-XRPD) experiments were made using a custom-made sample heater (Officina Elettrotecnica di Tenno, Ponte Arche, Italy) plugged in a Bruker AXS D8 Advance diffractometer with Bragg-Brentano geometry (University of Milan). About 20 mg of the as-synthesized compound were deposited in an aluminium sample-holder and heated in air from 30 °C until decomposition with steps of 20 °C (10 °C steps near crystalline phase transition temperatures between 170 and 300 °C). Temperature stabilisation time between each measurement was of circa two minutes. A XRPD pattern was acquired at each step, covering a sensible low-to-medium-angle 2θ range (6.0 - 29.5°, Cu-Kα). Whole powder pattern parametric refinements of the data acquired before the loss of crystallinity, carried out with the Le Bail method, disclosed the behaviour of the unit cell parameters as a function of temperature. The activated samples instead were filled in borosilicate glass capillaries (diameter = 0.5 mm) in the glovebox under Argon atmosphere (to exclude any impact of guest molecules, such as water from air humidity) and measured in Debye-Scherrer geometry on a STOE STADI P diffractometer (Technical University of Munich); X-ray Mo K-alpha radiation (λ = 0.70926 Å). Important to note is that the temperatures at which the main crystalline phase transition occur are different depending on the instrumental setup, this is because of the different heating system used.

High-resolution X-ray powder diffraction (HR-XRPD) measurements *in situ* and *operando* were performed at the European Synchrotron Radiation Facility (ESRF Grenoble, France; Proposals CH-5337 and CH-6073,[392] ID22 High-Resolution Powder-Diffraction Beamline) by using the gas handling system described by Brunelli *et al.*[400] Pre-activated $Fe_2(BDP)_3$ was gently ground and introduced into a 0.5 mm diameter borosilicate glass capillary. The capillary was first aligned, then connected to the gas handling system and further activated at 180 °C under high vacuum (7×10^{-6} bar) by means of a turbo vacuum pump for approximately 2 hours in order to remove any residual trapped solvent in the MOF 1-D channels. To minimize preferred-orientation effects and obtain very accurate diffracted intensities, the capillary-containing cell was screwed onto a motorized goniometric head that allowed ±120° rocking of the capillary with its axis co-linear with that of the goniometer. All the measurements were carried out

on the same capillary. The sample radiation damage was monitored and prevented by translating the capillary a total of three times during the whole experiment. All measurements were performed at 35 keV (λ = 0.355 Å, calibrated with the Si NIST standard SRM 640c at room temperature) with a beam size of 1 mm (horizontal) by 0.9 mm (vertical) defined by water-cooled slits and monochromated with a cryogenically cooled Si (111) channel-cut crystal. A bank of nine detectors, each preceded by a Si (111) analyser crystal, was scanned vertically to measure the diffracted intensity. For $Fe_2(BDP)_3$ two different temperatures were investigated, namely T = 0 and 25 °C, while varying the CO_2 loading in the pressure range of 0 to 8 bar. For $Fe_2(BDP-NH_2)_3$ T = 0 and 25 °C, while varying the CO_2 loading in the pressure range of 0 to 26 bar. $Fe_2(BDP)_{1.5}(BDP-NH_2)_{1.5}$ T = 0 °C, while varying the CO_2 loading in the pressure range of 0 to 26 bar. An equilibration time of 15 minutes was adopted at each pressure point.

6.2 Synthesis of Organic Likers

6.2.1 Bis-pyrazolate Ligands

The three organic ligands, namely H_2BDP, $H_2BDP-NO_2$ and $H_2BDP-NH_2$, have been synthesised according to reported procedures.[203–206] ^{1}H NMR (DMSO-d_6) δ (ppm): 12.89 (br, s), 8.17 (s, 2H), 7.92 (s, 2H), 7.58 (s, 4H). Anal. calc. for $C_{12}H_{10}N_4$ (FW = 210,2 g/mol) C, 68.63; H, 3.84; N, 26.68; found C, 68.60; H, 4.64; N, 26.51% for **H_2BDP**. ^{1}H NMR (DMSO-d_6) δ (ppm): 13.10 (br s), 8.22 (s, 2H), 8.08 (d, 1H), 7.89 (dd, 1H), 7.79 (s, 2H), 7.62 (d, 1H). IR (ATR): $\nu(NO)_{asym}$ 1516,38 cm^{-1}; $\nu(NO)_{sym}$ 1351,16 cm^{-1}; $\nu(CN)$ 920-850 cm^{-1}. Anal. calc. for $C_{12}H_9N_5O_2$ (FW = 255,2 g/mol) C, 56.4; H, 3.55; N, 27.4; found C, 47.61; H, 3.46; N, 13.17% for **$H_2BDP-NO_2$**. ^{1}H NMR (DMSO-d_6) δ (ppm): 12.87 (br s), 7.84 (br s, 4H), 7.15 (d, 1H), 6.97 (d, 1H), 6.85 (dd, 2H), 4.78 (s, 2H). IR (ATR): $\nu(NH)_{asym}$ 3423.52 cm^{-1}; $\nu(NH)_{sym}$ 3342.52 cm^{-1}; $\nu(NH_2)$ 1621.99 cm^{-1}. Anal. calc. for $C_{12}H_{11}N_5$ (FW = 225,2 g/mol) C, 63.99; H, 4.92; N, 31.09; found C, 63.60; H, 5,43; N, 31% for **$H_2BDP-NH_2$**.

6.2.2 Functionalised Benzenedicarboxylate Ligands

Alkoxy-functionalized linkers, namely $H_2(DM-bdc)$ and $H_2(BME-bdc)$, were prepared following the known procedures.[343] ^{1}H NMR (DMSO-d_6) δ (ppm): 7.30 (s, 2H, Ar-H), 3.78 (s, 6H, OCH$_3$) ppm. Anal. calc. for $C_{10}H_{10}O_6$ (FW = 226,18 g/mol) C, 53.10; H, 4.46; found C, 53.43; H, 4.60% for **$H_2(DM-bdc)$**. ^{1}H NMR (DMSO-d_6) δ (ppm): 7.31 (s, 2H, Ar-H), 4.16 – 4.09 (m, 4H, OCH$_2$), 3.66 – 3.60 (m, 4H, OCH$_2$), 3.31 (s, 6H, OCH$_3$) ppm. Anal. calc. for $C_{14}H_{18}O_8$ (FW = 314,29 g/mol) C, 53.50; H, 5.77; found C, 53.26; H, 5.98% for **$H_2(BME-bdc)$**.

6.3 Fe$_2$(BDP)$_{3x}$(BDP-NH$_2$)$_{3(1-x)}$ (x = 0, 0.5, 1)

6.3.1 Synthetic Procedure

Fe$_2$(BDP)$_{3x}$(BDP-NH$_2$)$_{3(1-x)}$ (x = 0, 0.5, 1) have been synthetized, washed and thermally activated following the reported procedures with minor modifications.[194] Anal. calc. for Fe$_2$(C$_{12}$N$_4$H$_8$)$_3$ [**Fe$_2$(BDP)$_3$**, FW = 736.36 g/mol]: C, 58.72; H, 3.29; N, 22.83%. Found: C, 57.06; H, 3.37; N, 21.13%. Anal. calc. for Fe$_2$(C$_{12}$N$_5$H$_9$)$_3$ [**Fe$_2$(BDP-NH$_2$)$_3$**, FW = 781.41 g/mol]: C, 55.34; H, 3.48 N, 26.89%. Found: C, 47.69; H, 3.27; N, 23.05%. Anal. calc. for Fe$_2$(C$_{12}$N$_4$H$_8$)$_{1.5}$(C$_{12}$N$_5$H$_9$)$_{1.5}$ [**Fe$_2$(BDP)$_{1.5}$(BDP-NH$_2$)$_{1.5}$**, FW = 758.88 g/mol]: C, 56.98; H, 3.39; N, 24.92%. Found: C, 49.90; H, 3.30; N, 23.03%.

6.3.2 XRPD Analysis
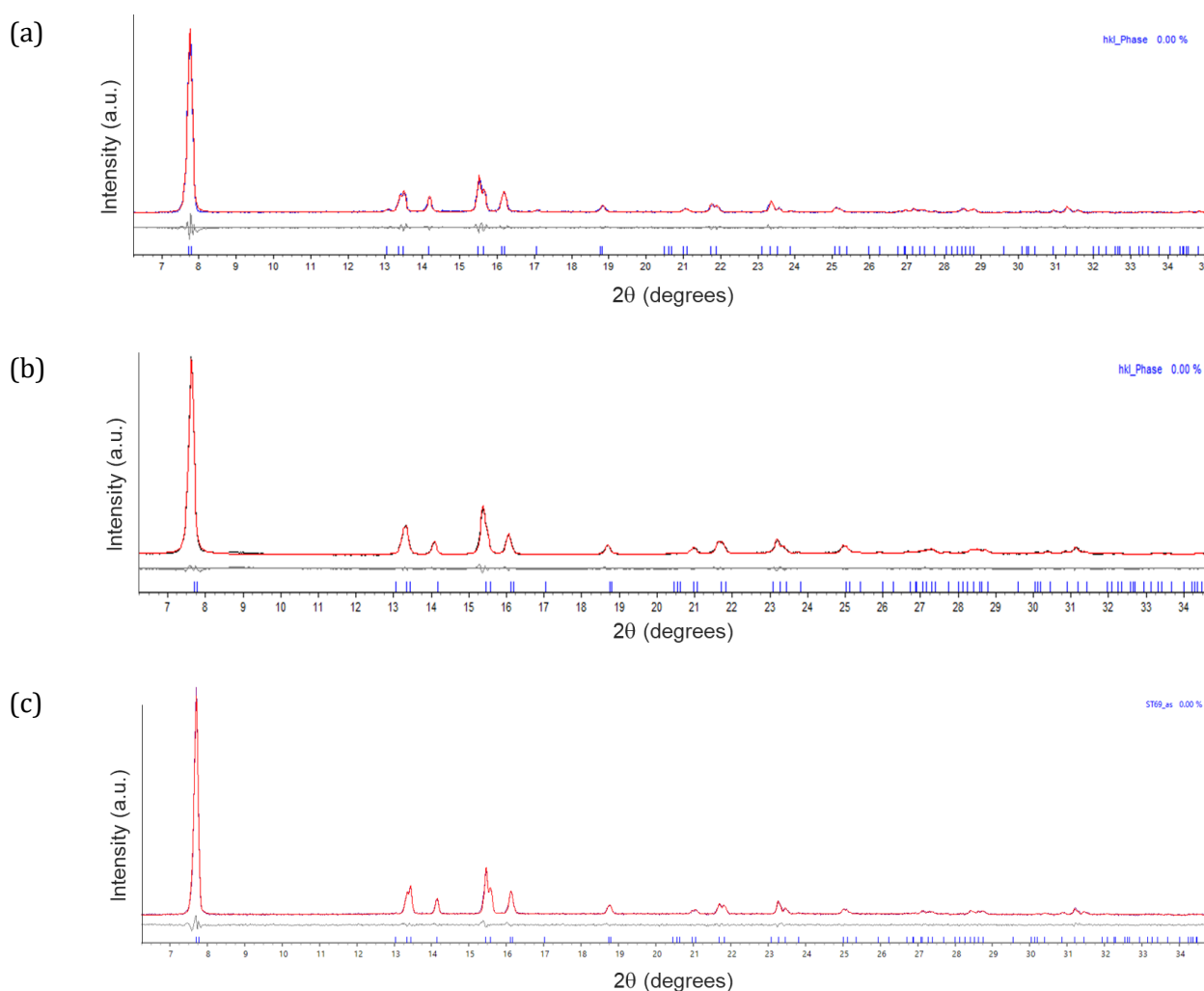
Figure 6.1 - Graphical representation of the whole powder pattern refinement carried out with the Le Bail method on the PXRD pattern of as-synthesized Fe$_2$(BDP)$_3$ (a), Fe$_2$(BDP-NH$_2$)$_3$ (b), Fe$_2$(BDP)$_{1.5}$(BDP-NH$_2$)$_{1.5}$ (c) showing experimental, calculated and difference traces (blue, red and grey, respectively). The positions of the Bragg reflections are indicated by blue ticks.

Table 6.1 – Unit cell parameters and space groups resulting from Le Bail refinements for the three isostructural MOFs studied.

	$Fe_2(BDP)_3$	$Fe_2(BDP-NH_2)_3$	$Fe_2(BDP)_{1.5}(BDP-NH_2)_{1.5}$
Space group	*Fddd*	*Fddd*	*Fddd*
a (Å)	7.1000(6)	7.0911(2)	7.0773(5)
b (Å)	26.4733(6)	26.5302(8)	26.2298(3)
c (Å)	45.3325(6)	45.4986(8)	45.8269(5)
V (Å³)	8520.82(1)	8559.64(4)	8507.22(1)
R_{Bragg}	0.305	0.186	0.111
Crystal size (nm)	252.5	145.9	182.4
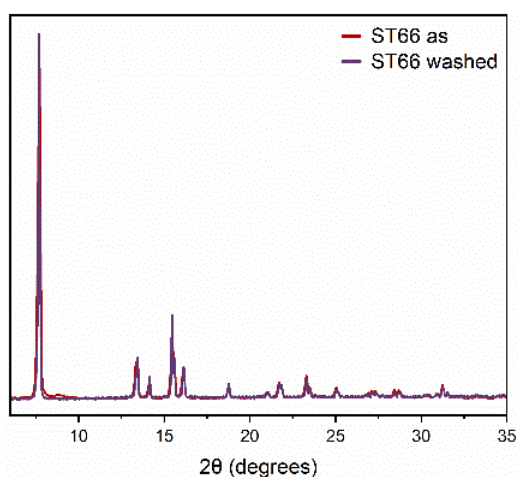
(a) $Fe_2(BDP)_3$
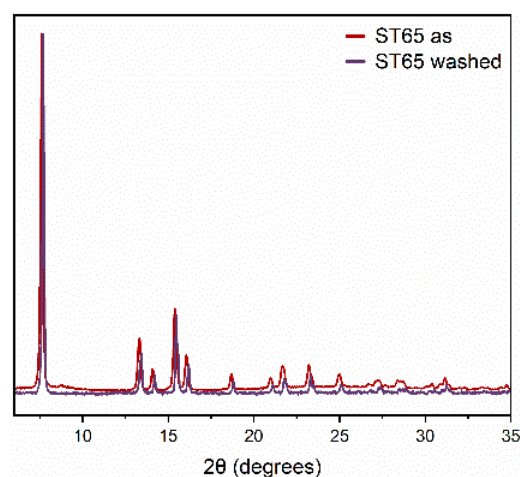
(b) $Fe_2(BDP-NH_2)_3$
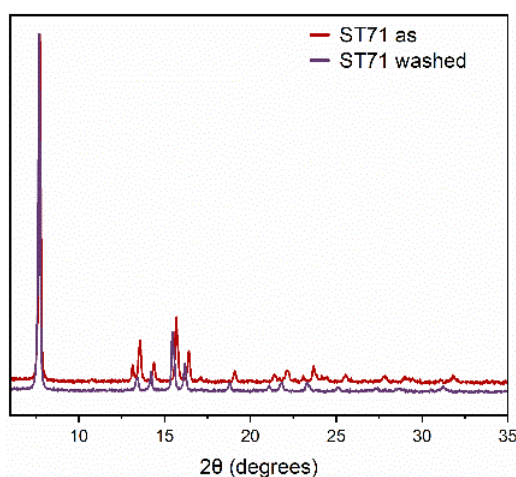
(c) $Fe_2(BDP)_{1.5}(BDP-NH_2)_{1.5}$

Figure 6.2 - Comparison of the XRPD patterns of as synthesized MOFs (red line) and MOFs after the washing procedure (violet line). A clear improvement in the quality of the diffraction pattern can be observed between *as* and *washed* samples, especially taking into consideration the background and the area around 2θ 9.5 degrees.

6.3.3 IR Spectroscopy
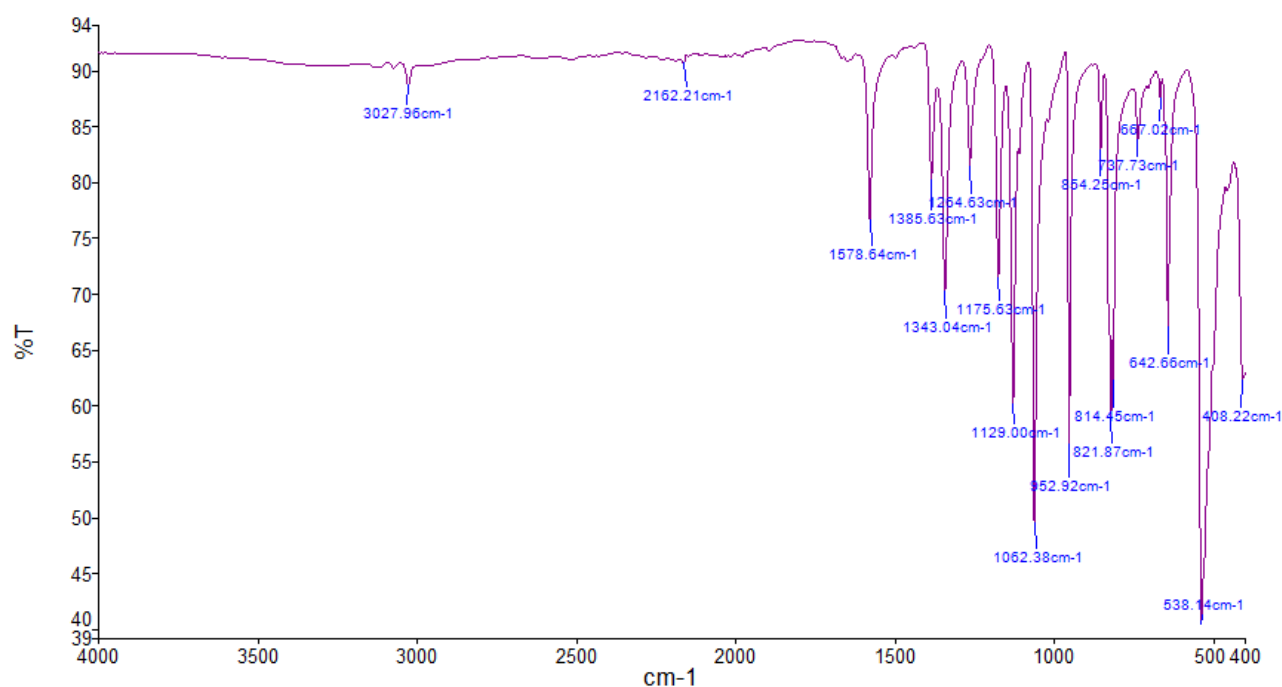
Figure 6.3 - Infrared spectrum of as-synthesized $Fe_2(BDP)_3$. FT-IR (solid, ATR, cm^{-1}). Selected frequencies: $\nu_{C=N}$ 1386, 1343, $\nu_{C=C}$ 1578 cm^{-1}.
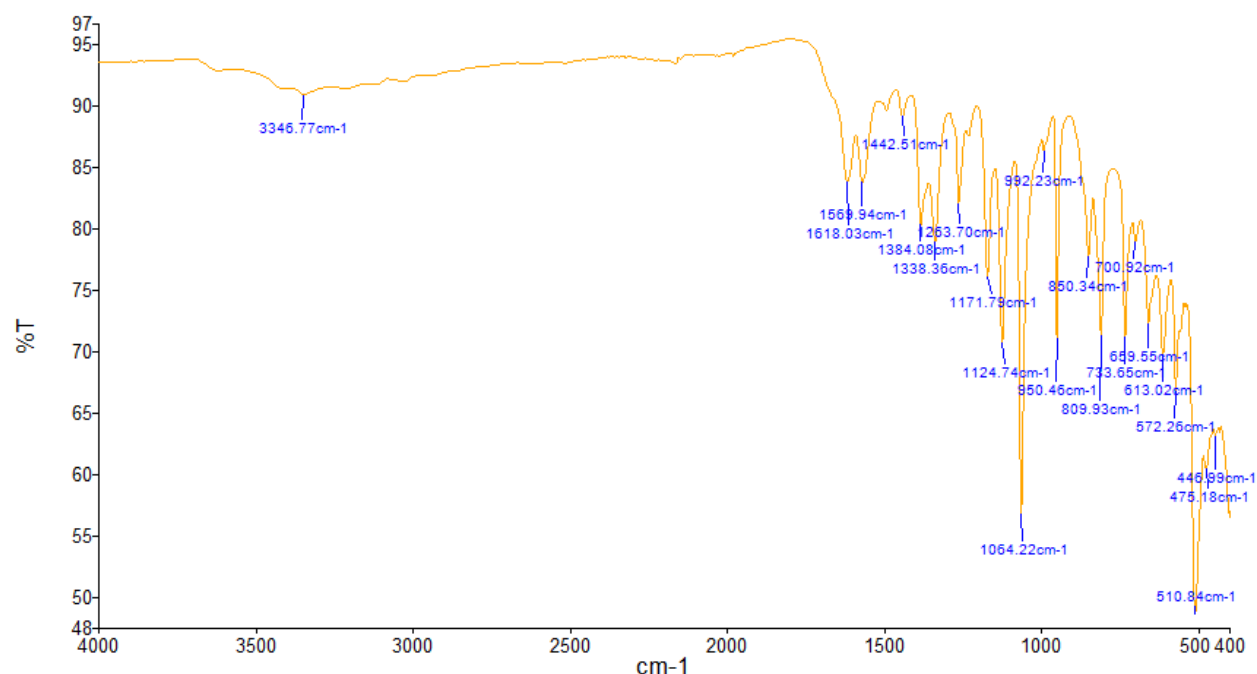
Figure 6.4 - Infrared spectrum of as-synthesized $Fe_2(BDP-NH_2)_3$. FT-IR (solid, ATR, cm^{-1}). Selected frequencies: $\nu_{C=N}$ 1384, 1338, $\nu_{C=C}$ 1569, $\nu_{N=H}$ 1618, ν_{N-H} 3346 cm^{-1}. The presence of amino groups can be verified by characteristic signals at 3346 cm^{-1} and at 1618 cm^{-1}, corresponding to the symmetric N–H stretching modes and N-H bending vibration (scissoring), respectively.
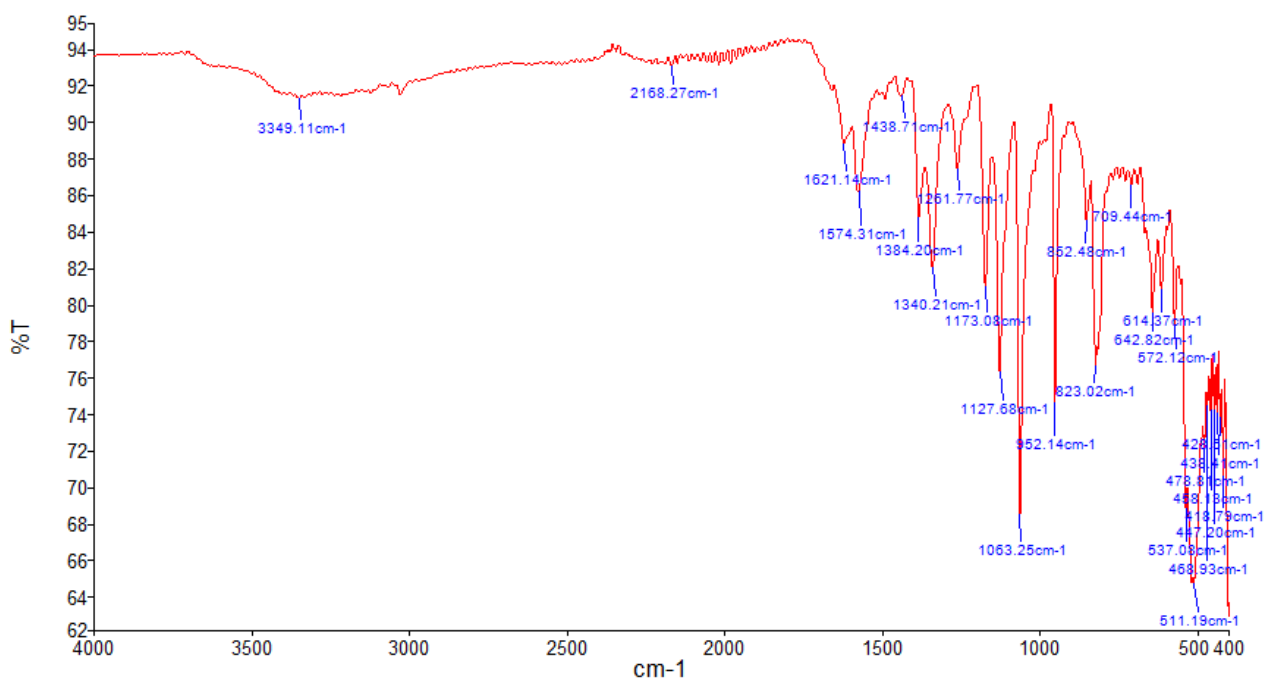
Figure 6.5 - Infrared spectrum of as-synthesized $Fe_2(BDP)_{1.5}(BDP-NH_2)_{1.5}$. FT-IR (solid, ATR, cm^{-1}). Selected frequencies: $\nu_{C=N}$ 1384, 1340, $\nu_{C=C}$ 1574, $\nu_{N=H}$ 1621, ν_{N-H} 3349 cm^{-1}. The presence of amino groups can be verified by characteristic signals at 3349 cm^{-1} and at 1621 cm^{-1}, corresponding to the symmetric N–H stretching modes and N–H bending vibration (scissoring), respectively.

6.3.4 STA Analysis
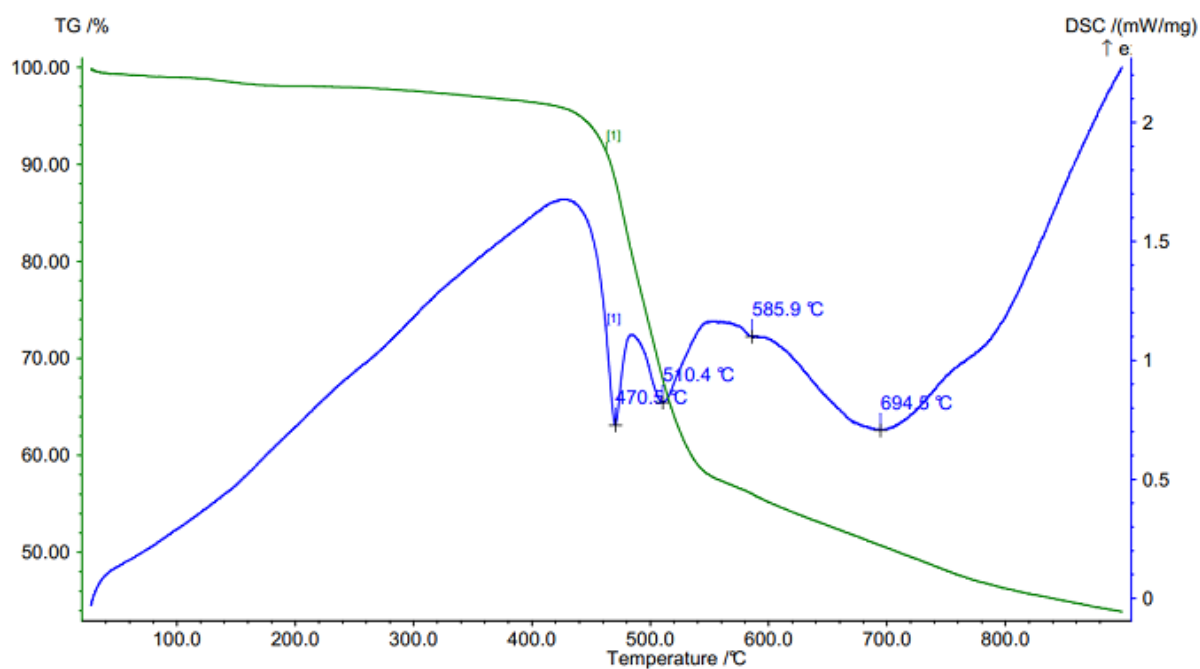
Figure 6.6 - Simultaneous differential scanning calorimetric (blue trace) and thermogravimetric analyses (green trace) for dry $Fe_2(BDP)_3$ carried out after adsorption of N_2 (77 K) and CO_2 (195 K).
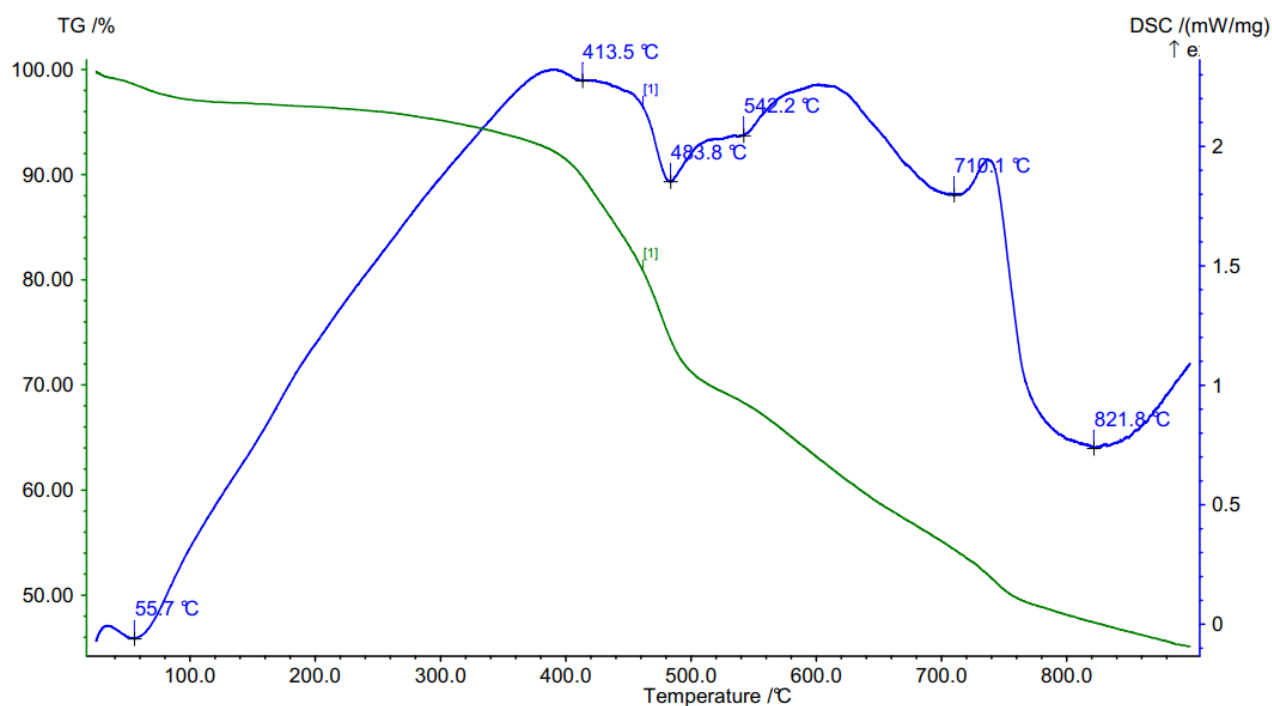
Figure 6.7 - Simultaneous differential scanning calorimetric (blue trace) and thermogravimetric analyses (green trace) for dry $Fe_2(BDP-NH_2)_3$ carried out after adsorption of N_2 (77 K) and CO_2 (195 K).

6.3.5 VT-XRPD Analysis
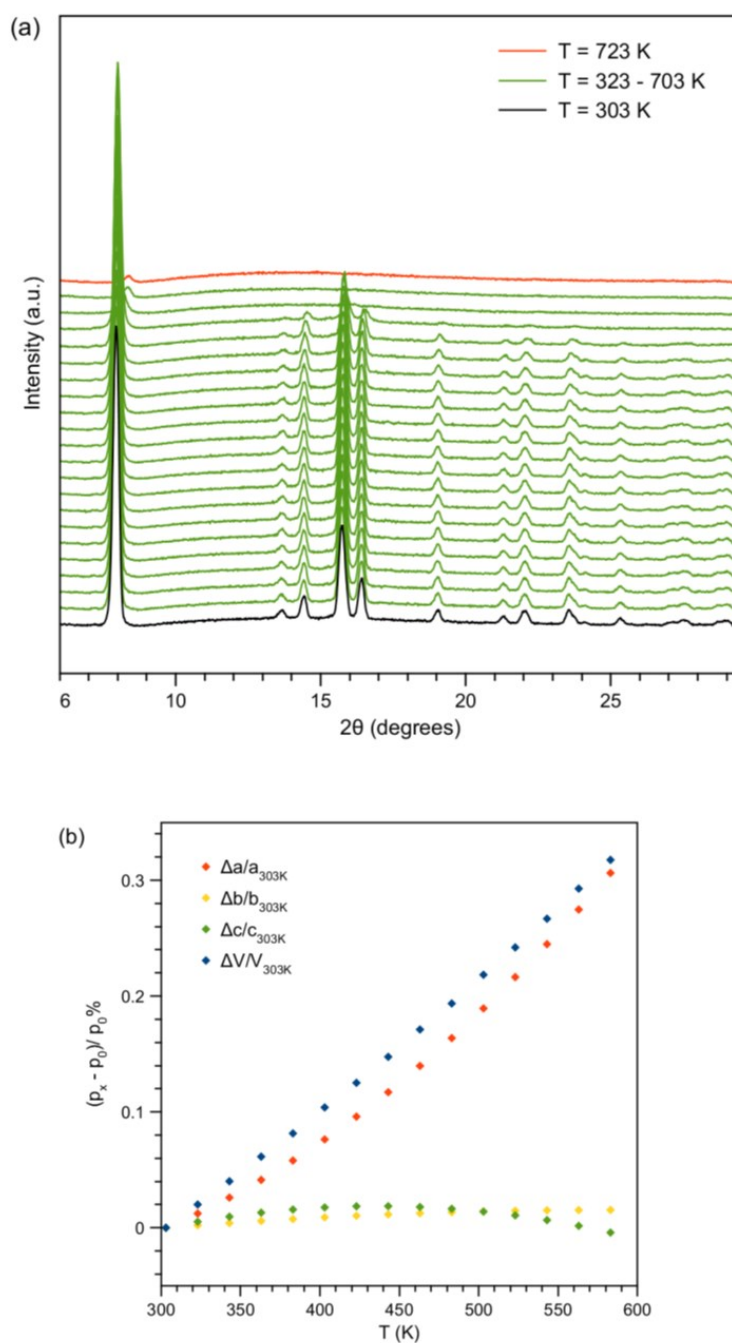
Figure 6.8 - (a) Powder X-ray diffraction patterns of as-synthesised $Fe_2(BDP)_3$ as a function of ascending temperature in air, with steps of 20 °C, in the temperature range 30 (bottom trace) – 50 (top trace) °C. (b) Relative percentage variation of the unit cell parameters (p_x) of as-synthesised $Fe_2(BDP)_3$ during the VT-PXRD experiment with respect to the values at T = 30 °C (p_0).
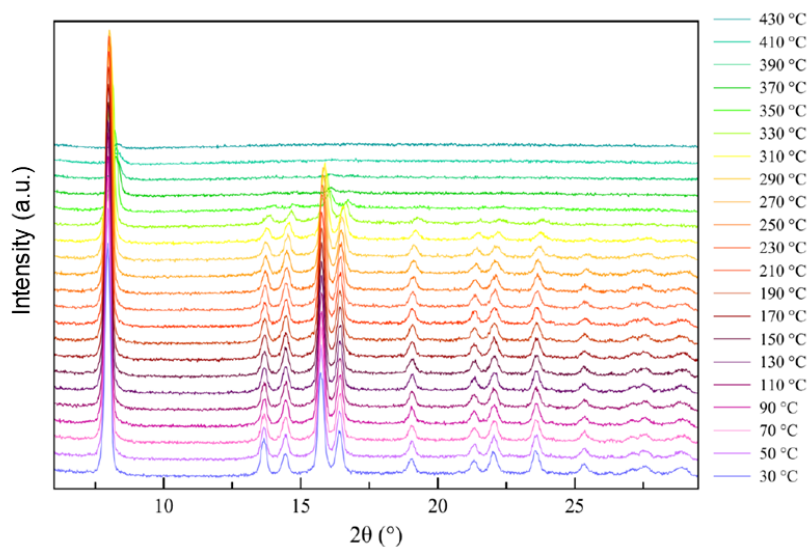
Figure 6.9 - Powder X-ray diffraction patterns of as-synthesised $Fe_2(BDP-NH_2)_3$ as a function of ascending temperature in air, with steps of 20 °C, in the temperature range 30 (bottom trace) – 430 (top trace) °C.

6.3.6 Static Gas Sorption Measurements
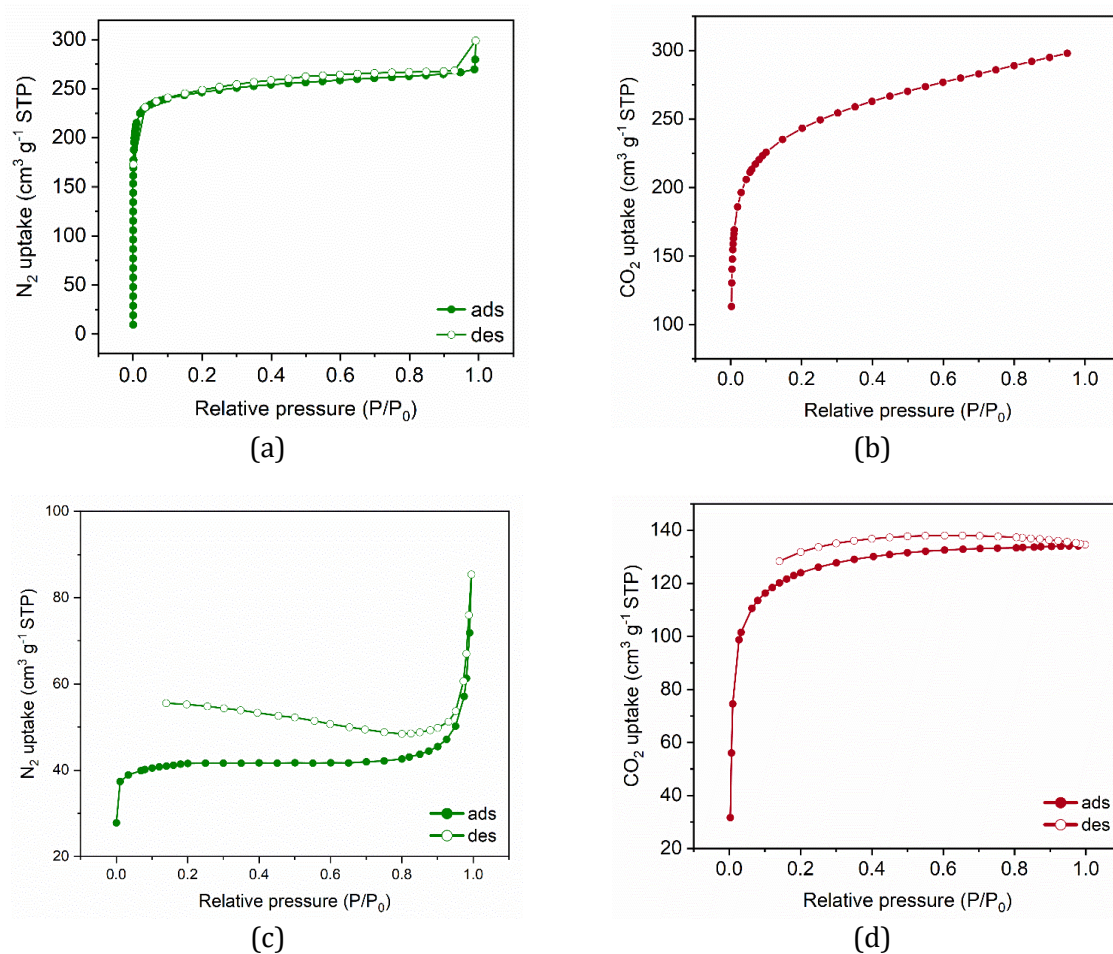
Figure 6.10 - N_2 sorption isotherms measured at 77 K on activated $Fe_2(BDP)_3$ (a) and $Fe_2(BDP-NH_2)_3$ (c). CO_2 sorption isotherms measured at 195 K on activated $Fe_2(BDP)_3$ (b) and $Fe_2(BDP-NH_2)_3$ (d).

Table 6.2 - Calculated Q_{st} values obtained from CO_2 adsorption isotherms at 0, 10 and 25 °C on $Fe_2(BDP)_3$.

Quantity Adsorbed (mmol/g)	Heat of Adsorption (kJ/mol)	Quantity Adsorbed (mmol/g)	Heat of Adsorption (kJ/mol)
0.20	28.26	1.78	29.54
0.30	28.32	1.88	29.64
0.35	28.37	1.98	29.71
0.37	28.40	2.08	29.80
0.40	28.42	2.18	29.93
0.50	28.52	2.28	30.03
0.55	28.55	2.38	30.12
0.59	28.59	2.48	30.24
0.69	28.68	2.58	30.37
0.74	28.72	2.68	30.46
0.79	28.75	2.78	30.56
0.84	28.79	2.88	30.67
0.89	28.82	2.97	30.78
0.94	28.86	3.07	30.86
0.99	28.91	3.17	30.95
1.09	28.99	3.27	31.05
1.19	29.08	3.37	31.18
1.29	29.18	3.47	31.30
1.39	29.26	3.57	31.40
1.49	29.31	3.67	31.57
1.59	29.36	3.77	31.72
1.69	29.45	3.82	31.83

continues ↕
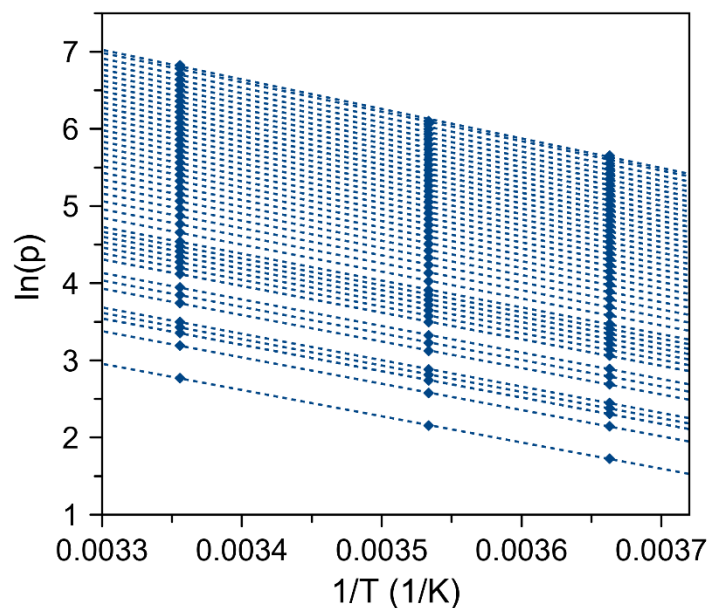
Figure 6.11 - Isosteric ln(p) against 1/T plot for T1 = 0 °C and T2 = 10 °C and T3 = 25 °C.

6.3.7 Dynamic Gas Sorption Experiments

Table 6.3 - CO_2 retention times and quantities resulting from the breakthrough experiments carried out at different temperatures on $Fe_2(BDP)_3$.

T (°C)	Retention time (min)	CO_2 retained (mmol/g)
0	5.18	1.46
30	2.86	0.80
50	1.89	0.53
80	1.24	0.35

Table 6.4 - CO_2 retention times and quantities resulting from the breakthrough experiments carried out at different temperatures on $Fe_2(BDP-NH_2)_3$.

T (°C)	Retention time (min)	CO_2 retained (mmol/g)
0	5.00	2.61
30	2.27	1.18
50	1.50	0.78
80	1.08	0.56

Table 6.5 - CO_2 retained quantities and relative percentage variation with respect to the first cycle resulting from the breakthrough recyclability test carried out at 30 °C.

Cycle	CO$_2$ retained (mmol/g)	Variation of CO$_2$ retained (%)
#1	0.38	100.0
#2	0.36	95.5
#3	0.38	99.3
#4	0.37	98.3
#5	0.36	95.3
#6	0.37	98.8
#7	0.39	101.9
#8	0.37	98.8
#9	0.38	99.3
#10	0.38	99.5
#11	0.37	98.7

6.3.8 *In situ* HR-XRPD Experiments

$Fe_2(BDP)_3$

Two different temperatures were investigated, namely T = 0 and 25 °C, while varying the CO_2 loading in the pressure range from 0 to 8 bar. An equilibration time of 15 minutes was adopted at each pressure point. HR-XRPD data treatment started with the space group and unit cell parameters determination and refinement through a whole powder pattern refinement carried out with the Le Bail method,[221] starting from the reported unit cell parameters.[194] The Rietveld refinements[395] on the data collected at 0 bar and T = 0 and 25 °C allowed the confirmation of the complete activation of the sample and were used as starting point for locating the adsorbed CO_2 molecules at higher pressures. The simulated annealing approach provided the location of the primary CO_2 adsorption sites.[394] Both crystallographically independent portions of the ligand (disordered ½ ligand and ¼ ligand) and the three crystallographically independent CO_2 molecules were modelled as rigid bodies in *z-matrix* formalism as implemented in Topas-Academic V6.[396] Fixed bond lengths and angles were used at this stage (bond lengths and angles for the rigid body describing the ligand: C-C and C-N of the pyrazolate ring 1.38 Å; C-H of the pyrazolate ring 0.95 Å; pyrazolate ring bond angle 108°; C-C and C-H of the benzene ring 1.50 Å and 0.95 Å, respectively; rigid body modelling CO_2: C=O, 1.21 Å; O=C=O, 180°). The position of the centre of mass, the orientation and the site occupation factors of the CO_2 molecules, together with the occupancy and the torsion angle of the disordered phenyl rings of both independent

ligands, were allowed to vary. The peak shape was described with the fundamental parameters approach.[401] The anisotropic peak broadening was successfully modelled by using the Stephen's description for orthorhombic space groups, taking into account both the Lorentzian and Gaussian contributions.[402] The background was modelled by a polynomial function of the Chebyshev type. Two independent refined, isotropic thermal parameters (B and B_{solv}) were assigned to the metal atom and CO_2 molecules, respectively, while a higher isotropic thermal parameter, B+2 $Å^2$, was given to the ligand atoms. During the final Rietveld refinement stages, ligand bond lengths (except for the C-H distance) were allowed to refine freely in a restrained range of values (refined bond lengths in the final stages of the Rietveld refinements: C–C 1.44-1.50 Å; C–C and C–N of the pyrazolate ring 1.32-1.42 Å; C–C of the benzene ring 1.34-1.43 Å). Figure 6.13, Figure 6.14, Figure 6.20 and Figure 6.23 show the final graphical output of a whole powder pattern and Rietveld refinements carried out on the HR-XRPD data, as representative examples. The R_{wp} and R_p figures of merit for all the whole powder pattern and Rietveld refinements carried out on the HR-XRPD data are reported in Table 6.6, Table 6.7, Table 6.16, Table 6.18(T = 0 °C) and Table 6.8, Table 6.9, Table 6.17 (T = 25 °C). Table 6.10, Table 6.11 collect details on the orientational disorder of the phenyl ring of the ligands in response to CO_2 loading. Finally, Table 6.12, Table 6.13 contain the occupancy values and quantity of gas adsorbed, at 0 and 25 °C respectively, and at increasing CO_2 loadings.

The CO_2 molecules site occupation factors obtained by Rietveld refinement were then used to build two adsorption isotherms at 0 and 25 °C in the range of the studied pressures (0-8 bar). The adsorption isotherms were then modelled using the Freundlich-Langmuir equation [Eq. (1)].[214]

$$n = \frac{a \cdot b \cdot p^c}{1 + b \cdot p^c} \qquad Eq.\,(1)$$

Where: n is the adsorbed amount (loading) in mmol/g, p is the pressure in kPa, a is the maximal loading in mmol/g, b is the affinity constant (1/kPa) and c is the heterogeneity exponent. Finally, the isosteric heats of adsorption (Q_{st}) as a function of the CO_2 uptake for $Fe_2(BDP)_3$ were calculated from the modelled adsorption isotherms at 0 and 25 °C retrieved from the HR-PXRD experiment. The calculation was performed based on the Clausius-Clapeyron equation [Eq.(2)].[214]

$$Q_{st} = -R[\Delta(lnP)/\Delta(1/T)]_N \quad Eq.\,(2)$$
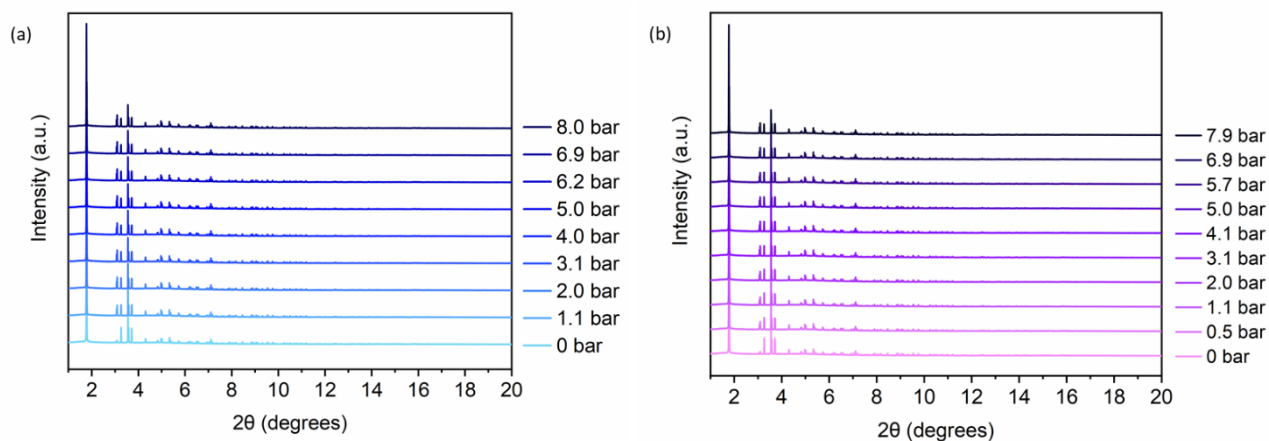
Figure 6.12 - Comparison of the low-to-medium angle portion of the HR-PXRD patterns of $Fe_2(BDP)_3$ acquired at (a) 0 °C and (b) 25 °C, at 0 bar of CO_2 and all the CO_2 loadings essayed at each temperature.
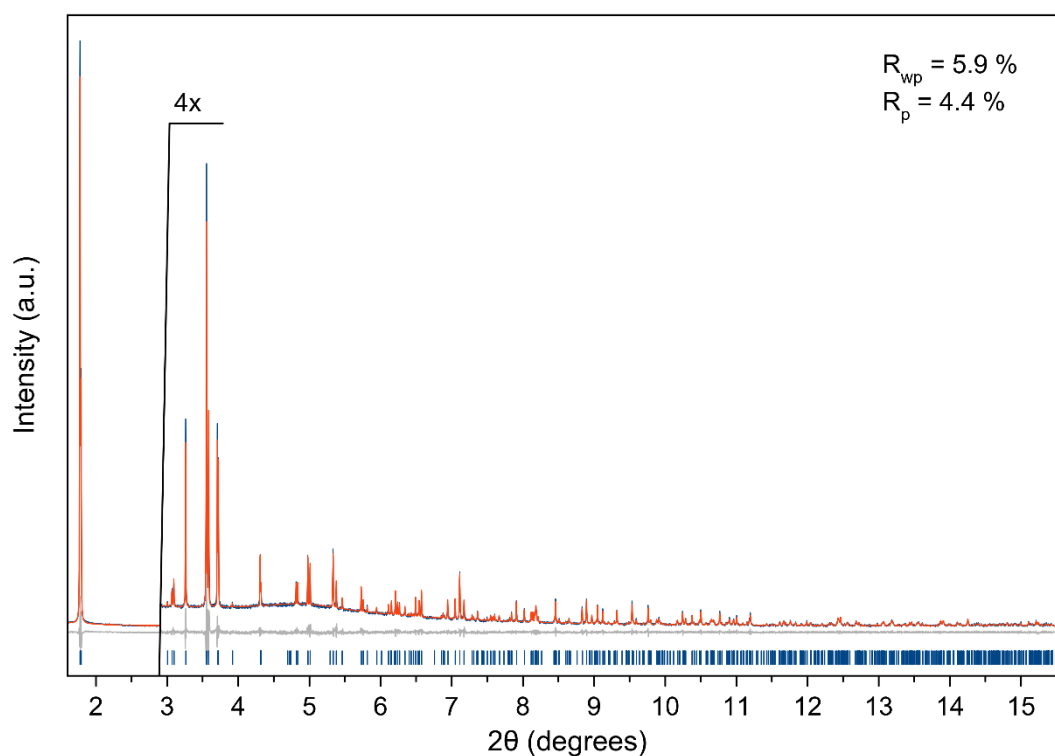
Figure 6.13 - Graphical representation of the whole powder pattern refinements carried out with the Le Bail method on data of $Fe_2(BDP)_3$ at T = 25 °C and p_{CO2} = 0 bar (as representative example of the data treatment), showing experimental, calculated and difference traces (blue, red and grey, respectively). The positions of the Bragg reflections are indicated by blue ticks. For 2θ higher than 2.9° the traces were magnified for clarity.
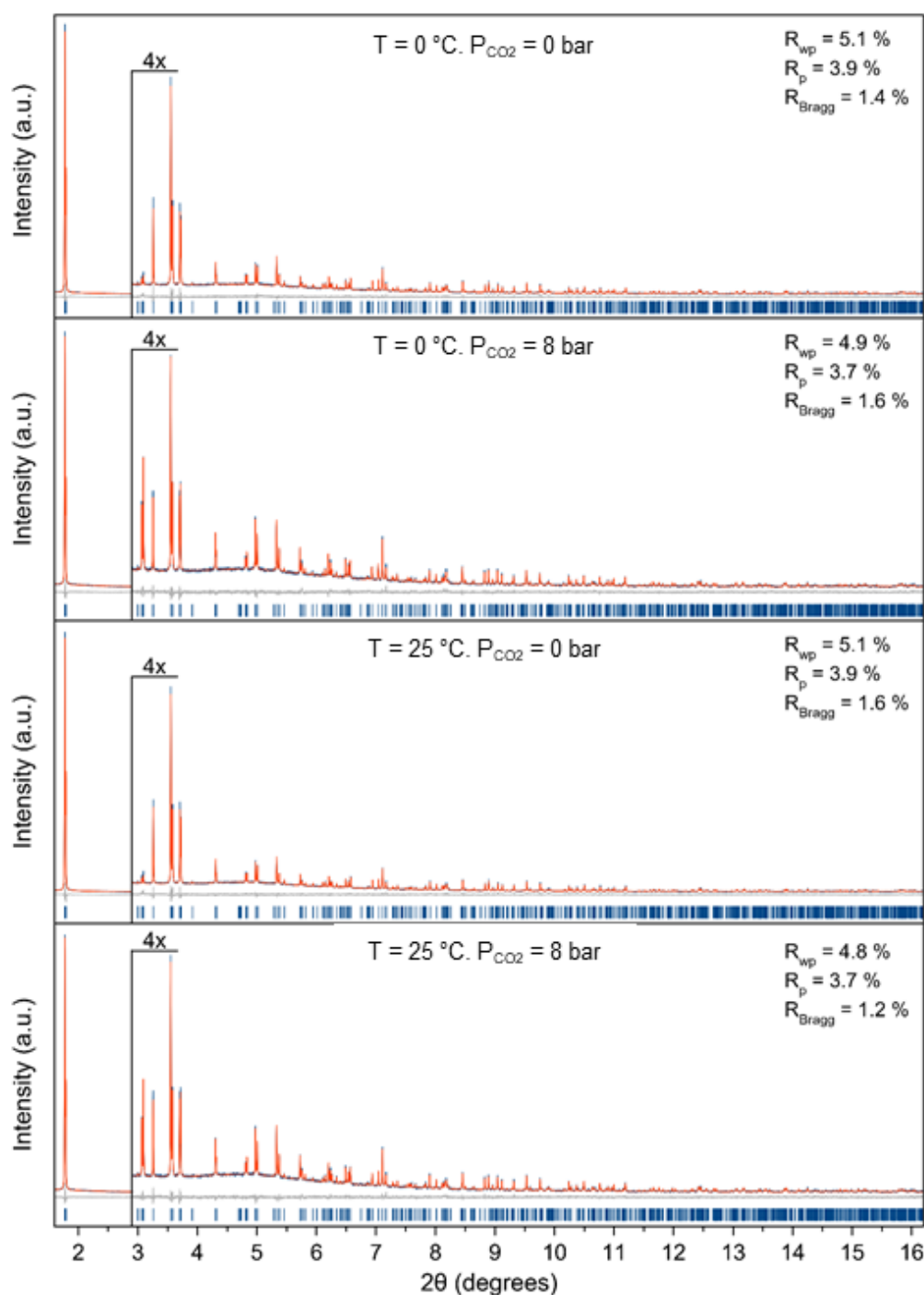
Figure 6.14 - Graphical representation of the Rietveld refinements carried out on the HR-PXRD data of $Fe_2(BDP)_3$ (from the top to the bottom as representative example of data treatment: T = 0 °C and p_{CO2} = 0 bar; T = 0 °C p_{CO2} = 8 bar, T = 25 °C and p_{CO2} = 0 bar; T = 25 °C and p_{CO2} = 8 bar) showing experimental, calculated and difference traces (blue, red and grey, respectively). The positions of the Bragg reflections are indicated by blue ticks. For 2θ higher than 2.9° the traces were magnified for clarity.
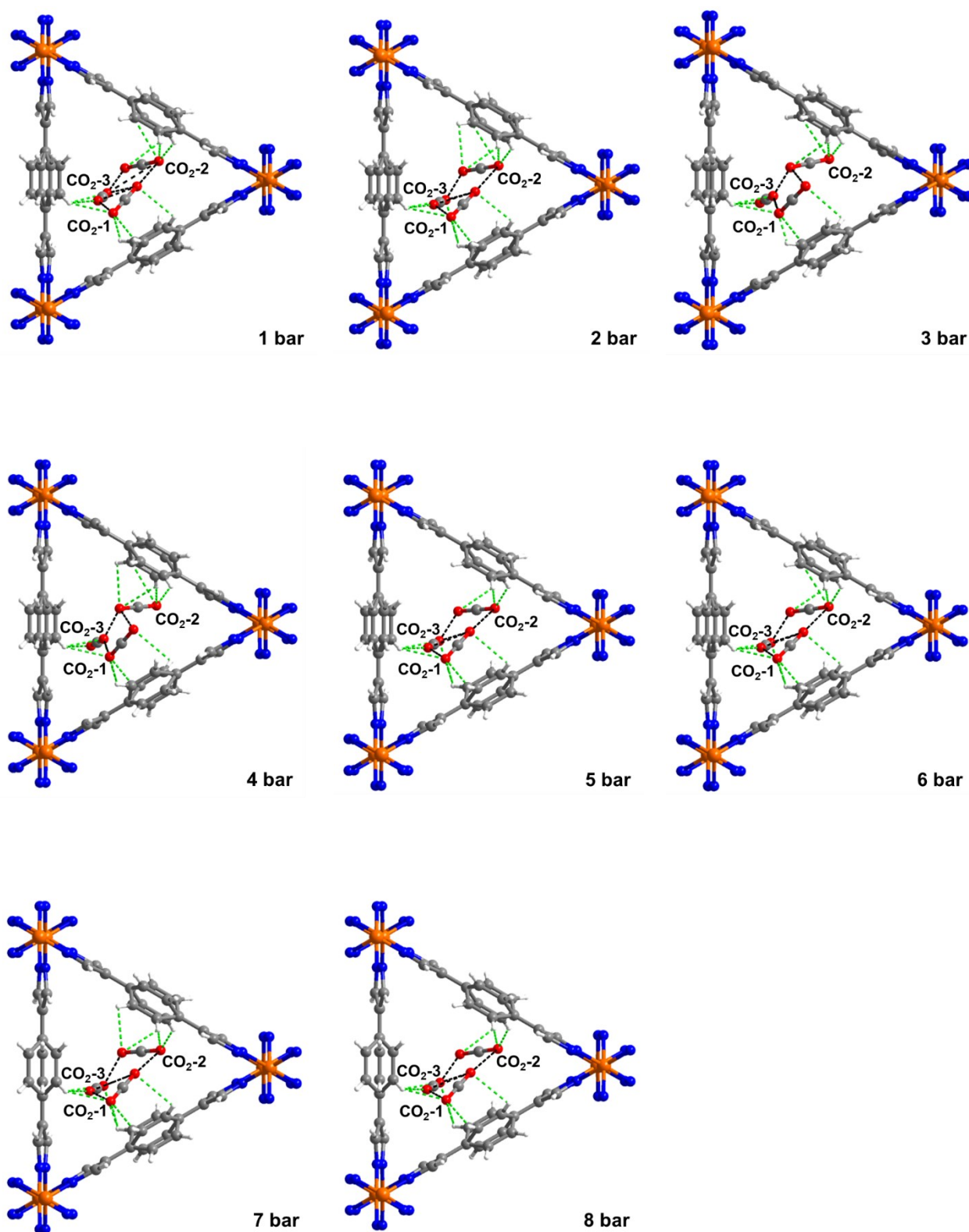
Figure 6.15 - Location of the three independent CO_2 molecules [CO_2–1, CO_2–2, and CO_2–3 in the text] in $Fe_2(BDP)_3$ at 0 °C and CO_2 loadings in the range 1-8 bar. Depicted with fragmented lines the CH−O *host-guest* (green) and O−O *guest-guest* (black) interactions. For the sake of clarity, only host-guest interactions shorter than 2.7 Å have been depicted.
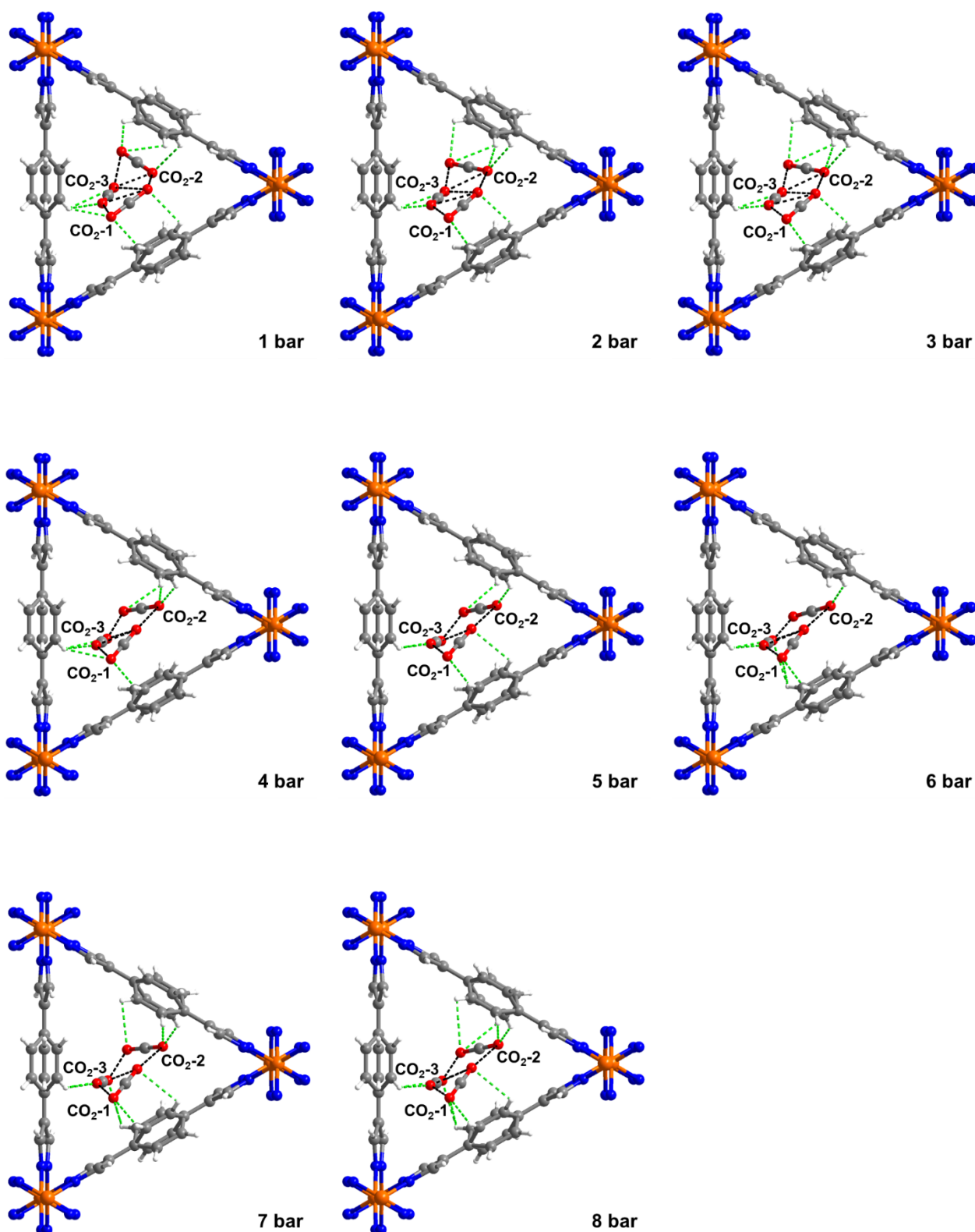
Figure 6.16 - Location of the three independent CO_2 molecules [CO_2–1, CO_2–2, and CO_2–3 in the text] in $Fe_2(BDP)_3$ at 25 °C and CO_2 loadings in the range 1-8 bar. Depicted with fragmented lines the CH–O *host-guest* (green) and O–O *guest-guest* (black) interactions. For the sake of clarity, only host-guest interactions shorter than 2.7 Å have been depicted.
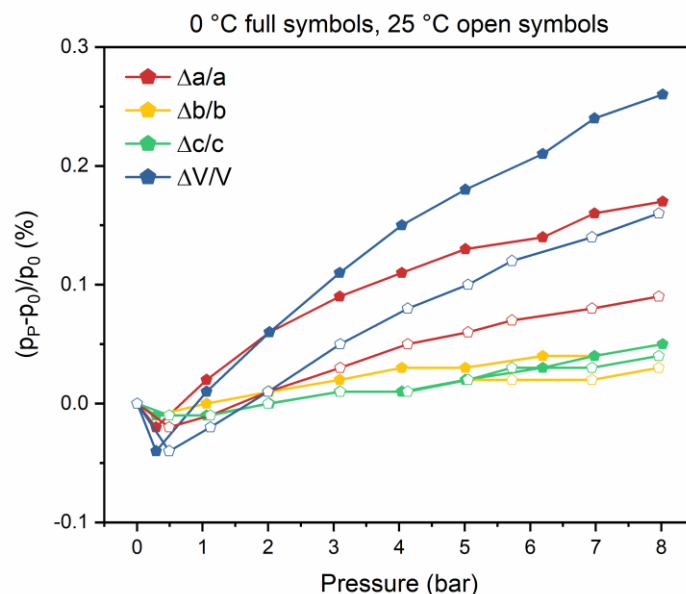
Figure 6.17 – Relative percentage variation of the unit cell parameters (p) of $Fe_2(BDP)_3$ as a function of the pressure of CO_2 at 0 °C and 25 °C (full and open symbols, respectively), as obtained by the Rietveld refinements on the HR-PXRD data. The values of the parameters at each pressure (p_p) have been normalized with respect to those shown prior to CO_2 dosing (p_0). Colour code: *a*-axis, red; *b*-axis, yellow; *c*-axis, green; *V*, blue. The lines have been added to guide the eye.
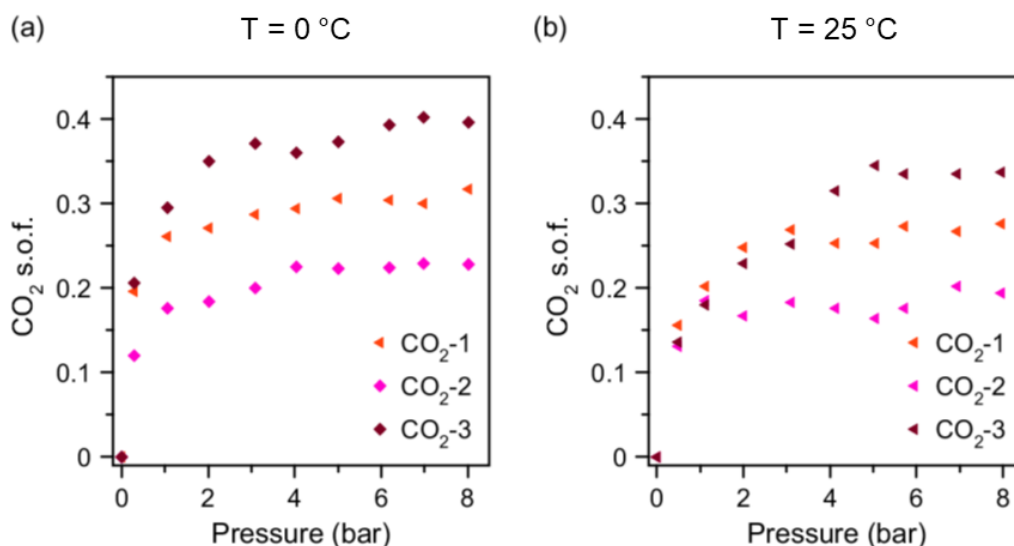
Figure 6.18 - Variation of the occupancy (s.o.f.) of the three crystallographically independent CO_2 molecules for the gas loading at 0 °C (a) and 25 °C (b), as obtained from the Rietveld refinements on the HR-PXRD data of $Fe_2(BDP)_3$.

Table 6.6 - Crystallographic data and figures of merit for the whole powder pattern refinements performed on the HR-PXRD data of $Fe_2(BDP)_3$ acquired at 0 °C for different CO_2 loadings.

p (bar)	a (Å)	b (Å)	c (Å)	V (Å³)	R_{wp} (%)	R_p (%)
0.00	7.0771(1)	26.4701(3)	45.3407(5)	8493.7(2)	5.9	4.4
0.29	7.0760(1)	26.4673(3)	45.3350(5)	8490.4(2)	5.6	4.2
1.06	7.0787(1)	26.4693(3)	45.3367(5)	8494.7(2)	5.5	4.2
2.02	7.0813(1)	26.4719(3)	45.3411(5)	8499.4(2)	5.5	4.1
3.09	7.0833(1)	26.4743(3)	45.3445(5)	8503.2(2)	5.5	4.1
4.04	7.0848(1)	26.4764(3)	45.3482(5)	8506.4(2)	5.4	4.1
5.01	7.0859(1)	26.4776(3)	45.3514(5)	8508.7(2)	5.5	4.1
6.19	7.0873(1)	26.4797(3)	45.3551(5)	8511.8(2)	5.5	4.1
6.98	7.0881(1)	26.4809(3)	45.3575(5)	8513.5(2)	5.3	4.1
8.02	7.0889(1)	26.4821(3)	45.3620(5)	8515.8(2)	5.3	4.0

Table 6.7 - Crystallographic data and figures of merit for the Rietveld refinements carried out on the HR-PXRD data of $Fe_2(BDP)_3$ acquired at 0 °C and different CO_2 loadings.

p (bar)	a (Å)	b (Å)	c (Å)	V (Å³)	R_{wp} (%)	R_p (%)
0.00	7.0787(1)	26.4744(1)	45.3519(3)	8499.0(1)	5.1	3.9
0.29	7.0775(1)	26.4716(1)	45.3453(3)	8495.5(1)	5.0	3.8
1.06	7.0802(1)	26.4739(1)	45.3467(3)	8499.8(1)	4.9	3.8
2.02	7.0828(1)	26.4765(1)	45.3508(3)	8504.5(1)	4.9	3.7
3.09	7.0848(1)	26.4790(1)	45.3542(3)	8508.4(1)	4.9	3.7
4.04	7.0863(1)	26.4812(1)	45.3586(3)	8511.7(1)	4.8	3.6
5.01	7.0875(1)	26.4828(2)	45.3623(3)	8514.4(1)	4.9	3.7
6.19	7.0888(1)	26.4846(2)	45.3651(3)	8517.1(1)	4.9	3.7
6.98	7.0896(1)	26.4860(2)	45.3683(3)	8519.0(1)	4.8	3.7
8.02	7.0904(1)	26.4869(2)	45.3725(3)	8521.1(1)	4.9	3.7

Table 6.8 - Crystallographic data and figures of merit for the whole powder pattern refinements performed on the HR-PXRD data of $Fe_2(BDP)_3$ acquired at 25 °C and different CO_2 loadings.

p (bar)	a (Å)	b (Å)	c (Å)	V (Å³)	R_{wp} (%)	R_p (%)
0.00	7.0757(1)	26.4690(3)	45.3409(5)	8491.7(1)	5.9	4.4
0.49	7.0746(1)	26.4667(3)	45.3372(5)	8489.0(2)	5.8	4.3
1.12	7.0751(1)	26.4677(3)	45.3403(5)	8490.5(2)	5.6	4.2
2.00	7.0766(1)	26.4698(3)	45.3433(5)	8493.5(2)	5.7	4.2
3.10	7.0782(1)	26.4717(3)	45.3475(5)	8496.8(2)	5.6	4.2
4.13	7.0794(1)	26.4730(3)	45.3499(5)	8499.1(2)	5.6	4.2
5.05	7.0802(1)	26.4744(3)	45.3527(5)	8501.1(2)	5.6	4.2
5.72	7.0809(1)	26.4753(3)	45.3560(5)	8502.9(2)	5.6	4.2
6.94	7.0818(1)	26.4767(3)	45.3596(5)	8505.1(2)	5.5	4.1
7.96	7.0825(1)	26.4777(3)	45.3623(5)	8506.7(2)	5.5	4.2

Table 6.9 - Crystallographic data and figures of merit for the Rietveld refinements carried out on the HR-PXRD data of $Fe_2(BDP)_3$ acquired at 25 °C for different CO_2 loadings.

p (bar)	a (Å)	b (Å)	c (Å)	V (Å³)	R_{wp} (%)	R_p (%)
0.00	7.0777(1)	26.4752(2)	45.3553(5)	8498.8(1)	5.1	3.9
0.49	7.0765(1)	26.4721(1)	45.3492(3)	8495.3(1)	4.9	3.7
1.12	7.0771(1)	26.4734(1)	45.3526(3)	8497.0(1)	4.8	3.7
2.00	7.0785(1)	26.4749(1)	45.3547(3)	8499.6(1)	4.8	3.7
3.10	7.0800(1)	26.4768(2)	45.3585(3)	8502.8(1)	4.9	3.8
4.13	7.0812(1)	26.4782(2)	45.3616(3)	8505.2(1)	4.8	3.7
5.05	7.0821(1)	26.4800(2)	45.3648(3)	8507.5(1)	4.8	3.7
5.72	7.0827(1)	26.4807(1)	45.3672(3)	8508.9(1)	4.8	3.7
6.94	7.0837(1)	26.4819(2)	45.3708(3)	8511.1(1)	4.7	3.6
7.96	7.0843(1)	26.4829(2)	45.3732(3)	8512.6(1)	4.8	3.7

Table 6.10 – Parameters of the central phenyl ring (X#) orientational disorder of the BDP^{2-} ligand in Fe$_2$(BDP)$_3$, including the site occupation factor, orientation *vs*. the pentatomic rings and weight, as obtained by the Rietveld refinements carried out on the HR-PXRD data acquired at 0 °C and different CO$_2$ loadings.

Disorder for ¼ ligand						
p (bar)	s.o.f. X1	tors1 (°)	X1[a] (%)	s.o.f. X2	tors2 (°)	X2[a] (%)
0.00	0.402	174.1	80.3	0.099	65.4	19.7
0.29	0.193	331.2	38.5	0.308	0.7	61.5
1.06	0.222	335.8	44.5	0.278	0.4	55.5
2.02	0.266	337.6	53.3	0.234	-0.7	46.7
3.09	0.302	339.4	60.3	0.198	6.4	39.7
4.04	0.270	339.4	54.1	0.230	2.9	45.9
5.01	0.264	340.0	52.7	0.236	-1.2	47.3
6.19	0.251	338.6	50.2	0.249	2.7	49.8
6.98	0.277	336.6	55.3	0.224	10.9	44.7
8.02	0.274	336.6	54.7	0.226	10.9	45.3

Disorder for ½ ligand						
p (bar)	s.o.f. X3	tors3 (°)	X3[b] (%)	s.o.f. X4 (%)	tors4 (°)	X4[b] (%)
0.00	0.556	154.1	55.6	0.445	27.6	44.5
0.29	0.562	152.3	56.2	0.438	25.0	43.8
1.06	0.596	153.6	59.6	0.404	26.4	40.4
2.02	0.608	154.2	60.8	0.392	27.2	39.2
3.09	0.603	154.3	60.2	0.398	26.6	39.8
4.04	0.597	153.3	59.7	0.403	25.5	40.3
5.01	0.567	152.5	56.7	0.434	23.3	43.3
6.19	0.590	153.0	59.0	0.410	23.5	41.0
6.98	0.582	152.6	58.2	0.418	25.1	41.8
8.02	0.590	152.6	59.0	0.410	25.1	41.0

[a]Weight percentage of ring X1 with respect to ring X2 in the ¼ disordered ligand (calculated as the ratio of s.o.f. X1 and s.o.f. X2). [b]Weight percentage of ring X3 with respect to ring X4 in the ½ disordered ligand (calculated as the ratio of s.o.f. X3 and s.o.f. X4).

Table 6.11 - Parameters of the central phenyl ring (X#) orientational disorder of the BDP^{2-} ligand in Fe$_2$(BDP)$_3$, including the site occupation factor, orientation *vs*. the pentatomic rings and weight, as obtained by the Rietveld refinements carried out on the HR-PXRD data acquired at 25 °C and different CO$_2$ loadings.

Disorder for ¼ ligand						
p (bar)	s.o.f. X1	tors1 (°)	X1[a] (%)	s.o.f. X2	tors2 (°)	X2[a] (%)
0.00	0.486	166.8	97.2	0.014	281.9	2.8
0.49	0.338	340.2	67.5	0.163	11.4	32.5
1.12	0.304	338.9	60.9	0.196	11.9	39.1
2.00	0.328	339.2	65.6	0.172	11.6	34.4
3.10	0.344	340.9	68.7	0.156	12.2	31.3
4.13	0.318	340.9	63.6	0.182	12.2	36.4
5.05	0.342	340.9	68.4	0.158	11.5	31.6
5.72	0.340	340.9	68.0	0.160	11.3	32.0
6.94	0.326	340.9	65.2	0.174	11.3	34.8
7.96	0.337	341.0	67.4	0.163	10.9	32.6
Disorder for ½ ligand						
p (bar)	s.o.f. X3	tors3 (°)	X3[b] (%)	s.o.f. X4	tors4 (°)	X4[b] (%)
0.00	0.535	150.8	53.5	0.465	27.7	46.5
0.49	0.541	152.5	54.1	0.459	26.1	45.9
1.12	0.548	152.8	54.8	0.452	26.6	45.2
2.00	0.562	153.2	56.2	0.438	26.0	43.8
3.10	0.565	156.0	56.5	0.435	25.3	43.5
4.13	0.565	154.5	56.5	0.435	26.3	43.5
5.05	0.594	156.2	59.4	0.406	29.6	40.6
5.72	0.556	152.6	55.6	0.444	25.2	44.4
6.94	0.558	152.5	55.8	0.442	26.5	44.2
7.96	0.587	154.6	58.7	0.413	29.6	41.3

[a]Weight percentage of ring X1 with respect to ring X2 in the ¼ disordered ligand (calculated as the ratio of s.o.f. X1 and s.o.f. X2). [b]Weight percentage of ring X3 with respect to ring X4 in the disordered ½ ligand (calculated as the ratio of s.o.f. X3 and s.o.f. X4).

Table 6.12 - Occupancies of the independent CO_2 molecules and quantity of adsorbed CO_2, as obtained from the Rietveld refinements carried out on the HR-PXRD data of $Fe_2(BPD)_3$ acquired at 0 °C and different CO_2 loadings.

p (bar)	Independent CO_2 molecules			CO_2 molecules adsorption		
	s.o.f. CO_2-1	s.o.f. CO_2-2	s.o.f. CO_2-3	mol(CO_2) per f.u.	mmol/g	wt (%)
0.00	0.000	0.000	0.000	0.00	0.00	0.00
0.29	0.196	0.120	0.206	2.09	2.52	11.10
1.06	0.261	0.176	0.295	2.93	3.38	14.89
2.02	0.271	0.184	0.350	3.22	3.67	16.14
3.09	0.287	0.200	0.371	3.43	3.87	17.03
4.04	0.294	0.225	0.360	3.52	3.95	17.38
5.01	0.306	0.223	0.373	3.61	4.03	17.73
6.19	0.304	0.224	0.393	3.68	4.10	18.04
6.98	0.300	0.229	0.402	3.72	4.13	18.19
8.02	0.317	0.228	0.396	3.77	4.18	18.37

Table 6.13 - Occupancies of the independent CO_2 molecules and quantity of CO_2 adsorbed, as retrieved from the Rietveld refinements carried out on the HR-PXRD data of $Fe_2(BPD)_3$ acquired at 25 °C and different CO_2 loadings.

p (bar)	Independent CO_2 molecules			CO_2 molecules adsorption		
	s.o.f. CO_2-1	s.o.f. CO_2-2	s.o.f. CO_2-3	mol(CO_2) per f.u.	mmol/g	wt (%)
0.00	0.000	0.000	0.000	0.00	0.00	0.00
0.49	0.156	0.131	0.136	1.69	2.09	9.18
1.12	0.202	0.185	0.180	2.27	2.71	11.93
2.00	0.248	0.167	0.229	2.58	3.03	13.35
3.10	0.269	0.183	0.252	2.81	3.27	14.40
4.13	0.253	0.176	0.315	2.98	3.43	15.10
5.05	0.253	0.164	0.345	3.05	3.50	15.42
5.72	0.273	0.176	0.335	3.13	3.59	15.78
6.94	0.267	0.202	0.335	3.22	3.66	16.12
7.96	0.276	0.194	0.337	3.23	3.68	16.19

Table 6.14 - Host-guest interactions of the three independent CO_2 molecules (CO_2-1, CO_2-2, and CO_2-3 in the text) in $Fe_2(BDP)_3$ at 0 °C and different CO_2 loadings, as obtained from the Rietveld refinements on the HR-PXRD data.

CO_2-#	guest-host contacts	1 bar	2 bar	3 bar	4 bar	5 bar	6 bar	7 bar	8 bar
CO_2-1	O1–H10x	2.19	2.25	2.21	2.65	2.25	2.29	2.21	2.19
	O1–H2	2.39	2.46	2.47	2.48	2.51	2.37	2.44	2.41
	O1–H2x	2.62	2.59	\	2.68	2.64	2.68	2.65	2.65
	O2–H4x	2.48	2.44	2.45	2.53	2.58	2.56	2.55	2.52
CO_2-2	O1–H7x	2.37	2.24	2.40	2.36	2.32	2.37	2.33	2.36
	O1–H2x	\	2.68	\	2.63	\	\	2.67	\
	O2–H7x	2.60	2.43	2.35	2.48	2.63	2.50	2.51	2.54
	O2–H10x	2.55	2.62	2.59	2.65	\	2.70	\	\
	O2–H4x	1.62	1.69	1.67	1.73	1.68	1.66	1.72	1.68
CO_2-3	O1–H2a	2.01	2.06	2.09	2.07	2.07	1.93	1.95	1.96
	O1–H2x	\	2.53	2.54	2.51	2.48	2.44	2.40	2.43
	O2–H2	1.99	1.90	1.88	1.87	1.91	1.90	1.77	1.82

Table 6.15 - Host-guest interactions of the three independent CO_2 molecules (CO_2-1, CO_2-2, and CO_2-3) in $Fe_2(BDP)_3$ at 25 °C and different CO_2 loadings, as obtained from the Rietveld refinements on the HR-PXRD data.

CO_2-#	guest-host contacts	1 bar	2 bar	3 bar	4 bar	5 bar	6 bar	7 bar	8 bar
CO_2-1	O1–H10x	2.09	2.10	2.10	2.22	2.30	2.29	2.26	2.16
	O1–H2	2.13	\	\	2.47	\	2.50	2.58	2.56
	O2–H4x	2.33	2.24	2.22	\	2.50	\	2.59	2.51
CO_2-2	O1–H2x	1.74	2.24	2.33	\	\	\	2.65	2.90
	O1–H7x	2.21	2.45	2.48	2.32	2.26	\	2.25	2.46
	O2–H4x	2.39	2.33	2.35	1.82	1.62	1.71	1.77	1.65
	O2–H7x	\	2.34	2.40	2.39	\	\	2.52	2.48
CO_2-3	O1–H2a	2.47	2.41	2.42	2.19	2.10	2.06	2.12	2.14
	O1–H2x	\	\	\	\	\	2.46	2.46	2.50
	O2–H2	2.39	2.03	2.00	2.06	1.99	1.99	1.95	1.93

Fe$_2$(BDP-NH$_2$)$_3$

The sample was investigated at temperatures T = 0 and 25 °C, while varying the CO$_2$ loading in the pressure range of 0 to 25-26 bar for each temperature. First, the space group and unit cell parameters were checked and refined through a whole powder pattern refinement carried out with the Le Bail method, starting from the reported unit cell parameters.[194] The Rietveld refinements are currently in progress.
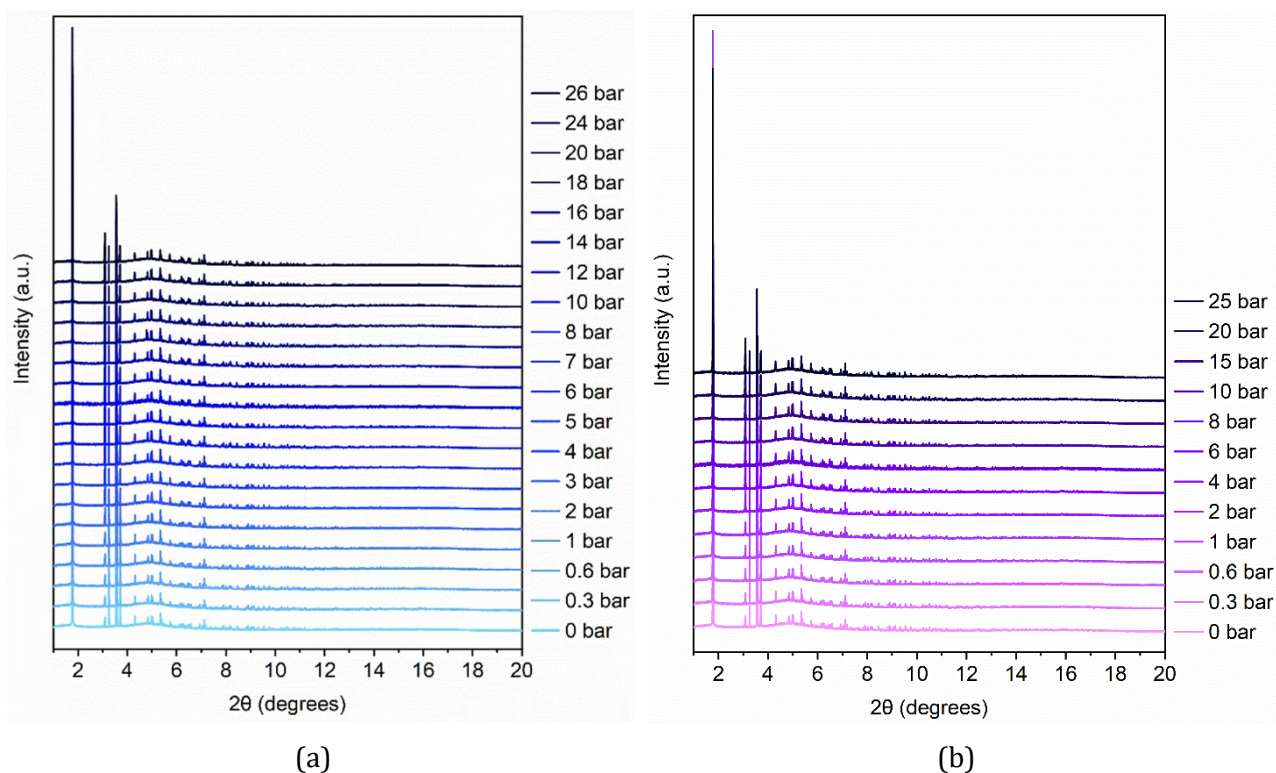
Figure 6.19 - Comparison of the low-to-medium angle portion of the HR-PXRD patterns of Fe$_2$(BDP-NH$_2$)$_3$ obtained at (a) 0 °C and (b) 25 °C, at 0 bar of CO$_2$ and all the CO$_2$ loadings probed at each temperature.
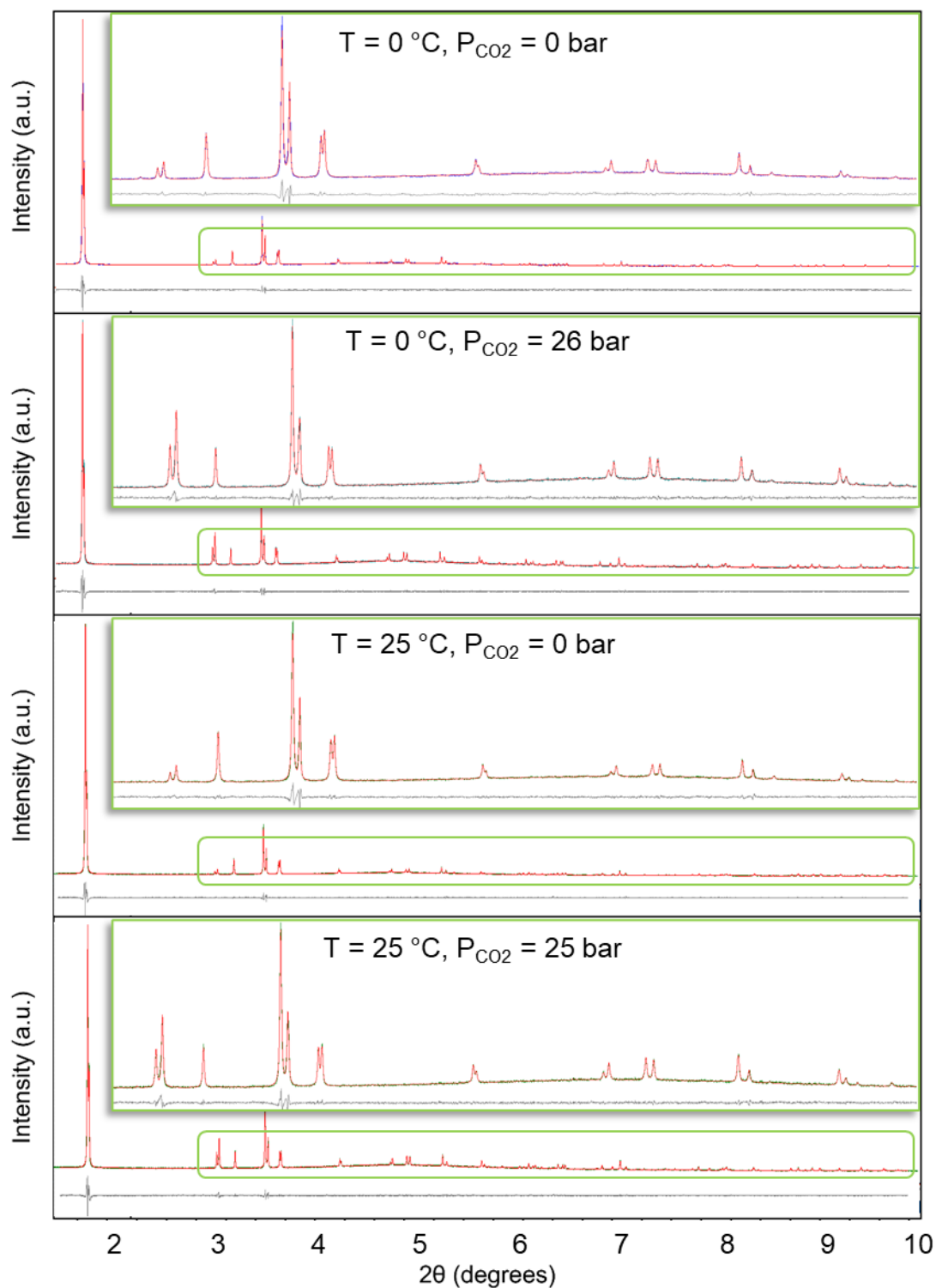
Figure 6.20 – Graphical representation of the whole powder pattern refinements carried out with the Le Bail method on the HR-PXRD data of $Fe_2(BDP-NH_2)_3$. From the top to the bottom as representative example of data treatment: T = 0 °C and p_{CO2} = 0 bar; T = 0 °C p_{CO2} = 26 bar, T = 25 °C and p_{CO2} = 0 bar; T = 25 °C and p_{CO2} = 26 bar, showing experimental, calculated and difference traces (blue, red and grey, respectively). The positions of the Bragg reflections are indicated by blue ticks. For 2θ higher than 2.9° the traces were magnified for clarity.

Table 6.16 - Crystallographic data and figures of merit for the whole powder pattern refinements performed on the HR-PXRD data of $Fe_2(BDP-NH_2)_3$ acquired at 0 °C for different CO_2 loadings.

p (bar)	a (Å)	b (Å)	c (Å)	V (Å³)	R_{wp} (%)	R_p (%)
0	7.0772(7)	26.4556(8)	45.3424(5)	8489.6(5)	5.9	4.2
0.3	7.0757(4)	26.4544(1)	45.3423(1)	8487.3(8)	6.3	4.5
0.6	7.0749(8)	26.4545(4)	45.3412(7)	8486.3(1)	6.3	4.5
1	7.0737(4)	26.4536(2)	45.3423(5)	8484.7(3)	5.9	4.3
2	7.0733(9)	26.4532(2)	45.3405(9)	8483.8(5)	5.8	4.2
3	7.0740(1)	26.4532(8)	45.3422(8)	8484.9(3)	5.8	4.2
4	7.0880(4)	26.4614(1)	45.3556(5)	8506.8(7)	5.4	4.0
5	7.0914(3)	26.4634(6)	45.3597(5)	8512.3(8)	5.2	3.8
6	7.0931(6)	26.4649(8)	45.3592(3)	8514.8(5)	5.4	3.8
7	7.0946(7)	26.4654(8)	45.3606(9)	8517.1(1)	5.6	3.8
8	7.0959(9)	26.4669(7)	45.3620(1)	8519.4(1)	5.3	3.9
10	7.0979(3)	26.4682(1)	45.3646(7)	8522.6(3)	6.0	3.9
12	7.0994(4)	26.4695(5)	45.3678(8)	8525.4(8)	5.2	3.8
14	7.1009(6)	26.4702(6)	45.3683(9)	8527.6(4)	5.1	3.7
16	7.1026(7)	26.4721(2)	45.3715(4)	8530.8(7)	5.1	3.5
18	7.1038(7)	26.4731(3)	45.3738(1)	8533.0(8)	5.3	3.8
20	7.1051(6)	26.4750(2)	45.3771(2)	8535.8(5)	5.3	3.9
24	7.1073(4)	26.4772(1)	45.3799(7)	8539.7(2)	5.2	3.7
26	7.1081(8)	26.4783(1)	45.3821(1)	8541.4(8)	4.8	3.4

Table 6.17 – Crystallographic data and figures of merit for the whole powder pattern refinements performed on the HR-PXRD data of $Fe_2(BDP-NH_2)_3$ acquired at 25 °C for different CO_2 loadings.

| p (bar)	a (Å)	b (Å)	c (Å)	V (Å^3)	R_{wp} (%)	R_p (%)
0	7.0779(1)	26.4563(1)	45.3430(9)	8490.7(1)	6.0	4.3
0.3	7.0761(6)	26.4548(2)	45.3409(8)	8487.7(7)	6.1	4.4
0.6	7.0752(3)	26.4549(7)	45.3419(1)	8486.8(7)	6.0	4.3
1	7.0743(1)	26.4538(3)	45.3399(2)	8485.0(2)	5.9	4.2
2	7.0738(1)	26.4535(6)	45.3397(3)	8484.2(9)	6.0	4.3
4	7.0757(3)	26.4549(9)	45.3427(7)	8487.6(4)	5.7	4.1
6	7.0834(5)	26.4582(7)	45.3500(6)	8499.3(1)	5.5	4.0
8	7.0877(5)	26.4607(8)	45.3543(9)	8506.1(0)	8.4	6.5
10	7.0897(1)	26.4637(9)	45.3575(1)	8509.9(9)	5.4	3.9
15	7.0926(9)	26.4660(5)	45.3612(8)	8515.0(1)	5.3	3.9
20	7.0950(5)	26.4683(7)	45.3656(9)	8519.4(2)	5.4	3.9
25	7.0967(5)	26.4693(3)	45.3672(3)	8522.0(5)	5.4	3.9
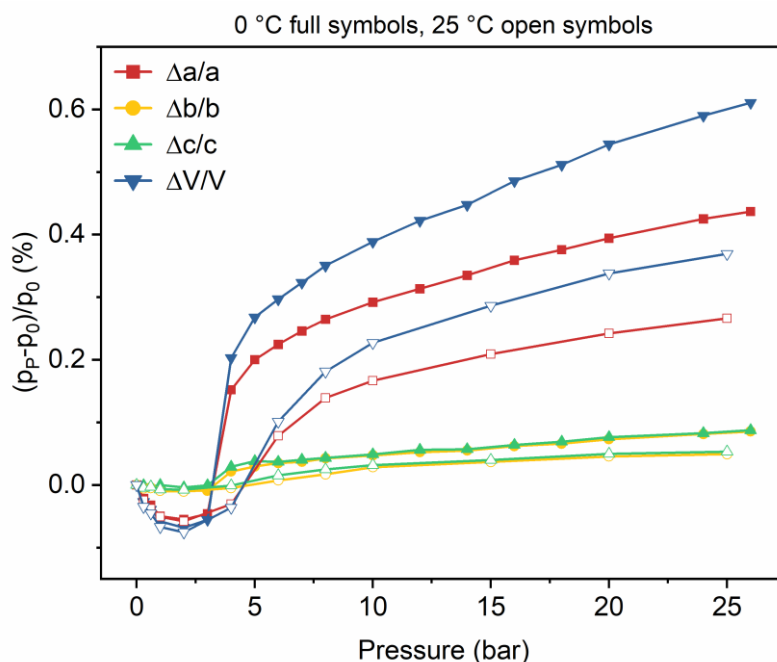
Figure 6.21 – Relative percentage variation of the unit cell parameters (p) of $Fe_2(BDP-NH_2)_3$ as a function of the pressure of CO_2 at 0 °C and 25 °C (full and open symbols, respectively), as obtained by the Le Bail refinements on the HR-PXRD data. Colour code: a-axis, red; b-axis, yellow; c-axis, green; V, blue. The lines have been added to guide the eye.

$Fe_2(BDP)_{1.5}(BDP-NH_2)_{1.5}$
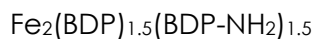
One temperature was investigated, namely T = 0 °C, while varying the CO_2 loading in the pressure range from 0 to 26 bar. First, the space group and unit cell parameters were checked and refined through a whole powder pattern refinement carried out with the Le Bail method, starting from the reported unit cell parameters.[194] The Rietveld refinements are currently being underway.
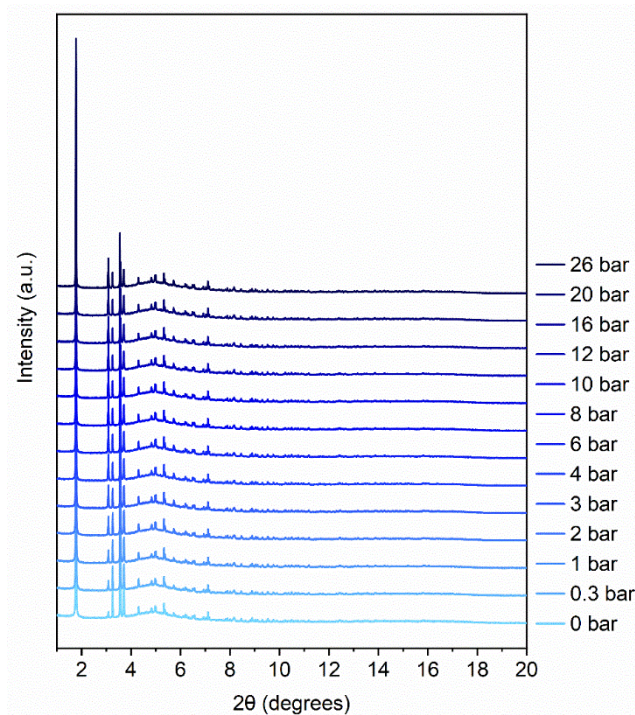
Figure 6.22 - Comparison of the low-to-medium angle portion of the HR-PXRD patterns of $Fe_2(BDP)_{1.5}(BDP-NH_2)_{1.5}$ obtained at 0 °C at 0 bar of CO_2 for all the CO_2 loadings.
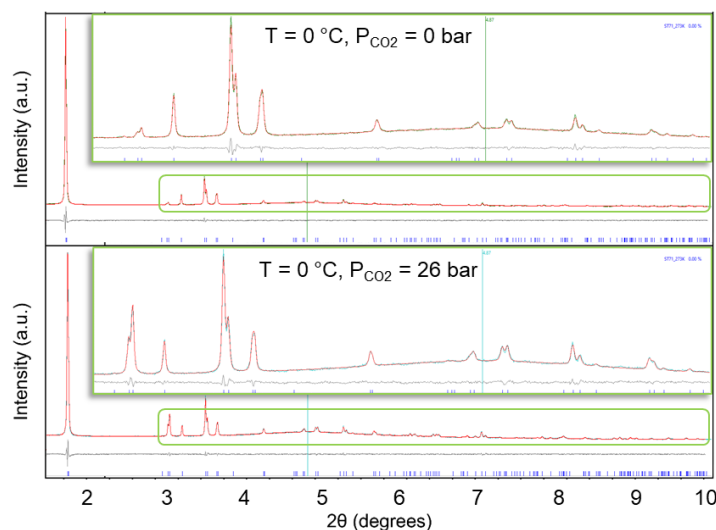
Figure 6.23 – Graphical representation of the whole powder pattern refinements carried out with the Le Bail method on the HR-PXRD data of $Fe_2(BDP)_{1.5}(BDP-NH_2)_{1.5}$. From the top to the bottom as representative example of data treatment: T = 0 °C and p_{CO2} = 0 bar; T = 0 °C p_{CO2} = 26 bar, showing experimental, calculated and difference traces (blue, red and grey, respectively). The positions of the Bragg reflections are indicated by blue ticks. For 2θ higher than 2.9° the traces were magnified for clarity.

Table 6.18 - Crystallographic data and figures of merit for the whole powder pattern refinements performed on the HR-PXRD data of $Fe_2(BDP)_{1.5}(BDP-NH_2)_{1.5}$ acquired at 0 °C for different CO_2 loadings.

| p (bar)	a (Å)	b (Å)	c (Å)	V (Å^3)	R_{wp} (%)	R_p (%)
0	7.0821(2)	26.4553(4)	45.4118(6)	8508.2(5)	3.8	2.9
0.3	7.0799(4)	26.4514(5)	45.4098(2)	8504.1(1)	3.7	2.9
0.6	7.0806(4)	26.4522(3)	45.4120(2)	8505.6(1)	3.7	2.8
1	7.0783(9)	26.4477(5)	45.4050(5)	8500.1(6)	3.7	2.9
2	7.0758(1)	26.4489(7)	45.4057(4)	8497.5(7)	3.5	2.7
3	7.0803(7)	26.4527(3)	45.4109(3)	8505.2(4)	3.6	2.8
4	7.0845(1)	26.4554(1)	45.4147(8)	8511.7(9)	3.4	2.7
6	7.0882(7)	26.4587(2)	45.4181(1)	8518.0(0)	3.4	2.7
8	7.0905(1)	26.4605(1)	45.4229(6)	8522.1(8)	3.4	2.6
10	7.0923(3)	26.4618(9)	45.4238(7)	8524.9(9)	3.4	2.6
12	7.0943(8)	26.4648(7)	45.4292(4)	8529.4(2)	3.3	2.6
16	7.0964(1)	26.4655(3)	45.4304(9)	8532.3(1)	3.6	2.8
20	7.0977(2)	26.4669(6)	45.4345(8)	8535.1(1)	3.3	2.5
26	7.0996(3)	26.4687(5)	45.4396(1)	8538.9(3)	3.3	2.5
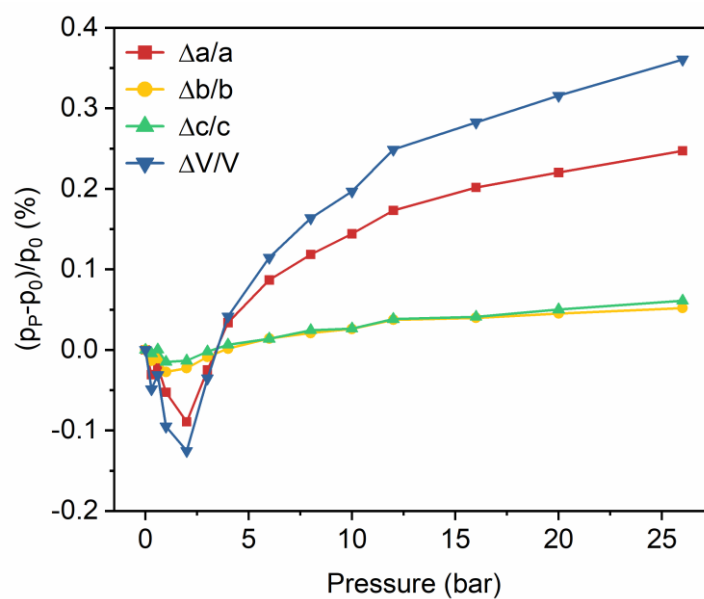
Figure 6.24 – Relative percentage variation of the unit cell parameters (p) of $Fe_2(BDP)_{1.5}(BDP-NH_2)_{1.5}$ as a function of the pressure of CO_2 at 0 °C, as obtained by the Le Bail refinements on the HR-PXRD data. Colour code: *a*-axis, red; *b*-axis, yellow; *c*-axis, green; *V*, blue. The lines have been added to guide the eye.

6.3.9 Theoretical calculations

Materials Studio 6.0[223] was used to simulate the CO_2 molecules positions in the framework. More specifically, the Adsorption Locator module in MS6.0 was employed to construct the simulated systems after lowering the crystal symmetry to $P1$ and to perform the Monte-Carlo (MC) simulation. A double cell along the a-axis was used during the simulation. Two different $Fe_2(BDP)_3$ structural conformations which were taken from HR-XRPD measurements were considered: a) the structural model of the activated material at 0 °C and 0 bar of CO_2, and b) that obtained from Rietveld refinement at 0 °C and 1 bar of CO_2. The used forcefield was COMPASS, the charge was forcefield assigned and the summation methods were group- and atom-based. The simulations were carried out inserting an increasing number of CO_2 molecules until reaching the theoretical structure saturation. Monte-Carlo simulation yielded several conformations of CO_2 molecules in $Fe_2(BDP)_3$. The results of the energetically most stable conformations are presented in this work. Two CO_2 adsorption isotherm simulations at 0 °C and 25 °C were carried out using the Sorption module, enabling a direct comparison with the observations. The same number of unit cells and force fields quoted above were taken into consideration.
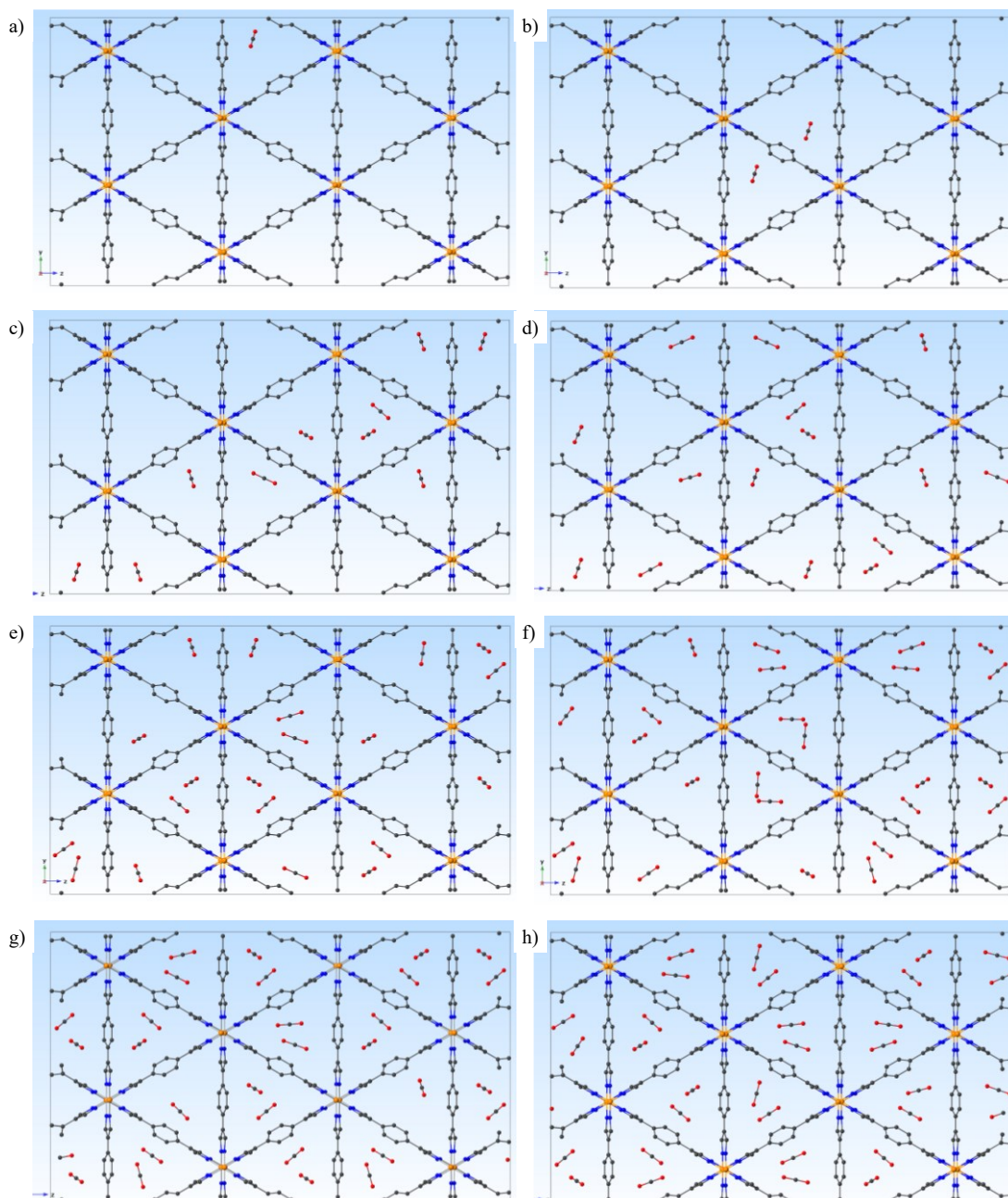
Figure 6.25 - Graphical representation of the simulated adsorption states in $Fe_2(BDP)_3$ loading an increasing number of CO_2 molecules, namely: a) 1 CO_2 molecule, b) 2 CO_2 molecules, c) 10 CO_2 molecules, d) 15 CO_2 molecules, e) 20 CO_2 molecules, f) 25 CO_2 molecules, g) 30 CO_2 molecules and h) 32 CO_2 molecules. The $Fe_2(BDP)_3$ crystal structure, obtained from the Rietveld refinement on the HR-PXRD data at 0 bar of CO_2 and 0 °C, is viewed along the [100] crystallographic direction; horizontal axis b, vertical axis a. The hydrogen atoms are omitted for clarity. Colour code: carbon, grey; iron, orange; nitrogen, blue; oxygen, red.
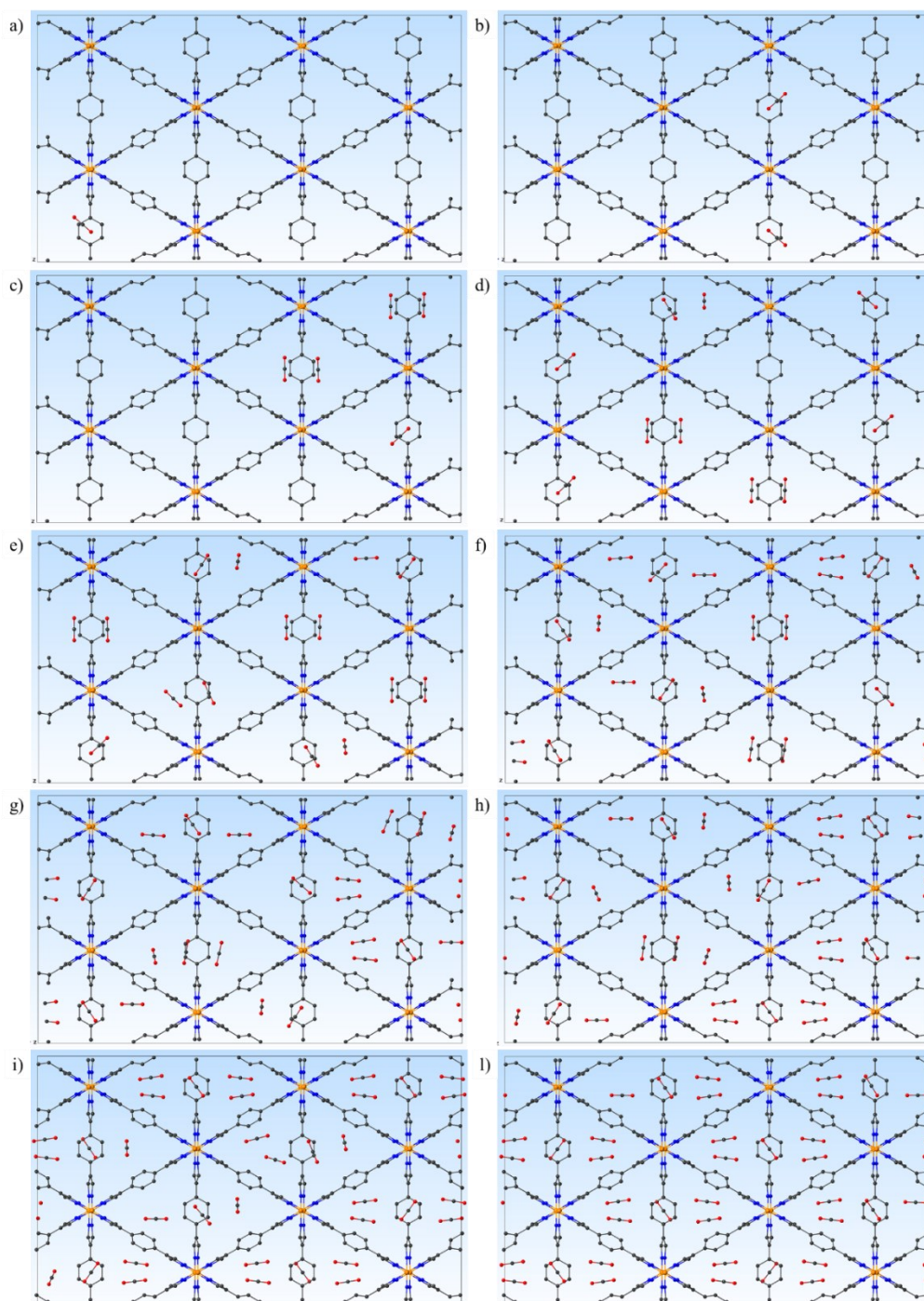
Figure 6.26 - Graphical representation of the simulated adsorption states in $Fe_2(BDP)_3$ loading an increasing number of CO_2 molecules, namely: a) 1 CO_2 molecule, b) 2 CO_2 molecules, c) 5 CO_2 molecules, d) 10 CO_2 molecules, e) 15 CO_2 molecules, f) 20 CO_2 molecules, g) 25 CO_2 molecules, h) 30 CO_2 molecules, i) 35 CO_2 molecules and l) 37 CO_2 molecules. The $Fe_2(BDP)_3$ crystal structure, obtained from the Rietveld refinement on the HR-PXRD data at 1 bar of CO_2 and 25 °C, is viewed along the [100] crystallographic direction; horizontal axis b, vertical axis c. The hydrogen atoms are omitted for clarity. Colour code: carbon, grey; iron, orange; nitrogen, blue; oxygen, red.

6.4 Zn(BDP)$_{0.5}$(BDP-X)$_{0.5}$ (X = NH$_2$ or NO$_2$)

6.4.1 Synthetic Procedure

Zn(BDP)$_{0.5}$(BDP-X)$_{0.5}$ (x = NH$_2$ or NO$_2$) have been synthetized according to a synthetic procedure previously reported in the literature for Zn(BDP)$_3$ by Natalia M. Padial *et al.*[189] The samples have been then washed CH$_2$Cl$_2$ at r.T. and thermally activated at under vacuum for about 4 hours.

Anal. calc. for Zn(C$_{12}$N$_4$H$_8$)$_{0.5}$(C$_{12}$N$_5$O$_2$H$_7$)$_{0.5}$ [**Zn(BDP)$_{0.5}$(BDP-NO$_2$)$_{0.5}$**, FW = 294.50 g/mol]: C, 48.68; H, 2.55; N, 21.29 %. Found: C, 48.14; H, 4.91; N, 20.07 %.

Anal. calc. for Zn(C$_{12}$N$_4$H$_8$)$_{0.5}$(C$_{12}$N$_5$H$_9$)$_{0.5}$ [**Zn(BDP)$_{0.5}$(BDP-NH$_2$)$_{0.5}$**, FW = 281.11 g/mol]: C, 51.27; H, 3.05; N, 22.42 %. Found: C, 49.93; H, 5.26; N, 20.92 %.

6.4.2 XRPD Analysis
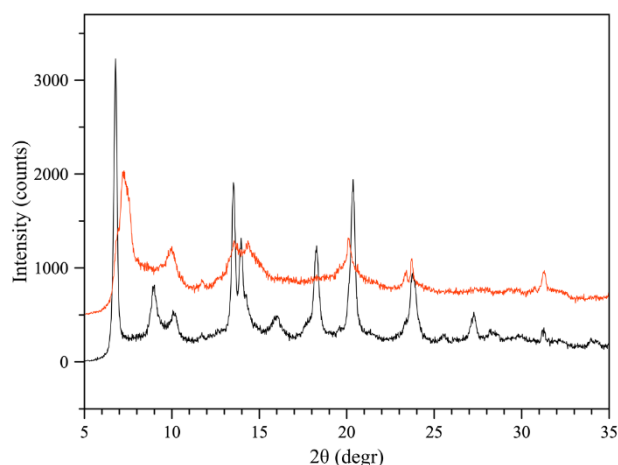
Figure 6.27 - XRPD patterns for Zn(BDP)$_{0.5}$(BDP-NO$_2$)$_{0.5}$.as synthesized (red) and re-solvated with DMF (black).
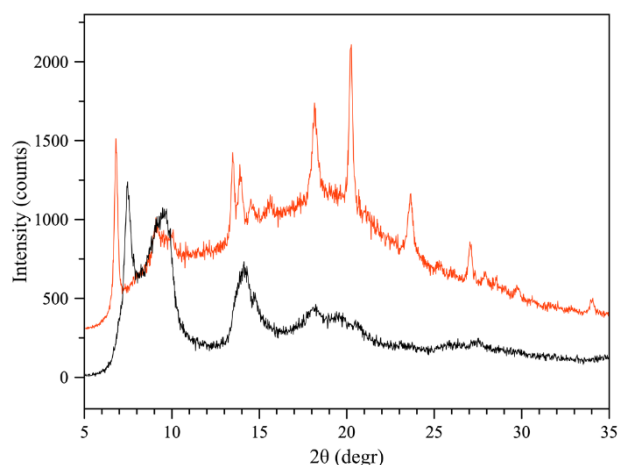
Figure 6.28 - XRPD patterns for Zn(BDP)$_{0.5}$(BDP-NH$_2$)$_{0.5}$.as synthesized (black) and re-solvated with DMF (red).

6.4.3 IR spectroscopy
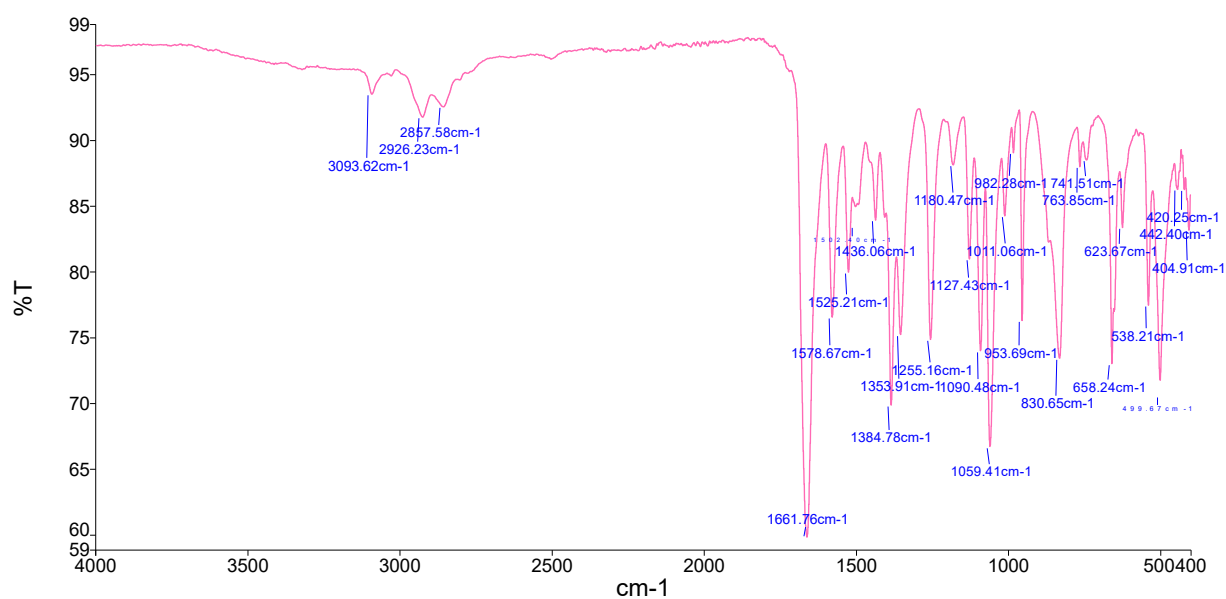
Figure 6.29 - ATR FT-IR spectra of as synthesised $Zn(BDP)_{0.5}(BDP-NO_2)_{0.5}$.. FT-IR (solid, ATR, cm^{-1}). Selected frequencies: $\nu_{C=N}$ 1384, 1353, $\nu_{N=O}$ 1525, $\nu_{C=C}$ 1578, ν_{N-H} 3093 cm^{-1}. The intense band at 1663 cm^{-1} corresponds to the C=O stretching vibration of DMF.
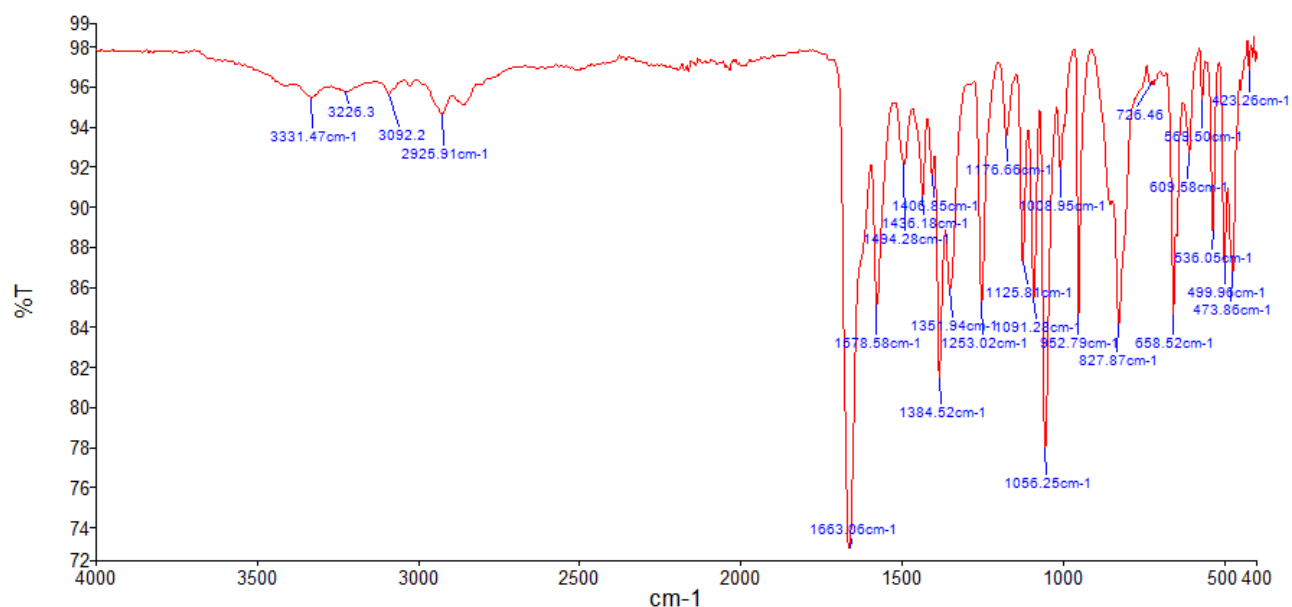
Figure 6.30 - ATR FT-IR spectra of as synthesised $Zn(BDP)_{0.5}(BDP-NH_2)_{0.5}$.. FT-IR (solid, ATR, cm^{-1}). Selected frequencies: $\nu_{C=N}$ 1384, 1353, $\nu_{N=O}$ 1525, $\nu_{C=C}$ 1578, $\nu_{N-H(pz)}$ 3092, $\nu_{N-H(NH2)}$ 3331 cm^{-1}. The intense band at 1663 cm^{-1} corresponds to the C=O stretching vibration of DMF, which partially hides the N–H bending vibration (scissoring) characteristic band generally found in the range 1620-1518 cm^{-1}.

6.5 Zn$_2$(fu-bdc)$_2$(dabco) and SiO$_2$@Zn$_2$(fu-bdc)$_2$(dabco)

6.5.1 Synthetic Procedure

MOFs synthesis. All pristine pillar-layered MOFs were prepared under the same reaction conditions as described in literature by S. Henke *et al.*[343,370] All composite materials NPs@MOFs were prepared via the *"bottle around the ship"* encapsulation method, where pre-formed fluorescent silica nanoparticles are put together with the MOF precursors to perform the same solvothermal reaction. Anal. calc. for Zn$_2$(C$_8$H$_4$O$_4$)$_2$(C$_6$H$_{12}$N$_2$) [**Zn$_2$(bdc)$_2$(dabco)**, FW = 517.17 g/mol]: C, 46.26; H, 3.53; N, 4.90%; found: C, 46.61; H, 5.40; N, 9.12%. Anal. calc. for Zn$_2$(C$_{10}$H$_8$O$_6$)$_2$(C$_6$H$_{12}$N$_2$) [**Zn$_2$(DM-bdc)$_2$(dabco)**, FW = 691.27 g/mol]: C, 45.18; H, 4.08; N, 4.05%; found: C, 40.84; H, 4.12; N, 3.30%. With SiO$_2$ embedded, found: C, 41.73; H, 3.90; N, 3.40%. With SiO$_2$COOH embedded, found: C, 41.88; H, 4.37; N, 3.89%. Anal. calc. for Zn$_2$(C$_{14}$H$_{16}$O$_8$)$_2$(C$_6$H$_{12}$N$_2$) [**Zn$_2$(BME-bdc)$_2$(dabco)**, FW = 867.48 g/mol]: C, 47.08; H, 5.11; N, 3.23%; found: C, 43.92; H, 4.86; N, 2.40%. With SiO$_2$ embedded, found: C, 44.15; H, 4.95; N, 3.01%. To note that the slightly different values obtained from elemental analysis are in line with not completely activated frameworks.

Activation. The *as* synthetised samples were thermally activated at high temperature under vacuum (150 °C for 2h, plus 80 °C overnight) and stored under argon in a glovebox.

Solvent re-infiltration. Re-infiltration was performed by immersing the dried MOF powder in a small quantity of DMF under stirring for some hours (2-4 h), or by simply dropping a small amount of solvent directly on the powder.

6.5.2 IR Spectroscopy
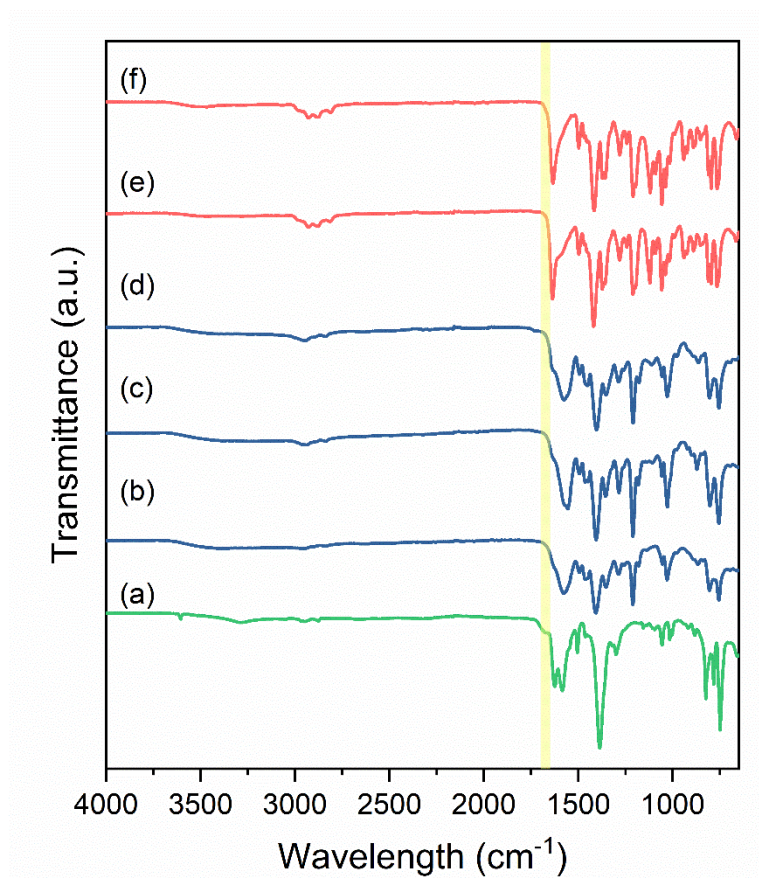
Figure 6.31 - ATR FT-IR spectra of $Zn_2(bdc)_2(dabco)$ (a), $Zn_2(DM\text{-}bdc)_2(dabco)$ (b), $SiO_2@Zn_2(DM\text{-}bdc)_2(dabco)$ (c), $SiO_2COOH@Zn_2(DM\text{-}bdc)_2(dabco)$ (d), $Zn_2(BME\text{-}bdc)_2(dabco)$ (e) and $SiO_2@Zn_2(BME\text{-}bdc)_2(dabco)$ (f). The spectra confirm the absence of DMF (C=O stretching vibration expected between 1650-1700 cm^{-1}, yellow band) and the presence of the three differently substituted organic linkers.

Table 6.19 - List of main IR signals divided into high, medium, and low ranges for the MOFs of the Zn$_2$(*fu*-bdc)$_2$(dabco) family presented in this work.

	Zn$_2$(bdc)$_2$(dabco)	Zn$_2$(DM-bdc)$_2$(dabco)	Zn$_2$(BME-bdc)$_2$(dabco)
High range *(4000-2500 cm^{-1})*	3607 (w)	2956 (w)	2981 (w)
	2969 (w)	2842 (w)	2928 (w)
	2952 (w)		2881 (w)
	2878 (w)		2817 (w)
Medium range *(2500-1150 cm^{-1})*	1581 (m)	1620 (s)	1638 (s)
	1510 (m)	1585 (s)	1499 (m)
	1464 (m)	1494 (m)	1467 (m)
	1387 (s)	1464 (m)	1419 (s)
	1321 (w)	1406 (s)	1374 (s)
	1305 (m)	1355 (s)	1359 (s)
		1286 (m)	1282 (m)
		1250 (w)	1244 (m)
		1212 (m)	1212 (s)
		1181 (w)	1197 (s)
Low range *(1150-600 cm^{-1})*	1157 (w)	1057 (m)	1122 (s)
	1094 (w)	1031 (m)	1094 (m)
	1057 (m)	867 (w)	1057 (s)
	1015 (m)	840 (w)	1039 (s)
	1000 (m)	806 (m)	1017 (s)
	918 (w)	755 (m)	995 (m)
	883 (w)		941 (m)
	825 (s)		924 (m)
	783 (s)		891 (m)
	749 (s)		883 (m)
	657 (m)		854 (w)
			812 (s)
			797 (s)
			766 (s)
			666 (w)

6.5.3 XRPD Analysis

(a)

(b)

(c)

(d)

(e)

(f)
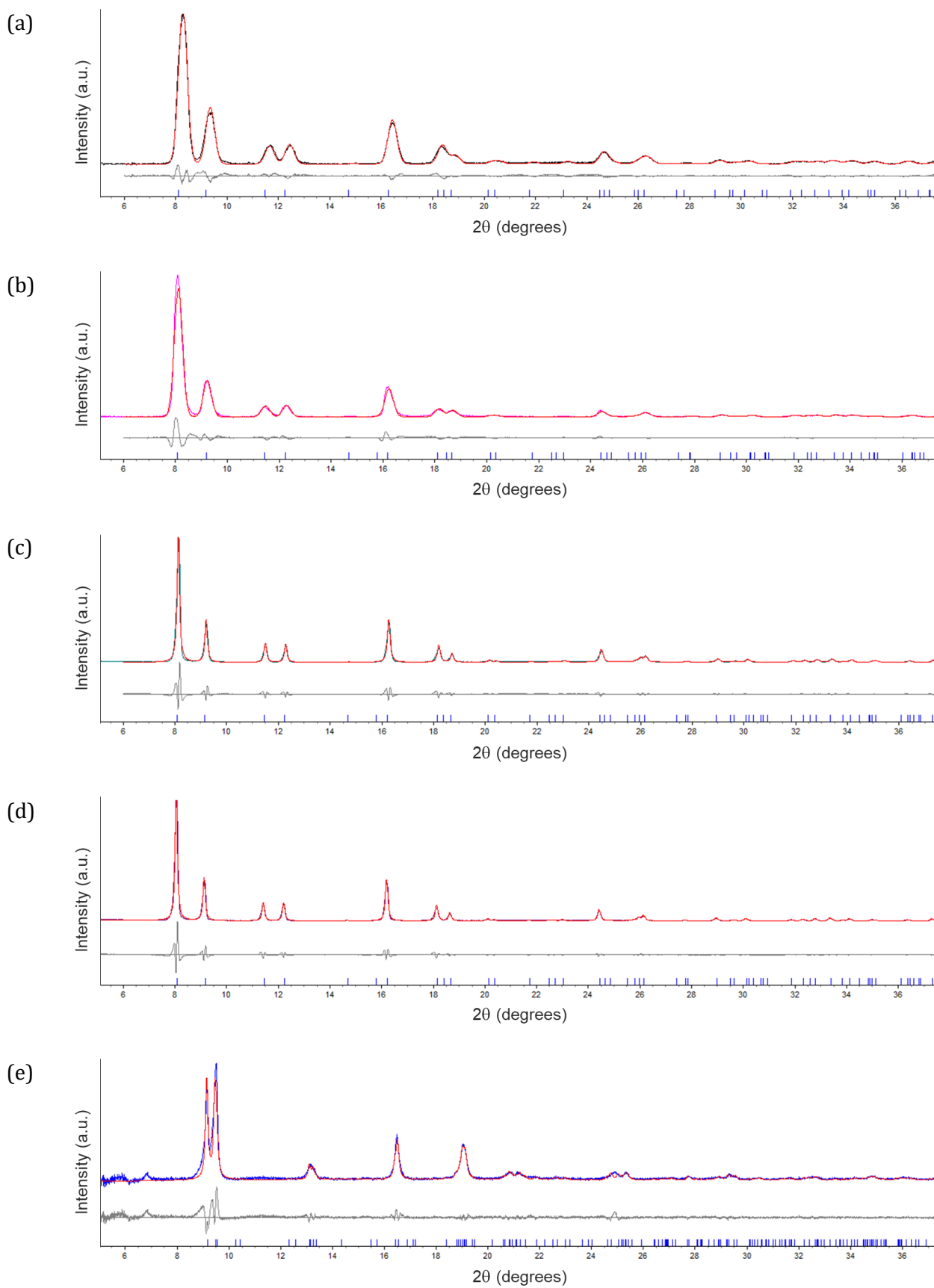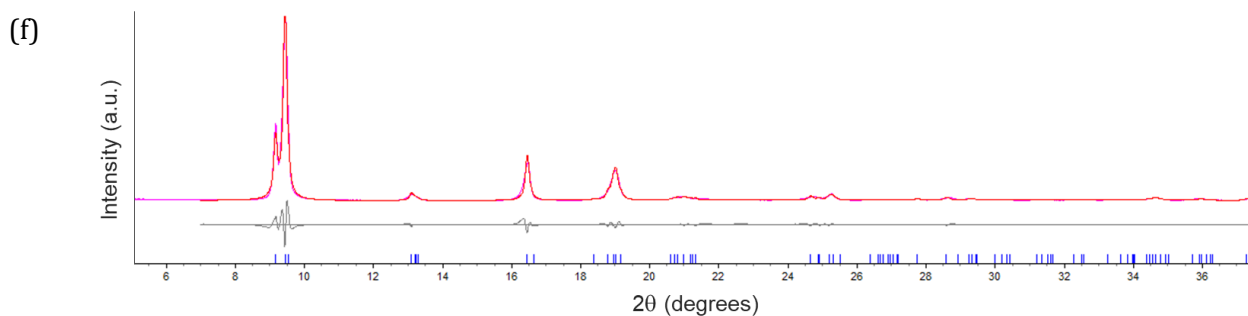
Figure 6.32 - Profile fits of XRPD patterns (Le Bail method) for the as-synthesized pain and NPs embedded MOFs: a) $Zn_2(bdc)_2(dabco)$, b) $Zn_2(DM-bdc)_2(dabco)$, c) $SiO_2@Zn_2(DM-bdc)_2(dabco)$, d) $SiO_2COOH@Zn_2(DM-bdc)_2(dabco)$, e) $Zn_2(BME-bdc)_2(dabco)$ dry, f) $SiO_2@Zn_2(BME-bdc)_2(dabco)$. Calculated and difference traces are represented in red and grey, respectively; experimental data is represented by the third color. The positions of the Bragg reflections are indicated by blue ticks.

Table 6.20 - Unit cell parameters of *as synthesised* and *dry* crystalline phases for $Zn_2(bdc)_2(dabco)$, $Zn_2(DM-bdc)_2(dabco)$, $Zn_2(BME-bdc)_2(dabco)$ as described in literature.

MOF [reference]	Space group	a (Å)	b (Å)	c (Å)	α (°)	β (°)	γ (°)	V (Å³)	Form
Zn_2(**bdc**)$_2$(dabco) [363]	*I4/mcm*	15.063(2)	15.063(2)	19.247(5)	90	90	90	4367.1(14)	as
	P4/mmm	10.929(2)	10.929(2)	9.608(1)	90	90	90	1147.6(3)	dry
Zn_2(**DM-bdc**)$_2$(dabco) [370]	*P4/nbm*	15.445(5)	15.445(5)	9.682(5)	90	90	90	2309.8(18)	as
	no data available								dry
Zn_2(**BME-bdc**)$_2$(dabco) [343]	*C2/m*	16.72(2)	14.11(3)	9.69(1)	90	91.78(1)	90	2284(6)	as
	C2/m	18.72(4)	10.73(1)	9.62(1)	90	91.38(1)	90	1931(4)	dry

Table 6.21 - Unit cell parameters and cell volumes determined by Le Bail refinement of the XRPD patterns and the corresponding R_{wp}, R_p and R_{Bragg} values for all the synthesised and activated MOFs. The XRPD data have been refined using unit cell parameters that were taken from the literature (see Table 6.20).

Space group	a (Å)	b (Å)	c (Å)	α (°)	β (°)	γ (°)	V (Å³)	R_{wp} (%)	R_p (%)	R_{Bragg} (%)	NPs	Form
						$Zn_2(\mathbf{bdc})_2(dabco)$						
I4/mcm	15.44(5)	15.44(5)	19.33(1)	90	90	90	4593.3(6)	6.2	5.4	0.68	none	as
P4/mmm	10.94(4)	10.94(4)	9.634(9)	90	90	90	1154.5(2)	10.3	7.1	0.92	none	dry
							$Zn_2(\mathbf{DM\text{-}bdc})_2(dabco)$						
P4/nbm	15.47(5)	15.47(5)	9.617(7)	90	90	90	2303.7(3)	6.5	5.0	0.62	none	as
				no data available								dry
P4/nbm	15.44(3)	15.44(3)	9.642(2)	90	90	90	2300.0(4)	6.6	5.0	0.27	SiO_2	as
P4/nbm	15.43(4)	15.43(4)	9.633(3)	90	90	90	2295.1(7)	6.9	5.2	0.53	SiO_2-COOH	as
							$Zn_2(\mathbf{BME\text{-}bdc})_2(dabco)$						
C2/m	16.74(3)	14.12(4)	9.636(3)	90	91.7(7)	90	2288.9(4)	12.4	9.8	1.5	none	as
C2/m	18.87(9)	10.56(2)	9.625(5)	90	90.8(3)	90	1923.7(2)	12.9	8.9	1.6	none	dry
C2/m	16.90(5)	14.19(4)	9.731(9)	90	91.3(1)	90	2336.5(1)	14.1	10.4	2.0	SiO_2	as
C2/m	18.59(4)	10.88(6)	9.621(2)	90	91.3(8)	90	1947.3(9)	13.9	10.8	1.7	SiO_2	dry

(a)

as synthesised   *dry*

(b)

as synthesised (no published structure for dry form)

(c)

as synthesised   *dry*
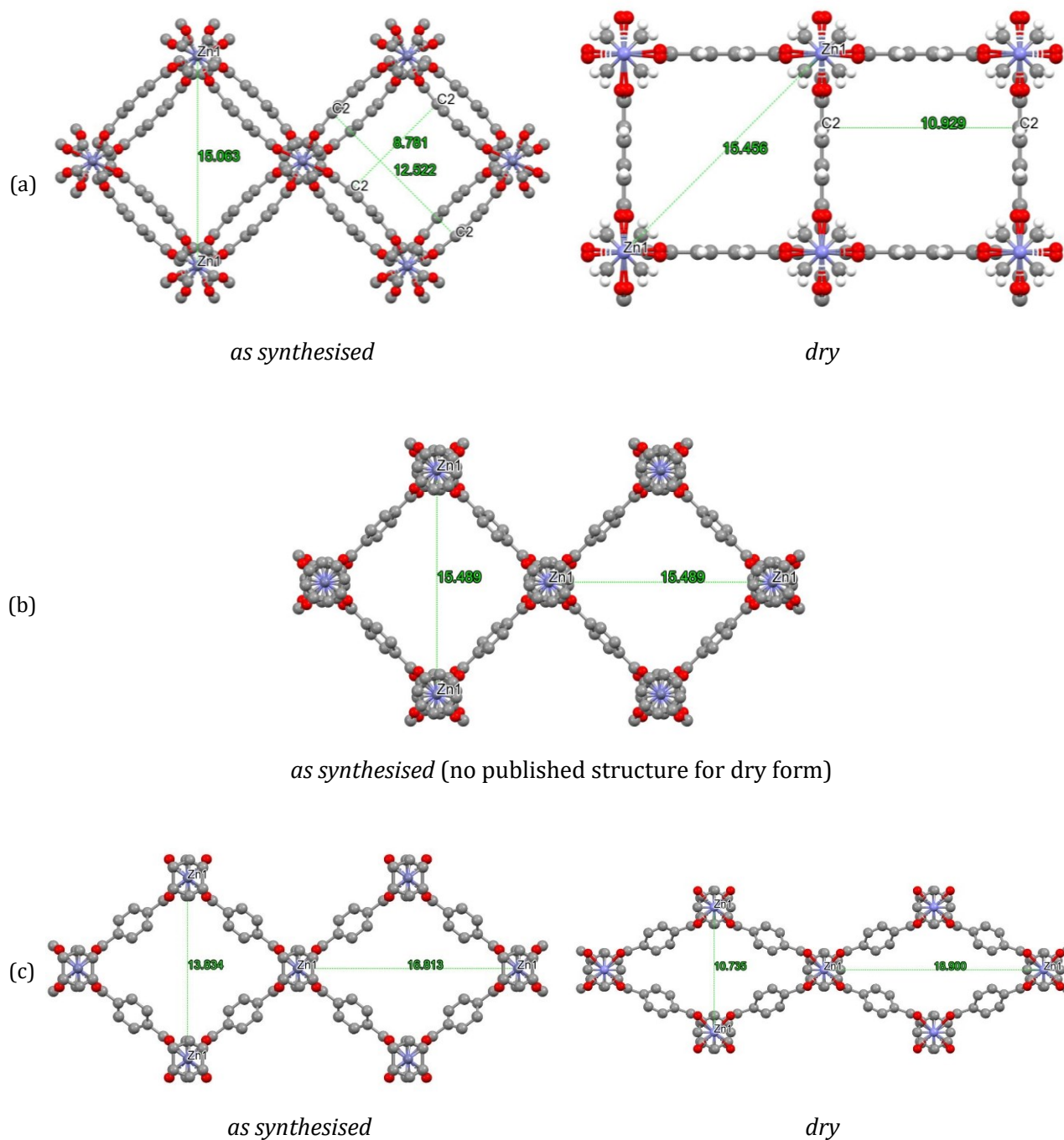
Figure 6.33 - Representation of pore dimension of the *as* and *dry* forms for a) $Zn_2(bdc)_2(dabco)$ [CCDC n° 238859, refcode WAFKAQ], b) $Zn_2(DM-bdc)_2(dabco)$ [CCDC n° 1426631, refcode WAFKEU04], c) $Zn_2(BME-bdc)_2(dabco)$ [CCDC n° 788019, refcode AJORAT]. Crystal structure viewed along the [001] direction. The flexible side chains on linker are not included in the structural model due to the high degree of disorder. Colour code: Zn, violet; O, red; C, grey.

6.5.4 UV-Visible and Photoluminescence Measurements

(a)

(b)

(c)

(d)
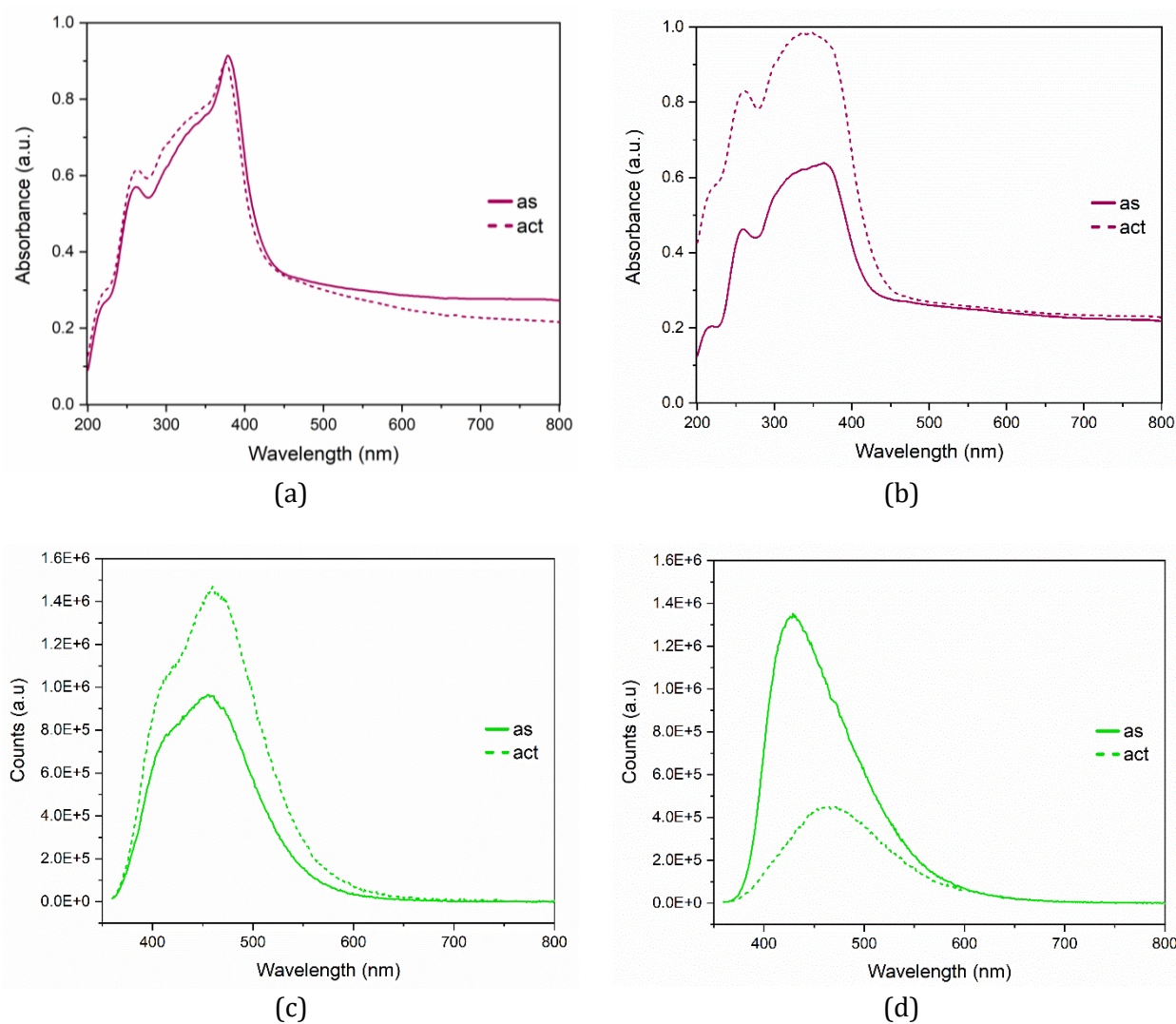
Figure 6.34 – Results of solid-sate UV-Visible measurements for $SiO_2@Zn_2(DM\text{-}bdc)_2(dabco)$ (a) and $SiO_2@Zn_2(BME\text{-}bdc)_2(dabco)$ (b). PL emission signals measured in solid state for $SiO_2@Zn_2(DM\text{-}bdc)_2(dabco)$ (c) and $SiO_2@Zn_2(BME\text{-}bdc)_2(dabco)$ (d). Measurements are not quantitative.

6.5.5 EFTEM-EDX and TEM Tomography

a. *SiO₂@Zn₂(DM-bdc)₂(dabco)*
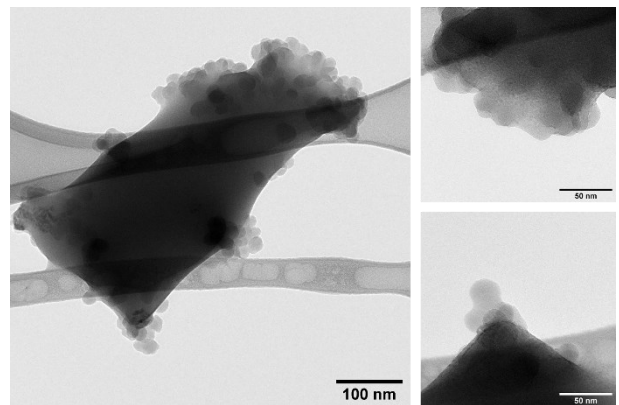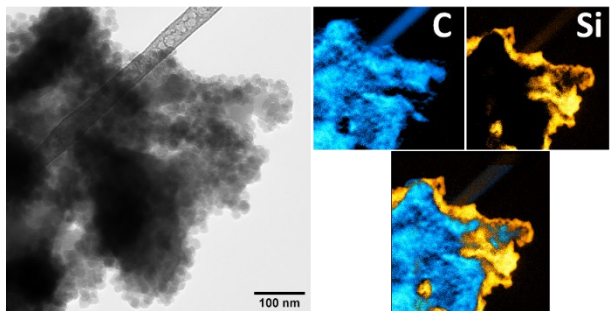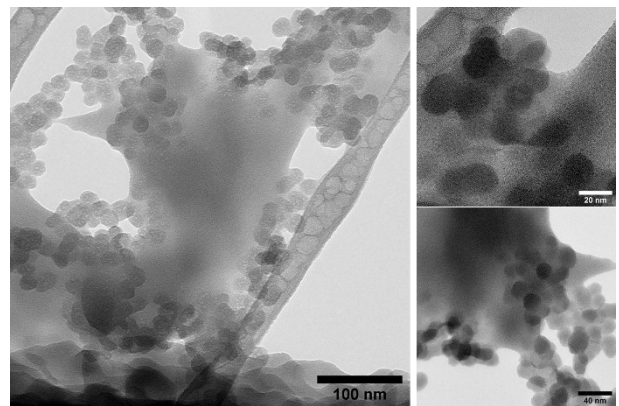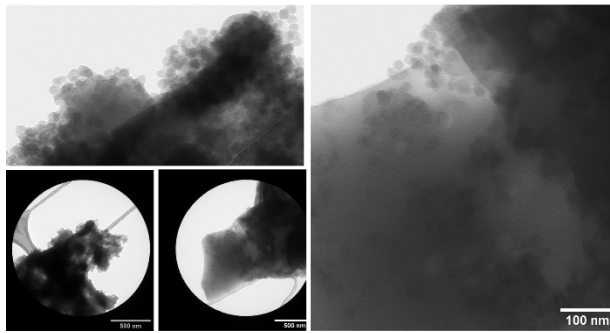
b. *SiO₂COOH@Zn₂(DM-bdc)₂(dabco)*
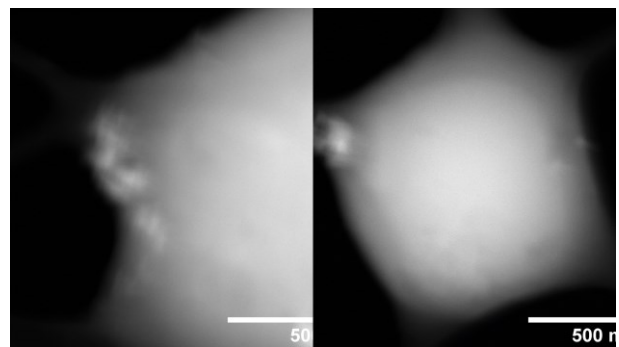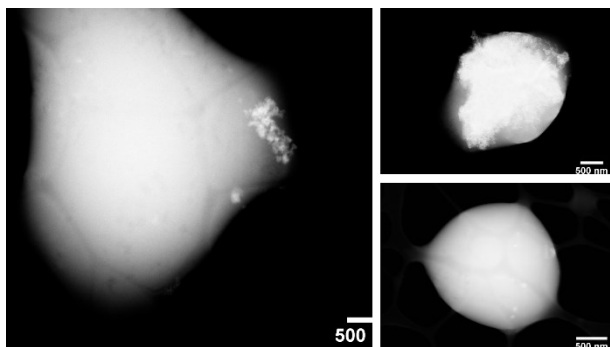
c.   SiO₂@Zn₂(BME-bdc)₂(dabco)
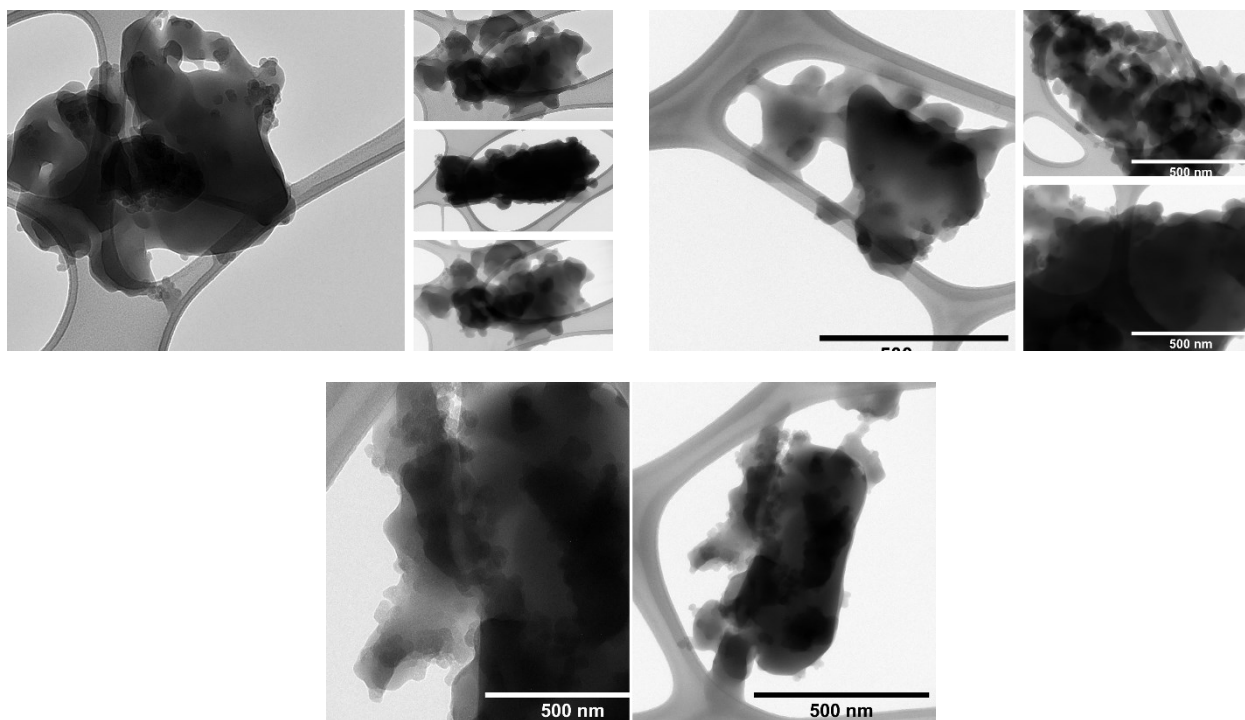
Figure 6.35 – EFTEM images of different crystallites of SiO$_2$@Zn$_2$(DM-bdc)$_2$(dabco) (a) coupled with EDX highlighting the presence of the light elements Si and C; SiO$_2$COOH@Zn$_2$(DM-bdc)$_2$(dabco) (b); SiO$_2$@Zn$_2$(BME-bdc)$_2$(dabco) (c).

6.5.6 Static Gas Sorption Measurements

a)
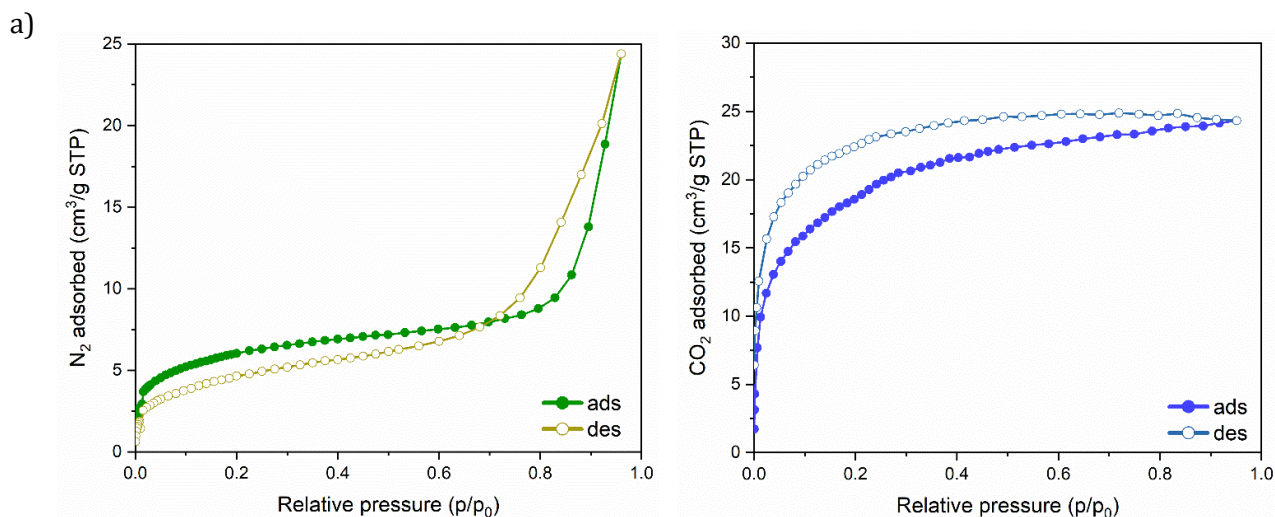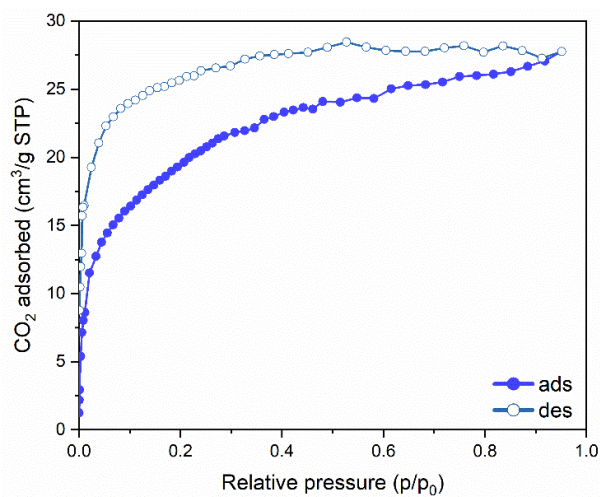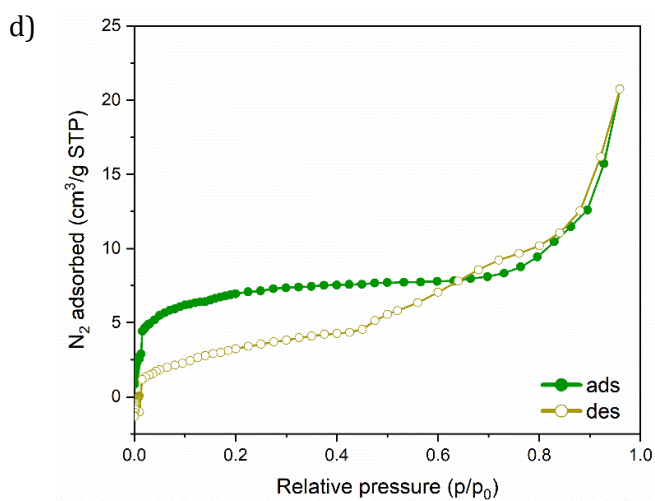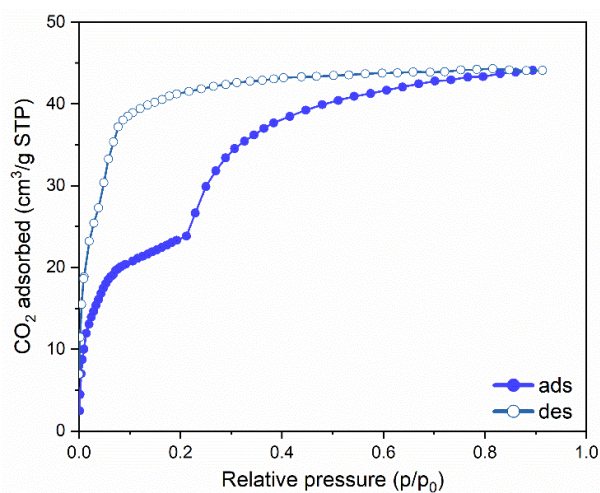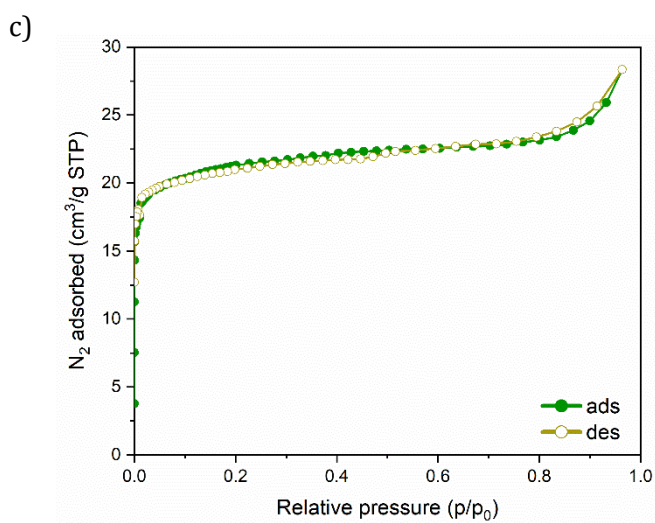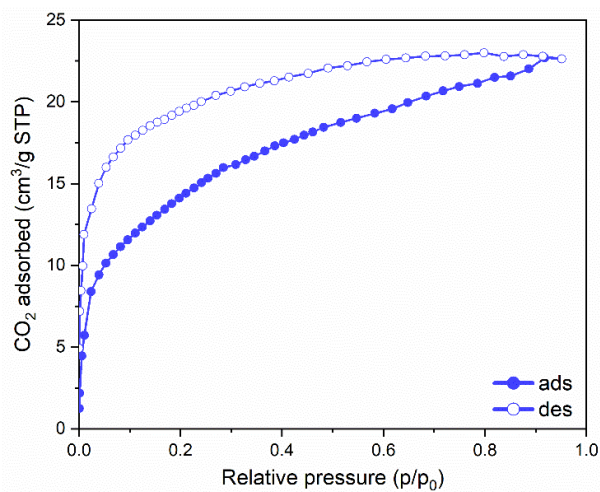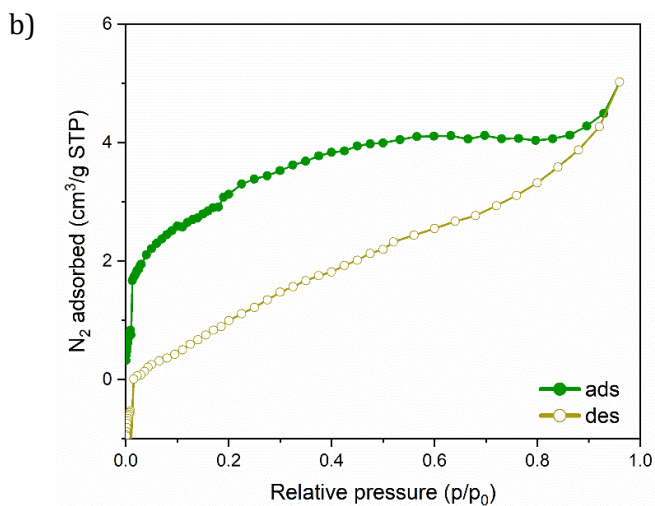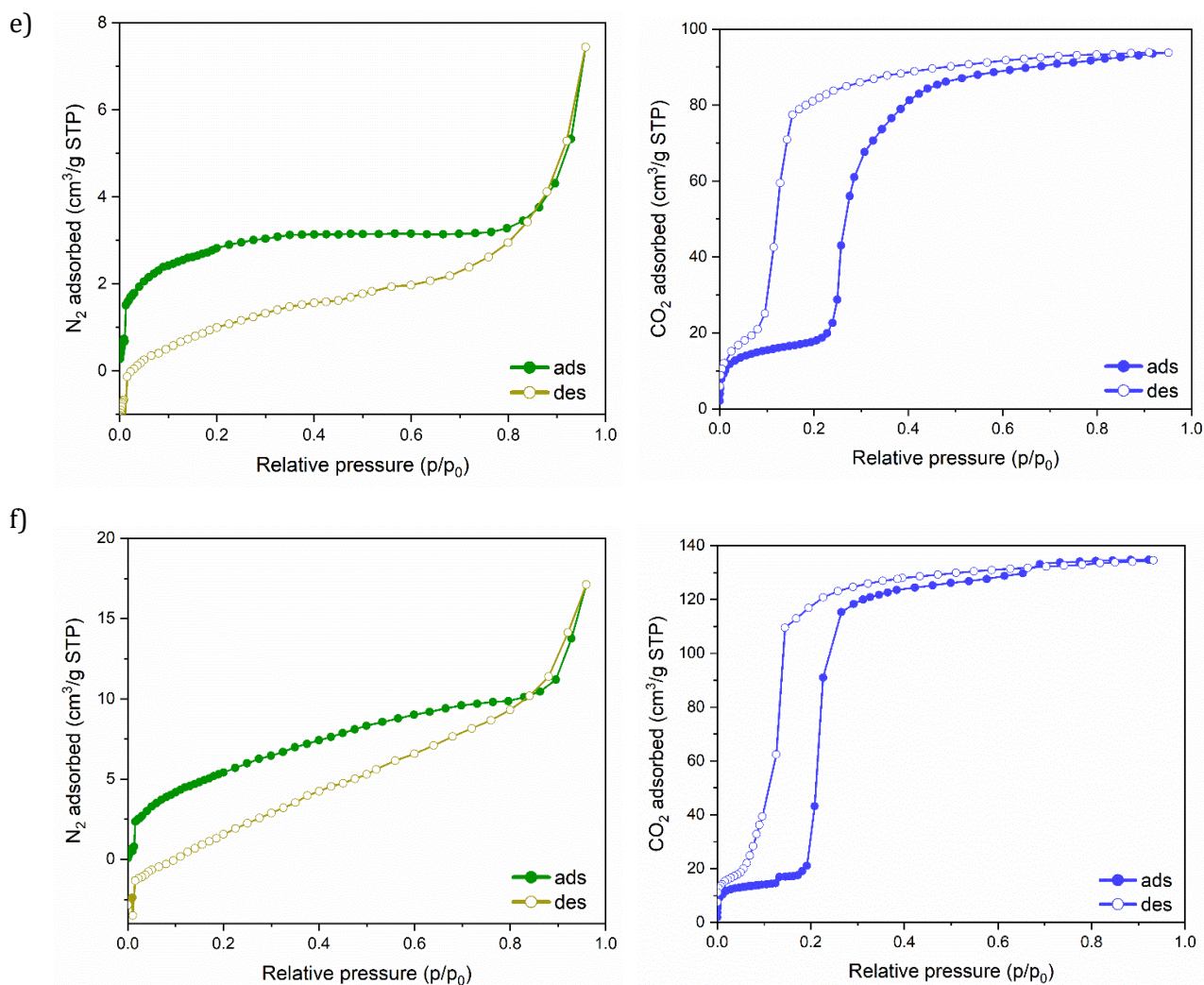
Figure 6.36 - N$_2$ (77 K) and CO$_2$ (195 K) gas sorption isotherms for a) Zn$_2$(DM-bdc)$_2$(dabco) (synthesis method 1: 120 °C for 48 h, glass vial in oven); b) SiO$_2$@Zn$_2$(DM-bdc)$_2$(dabco) (synthesis method 1: 0.100 mL of SiO$_2$ solution, 120 °C for 48 h, glass vial in oven); c) SiO$_2$@Zn$_2$(DM-bdc)$_2$(dabco) (synthesis method 2: 0.100 mL of SiO$_2$ solution, 120 °C for 48 h, autoclave in oven); d) SiO$_2$COOH@Zn$_2$(DM-bdc)$_2$(dabco) (synthesis method 3: 0.125 mL of SiO$_2$COOH solution, 120 °C for 48 h, glass bottle in oven); e) Zn$_2$(BME-bdc)$_2$(dabco) (synthesis method 1: 120 °C for 48 h, glass bottle in oven); f) SiO$_2$@Zn$_2$(BME-bdc)$_2$(dabco) (synthesis method 2: 0.100 mL of SiO$_2$ solution, 120 °C for 48 h, autoclave in oven).

6.5.7 STA Analysis
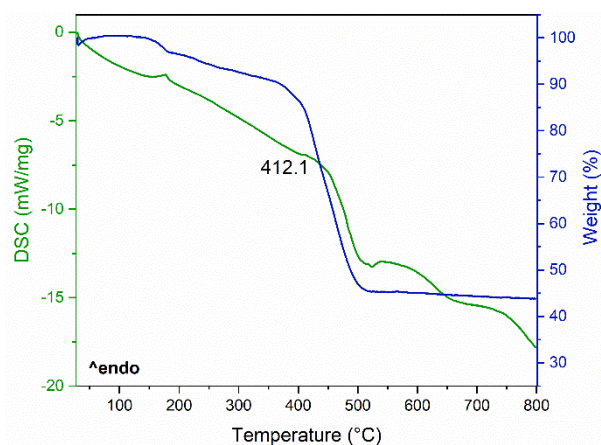
Figure 6.37 - Simultaneous TG/DSC analysis of $Zn_2(bdc)_2(dabco)$ in the temperature range 30-800 °C (10 °C/min).

(a)

(b)

(c)
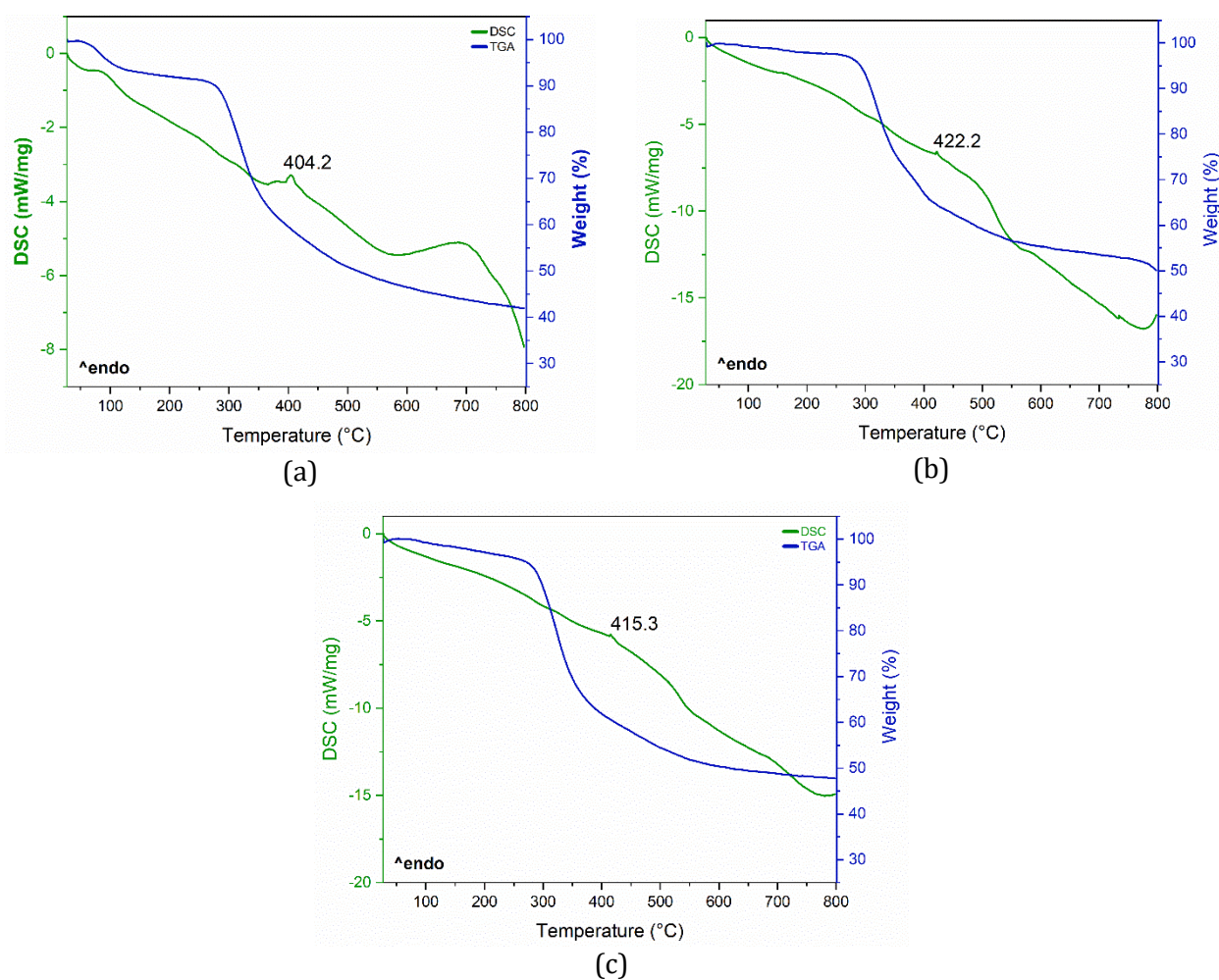
Figure 6.38 - Simultaneous TG/DSC analysis $Zn_2(DM-bdc)_2(dabco)$ (a), $SiO_2@Zn_2(DM-bdc)_2(dabco)$ (b) and $SiO_2COOH@Zn_2(DM-bdc)_2(dabco)$ (c) in the temperature range 30-800 °C (10 °C/min). The small weight-loss below 150 °C is ascribed to the release of water, adsorbed by the sample which was stored in air.
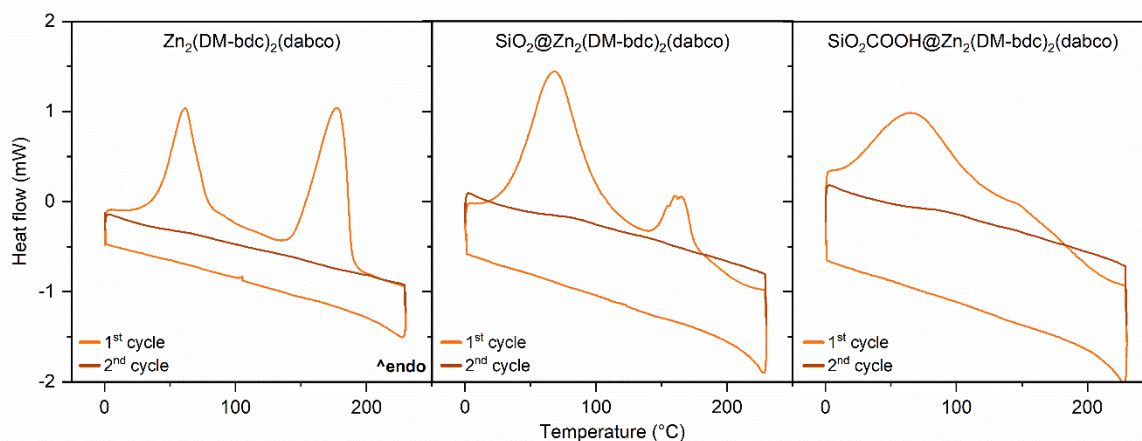
Figure 6.39 - Cyclic DSC experiments (temperature range: 0-230 °C, 10 °C/min) for Zn_2(DM-bdc)$_2$(dabco) (left), SiO_2@Zn_2(DM-bdc)$_2$(dabco) (center) and SiO_2COOH@Zn_2(DM-bdc)$_2$(dabco) (right). The first complete heating/cooling cycle is represented in orange, the second heating cycle in brown (for a total of 1½ cycles). The visible endothermic events between 50 and 200 °C are ascribed to the release of CH_2Cl_2 and DMF present in the framework after synthesis and washing of the samples.

(a)

(b)

(c)

(d)
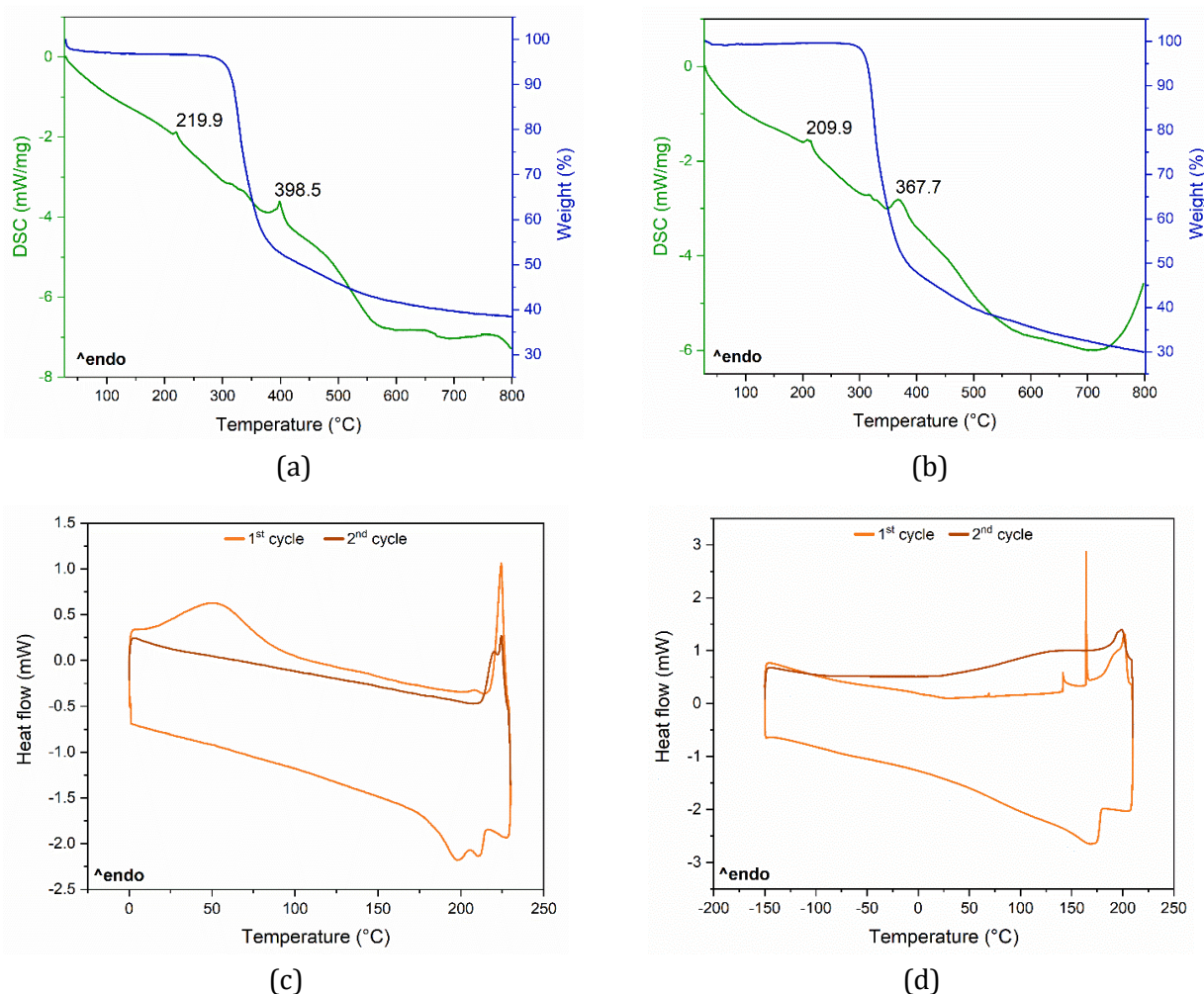
Figure 6.40 - Simultaneous TG/DSC analysis Zn_2(BME-bdc)$_2$(dabco) (a), SiO_2@Zn_2(BME-bdc)$_2$(dabco) (b) in the temperature range 30-800 °C (10 °C/min). Cyclic DSC experiments (temperature range: 0-230 °C and -150–210 °C, 10 °C/min) for Zn_2(BME-bdc)$_2$(dabco) (c), SiO_2@Zn_2(BME-bdc)$_2$(dabco) (d).

Table 6.22 - Decomposition temperatures of all synthesised MOF and NPs@MOFs obtained from TG-DSC.

Sample	$T_{decomposition}$ (°C)
$Zn_2(\mathbf{bdc})_2(dabco)$	∼ 370
$Zn_2(\mathbf{DM\text{-}bdc})_2(dabco)$	∼ 277
$SiO_2@Zn_2(\mathbf{DM\text{-}bdc})_2(dabco)$	∼ 270
$SiO_2COOH@Zn_2(\mathbf{DM\text{-}bdc})_2(dabco)$	∼ 271
$Zn_2(\mathbf{BME\text{-}bdc})_2(dabco)$	∼ 303
$SiO_2@Zn_2(\mathbf{BME\text{-}bdc})_2(dabco)$	∼ 283

6.5.8 VT-XRPD Analysis

Data analysis has been more difficult for the samples measured in Debye-Scherrer geometry (STOE STADI P diffractometer) because of the poor data quality obtained: low peak intensities, background highly influenced by the contribution of the glass capillary and other instrumental setup. For this reason, complete data treatment has been performed only on the set of measurements performed with the other instrumental setup (Bragg-Brentano geometry, flat sample, in air) and the results are described in Chapter 4.4.8. Moreover, the temperature ranges for the crystalline phase transitions reported are different for the two instrumental setups used, with higher values obtained for the VT-XRPD study performed on Bruker D8 on a flat sample and in air. This is due to the different heating system and general sample setup conditions.
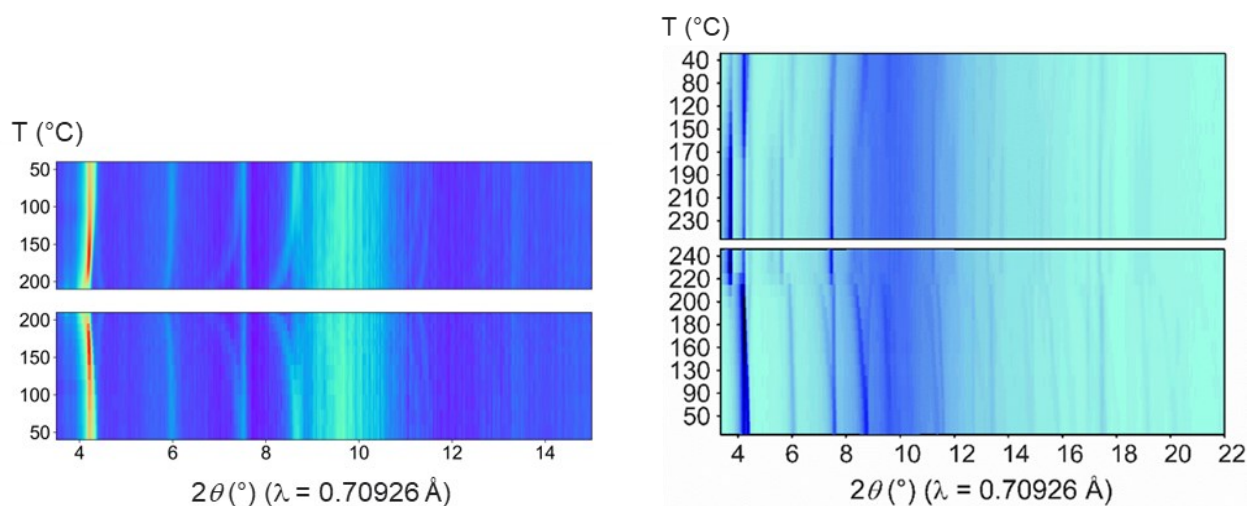
Figure 6.41 - 2D plots for VT-XRPD measurements performed on the activated samples in Debye-Scherrer geometry (used borosilicate glass capillaries of diameter 0.5 mm) for $Zn_2(BME\text{-}bdc)_2(dabco)$ (left) and $SiO_2@Zn_2(BME\text{-}bdc)_2(dabco)$ (right). XRPD patterns have been recorded at room temperature with 10 °C steps in the range 30-240 °C. All patterns are normalised to the most intense reflection (001) at $2\theta = 9.71°$ with $\lambda_{Mo} = 0.70926$ Å.
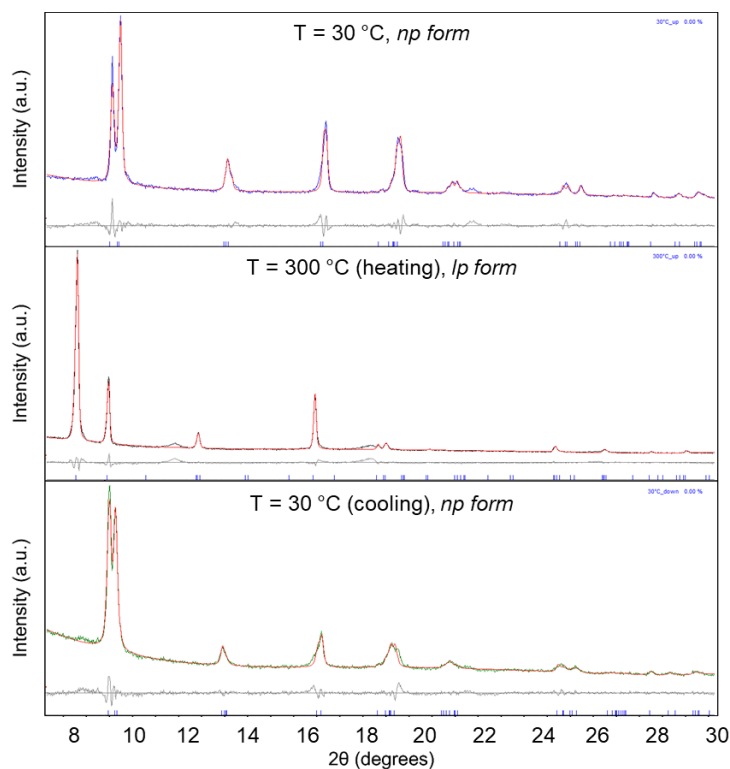
Figure 6.42 – Graphical representation of the whole powder pattern refinements carried out with the Le Bail method on the VT-XRPD data of $Zn_2(BME\text{-}bdc)_2(dabco)$. From the top to the bottom as representative example of data treatment: T = 30°C, T = 300 °C (heating), T = 30°C (cooling), showing experimental, calculated and difference traces (third colour, red and grey, respectively). Bragg reflections positions are indicated by blue ticks.
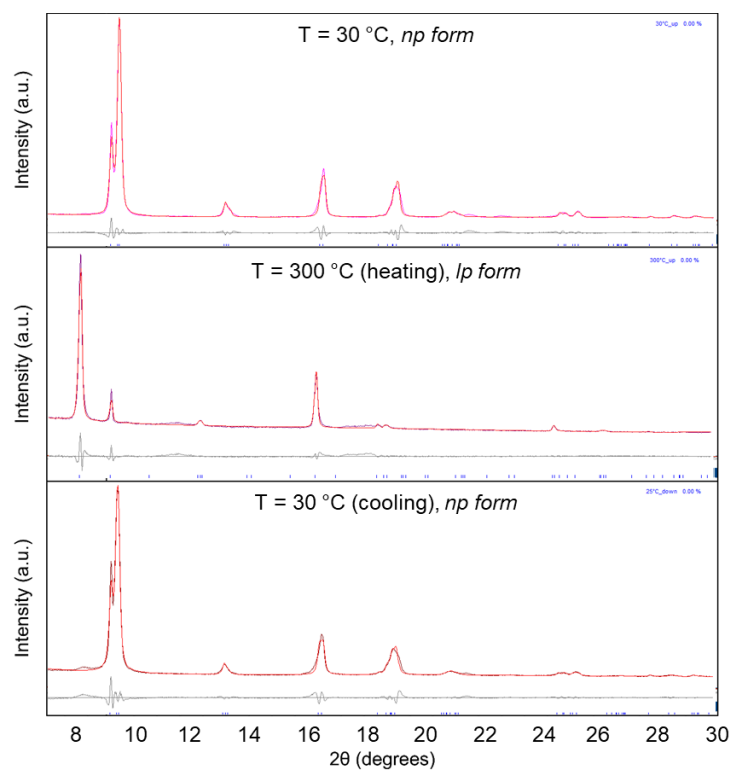
Figure 6.43 - Graphical representation of the whole powder pattern refinements carried out with the Le Bail method on the VT-XRPD data of $SiO_2@Zn_2(BME\text{-}bdc)_2(dabco)$. From the top to the bottom as representative example of data treatment: T = 30°C, T = 300 °C (heating), T = 30°C (cooling), showing experimental, calculated and difference traces (third colour, red and grey, respectively). Bragg reflections positions are indicated by blue ticks. To note that upon cooling, the crystalline phase never returns to the full narrow pore, (100) reflection always present even if with really low intensity.

Table 6.23 - Temperature dependent crystallographic data of Zn_2(BME-bdc)$_2$(dabco) extracted from VT-PXRD.

T (°C)	Space group	a (Å)	b (Å)	c (Å)	β (°)	V (Å^3)	Phase	R_{Bragg} (%)
heating								
30	*C*2/*m*	18.693(2)	10.721(4)	9.625(7)	90.673(6)	1929.0(2)	full *np*	0.95
50	*C*2/*m*	18.652(2)	10.720(8)	9.622(9)	90.820(0)	1924.0(6)	*np*	0.55
70	*C*2/*m*	18.667(1)	10.722(7)	9.623(4)	90.753(2)	1926.0(7)	*np*	0.56
90	*C*2/*m*	18.694(0)	10.725(9)	9.627(8)	90.683(1)	1930.3(2)	*np*	0.85
110	*C*2/*m*	18.753(6)	10.736(2)	9.628(2)	90.568(3)	1938.4(8)	*np*	1.14
130	*C*2/*m*	18.820(0)	10.758(8)	9.640(2)	90.546(4)	1951.8(7)	*np*	0.94
150	*C*2/*m*	18.883(6)	10.767(8)	9.645(1)	90.482(8)	1961.1(1)	*np*	0.93
170	*C*2/*m*	18.948(7)	10.768(7)	9.639(7)	90.674(8)	1966.8(6)	*np*	0.76
190	*C*2/*m*	19.009(2)	10.765(4)	9.626(4)	90.805(6)	1969.7(6)	*np – op*	0.61
210	*C*2/*m*	19.051(6)	10.781(2)	9.627(5)	91.057(4)	1977.1(4)	*np – op*	0.76
230	*C*2/*m*	19.050(7)	10.771(4)	9.643(2)	91.078(3)	1978.4(5)	*np – op*	0.48
250	*C*2/*m*	19.070(2)	10.851(3)	9.839(0)	91.754(7)	2035.0(9)	*np – op*	1.94
270	*C*2/*m*	19.319(8)	10.759(5)	9.964(5)	90.273(9)	2071.3(2)	*np – op* (50:50)	1.48
290	*C*2/*m*	16.832(5)	14.314(5)	9.636(2)	90.361(6)	2321.7(7)	*op*	0.63
300	*C*2/*m*	16.838(5)	14.316(9)	9.635(6)	90.328(9)	2322.8(7)	full *op*	0.41
cooling								
280	*C*2/*m*	16.830(6)	14.321(7)	9.631(7)	90.302(0)	2321.6(3)	full *op*	0.31
260	*C*2/*m*	16.826(8)	14.319(0)	9.630(6)	90.349(5)	2320.3(9)	*op*	0.29
240	*C*2/*m*	16.756(1)	14.338(0)	9.629(3)	90.382(8)	2313.3(7)	*op - np*	0.35
220	*C*2/*m*	16.704(2)	14.312(2)	9.639(1)	90.541(2)	2304.3(6)	*op - np*	2.25
200	*C*2/*m*	18.880(3)	10.759(3)	9.625(0)	91.473(7)	1954.5(6)	*op - np*	0.87
180	*C*2/*m*	18.918(1)	10.774(1)	9.624(5)	91.409(3)	1961.1(2)	*op - np*	0.23
160	*C*2/*m*	19.074(9)	10.806(0)	9.647(1)	90.832(7)	1988.2(7)	*op - np*	0.48
120	*C*2/*m*	19.038(3)	10.812(2)	9.673(9)	90.511(3)	1991.2(5)	*op - np*	0.52
100	*C*2/*m*	18.887(1)	10.766(0)	9.617(2)	90.697(2)	1955.4(0)	*op - np*	0.52
80	*C*2/*m*	18.849(3)	10.761(5)	9.622(0)	90.626(2)	1951.6(7)	*np*	0.55
60	*C*2/*m*	18.846(2)	10.769(1)	9.639(1)	90.584(8)	1956.2(0)	full *np*	0.56
40	*C*2/*m*	18.850(3)	10.769(4)	9.642(7)	90.621(1)	1957.4(2)	full *np*	0.53
30	*C*2/*m*	18.846(3)	10.762(7)	9.636(8)	90.600(6)	1954.5(9)	full *np*	0.56

Table 6.24 - Temperature dependent crystallographic data of SiO$_2$@Zn$_2$(BME-bdc)$_2$(dabco) extracted from VT-PXRD.

T (°C)	Space group	a (Å)	b (Å)	c (Å)	β (°)	V (Å^3)	Phase	R$_{wp}$ (%)
heating								
30	$C2/m$	18.757(7)	10.740(2)	9.633(9)	90.656(6)	1940.7(3)	full *np*	1.22
50	$C2/m$	18.745(8)	10.750(2)	9.655(8)	90.900(1)	1945.6(0)	*np*	0.80
70	$C2/m$	18.745(1)	10.749(3)	9.652(6)	90.915(3)	1944.7(1)	*np*	0.82
90	$C2/m$	18.726(1)	10.734(5)	9.624(3)	90.870(2)	1934.4(1)	*np*	0.89
110	$C2/m$	18.789(0)	10.752(3)	9.635(3)	90.641(7)	1946.4(5)	*np*	1.26
130	$C2/m$	18.809(9)	10.749(7)	9.620(8)	90.581(9)	1945.2(1)	*np*	1.64
150	$C2/m$	18.899(6)	10.772(9)	9.643(8)	90.534(9)	1963.4(2)	*np - op*	1.99
170	$C2/m$	18.981(0)	10.785(0)	9.650(1)	90.614(9)	1975.3(6)	*np - op*	2.17
180	$C2/m$	18.992(6)	10.778(6)	9.635(6)	90.781(2)	1972.3(5)	*np - op*	2.18
190	$C2/m$	18.995(2)	10.769(6)	9.620(3)	90.836(0)	1967.8(2)	*np - op*	2.14
200	$C2/m$	18.991(6)	10.757(5)	9.598(0)	90.952(6)	1960.6(0)	*np - op*	2.10
210	$C2/m$	19.004(8)	10.750(8)	9.586(2)	91.022(2)	1958.3(1)	*np - op*	2.06
220	$C2/m$	18.971(5)	10.814(0)	9.665(7)	91.460(6)	1982.3(4)	*np - op*	1.74
230	$C2/m$	18.962(4)	10.807(2)	9.675(9)	91.613(6)	1982.1(0)	*np - op*	1.56
240	$C2/m$	19.073(7)	10.792(4)	9.683(2)	91.174(4)	1992.8(8)	*np - op*	1.39
250	$C2/m$	19.161(5)	10.806(3)	9.747(1)	91.129(0)	2017.9(0)	*np - op*	2.32
260	$C2/m$	16.155(2)	14.236(1)	9.581(7)	92.260(0)	2201.9(7)	*np – op* (50:50)	6.90
270	$C2/m$	16.795(7)	14.314(1)	9.628(6)	90.524(0)	2314.7(6)	*np – op*	1.87
280	$C2/m$	16.803(1)	14.301(9)	9.626(7)	90.513(4)	2313.3(7)	*op*	1.61
290	$C2/m$	16.798(7)	14.301(1)	9.627(2)	90.558(7)	2312.7(3)	*op*	1.28
300	$C2/m$	16.792(7)	14.301(6)	9.629(0)	90.611(2)	2312.3(7)	full *op*	0.94
cooling								
275	$C2/m$	16.788(4)	14.298(5)	9.622(7)	90.562(5)	2309.8(0)	full *op*	1.63
260	$C2/m$	16.783(3)	14.296(3)	9.620(9)	90.572(6)	2308.3(1)	*op*	7.47
250	$C2/m$	16.781(1)	14.294(4)	9.623(6)	90.537(4)	2308.3(6)	*op*	1.44
240	$C2/m$	16.777(6)	14.293(2)	9.630(5)	90.585(4)	2309.3(4)	*op*	1.74
230	$C2/m$	16.751(9)	14.271(8)	9.643(4)	90.750(8)	2305.3(4)	*op – np*	4.84
220	$C2/m$	16.329(1)	14.315(0)	9.643(6)	91.927(7)	2252.9(2)	*op – np* (50:50)	6.11
210	$C2/m$	16.340(4)	14.277(0)	9.613(6)	92.266(6)	2241.0(0)	*op – np*	3.76
200	$C2/m$	20.195(0)	11.049(2)	9.764(9)	90.787(5)	2178.7(2)	*op – np*	3.04
180	$C2/m$	19.990(1)	11.011(8)	9.727(4)	90.596(1)	2141.1(5)	*op – np*	1.48

160	C2/m	19.342(3)	10.844(0)	9.670(9)	90.718(5)	2028.2(7)	op – np	1.80
140	C2/m	19.051(6)	10.795(9)	9.643(3)	90.516(0)	1983.3(4)	op – np	1.63
120	C2/m	19.001(1)	10.800(4)	9.659(4)	90.574(0)	1982.2(1)	op – np	1.49
100	C2/m	18.849(1)	10.755(0)	9.609(5)	90.625(8)	1947.9(3)	op – np	1.39
80	C2/m	18.832(8)	10.762(8)	9.626(7)	90.702(6)	1951.1(2)	op – np	1.24
60	C2/m	18.804(2)	10.755(5)	9.628(2)	90.721(3)	1947.1(4)	np	1.06
40	C2/m	18.807(2)	10.759(8)	9.639(3)	90.716(2)	1950.4(6)	np	1.11
25	C2/m	18.804(5)	10.752(6)	9.630(6)	90.683(3)	1947.1(4)	np*	1.17

* never returns to full narrow pore, (100) reflection always present even if with really low intensity.

Appendix

I. Nomenclature and Abbreviations

1,3-H$_2$BDP	1,3-bis(pyrazol-4-yl)benzene
1,4-H$_2$BDP	1,4-bis(pyrazol-4-yl)benzene
4-peia	N-(2-pyridin-4-yl-ethyl)-isonicotinamide ($C_{13}H_{13}N_3O$)
AC	Activated carbon
act	Activated
ADI	Adiponitrile ($CN(CH_2)_4CN$)
ads	Adsorption
AFM	Atomic force spectroscopy
AFOLU	Agriculure, forestry and other land use
***a*MOF**	amorphous MOF
as	As synthesised
ATR-IR	Attenuated total reflection Infrared spectroscopy
BET	Brunauer-Emmett-Teller surface area
bipy	4,4′-bipyridine
BME	bis-(2-methoxyethoxy)
BU	Building unit
CALF-20	Zn_2(1,2,4-triazolate)$_2$(oxalate)
cbIm	5-chlorobenzenimidazolate ($C_7H_4N_2Cl^-$)
CCDC	Cambridge Crystallographic Data Centre
CCS	Carbon capture and sequestration
CCU	Carbon capture and utilization
CDC	Trans-1,4-cyclohexanedicarboxylicacid ($C_8H_{10}O_4^{2-}$)
CMP	Conjugated microporous polymers
COF	Covalent-organic framework
CP	Coordination polymer
CSD	Cambrige structural database
CVD	Chemical vapor deposition
dabco	1,4-diazabicyclo[2.2.2]octane
DAC	Direct air capture
DE	Diethoxy
DEA	Diethanolamine
DEF	Diethylformamide
Des	Desorption
DFT	Density functional theory
dia	Diamond net (topology)
dipn	N,N-di(3-aminopropyl)-amine (($NH_2CH_2CH_2CH_2)_2NH$)
DM	Dimethoxy
DMF	*N,N*-dimethylformamide
DMSO	Dimethylsulfoxide

DSA	Double solvent approach
DSC	Differential scanning calorimetry
DUT	Dresden University of Technology
DUT-49	$Cu_2(bbcdc)$
DUT-8(Ni)	$Ni_2(2,6\text{-}ndc)_2(dabco)$
EA	Elemental analysis
EDX	Energy-dispersive X-ray analysis
EFTEM	Energy-filtered TEM
ELM-11	$Cu(4,4'\text{-bipyridine})_2(BF_4)_2$
ESRF	European Synchrotron Radiation Facility
EXAFS	Extended X-ray absorption spectroscopy
FAU	Faujasite (structure type)
FTIR	Fourier-transform infrared spectroscopy
FWHM	Full width at half-maximum
GCMC	Grand canonical Monte Carlo
GHG	Greenhouse gases
H$_2$BDP	1,4-Di(4'-pyrazolyl)benzene
H$_2$bdc	Benzene-1,4-dicarboxylic acid (terephthalic acid)
H$_2$(fu-bdc)	Functionalised benzene-1,4-dicarboxylic acid (terephthalic acid)
H$_2$BPE	4,4'-buta-1,3-diyne-1,4-diylbis(1H-pyrazole)
H$_2$BPEB	1,4-bis(1*H*-pyrazol-4-ylethynyl)benzene
H$_2$BPZ	4,4'-bis(pyrazole)
H$_2$dmcapz	3,5-dimethyl-4-carboxypyrazole
H$_2$ndc	2,6-naphthalenedicarboxylic acid
H$_2$PBP	4,4'-bis(1H-pyrazol-4-yl)biphenyl
H$_2$NDI-H	bis(N-(3,5-dimethyl-1H-pyrazol-4-yl))naphtalenetetracarboxylic-dianhydride
H$_3$btb	1,3,5-tris(4-carboxyphenyl)
H$_3$BTC	1,3,5-benzenetricarboxylic acid
H$_3$BTP	1,3,5-tris(1H-pyrazol-4-yl)benzene
H$_3$BTPP	1,3,5-tris((1Hpyrazol-4-yl)phenyl)benzene
H$_4$bbcdc	9,9'-([1,1'-biphenyl]-4,4'-diyl)bis(9H-carbazole-3,6-dicarboxylate)
HKUST	Hongkong University of Science and Technology
HKUST-1	Cu_2BTC_3
HR-PXRD	High-resolution powder X-ray diffraction
HSAB	Hard-soft acid-base theory
IAST	Ideal adsorption solution theory
ICA	Imidazolate-2-carboxaldehyde ($C_4H_3N_2O^-$)
Im	Imidazolate ($C_3H_3N_2^-$)
IPCC	Intergovernmental Panel on Climate Change
IRMOF	Isoreticular metal-organic framework
IUPAC	International Union of Pure and Applied Chemistry
L	Linker
lp **(or** *op***)**	Large pore (or open pore)
M	Metal
MAF	Metal-azolate framework
MEA	Monoethanolamine
MIL	Materiaux de l'Institut Lavoisier

MIL-100	$M_3O(H_2O)_2F\{C_6H_3(CO_2)_3\}_2 \cdot nH_2O$ (n ~14.5) (M = Fe^{3+}, Cr^{3+})
MIL-101	$Cr_3F(H_2O)_2O(BDC)_3 \cdot nH_2O$ (n ~25)
MIL-125	$[Ti_8O_8(OH)_4(BDC)_6]$
MIL-53	$[M(OH)(BDC)]_n$ (M = Fe^{3+}, Al^{3+})
MIL-88	$Fe_3O(CH_3OH)_3(1,3\text{-benzenedicarboxylate})_3$ (M = Cr^{3+}, Fe^{3+})
mIm	2-methylimidazolate ($C_4H_5N_3^-$)
MNP	Metal nanoparticle
MOF	Metal-organic framework
MOF-177	$[Zn_4O(btb)_2]$
MOF-5	$[Zn_4O(BDC)_3]$
MOF-74	$[M_2(dobdc)(H_2O)_2]$ (M = Mg^{2+}, Ni^{2+}, Co^{2+}, Zn^{2+})
MOF-808	$Zr_6O_4(OH)_4(BTC)_2(HCOO)_6$
NET	Negative emission technologies
NGA	Negative gas adsorption
NMR	Nuclear magnetic resonance
NP	Nanoparticle
***np* (or *cp*)**	narrow pore (closed pore)
OMS	Open metal site
P	Pillar
PCC	Pyridinium cholorochromate
PCN	Porous coordination network
PCN-700	$Zr_6O_4(OH)_8(COO)_8$
PCP	Porous coordination polymer
pdt	2,3-pyrazinedithiolate ($C_4H_2N_2S_2^{2-}$)
PIM	Polymer of intrinsic microporosity
PL	Photoluminescence
POP	Porous organic polymer
ppm	Parts per million
PSA	Pressure swing gas adsorption
PSD	Post-synthetic deprotection
PSE	Post-synthetic exchange
PSM	Post-synthetic modification
PVP	Polyvinylpyrrolidone
pz	Pyrazole
Q_{st}	Isosteric heat of adsorption
SALE	Solvent-assisted linker exchange
SBU	Secondary building unit
SEM	Scanning electron microscopy
SPC	Soft porous crystal
SSA	Specific surface area
SS-NMR	Solid-state NMR
STA	Simultaneous thermal analysis
STP	Standard temperature and pressure
SUMOF	Stockholm University MOF
SUMOF-7	$[Ln(L)(H_2O)]_n$ (Ln^{3+} = La, Ce, Pr, Nd, Sm, Eu, Gd; L = v. tricarboxylate ligands)
TBAF	Tetra-n-butylammonium fluoride
T_d	Decomposition temperature

TEM	Transmission electron microscopy
TGA	Thermogravimetric analysis
THF	Tetrahydrofuran
TPT	2,4,6-tris(4-pyridyl)triazine ($C_{18}H_{12}N_6$)
TSA	Temperature swing gas adsorption
UiO	Universitetet i Oslo
UiO-66(Zr)	$[Zr_6O_4(OH)_4(BDC)_6]_n$
UV-Vis	Ultra-violet Visible spectroscopy
V	Volume ($Å^3$)
VOC	Volatile organic compound
VP-XRPD	Variable pressure X-ray powder diffraction
VT-PXRD	Variable temperature X-ray powder diffraction
XAS	X-ray absorption spectroscopy
XRPD	X-ray powder diffraction
ZIF	Zeolitic imidazolate framework
ZIF-7	Zn(benzimidazolate)$_2$
ZIF-8	Zn(2-methylimidazolate)$_2$
ZIF-11	Zn(benzimidazolate)$_2$
ZSM-5	$Na_nAl_nSi_{96-n}O_{192}\cdot16H_2O$ (0<n<27) (Zeolite Socony Mobil–5)

II. List of Publications

1) Terruzzi S., Grell T., Colombo V., "Metal-organic frameworks: spugne molecolari al servizio della sostenibilità", *la Chimica e l'Industria – special issue: Cristallografia: da scienza antica a moderna tecnologia*, anno IV, n. 5, *30-39,* **2020**

2) Terruzzi S., Bellomi S., Barreca G., Ventimiglia G. and Masciocchi N., "Disclosing the rich crystal chemistry of Lesinurad by ab-initio laboratory X-ray powder diffraction methods", *Cryst. Growth Des.* **2018**, 18, 6863–6872

3) Vismara,R.[+]; Terruzzi, S.[+]; Maspero, A.; Grell, T.; Bossola, F.; Sironi, A.; Galli, S.; Navarro, J.A.R. and Colombo, V. "CO_2 adsorption in a robust pyrazolate-bridged metal-organic framework: a HR-powder X-ray diffraction and computational study", JACS **2022**, *manuscript in submission* ([+] equal contribution)

4) Terruzzi S., Sironi A., Navarro J. A., Colombo V. "Modulation of structural and adsorptive properties of solid solutions of $[Ni_8(OH)_4(H_2O)_2(BDP)_{6x}(BDP\_SO_3H)_{6(1-x)}]$", *manuscript in preparation*

III. List of Presentations

Oral Presentations

14-22/08/2021 - *Elucidation of CO_2 Adsorption Process in a Bis-pyrazolate Based MOF through HR-PXRD*, IUCr2021, Prague (Czech Republic)

07/11/2019 - *Elucidation of Adsorption Processes in Bis-pyrazolate Based MOFs through in situ XRPD*, Technische Universität München (TUM), Garching bei München (Germany) – *invited seminar*

Poster Presentations

10-16/09/2021 – *Multivariate Flexible MOFs: the Role of Functionalized Linkers, Heterogeneity and Defects*, EuroMOF2021, Krakow (Poland)

6-9/09/2021 - *High-resolution PXRD Study of CO_2 Adsorption Process in a Bis-pyrazolate Based MOF*, AIC2021, Parma (Italy)

21-25/06/2021 - *SiO_2@flexible MOFs: the Role of Functionalized Linkers, Heterogeneity and Defects*, MOFschool2021, Como (Italy)

4-7/09/2019 - *Elucidation of Adsorption Induced Phase Change in Flexible Bis-pyrazolate Based MOFs through in-situ XRPD*, MISCA V, Naples (Italy)

17-21/06/2019 - *Solid Solutions of Isoreticular Functionalized Pyrazolate-based MOFs: Adsorption Properties and Structural Defects*, MOFschool2019, Como (Italy)

27-31/03/2019 - *Modulation of Structural and Adsorptive Properties of Solid Solutions of $[Ni_8(OH)_4(H_2O)_2(BDP)_{6x}(BDP\_SO_3H)_{6(1-x)}]$*, School on Reticular Chemistry, Stockholm (Sweden)

Acknowledgements

First and foremost, I would like to thank my supervisor Prof. **Valentina Colombo** for giving me the opportunity to work in such interesting projects during my long research period in her group; thanks for giving me the opportunity to start a PhD and always excellent support, motivation, scientific freedom and trust during the last years. This has been a wonderful and formative journey full of new discoveries, experiences abroad, awesome trips to conferences and schools, inspiring stays at synchrotron facilities and, most of all, it has been fantastic to see our research group grow year by year!

A huge thanks also to Prof. **Roland A. Fischer** for inviting me at the Technical University of Munich and for the amazing research period I spent in the AMC research group for nine months. Thanks for the continuous motivation, scientific freedom, helpful discussions and the nice working atmosphere. The whole group made me feel very welcome and gave me constant help with everyday problems, especially during the very difficult weeks of the lockdown.

I also deeply thank Prof. **Angelo Sironi** for all the scientific help received, the many scientific discussions and for accepting to be the co-supervisor of this thesis. Without your contributions this work would not be as it is now.

Warm thanks to Dr. **Gregor Kieslich** for welcoming me into the HyFM subgroup and giving me the opportunity to give and share so many interesting presentations with the other team members. And definitely thanks for all the scientific advice and support, but also for the funny and lovely evenings at the Biergarten!

I thank all the members of the AMC research group and in particular **Jan Berger**, **Thomas Pickl**, **Samuele Neuberg**, **Pia Vervoorts**, **Lisa Semrau**, **Dardan Ukaj**, **Kathrin Kollmannsberger**, **Silva Kronawitter**, **Philip Stanley** for helping me a lot both scientifically and outside university during my stay at Munich.

Of course, I am deeply thankful to all the past and present members of my research group, especially **Toni Grell**, **Marco Vandone**, **Simona Sorbara**, **Giulia Taini**, **Giovanni Moreddu**, **Andrea Caruso** for the great time we had (and still have) together in the lab and outside! With regard to this thesis, I have to deeply thank Toni for all the time spent helping me during the writing and revision and for all the valuable hints and tips.

As well, I would like to thank the following people without whom it would not have been possible to accomplish this work:

– **Jorge A. R. Navarro**, **Simona Galli** and **Rebecca Vismara** for the long-term scientific collaboration, invaluable help during the preparation of our shared manuscript and the great time we had while organising two editions of the MOFSchool.

– **Angelo Maspero** for the research stay in his lab and the many things I learned on the topic of organic synthesis.

– **Jan Berger** for his help during my stay at TUM, especially in the lab, for the gas adsorption measurements and for the fruitful scientific discussions.

– **Stefan Burger** for helping me with the XRD and cyclic DSC measurements and letting me use his workspace in the lab every time I needed it.

– **Sebastian Weishäupl** for recording the solid state UV-Visible and photoluminescence measurements.

– **Filippo Bossola** for measuring the gas sorption isotherms.

– **Marcello Marelli** for doing the EFTEM and tomography experiments.

Finally yet importantly, thanks to my **father** and **Robert** for their continuous support, patience and love during my studies and research career. Thank you both for always being at my side!

References

(1) Slater, A. G.; Cooper, A. I. *Science* **2015**, *348* (6238), 8075. DOI: 10.1126/science.aaa8075.

(2) A. Z. Werner. *Anorg. Allg. Chem.* **1895**, *8*, 153–188.

(3) Buser, H. J.; Schwarzenbach, D.; Petter, W.; Ludi, A. *Inorganic chemistry* **1977**, *16* (11), 2704–2710. DOI: 10.1021/ic50177a008.

(4) Simonov, A.; Baerdemaeker, T. de; Boström, H. L. B.; Ríos Gómez, M. L.; Gray, H. J.; Chernyshov, D.; Bosak, A.; Bürgi, H.-B.; Goodwin, A. L. *Nature* **2020**, *578* (7794), 256–260. DOI: 10.1038/s41586-020-1980-y.

(5) K.A. Hofmann, F. K. *Z. Compounds of hydrocarbons with metal salts*, 1897.

(6) Rayner, J. H.; Powell, H. M. *J. Chem. Soc.* **1952**, 319–328. DOI: 10.1039/JR9520000319.

(7) Kinoshita, Y.; Matsubara, I.; Higuchi, T.; Saito, Y. *Bulletin of the Chemical Society of Japan* **1959**, *32* (11), 1221–1226. DOI: 10.1246/bcsj.32.1221.

(8) Kinoshita, Y.; Matsubara, I.; Saito, Y. *Bulletin of the Chemical Society of Japan* **1959**, *32* (11), 1216–1221. DOI: 10.1246/bcsj.32.1216.

(9) Kinoshita, Y.; Matsubara, I.; Saito, Y. *Bulletin of the Chemical Society of Japan* **1959**, *32* (7), 741–747. DOI: 10.1246/bcsj.32.741.

(10) KEGGIN, J. F.; MILES, F. D. *Nature* **1936**, *137* (3466), 577–578. DOI: 10.1038/137577a0.

(11) Cronstedt Axel Fredric. *Rön och beskrifning om en obekant bärg art, som kallas Zeolites*, 1756.

(12) Colella, C.; Gualtieri, A. F. *Microporous and Mesoporous Materials* **2007**, *105* (3), 213–221. DOI: 10.1016/j.micromeso.2007.04.056.

(13) Batten, S. R.; Champness, N. R.; Chen, X.-M.; Garcia-Martinez, J.; Kitagawa, S.; Öhrström, L.; O'Keeffe, M.; Paik Suh, M.; Reedijk, J. *Pure and Applied Chemistry* **2013**, *85* (8), 1715–1724. DOI: 10.1351/PAC-REC-12-11-20.

(14) Yaghi, O. M.; Li, H. *J. Am. Chem. Soc.* **1995**, *117* (41), 10401–10402. DOI: 10.1021/ja00146a033.

(15) Kitagawa, S.; Kitaura, R.; Noro, S. *Angew. Chem. Int. Ed.* **2004**, *43* (18), 2334–2375. DOI: 10.1002/anie.200300610.

(16) O'Keeffe, M.; Yaghi, O. M. *Chemical reviews* **2012**, *112* (2), 675–702. DOI: 10.1021/cr200205j.

(17) Rungtaweevoranit, B.; Diercks, C. S.; Kalmutzki, M. J.; Yaghi, O. M. *Faraday discussions* **2017**, *201*, 9–45. DOI: 10.1039/c7fd00160f.

(18) Diercks, C. S.; Kalmutzki, M. J.; Diercks, N. J.; Yaghi, O. M. *ACS central science* **2018**, *4* (11), 1457–1464. DOI: 10.1021/acscentsci.8b00677.

(19) Kalmutzki, M. J.; Hanikel, N.; Yaghi, O. M. *Science advances* **2018**, *4* (10), 9180. DOI: 10.1126/sciadv.aat9180.

(20) Moghadam, P. Z.; Li, A.; Wiggin, S. B.; Tao, A.; Maloney, A. G. P.; Wood, P. A.; Ward, S. C.; Fairen-Jimenez, D. *Chemistry of Materials* **2017**, *29* (7), 2618–2625. DOI: 10.1021/acs.chemmater.7b00441.

(21) Furukawa, H.; Müller, U.; Yaghi, O. M. *Angewandte Chemie Int. Ed.* **2015**, *54* (11), 3417–3430. DOI: 10.1002/anie.201410252.

(22) Howarth, A. J.; Peters, A. W.; Vermeulen, N. A.; Wang, T. C.; Hupp, J. T.; Farha, O. K. *Chemistry of Materials* **2017**, *29* (1), 26–39. DOI: 10.1021/acs.chemmater.6b02626.

(23) Seoane, B.; Castellanos, S.; Dikhtiarenko, A.; Kapteijn, F.; Gascon, J. *Coordination Chemistry Reviews* **2016**, *307*, 147–187. DOI: 10.1016/j.ccr.2015.06.008.

(24) Kitagawa, S.; Kondo, M. *Bulletin of the Chemical Society of Japan* **1998**, *71* (8), 1739–1753. DOI: 10.1246/bcsj.71.1739.

(25) Horike, S.; Shimomura, S.; Kitagawa, S. *Nature chemistry* **2009**, *1* (9), 695–704. DOI: 10.1038/nchem.444.

(26) Férey, G. *New Journal of Chemistry* **2016**, *40* (5), 3950–3967. DOI: 10.1039/C5NJ02747K.

(27) Kitagawa, S. *Angewandte Chemie Int. Ed.* **2015**, *54* (37), 10686–10687. DOI: 10.1002/anie.201503835.

(28) Kitagawa, S. *Accounts of Chemical Research* **2017**, *50* (3), 514–516. DOI: 10.1021/acs.accounts.6b00500.

(29) Falcaro, P.; Ricco, R.; Doherty, C. M.; Liang, K.; Hill, A. J.; Styles, M. J. *Chemical Society reviews* **2014**, *43* (16), 5513–5560. DOI: 10.1039/c4cs00089g.

(30) Zhang, Z.; Nguyen, H. T. H.; Miller, S. A.; Cohen, S. M. *Angewandte Chemie Int. Ed.* **2015**, *54* (21), 6152–6157. DOI: 10.1002/anie.201502733.

(31) Furukawa, S.; Reboul, J.; Diring, S.; Sumida, K.; Kitagawa, S. *Chemical Society reviews* **2014**, *43* (16), 5700–5734. DOI: 10.1039/c4cs00106k.

(32) Fang, Z.; Bueken, B.; Vos, D. E. de; Fischer, R. A. *Angewandte Chemie Int. Ed.* **2015**, *54* (25), 7234–7254. DOI: 10.1002/anie.201411540.

(33) Braga, D.; Grepioni, F. *Making crystals by design*:*Methods, techniques and applications*; Wiley-VCH, 2007.

(34) Sing, K. S. W. *Pure and Applied Chemistry* **1985**, *57* (4), 603–619. DOI: 10.1351/pac198557040603.

(35) Thommes, M.; Kaneko, K.; Neimark, A. V.; Olivier, J. P.; Rodriguez-Reinoso, F.; Rouquerol, J.; Sing, K. S. *Pure and Applied Chemistry* **2015**, *87* (9-10), 1051–1069. DOI: 10.1515/pac-2014-1117.

(36) Thommes, M.; Cychosz, K. A. *Adsorption* **2014**, *20* (2-3), 233–250. DOI: 10.1007/s10450-014-9606-z.

(37) Monson, P. A. *Microporous and Mesoporous Materials* **2012**, *160*, 47–66. DOI: 10.1016/j.micromeso.2012.04.043.

(38) Yaghi, O. M.; O'Keeffe, M.; Ockwig, N. W.; Chae, H. K.; Eddaoudi, M.; Kim, J. *Nature* **2003**, *423* (6941), 705–714. DOI: 10.1038/nature01650.

(39) Hasegawa, S.; Horike, S.; Matsuda, R.; Furukawa, S.; Mochizuki, K.; Kinoshita, Y.; Kitagawa, S. *J. Am. Chem. Soc.* **2007**, *129* (9), 2607–2614. DOI: 10.1021/ja067374y.

(40) He, J.; Yee, K.-K.; Xu, Z.; Zeller, M.; Hunter, A. D.; Chui, S. S.-Y.; Che, C.-M. *Chemistry of Materials* **2011**, *23* (11), 2940–2947. DOI: 10.1021/cm200557e.

(41) Henke, S.; Schmid, R.; Grunwaldt, J.-D.; Fischer, R. A. *Chemistry* **2010**, *16* (48), 14296–14306. DOI: 10.1002/chem.201002341.

(42) Henke, S.; Florian Wieland, D. C.; Meilikhov, M.; Paulus, M.; Sternemann, C.; Yusenko, K.; Fischer, R. A. *CrystEngComm* **2011**, *13* (21), 6399. DOI: 10.1039/c1ce05446e.

(43) Cohen, S. M. *Chemical reviews* **2012**, *112* (2), 970–1000. DOI: 10.1021/cr200179u.

(44) Wang, Z.; Cohen, S. M. *J. Am. Chem. Soc.* **2007**, *129* (41), 12368–12369. DOI: 10.1021/ja074366o.

(45) Burrows, A. D.; Frost, C. G.; Mahon, M. F.; Richardson, C. *Angewandte Chemie Int. Ed.* **2008**, *47* (44), 8482–8486. DOI: 10.1002/anie.200802908.

(46) Wang, Z.; Cohen, S. M. *J. Am. Chem. Soc.* **2009**, *131* (46), 16675–16677. DOI: 10.1021/ja907742z.

(47) Gadzikwa, T.; Farha, O. K.; Malliakas, C. D.; Kanatzidis, M. G.; Hupp, J. T.; Nguyen, S. T. *J. Am. Chem. Soc.* **2009**, *131* (38), 13613–13615. DOI: 10.1021/ja904189d.

(48) Savonnet, M.; Bazer-Bachi, D.; Bats, N.; Perez-Pellitero, J.; Jeanneau, E.; Lecocq, V.; Pinel, C.; Farrusseng, D. *J. Am. Chem. Soc.* **2010**, *132* (13), 4518–4519. DOI: 10.1021/ja909613e.

(49) Yamada, T.; Kitagawa, H. *J. Am. Chem. Soc.* **2009**, *131* (18), 6312–6313. DOI: 10.1021/ja809352y.

(50) Tanabe, K. K.; Allen, C. A.; Cohen, S. M. *Angewandte Chemie Int. Ed.* **2010**, *49* (50), 9730–9733. DOI: 10.1002/anie.201004736.

(51) Lun, D. J.; Waterhouse, G. I. N.; Telfer, S. G. *J. Am. Chem. Soc.* **2011**, *133* (15), 5806–5809. DOI: 10.1021/ja202223d.

(52) Takaishi, S.; DeMarco, E. J.; Pellin, M. J.; Farha, O. K.; Hupp, J. T. *Chemical science* **2013**, *4* (4), 1509. DOI: 10.1039/c2sc21516k.

(53) Karagiaridi, O.; Bury, W.; Mondloch, J. E.; Hupp, J. T.; Farha, O. K. *Angewandte Chemie Int. Ed.* **2014**, *53* (18), 4530–4540. DOI: 10.1002/anie.201306923.

(54) Kalaj, M.; Cohen, S. M. *ACS central science* **2020**, *6* (7), 1046–1057. DOI: 10.1021/acscentsci.0c00690.

(55) Banerjee, D.; Kim, S. J.; Wu, H.; Xu, W.; Borkowski, L. A.; Li, J.; Parise, J. B. *Inorg. Chem.* **2011**, *50* (1), 208–212. DOI: 10.1021/ic101789u.

(56) An, J.; Geib, S. J.; Rosi, N. L. *J. Am. Chem. Soc.* **2009**, *131* (24), 8376–8377. DOI: 10.1021/ja902972w.

(57) Yang, Q.; Xu, Q.; Jiang, H.-L. *Chemical Society reviews* **2017**, *46* (15), 4774–4808. DOI: 10.1039/c6cs00724d.

(58) Li, G.; Zhao, S.; Zhang, Y.; Tang, Z. *Advanced materials* **2018**, *30* (51), e1800702. DOI: 10.1002/adma.201800702.

(59) Li, B.; Ma, J.-G.; Cheng, P. *Small* **2019**, *15* (32), e1804849. DOI: 10.1002/smll.201804849.

(60) Siegelman, R. L.; McDonald, T. M.; Gonzalez, M. I.; Martell, J. D.; Milner, P. J.; Mason, J. A.; Berger, A. H.; Bhown, A. S.; Long, J. R. *J. Am. Chem. Soc.* **2017**, *139* (30), 10526–10538. DOI: 10.1021/jacs.7b05858.

(61) Hwang, Y. K.; Hong, D.-Y.; Chang, J.-S.; Jhung, S. H.; Seo, Y.-K.; Kim, J.; Vimont, A.; Daturi, M.; Serre, C.; Férey, G. *Angewandte Chemie Int. Ed.* **2008**, *47* (22), 4144–4148. DOI: 10.1002/anie.200705998.

(62) Kökçam-Demir, Ü.; Goldman, A.; Esrafili, L.; Gharib, M.; Morsali, A.; Weingart, O.; Janiak, C. *Chemical Society reviews* **2020**, *49* (9), 2751–2798. DOI: 10.1039/c9cs00609e.

(63) Fukushima, T.; Horike, S.; Inubushi, Y.; Nakagawa, K.; Kubota, Y.; Takata, M.; Kitagawa, S. *Angew. Chem. Int. Ed.* **2010**, *49* (28), 4820–4824. DOI: 10.1002/anie.201000989.

(64) Deng, H.; Doonan, C. J.; Furukawa, H.; Ferreira, R. B.; Towne, J.; Knobler, C. B.; Wang, B.; Yaghi, O. M. *Science* **2010**, *327* (5967), 846–850. DOI: 10.1126/science.1181761.

(65) Chen, L.; Wang, H.-F.; Li, C.; Xu, Q. *Chemical science* **2020**, *11* (21), 5369–5403. DOI: 10.1039/D0SC01432J.

(66) Zones, S.; Cejka, J.; Corma, A. *Volume 1*; Zeolites and catalysis, Vol. 1; Wiley-VCH Verlag, 2010.

(67) *Database of Zeolite Structures, www.iza-structure.org/databases*.

(68) Silva, P.; Vilela, S. M. F.; Tomé, J. P. C.; Almeida Paz, F. A. *Chemical Society reviews* **2015**, *44* (19), 6774–6803. DOI: 10.1039/c5cs00307e.

(69) www.moftechnologies.com, www.numat-tech.com, www.novomof.com, www.particularmaterials.com, www.mosaicmaterials.com.

(70) Meek, S. T.; Greathouse, J. A.; Allendorf, M. D. *Advanced materials* **2011**, *23* (2), 249–267. DOI: 10.1002/adma.201002854.

(71) Petit, C. *Current Opinion in Chemical Engineering* **2018**, *20*, 132–142. DOI: 10.1016/j.coche.2018.04.004.

(72) Zhao, X.; Wang, Y.; Li, D.-S.; Bu, X.; Feng, P. *Advanced materials* **2018**, *30* (37), e1705189. DOI: 10.1002/adma.201705189.

(73) Lin, R.-B.; Xiang, S.; Xing, H.; Zhou, W.; Chen, B. *Coordination Chemistry Reviews* **2019**, *378*, 87–103. DOI: 10.1016/j.ccr.2017.09.027.

(74) Kang, Y.-S.; Lu, Y.; Chen, K.; Zhao, Y.; Wang, P.; Sun, W.-Y. *Coordination Chemistry Reviews* **2019**, *378*, 262–280. DOI: 10.1016/j.ccr.2018.02.009.

(75) Xu, C.; Fang, R.; Luque, R.; Chen, L.; Li, Y. *Coordination Chemistry Reviews* **2019**, *388*, 268–292. DOI: 10.1016/j.ccr.2019.03.005.

(76) Bavykina, A.; Kolobov, N.; Khan, I. S.; Bau, J. A.; Ramirez, A.; Gascon, J. *Chemical reviews* **2020**, *120* (16), 8468–8535. DOI: 10.1021/acs.chemrev.9b00685.

(77) Rojas, S.; Horcajada, P. *Chemical reviews* **2020**, *120* (16), 8378–8415. DOI: 10.1021/acs.chemrev.9b00797.

(78) Yang, J.; Yang, Y.-W. *Small* **2020**, *16* (10), e1906846. DOI: 10.1002/smll.201906846.

(79) Wang, H.; Lustig, W. P.; Li, J. *Chemical Society reviews* **2018**, *47* (13), 4729–4756. DOI: 10.1039/c7cs00885f.

(80) Denny, M. S.; Moreton, J. C.; Benz, L.; Cohen, S. M. *Nature Reviews Materials* **2016**, *1* (12). DOI: 10.1038/natrevmats.2016.78.

(81) Islamoglu, T.; Chen, Z.; Wasson, M. C.; Buru, C. T.; Kirlikovali, K. O.; Afrin, U.; Mian, M. R.; Farha, O. K. *Chemical reviews* **2020**, *120* (16), 8130–8160. DOI: 10.1021/acs.chemrev.9b00828.

(82) Zagorodniy, K.; Seifert, G.; Hermann, H. *Appl. Phys. Lett.* **2010**, *97* (25), 251905. DOI: 10.1063/1.3529461.

(83) Sun, L.; Campbell, M. G.; Dincă, M. *Angewandte Chemie Int. Ed.* **2016**, *55* (11), 3566–3579. DOI: 10.1002/anie.201506219.

(84) Sato, H.; Kosaka, W.; Matsuda, R.; Hori, A.; Hijikata, Y.; Belosludov, R. V.; Sakaki, S.; Takata, M.; Kitagawa, S. *Science* **2014**, *343* (6167), 167–170. DOI: 10.1126/science.1246423.

(85) Wang, H.; Dong, X.; Colombo, V.; Wang, Q.; Liu, Y.; Liu, W.; Wang, X.-L.; Huang, X.-Y.; Proserpio, D. M.; Sironi, A.; Han, Y.; Li, J. *Advanced materials* **2018**, *30* (49), e1805088. DOI: 10.1002/adma.201805088.

(86) Li, H.; Li, L.; Lin, R.-B.; Zhou, W.; Zhang, Z.; Xiang, S.; Chen, B. *EnergyChem* **2019**, *1* (1), 100006. DOI: 10.1016/j.enchem.2019.100006.

(87) Gomollón-Bel, F. *Chemistry International* **2019**, *41* (2), 12–17. DOI: 10.1515/ci-2019-0203.

(88) R.K. Pachauri and L.A. Meyer. *Climate Change 2014: Synthesis Report. Contribution of Working Groups I, II and III to the Fifth Assessment Report of the Intergovernmental Panel on Climate Change*.

(89) UNFCCC. *Paris Agreement to the United Nations Framework Convention on Climate Change*.

(90) Blandford, D.; K. Hassapoyannes. *OECD Food, Agriculture and Fisheries Papers* **2018** (112).

(91) Jens K. Nørskov, Gabriele Centi, Robert Schloegl, Bert Weckhuysen, Ib Chorkendorff, Christoph Schmidt. *Research needs towards sustainable production of fuels and chemicals*. www.energy-x.eu/wp-content/uploads/2019/09/Energy_X_Research-needs-report.pdf.

(92) Ed Dlugokencky; Pieter Tans. *Trends in Atmospheric Carbon Dioxide*. www.gml.noaa.gov/ccgg/trends/.

(93) European Parliament Council. *Official Journal of the European Union* **2009**, *L140*, 114–135.

(94) Breeze, P., Ed. *Chapter 7 - Carbon Capture and Storage*; Elsevier, 2015. DOI: 10.1016/B978-0-12-804006-5.00013-7.

(95) Jansen, D.; Gazzani, M.; Manzolini, G.; van Dijk, E.; Carbo, M. *International Journal of Greenhouse Gas Control* **2015**, *40*, 167–187. DOI: 10.1016/j.ijggc.2015.05.028.

(96) Sanz-Pérez, E. S.; Murdock, C. R.; Didas, S. A.; Jones, C. W. *Chemical reviews* **2016**, *116* (19), 11840–11876. DOI: 10.1021/acs.chemrev.6b00173.

(97) Leung, D. Y.; Caramanna, G.; Maroto-Valer, M. M. *Renewable and Sustainable Energy Reviews* **2014**, *39*, 426–443. DOI: 10.1016/j.rser.2014.07.093.

(98) D'Alessandro, D. M.; Smit, B.; Long, J. R. *Angewandte Chemie Int. Ed.* **2010**, *49* (35), 6058–6082. DOI: 10.1002/anie.201000431.

(99) DAVISON, J. *Energy* **2007**, *32* (7), 1163–1176. DOI: 10.1016/j.energy.2006.07.039.

(100) Patel, H. A.; Byun, J.; Yavuz, C. T. *ChemSusChem* **2017**, *10* (7), 1303–1317. DOI: 10.1002/cssc.201601545.

(101) Darren Broom. *Chemical Engineering Progress* **2018**, 30–37.

(102) Valenzano, L.; Civalleri, B.; Chavan, S.; Palomino, G. T.; Areán, C. O.; Bordiga, S. *J. Phys. Chem. C* **2010**, *114* (25), 11185–11191. DOI: 10.1021/jp102574f.

(103) Graham, C.; Pierrus, J.; Raab, R. E. *Molecular Physics* **1989**, *67* (4), 939–955. DOI: 10.1080/00268978900101551.

(104) Lee, J.-S.; Kim, J.-H.; Kim, J.-T.; Suh, J.-K.; Lee, J.-M.; Lee, C.-H. *J. Chem. Eng. Data* **2002**, *47* (5), 1237–1242. DOI: 10.1021/je020050e.

(105) Sanz-Pérez, E.; Arencibia Villagrá, A.; Sanz Martín, R.; Calleja Pardo, G. *Materiales en Adsorción y Catálisis* **2012** (3), 5–16.

(106) van der Vaart, R. *Adsorption* **2000**, *6* (4), 311–323. DOI: 10.1023/A:1026560915422.

(107) Li, J.-R.; Kuppler, R. J.; Zhou, H.-C. *Chemical Society reviews* **2009**, *38* (5), 1477–1504. DOI: 10.1039/b802426j.

(108) Kuppler, R. J.; Timmons, D. J.; Fang, Q.-R.; Li, J.-R.; Makal, T. A.; Young, M. D.; Yuan, D.; Zhao, D.; Zhuang, W.; Zhou, H.-C. *Coordination Chemistry Reviews* **2009**, *253* (23-24), 3042–3066. DOI: 10.1016/j.ccr.2009.05.019.

(109) Morris, R. E.; Wheatley, P. S. *Angewandte Chemie Int. Ed.* **2008**, *47* (27), 4966–4981. DOI: 10.1002/anie.200703934.

(110) Sumida, K.; Rogow, D. L.; Mason, J. A.; McDonald, T. M.; Bloch, E. D.; Herm, Z. R.; Bae, T.-H.; Long, J. R. *Chemical reviews* **2012**, *112* (2), 724–781. DOI: 10.1021/cr2003272.

(111) Yaghi, O. M.; Kalmutzki, M. J.; Diercks, C. S. *Introduction to reticular chemistry*:*Metal-organic frameworks and covalent organic frameworks*; Wiley, 2019.

(112) Reinsch, H.; Waitschat, S.; Stock, N. *Dalton Transactions* **2013**, *42* (14), 4840–4847. DOI: 10.1039/c3dt32355b.

(113) Eum, K.; Jayachandrababu, K. C.; Rashidi, F.; Zhang, K.; Leisen, J.; Graham, S.; Lively, R. P.; Chance, R. R.; Sholl, D. S.; Jones, C. W.; Nair, S. *J. Am. Chem. Soc.* **2015**, *137* (12), 4191–4197. DOI: 10.1021/jacs.5b00803.

(114) Demessence, A.; D'Alessandro, D. M.; Foo, M. L.; Long, J. R. *J. Am. Chem. Soc.* **2009**, *131* (25), 8784–8786. DOI: 10.1021/ja903411w.

(115) Debatin, F.; Thomas, A.; Kelling, A.; Hedin, N.; Bacsik, Z.; Senkovska, I.; Kaskel, S.; Junginger, M.; Müller, H.; Schilde, U.; Jäger, C.; Friedrich, A.; Holdt, H.-J. *Angewandte Chemie Int. Ed.* **2010**, *49* (7), 1258–1262. DOI: 10.1002/anie.200906188.

(116) Gassensmith, J. J.; Furukawa, H.; Smaldone, R. A.; Forgan, R. S.; Botros, Y. Y.; Yaghi, O. M.; Stoddart, J. F. *J. Am. Chem. Soc.* **2011**, *133* (39), 15312–15315. DOI: 10.1021/ja206525x.

(117) Zhang, G.; Wei, G.; Liu, Z.; Oliver, S. R. J.; Fei, H. *Chemistry of Materials* **2016**, *28* (17), 6276–6281. DOI: 10.1021/acs.chemmater.6b02511.

(118) Mosca, N.; Vismara, R.; Fernandes, J. A.; Tuci, G.; Di Nicola, C.; Domasevitch, K. V.; Giacobbe, C.; Giambastiani, G.; Pettinari, C.; Aragones-Anglada, M.; Moghadam, P. Z.; Fairen-Jimenez, D.; Rossin, A.; Galli, S. *Chemistry* **2018**, *24* (50), 13170–13180. DOI: 10.1002/chem.201802240.

(119) Prasad, T. K.; Suh, M. P. *Chemistry* **2012**, *18* (28), 8673–8680. DOI: 10.1002/chem.201200456.

(120) Taylor, M. K.; Runčevski, T.; Oktawiec, J.; Bachman, J. E.; Siegelman, R. L.; Jiang, H.; Mason, J. A.; Tarver, J. D.; Long, J. R. *J. Am. Chem. Soc.* **2018**, *140* (32), 10324–10331. DOI: 10.1021/jacs.8b06062.

(121) Trickett, C. A.; Helal, A.; Al-Maythalony, B. A.; Yamani, Z. H.; Cordova, K. E.; Yaghi, O. M. *Nature Reviews Materials* **2017**, *2* (8). DOI: 10.1038/natrevmats.2017.45.

(122) Ding, M.; Flaig, R. W.; Jiang, H.-L.; Yaghi, O. M. *Chemical Society reviews* **2019**, *48* (10), 2783–2828. DOI: 10.1039/c8cs00829a.

(123) Liu, J.; Wei, Y.; Zhao, Y. *ACS Sustainable Chem. Eng.* **2019**, *7* (1), 82–93. DOI: 10.1021/acssuschemeng.8b05590.

(124) Millward, A. R.; Yaghi, O. M. *J. Am. Chem. Soc.* **2005**, *127* (51), 17998–17999. DOI: 10.1021/ja0570032.

(125) Aniruddha, R.; Sreedhar, I.; Reddy, B. M. *Journal of CO_2 Utilization* **2020**, *42*, 101297. DOI: 10.1016/j.jcou.2020.101297.

(126) Elhenawy, S. E. M.; Khraisheh, M.; AlMomani, F.; Walker, G. *Catalysts* **2020**, *10* (11), 1293. DOI: 10.3390/catal10111293.

(127) Bao, Z.; Yu, L.; Ren, Q.; Lu, X.; Deng, S. *Journal of colloid and interface science* **2011**, *353* (2), 549–556. DOI: 10.1016/j.jcis.2010.09.065.

(128) Lin, J.-B.; Nguyen, T. T. T.; Vaidhyanathan, R.; Burner, J.; Taylor, J. M.; Durekova, H.; Akhtar, F.; Mah, R. K.; Ghaffari-Nik, O.; Marx, S.; Fylstra, N.; Iremonger, S. S.; Dawson, K. W.; Sarkar, P.; Hovington, P.; Rajendran, A.; Woo, T. K.; Shimizu, G. K. H. *Science* **2021**, *374* (6574), 1464–1469. DOI: 10.1126/science.abi7281.

(129) Cavka, J. H.; Jakobsen, S.; Olsbye, U.; Guillou, N.; Lamberti, C.; Bordiga, S.; Lillerud, K. P. *Journal of the American Chemical Society* **2008**, *130* (42), 13850–13851. DOI: 10.1021/ja8057953.

(130) Yao, Q.; Bermejo Gómez, A.; Su, J.; Pascanu, V.; Yun, Y.; Zheng, H.; Chen, H.; Liu, L.; Abdelhamid, H. N.; Martín-Matute, B.; Zou, X. *Chemistry of Materials* **2015**, *27* (15), 5332–5339. DOI: 10.1021/acs.chemmater.5b01711.

(131) Burtch, N. C.; Jasuja, H.; Walton, K. S. *Chemical reviews* **2014**, *114* (20), 10575–10612. DOI: 10.1021/cr5002589.

(132) Yuan, S.; Feng, L.; Wang, K.; Pang, J.; Bosch, M.; Lollar, C.; Sun, Y.; Qin, J.; Yang, X.; Zhang, P.; Wang, Q.; Zou, L.; Zhang, Y.; Zhang, L.; Fang, Y.; Li, J.; Zhou, H.-C. *Advanced materials* **2018**, *30* (37), e1704303. DOI: 10.1002/adma.201704303.

(133) Rosi, N. L.; Eckert, J.; Eddaoudi, M.; Vodak, D. T.; Kim, J.; O'Keeffe, M.; Yaghi, O. M. *Science* **2003**, *300* (5622), 1127–1129. DOI: 10.1126/science.1083440.

(134) Kang, I. J.; Khan, N. A.; Haque, E.; Jhung, S. H. *Chemistry* **2011**, *17* (23), 6437–6442. DOI: 10.1002/chem.201100316.

(135) Loiseau, T.; Serre, C.; Huguenard, C.; Fink, G.; Taulelle, F.; Henry, M.; Bataille, T.; Férey, G. *Chemistry* **2004**, *10* (6), 1373–1382. DOI: 10.1002/chem.200305413.

(136) Li, Z.; Zeng, H. C. *Journal of the American Chemical Society* **2014**, *136* (15), 5631–5639. DOI: 10.1021/ja409675j.

(137) Férey, G.; Mellot-Draznieks, C.; Serre, C.; Millange, F.; Dutour, J.; Surblé, S.; Margiolaki, I. *Science* **2005**, *309* (5743), 2040–2042. DOI: 10.1126/science.1116275.

(138) Leus, K.; Bogaerts, T.; Decker, J. de; Depauw, H.; Hendrickx, K.; Vrielinck, H.; van Speybroeck, V.; van der Voort, P. *Microporous and Mesoporous Materials* **2016**, *226*, 110–116. DOI: 10.1016/j.micromeso.2015.11.055.

(139) Park, K. S.; Ni, Z.; Côté, A. P.; Choi, J. Y.; Huang, R.; Uribe-Romo, F. J.; Chae, H. K.; O'Keeffe, M.; Yaghi, O. M. *Proceedings of the National Academy of Sciences of the United States of America* **2006**, *103* (27), 10186–10191. DOI: 10.1073/pnas.0602439103.

(140) Huang, X.-C.; Lin, Y.-Y.; Zhang, J.-P.; Chen, X.-M. *Angewandte Chemie Int. Ed.* **2006**, *45* (10), 1557–1559. DOI: 10.1002/anie.200503778.

(141) Colombo, V.; Galli, S.; Choi, H. J.; Han, G. D.; Maspero, A.; Palmisano, G.; Masciocchi, N.; Long, J. R. *Chemical science* **2011**, *2* (7), 1311. DOI: 10.1039/c1sc00136a.

(142) Li, H.; Shi, W.; Zhao, K.; Li, H.; Bing, Y.; Cheng, P. *Inorganic chemistry* **2012**, *51* (17), 9200–9207. DOI: 10.1021/ic3002898.

(143) Montoro, C.; Linares, F.; Procopio, E. Q.; Senkovska, I.; Kaskel, S.; Galli, S.; Masciocchi, N.; Barea, E.; Navarro, J. A. R. *J. Am. Chem. Soc.* **2011**, *133* (31), 11888–11891. DOI: 10.1021/ja2042113.

(144) Yang, J.; Grzech, A.; Mulder, F. M.; Dingemans, T. J. *Chemical communications* **2011**, *47* (18), 5244–5246. DOI: 10.1039/c1cc11054c.

(145) Tan, Y.-X.; He, Y.-P.; Zhang, J. *Inorg. Chem.* **2012**, *51* (18), 9649–9654. DOI: 10.1021/ic300778m.

(146) Jasuja, H.; Walton, K. S. *Dalton Transactions* **2013**, *42* (43), 15421–15426. DOI: 10.1039/C3DT51819A.

(147) Yang, J.; Wang, X.; Dai, F.; Zhang, L.; Wang, R.; Sun, D. *Inorg. Chem.* **2014**, *53* (19), 10649–10653. DOI: 10.1021/ic5017092.

(148) Nguyen, J. G.; Cohen, S. M. *Journal of the American Chemical Society* **2010**, *132* (13), 4560–4561. DOI: 10.1021/ja100900c.

(149) Zhang, W.; Hu, Y.; Ge, J.; Jiang, H.-L.; Yu, S.-H. *Journal of the American Chemical Society* **2014**, *136* (49), 16978–16981. DOI: 10.1021/ja509960n.

(150) Zu, D.-D.; Lu, L.; Liu, X.-Q.; Zhang, D.-Y.; Sun, L.-B. *J. Phys. Chem. C* **2014**, *118* (34), 19910–19917. DOI: 10.1021/jp506335x.

(151) Gamage, N.-D. H.; McDonald, K. A.; Matzger, A. J. *Angewandte Chemie Int. Ed.* **2016**, *55* (39), 12099–12103. DOI: 10.1002/anie.201606926.

(152) Ding, N.; Li, H.; Feng, X.; Wang, Q.; Wang, S.; Ma, L.; Zhou, J.; Wang, B. *Journal of the American Chemical Society* **2016**, *138* (32), 10100–10103. DOI: 10.1021/jacs.6b06051.

(153) Wu, C.-M.; Rathi, M.; Ahrenkiel, S. P.; Koodali, R. T.; Wang, Z. *Chemical communications* **2013**, *49* (12), 1223–1225. DOI: 10.1039/c2cc38366g.

(154) Yoo, Y.; Varela-Guerrero, V.; Jeong, H.-K. *Langmuir: the ACS journal of surfaces and colloids* **2011**, *27* (6), 2652–2657. DOI: 10.1021/la104775d.

(155) DeCoste, J. B.; Denny, M. S.; Peterson, G. W.; Mahle, J. J.; Cohen, S. M. *Chemical science* **2016**, *7* (4), 2711–2716. DOI: 10.1039/c5sc04368a.

(156) Armstrong, M.; Sirous, P.; Shan, B.; Wang, R.; Zhong, C.; Liu, J.; Mu, B. *Microporous and Mesoporous Materials* **2018**, *270*, 34–39. DOI: 10.1016/j.micromeso.2018.05.004.

(157) Yang, S. J.; Choi, J. Y.; Chae, H. K.; Cho, J. H.; Nahm, K. S.; Park, C. R. *Chemistry of Materials* **2009**, *21* (9), 1893–1897. DOI: 10.1021/cm803502y.

(158) Wang, Z.; Bilegsaikhan, A.; Jerozal, R. T.; Pitt, T. A.; Milner, P. J. *ACS applied materials & interfaces* **2021**, *13* (15), 17517–17531. DOI: 10.1021/acsami.1c01329.

(159) DeCoste, J. B.; Peterson, G. W.; Jasuja, H.; Glover, T. G.; Huang, Y.; Walton, K. S. *J. Mater. Chem. A* **2013**, *1* (18), 5642. DOI: 10.1039/c3ta10662d.

(160) Liu, J.; Wei, Y.; Li, P.; Zhao, Y.; Zou, R. *J. Phys. Chem. C* **2017**, *121* (24), 13249–13255. DOI: 10.1021/acs.jpcc.7b04465.

(161) Hamon, L.; Serre, C.; Devic, T.; Loiseau, T.; Millange, F.; Férey, G.; Weireld, G. de. *Journal of the American Chemical Society* **2009**, *131* (25), 8775–8777. DOI: 10.1021/ja901587t.

(162) Rieth, A. J.; Tulchinsky, Y.; Dincă, M. *Journal of the American Chemical Society* **2016**, *138* (30), 9401–9404. DOI: 10.1021/jacs.6b05723.

(163) Cozzolino, A. F.; Brozek, C. K.; Palmer, R. D.; Yano, J.; Li, M.; Dincă, M. *Journal of the American Chemical Society* **2014**, *136* (9), 3334–3337. DOI: 10.1021/ja411808r.

(164) Tulchinsky, Y.; Hendon, C. H.; Lomachenko, K. A.; Borfecchia, E.; Melot, B. C.; Hudson, M. R.; Tarver, J. D.; Korzyński, M. D.; Stubbs, A. W.; Kagan, J. J.; Lamberti, C.; Brown, C. M.; Dincă, M. *Journal of the American Chemical Society* **2017**, *139* (16), 5992–5997. DOI: 10.1021/jacs.7b02161.

(165) Vismara, R.; Terruzzi, S.; Maspero, A.; Grell, T.; Bossola, F.; Sironi, A.; Galli, S.; Navarro, J.A.R. and Colombo, V. *J. Am. Chem. Soc.* **2022**, *manuscript in submission*.

(166) Galli, S.; Maspero, A.; Giacobbe, C.; Palmisano, G.; Nardo, L.; Comotti, A.; Bassanetti, I.; Sozzani, P.; Masciocchi, N. *J. Mater. Chem. A* **2014**, *2* (31), 12208. DOI: 10.1039/C4TA01798F.

(167) Pearson, R. G. *J. Am. Chem. Soc.* **1963**, *85* (22), 3533–3539. DOI: 10.1021/ja00905a001.

(168) Howarth, A. J.; Liu, Y.; Li, P.; Li, Z.; Wang, T. C.; Hupp, J. T.; Farha, O. K. *Nature Reviews Materials* **2016**, *1* (3). DOI: 10.1038/natrevmats.2015.18.

(169) Julien, P. A.; Mottillo, C.; Friščić, T. *Green Chemistry* **2017**, *19* (12), 2729–2747. DOI: 10.1039/C7GC01078H.

(170) Eicher, T.; Speicher, A.; Hauptmann, S.; Suschitzky, H. *The chemistry of heterocycles*:*Structure, reactions, syntheses, and applications*; Wiley-VCH, 2012.

(171) Pozharskiĭ, A. F.; Katritzky, A. R.; Soldatenkov, A. T. *Heterocycles in life and society*:*An introduction to heterocyclic chemistry, biochemistry, and applications*, 2nd ed.; Wiley, 2011.

(172) Corey, E. J.; Kürti, L.; Czako, B. *Molecules and medicine*; J. Wiley, 2007.

(173) Sica, D.; Zollo, F. *Chimica dei composti eterociclici farmacologicamente attivi*; Piccin, 2008.

(174) Reedijk, J. *Heterocyclic Nitrogen-Donor Ligands. Vol. II (73-98)*; Pergamon, Oxford, 1987.

(175) Garnovskii, A. D.; Osipov, O. A.; Kuznetsova, L.,I.; Bogdashev, N. N. *Russ. Chem. Rev* **1973** (42), 89.

(176) Hayashi, H.; Côté, A. P.; Furukawa, H.; O'Keeffe, M.; Yaghi, O. M. *Nature materials* **2007**, *6* (7), 501–506. DOI: 10.1038/nmat1927.

(177) Katritzky, A. R.; Scriven, E. F. V.; Rees, C. W. *Comprehensive heterocyclic chemistry 2*:*A review of the literature 1982-1995 / the structure, reactions, synthesis and uses of heterocyclic compounds*; Pergamon.

(178) La Monica, G.; Ardizzoia, G. A. The Role of the Pyrazolate Ligand in Building Polynuclear Transition Metal Systems. In *Progress in Inorganic Chemistry*; Karlin, K. D., Ed.; Progress in Inorganic Chemistry; John Wiley & Sons, Inc, 1997; pp 151–238. DOI: 10.1002/9780470166475.ch3.

(179) v. Pechmann, H. *Berichte der deutschen chemischen Gesellschaft* **1898**, *31* (3), 2950–2951. DOI: 10.1002/cber.18980310363.

(180) C.H., & Wiley, R.H., Ed. *Pyrazoles, Pyrazolines, Pyrazolidines, Indazoles and Condensed Rings*; Wiley, 1967.

(181) Campo, J. A.; Cano, M.; Heras, J. V.; Pinilla, E.; Monge, A.; McCleverty, J. A. *J. Chem. Soc., Dalton Trans.* **1998** (18), 3065–3070. DOI: 10.1039/a803680b.

(182) Rheingold, A. L.; Ostrander, R. L.; Haggerty, B. S.; Trofimenko, S. *Inorganic chemistry* **1994**, *33* (17), 3666–3676. DOI: 10.1021/ic00095a009.

(183) Marson, C. M. *Tetrahedron* **1992**, *48* (18), 3659–3726. DOI: 10.1016/S0040-4020(01)92263-X.

(184) Schnürch, M.; Flasik, R.; Khan, A. F.; Spina, M.; Mihovilovic, M. D.; Stanetty, P. *Eur. J. Org. Chem.* **2006**, *2006* (15), 3283–3307. DOI: 10.1002/ejoc.200600089.

(185) Pettinari, C.; Tăbăcaru, A.; Boldog, I.; Domasevitch, K. V.; Galli, S.; Masciocchi, N. *Inorganic chemistry* **2012**, *51* (9), 5235–5245. DOI: 10.1021/ic3001416.

(186) Galli, S.; Masciocchi, N.; Colombo, V.; Maspero, A.; Palmisano, G.; López-Garzón, F. J.; Domingo-García, M.; Fernández-Morales, I.; Barea, E.; Navarro, J. A. R. *Chemistry of Materials* **2010**, *22* (5), 1664–1672. DOI: 10.1021/cm902899t.

(187) Masciocchi, N.; Galli, S.; Colombo, V.; Maspero, A.; Palmisano, G.; Seyyedi, B.; Lamberti, C.; Bordiga, S. *J. Am. Chem. Soc.* **2010**, *132* (23), 7902–7904. DOI: 10.1021/ja102862j.

(188) Wade, C. R.; Corrales-Sanchez, T.; Narayan, T. C.; Dincă, M. *Energy Environ. Sci.* **2013**, *6* (7), 2172. DOI: 10.1039/c3ee40876k.

(189) Padial, N. M.; Quartapelle Procopio, E.; Montoro, C.; López, E.; Oltra, J. E.; Colombo, V.; Maspero, A.; Masciocchi, N.; Galli, S.; Senkovska, I.; Kaskel, S.; Barea, E.; Navarro, J. A. R. *Angewandte Chemie Int. Ed.* **2013**, *52* (32), 8290–8294. DOI: 10.1002/anie.201303484.

(190) Choi, H. J.; Dincă, M.; Dailly, A.; Long, J. R. *Energy Environ. Sci.* **2010**, *3* (1), 117–123. DOI: 10.1039/B917512A.

(191) Tăbăcaru, A.; Galli, S.; Pettinari, C.; Masciocchi, N.; McDonald, T. M.; Long, J. R. *CrystEngComm* **2015**, *17* (27), 4992–5001. DOI: 10.1039/C5CE00561B.

(192) Zhang, J.-P.; Zhang, Y.-B.; Lin, J.-B.; Chen, X.-M. *Chemical reviews* **2012**, *112* (2), 1001–1033. DOI: 10.1021/cr200139g.

(193) Choi, H. J.; Dincă, M.; Long, J. R. *J. Am. Chem. Soc.* **2008**, *130* (25), 7848–7850. DOI: 10.1021/ja8024092.

(194) Herm, Z. R.; Wiers, B. M.; Mason, J. A.; van Baten, J. M.; Hudson, M. R.; Zajdel, P.; Brown, C. M.; Masciocchi, N.; Krishna, R.; Long, J. R. *Science* **2013**, *340* (6135), 960–964. DOI: 10.1126/science.1234071.

(195) Hou, L.; Lin, Y.-Y.; Chen, X.-M. *Inorganic chemistry* **2008**, *47* (4), 1346–1351. DOI: 10.1021/ic702085x.

(196) Tonigold, M.; Lu, Y.; Bredenkötter, B.; Rieger, B.; Bahnmüller, S.; Hitzbleck, J.; Langstein, G.; Volkmer, D. *Angew. Chem. Int. Ed.* **2009**, *48* (41), 7546–7550. DOI: 10.1002/anie.200901241.

(197) Xu, J.-Y.; Qiao, X.; Song, H.-B.; Yan, S.-P.; Liao, D.-Z.; Gao, S.; Journaux, Y.; Cano, J. *Chemical communications* **2008** (47), 6414–6416. DOI: 10.1039/b813705f.

(198) Barea, E.; Tagliabue, G.; Wang, W.-G.; Pérez-Mendoza, M.; Mendez-Liñan, L.; López-Garzon, F. J.; Galli, S.; Masciocchi, N.; Navarro, J. A. R. *Chemistry* **2010**, *16* (3), 931–937. DOI: 10.1002/chem.200902346.

(199) Colombo, V.; Montoro, C.; Maspero, A.; Palmisano, G.; Masciocchi, N.; Galli, S.; Barea, E.; Navarro, J. A. R. *J. Am. Chem. Soc.* **2012**, *134* (30), 12830–12843. DOI: 10.1021/ja305267m.

(200) Rodríguez-Albelo, L. M.; López-Maya, E.; Hamad, S.; Ruiz-Salvador, A. R.; Calero, S.; Navarro, J. A. R. *Nature communications* **2017**, *8*, 14457. DOI: 10.1038/ncomms14457.

(201) Vismara, R.; Tuci, G.; Mosca, N.; Domasevitch, K. V.; Di Nicola, C.; Pettinari, C.; Giambastiani, G.; Galli, S.; Rossin, A. *Inorganic Chemistry Frontiers* **2019**, *6* (2), 533–545. DOI: 10.1039/C8QI00997J.

(202) Bury, W.; Walczak, A. M.; Leszczyński, M. K.; Navarro, J. A. R. *J. Am. Chem. Soc.* **2018**, *140* (44), 15031–15037. DOI: 10.1021/jacs.8b09522.

(203) Maspero, A.; Galli, S.; Masciocchi, N.; Palmisano, G. *Chem. Lett.* **2008**, *37* (9), 956–957. DOI: 10.1246/cl.2008.956.

(204) Holý, A.; Arnold, Z. *Collect. Czech. Chem. Commun.* **1965**, *30* (1), 53–60. DOI: 10.1135/cccc19650053.

(205) Gross, R. S.; Guo, Z.; Dyck, B.; Coon, T.; Huang, C. Q.; Lowe, R. F.; Marinkovic, D.; Moorjani, M.; Nelson, J.; Zamani-Kord, S.; Grigoriadis, D. E.; Hoare, S. R. J.; Crowe, P. D.; Bu, J. H.; Haddach, M.; McCarthy,

J.; Saunders, J.; Sullivan, R.; Chen, T.; Williams, J. P. *Journal of medicinal chemistry* **2005**, *48* (18), 5780–5793. DOI: 10.1021/jm049085v.

(206) Jagtap, P. G.; Baloglu, E.; Southan, G. J.; Mabley, J. G.; Li, H.; Zhou, J.; van Duzer, J.; Salzman, A. L.; Szabó, C. *Journal of medicinal chemistry* **2005**, *48* (16), 5100–5103. DOI: 10.1021/jm0502891.

(207) Aubrey, M. L.; Wiers, B. M.; Andrews, S. C.; Sakurai, T.; Reyes-Lillo, S. E.; Hamed, S. M.; Yu, C.-J.; Darago, L. E.; Mason, J. A.; Baeg, J.-O.; Grandjean, F.; Long, G. J.; Seki, S.; Neaton, J. B.; Yang, P.; Long, J. R. *Nature materials* **2018**, *17* (7), 625–632. DOI: 10.1038/s41563-018-0098-1.

(208) Bon, V.; Brunner, E.; Pöppl, A.; Kaskel, S. *Adv. Funct. Mater.* **2020**, *30* (41), 1907847. DOI: 10.1002/adfm.201907847.

(209) Giacobbe, C.; Lavigna, E.; Maspero, A.; Galli, S. *J. Mater. Chem. A* **2017**, *5* (32), 16964–16975. DOI: 10.1039/C7TA04501H.

(210) Braglia, L.; Tavani, F.; Mauri, S.; Edla, R.; Krizmancic, D.; Tofoni, A.; Colombo, V.; D'Angelo, P.; Torelli, P. *The journal of physical chemistry letters* **2021**, *12* (37), 9182–9187. DOI: 10.1021/acs.jpclett.1c02585.

(211) Jaramillo, D. E.; Reed, D. A.; Jiang, H. Z. H.; Oktawiec, J.; Mara, M. W.; Forse, A. C.; Lussier, D. J.; Murphy, R. A.; Cunningham, M.; Colombo, V.; Shuh, D. K.; Reimer, J. A.; Long, J. R. *Nature materials* **2020**, *19* (5), 517–521. DOI: 10.1038/s41563-019-0597-8.

(212) Perego, J.; Bezuidenhout, C. X.; Pedrini, A.; Bracco, S.; Negroni, M.; Comotti, A.; Sozzani, P. *J. Mater. Chem. A* **2020**, *8* (22), 11406–11413. DOI: 10.1039/D0TA02529A.

(213) Biggins, N.; Ziebel, M. E.; Gonzalez, M. I.; Long, J. R. *Chemical science* **2020**, *11* (34), 9173–9180. DOI: 10.1039/D0SC03383A.

(214) Nuhnen, A.; Janiak, C. *Dalton Transactions* **2020**, *49* (30), 10295–10307. DOI: 10.1039/d0dt01784a.

(215) Wang, S.; Cao, T.; Yan, H.; Li, Y.; Lu, J.; Ma, R.; Li, D.; Dou, J.; Bai, J. *Inorganic chemistry* **2016**, *55* (11), 5139–5151. DOI: 10.1021/acs.inorgchem.5b02801.

(216) Manish K Sharma, Prem Lama, Parimal K Bharadwaj. *Crystal Growth & Design* **2011**, *11* (4), 1411–1416.

(217) Miller, S. R.; Wright, P. A.; Devic, T.; Serre, C.; Férey, G.; Llewellyn, P. L.; Denoyel, R.; Gaberova, L.; Filinchuk, Y. *Langmuir : the ACS journal of surfaces and colloids* **2009**, *25* (6), 3618–3626. DOI: 10.1021/la803788u.

(218) Mowat, J. P. S.; Miller, S. R.; Griffin, J. M.; Seymour, V. R.; Ashbrook, S. E.; Thompson, S. P.; Fairen-Jimenez, D.; Banu, A.-M.; Düren, T.; Wright, P. A. *Inorg. Chem.* **2011**, *50* (21), 10844–10858. DOI: 10.1021/ic201387d.

(219) Gao, F.; Li, Y.; Ye, Y.; Zhao, L. *Inorganic Chemistry Communications* **2017**, *86*, 137–139. DOI: 10.1016/j.inoche.2017.10.010.

(220) Myers, A. L.; Prausnitz, J. M. *AIChE J.* **1965**, *11* (1), 121–127. DOI: 10.1002/aic.690110125.

(221) Le Bail, A.; Duroy, H.; Fourquet, J. L. *Materials Research Bulletin* **1988**, *23* (3), 447–452. DOI: 10.1016/0025-5408(88)90019-0.

(222) Yang, Q.; Zhong, C. *The journal of physical chemistry. B* **2005**, *109* (24), 11862–11864. DOI: 10.1021/jp051903n.

(223) Biovia Materials. *Biovia Materials Studio 6.0. Dassault Systémes BIOVIA, San Diego 2018, www.3ds.com/products-services/biovia/products/molecular-modeling-simulation/biovia-materials-studio*.

(224) Chang, Z.; Yang, D.-H.; Xu, J.; Hu, T.-L.; Bu, X.-H. *Advanced materials* **2015**, *27* (36), 5432–5441. DOI: 10.1002/adma.201501523.

(225) Bennett, T. D.; Fuchs, A. H.; Cheetham, A. K.; Coudert, F.-X. *Dalton Transactions* **2016**, *45* (10), 4058–4059. DOI: 10.1039/c6dt90026g.

(226) Férey, G.; Serre, C. *Chemical Society reviews* **2009**, *38* (5), 1380–1399. DOI: 10.1039/b804302g.

(227) Lin, K.-S.; Adhikari, A. K.; Ku, C.-N.; Chiang, C.-L.; Kuo, H. *International Journal of Hydrogen Energy* **2012**, *37* (18), 13865–13871. DOI: 10.1016/j.ijhydene.2012.04.105.

(228) *Basolite® C300, www.sigmaaldrich.com/IT/it/product/aldrich/688614*.

(229) Kondo, A.; Kajiro, H.; Noguchi, H.; Carlucci, L.; Proserpio, D. M.; Ciani, G.; Kato, K.; Takata, M.; Seki, H.; Sakamoto, M.; Hattori, Y.; Okino, F.; Maeda, K.; Ohba, T.; Kaneko, K.; Kanoh, H. *J. Am. Chem. Soc.* **2011**, *133* (27), 10512–10522. DOI: 10.1021/ja201170c.

(230) Kondo, A.; Noguchi, H.; Ohnishi, S.; Kajiro, H.; Tohdoh, A.; Hattori, Y.; Xu, W.-C.; Tanaka, H.; Kanoh, H.; Kaneko, K. *Nano letters* **2006**, *6* (11), 2581–2584. DOI: 10.1021/nl062032b.

(231) Di Li; Kaneko, K. *Chemical Physics Letters* **2001**, *335* (1-2), 50–56. DOI: 10.1016/S0009-2614(00)01419-6.

(232) Millange, F.; Serre, C.; Férey, G. *Chemical communications* **2002** (8), 822–823. DOI: 10.1039/b201381a.

(233) Serre, C.; Mellot-Draznieks, C.; Surblé, S.; Audebrand, N.; Filinchuk, Y.; Férey, G. *Science* **2007**, *315* (5820), 1828–1831. DOI: 10.1126/science.1137975.

(234) Serre, C.; Millange, F.; Thouvenot, C.; Noguès, M.; Marsolier, G.; Louër, D.; Férey, G. *J. Am. Chem. Soc.* **2002**, *124* (45), 13519–13526. DOI: 10.1021/ja0276974.

(235) Chen, B.; Yang, Z.; Zhu, Y.; Xia, Y. *J. Mater. Chem. A* **2014**, *2* (40), 16811–16831. DOI: 10.1039/C4TA02984D.

(236) Senkovska, I.; Hoffmann, F.; Fröba, M.; Getzschmann, J.; Böhlmann, W.; Kaskel, S. *Microporous and Mesoporous Materials* **2009**, *122* (1-3), 93–98. DOI: 10.1016/j.micromeso.2009.02.020.

(237) ZareKarizi, F.; Joharian, M.; Morsali, A. *J. Mater. Chem. A* **2018**, *6* (40), 19288–19329. DOI: 10.1039/C8TA03306D.

(238) Garai, B.; Bon, V.; Walenszus, F.; Khadiev, A.; Novikov, D. V.; Kaskel, S. *Crystal Growth & Design* **2021**, *21* (1), 270–276. DOI: 10.1021/acs.cgd.0c01080.

(239) Sakata, Y.; Furukawa, S.; Kondo, M.; Hirai, K.; Horike, N.; Takashima, Y.; Uehara, H.; Louvain, N.; Meilikhov, M.; Tsuruoka, T.; Isoda, S.; Kosaka, W.; Sakata, O.; Kitagawa, S. *Science* **2013**, *339* (6116), 193–196. DOI: 10.1126/science.1231451.

(240) Zhang, C.; Gee, J. A.; Sholl, D. S.; Lively, R. P. *J. Phys. Chem. C* **2014**, *118* (35), 20727–20733. DOI: 10.1021/jp5081466.

(241) Krause, S.; Bon, V.; Senkovska, I.; Többens, D. M.; Wallacher, D.; Pillai, R. S.; Maurin, G.; Kaskel, S. *Nature communications* **2018**, *9* (1), 1573. DOI: 10.1038/s41467-018-03979-2.

(242) Bon, V.; Klein, N.; Senkovska, I.; Heerwig, A.; Getzschmann, J.; Wallacher, D.; Zizak, I.; Brzhezinskaya, M.; Mueller, U.; Kaskel, S. *Physical chemistry chemical physics* **2015**, *17* (26), 17471–17479. DOI: 10.1039/c5cp02180d.

(243) Kavoosi, N.; Bon, V.; Senkovska, I.; Krause, S.; Atzori, C.; Bonino, F.; Pallmann, J.; Paasch, S.; Brunner, E.; Kaskel, S. *Dalton Transactions* **2017**, *46* (14), 4685–4695. DOI: 10.1039/c7dt00015d.

(244) Miura, H.; Bon, V.; Senkovska, I.; Ehrling, S.; Watanabe, S.; Ohba, M.; Kaskel, S. *Dalton Transactions* **2017**, *46* (40), 14002–14011. DOI: 10.1039/c7dt02809a.

(245) Sin, M.; Kavoosi, N.; Rauche, M.; Pallmann, J.; Paasch, S.; Senkovska, I.; Kaskel, S.; Brunner, E. *Langmuir: the ACS journal of surfaces and colloids* **2019**, *35* (8), 3162–3170. DOI: 10.1021/acs.langmuir.8b03554.

(246) Schneemann, A.; Bon, V.; Schwedler, I.; Senkovska, I.; Kaskel, S.; Fischer, R. A. *Chemical Society reviews* **2014**, *43* (16), 6062–6096. DOI: 10.1039/c4cs00101j.

(247) Mason, J. A.; Oktawiec, J.; Taylor, M. K.; Hudson, M. R.; Rodriguez, J.; Bachman, J. E.; Gonzalez, M. I.; Cervellino, A.; Guagliardi, A.; Brown, C. M.; Llewellyn, P. L.; Masciocchi, N.; Long, J. R. *Nature* **2015**, *527* (7578), 357–361. DOI: 10.1038/nature15732.

(248) Krause, S.; Bon, V.; Senkovska, I.; Stoeck, U.; Wallacher, D.; Többens, D. M.; Zander, S.; Pillai, R. S.; Maurin, G.; Coudert, F.-X.; Kaskel, S. *Nature* **2016**, *532* (7599), 348–352. DOI: 10.1038/nature17430.

(249) Surblé, S.; Serre, C.; Mellot-Draznieks, C.; Millange, F.; Férey, G. *Chemical communications* **2006** (3), 284–286. DOI: 10.1039/b512169h.

(250) Horcajada, P.; Salles, F.; Wuttke, S.; Devic, T.; Heurtaux, D.; Maurin, G.; Vimont, A.; Daturi, M.; David, O.; Magnier, E.; Stock, N.; Filinchuk, Y.; Popov, D.; Riekel, C.; Férey, G.; Serre, C. *J. Am. Chem. Soc.* **2011**, *133* (44), 17839–17847. DOI: 10.1021/ja206936e.

(251) Fairen-Jimenez, D.; Moggach, S. A.; Wharmby, M. T.; Wright, P. A.; Parsons, S.; Düren, T. *J. Am. Chem. Soc.* **2011**, *133* (23), 8900–8902. DOI: 10.1021/ja202154j.

(252) Coudert, F.-X. *Chemphyschem: a European journal of chemical physics and physical chemistry* **2017**, *18* (19), 2732–2738. DOI: 10.1002/cphc.201700463.

(253) Ania, C. O.; García-Pérez, E.; Haro, M.; Gutiérrez-Sevillano, J. J.; Valdés-Solís, T.; Parra, J. B.; Calero, S. *The journal of physical chemistry letters* **2012**, *3* (9), 1159–1164. DOI: 10.1021/jz300292y.

(254) Maji, T. K.; Matsuda, R.; Kitagawa, S. *Nature materials* **2007**, *6* (2), 142–148. DOI: 10.1038/nmat1827.

(255) Kanoo, P.; Matsuda, R.; Higuchi, M.; Kitagawa, S.; Maji, T. K. *Chemistry of Materials* **2009**, *21* (24), 5860–5866. DOI: 10.1021/cm9025683.

(256) Bureekaew, S.; Sato, H.; Matsuda, R.; Kubota, Y.; Hirose, R.; Kim, J.; Kato, K.; Takata, M.; Kitagawa, S. *Angewandte Chemie* **2010**, *122* (42), 7826–7830. DOI: 10.1002/ange.201002259.

(257) Boutin, A.; Springuel-Huet, M.-A.; Nossov, A.; Gédéon, A.; Loiseau, T.; Volkringer, C.; Férey, G.; Coudert, F.-X.; Fuchs, A. H. *Angew. Chem. Int. Ed.* **2009**, *48* (44), 8314–8317. DOI: 10.1002/anie.200903153.

(258) Boutin, A.; Coudert, F.-X.; Springuel-Huet, M.-A.; Neimark, A. V.; Férey, G.; Fuchs, A. H. *J. Phys. Chem. C* **2010**, *114* (50), 22237–22244. DOI: 10.1021/jp108710h.

(259) Salles, F.; Maurin, G.; Serre, C.; Llewellyn, P. L.; Knöfel, C.; Choi, H. J.; Filinchuk, Y.; Oliviero, L.; Vimont, A.; Long, J. R.; Férey, G. *J. Am. Chem. Soc.* **2010**, *132* (39), 13782–13788. DOI: 10.1021/ja104357r.

(260) Klein, N.; Herzog, C.; Sabo, M.; Senkovska, I.; Getzschmann, J.; Paasch, S.; Lohe, M. R.; Brunner, E.; Kaskel, S. *Physical chemistry chemical physics* **2010**, *12* (37), 11778–11784. DOI: 10.1039/c003835k.

(261) Klein, N.; Hoffmann, H. C.; Cadiau, A.; Getzschmann, J.; Lohe, M. R.; Paasch, S.; Heydenreich, T.; Adil, K.; Senkovska, I.; Brunner, E.; Kaskel, S. *J. Mater. Chem.* **2012**, *22* (20), 10303. DOI: 10.1039/c2jm15601f.

(262) Coudert, F.-X.; Jeffroy, M.; Fuchs, A. H.; Boutin, A.; Mellot-Draznieks, C. *J. Am. Chem. Soc.* **2008**, *130* (43), 14294–14302. DOI: 10.1021/ja805129c.

(263) Seo, J.; Bonneau, C.; Matsuda, R.; Takata, M.; Kitagawa, S. *J. Am. Chem. Soc.* **2011**, *133* (23), 9005–9013. DOI: 10.1021/ja201484s.

(264) Iacomi, P.; Alabarse, F.; Appleyard, R.; Lemaire, T.; Thessieu, C.; Wang, S.; Serre, C.; Maurin, G.; Yot, P. G. *Angew. Chem. Int. Ed.* **2022**, *61* (22), e202201924. DOI: 10.1002/anie.202201924.

(265) Yang, H.; Guo, F.; Lama, P.; Gao, W.-Y.; Wu, H.; Barbour, L. J.; Zhou, W.; Zhang, J.; Aguila, B.; Ma, S. *ACS central science* **2018**, *4* (9), 1194–1200. DOI: 10.1021/acscentsci.8b00378.

(266) Kubota, Y.; Takata, M.; Matsuda, R.; Kitaura, R.; Kitagawa, S.; Kobayashi, T. C. *Angew. Chem. Int. Ed.* **2006**, *45* (30), 4932–4936. DOI: 10.1002/anie.200600976.

(267) Lama, P.; Barbour, L. J. *J. Am. Chem. Soc.* **2018**, *140* (6), 2145–2150. DOI: 10.1021/jacs.7b10352.

(268) Yang, Q.-Y.; Lama, P.; Sen, S.; Lusi, M.; Chen, K.-J.; Gao, W.-Y.; Shivanna, M.; Pham, T.; Hosono, N.; Kusaka, S.; Perry, J. J.; Ma, S.; Space, B.; Barbour, L. J.; Kitagawa, S.; Zaworotko, M. J. *Angew. Chem. Int. Ed.* **2018**, *57* (20), 5684–5689. DOI: 10.1002/anie.201800820.

(269) Yoskamtorn, T.; Zhao, P.; Wu, X.-P.; Purchase, K.; Orlandi, F.; Manuel, P.; Taylor, J.; Li, Y.; Day, S.; Ye, L.; Tang, C. C.; Zhao, Y.; Tsang, S. C. E. *J. Am. Chem. Soc.* **2021**, *143* (8), 3205–3218. DOI: 10.1021/jacs.0c12483.

(270) Zhao, P.; Fang, H.; Mukhopadhyay, S.; Li, A.; Rudić, S.; McPherson, I. J.; Tang, C. C.; Fairen-Jimenez, D.; Tsang, S. C. E.; Redfern, S. A. T. *Nature communications* **2019**, *10* (1), 999. DOI: 10.1038/s41467-019-08939-y.

(271) Zhao, P.; Lampronti, G. I.; Lloyd, G. O.; Suard, E.; Redfern, S. A. T. *J. Mater. Chem. A* **2014**, *2* (3), 620–623. DOI: 10.1039/C3TA13981F.

(272) Allan, P. K.; Xiao, B.; Teat, S. J.; Knight, J. W.; Morris, R. E. *J. Am. Chem. Soc.* **2010**, *132* (10), 3605–3611. DOI: 10.1021/ja910600b.

(273) Huang, Z.; Grape, E. S.; Li, J.; Inge, A. K.; Zou, X. *Coordination Chemistry Reviews* **2021**, *427*, 213583. DOI: 10.1016/j.ccr.2020.213583.

(274) Liu, L.; Zhang, D.; Zhu, Y.; Han, Y. *Communications Chemistry* **2020**, *3* (1). DOI: 10.1038/s42004-020-00361-6.

(275) Rosen, P. F.; Dickson, M. S.; Calvin, J. J.; Ross, N. L.; Friščić, T.; Navrotsky, A.; Woodfield, B. F. *J. Am. Chem. Soc.* **2020**, *142* (10), 4833–4841. DOI: 10.1021/jacs.9b13883.

(276) Devautour-Vinot, S.; Maurin, G.; Henn, F.; Serre, C.; Devic, T.; Férey, G. *Chemical communications* **2009** (19), 2733–2735. DOI: 10.1039/b822834e.

(277) Ryder, M. R.; Civalleri, B.; Bennett, T. D.; Henke, S.; Rudić, S.; Cinque, G.; Fernandez-Alonso, F.; Tan, J.-C. *Physical review letters* **2014**, *113* (21), 215502. DOI: 10.1103/PhysRevLett.113.215502.

(278) Ryder, M. R.; Civalleri, B.; Cinque, G.; Tan, J.-C. *CrystEngComm* **2016**, *18* (23), 4303–4312. DOI: 10.1039/C5CE02347E.

(279) Schaber, J.; Krause, S.; Paasch, S.; Senkovska, I.; Bon, V.; Többens, D. M.; Wallacher, D.; Kaskel, S.; Brunner, E. *J. Phys. Chem. C* **2017**, *121* (9), 5195–5200. DOI: 10.1021/acs.jpcc.7b01204.

(280) Springuel-Huet, M.-A.; Nossov, A.; Adem, Z.; Guenneau, F.; Volkringer, C.; Loiseau, T.; Férey, G.; Gédéon, A. *J. Am. Chem. Soc.* **2010**, *132* (33), 11599–11607. DOI: 10.1021/ja103105y.

(281) Kolbe, F.; Krause, S.; Bon, V.; Senkovska, I.; Kaskel, S.; Brunner, E. *Chemistry of Materials* **2019**, *31* (16), 6193–6201. DOI: 10.1021/acs.chemmater.9b02003.

(282) Kong, X.; Scott, E.; Ding, W.; Mason, J. A.; Long, J. R.; Reimer, J. A. *J. Am. Chem. Soc.* **2012**, *134* (35), 14341–14344. DOI: 10.1021/ja306822p.

(283) Melix, P.; Heine, T. *Chemphyschem: a European journal of chemical physics and physical chemistry* **2021**, *22* (22), 2336–2341. DOI: 10.1002/cphc.202100489.

(284) Hoffmann, H.; Debowski, M.; Müller, P.; Paasch, S.; Senkovska, I.; Kaskel, S.; Brunner, E. *Materials* **2012**, *5* (12), 2537–2572. DOI: 10.3390/ma5122537.

(285) Parent, L. R.; Pham, C. H.; Patterson, J. P.; Denny, M. S.; Cohen, S. M.; Gianneschi, N. C.; Paesani, F. *J. Am. Chem. Soc.* **2017**, *139* (40), 13973–13976. DOI: 10.1021/jacs.7b06585.

(286) Bordiga, S.; Bonino, F.; Lillerud, K. P.; Lamberti, C. *Chemical Society reviews* **2010**, *39* (12), 4885–4927. DOI: 10.1039/c0cs00082e.

(287) Soldatov, M. A.; Martini, A.; Bugaev, A. L.; Pankin, I.; Medvedev, P. V.; Guda, A. A.; Aboraia, A. M.; Podkovyrina, Y. S.; Budnyk, A. P.; Soldatov, A. A.; Lamberti, C. *Polyhedron* **2018**, *155*, 232–253. DOI: 10.1016/j.poly.2018.08.004.

(288) Ronda-Lloret, M.; Pellicer-Carreño, I.; Grau-Atienza, A.; Boada, R.; Diaz-Moreno, S.; Narciso-Romero, J.; Serrano-Ruiz, J. C.; Sepúlveda-Escribano, A.; Ramos-Fernandez, E. V. *Adv. Funct. Mater.* **2021**, *31* (29), 2102582. DOI: 10.1002/adfm.202102582.

(289) Boada, R.; Chaboy, J.; Hayama, S.; Keenan, L. L.; Freeman, A. A.; Amboage, M.; Díaz-Moreno, S. *J. Phys. Chem. C* **2022**, *126* (13), 5935–5943. DOI: 10.1021/acs.jpcc.2c00373.

(290) Aguilar-Tapia, A.; Ould-Chikh, S.; Lahera, E.; Prat, A.; Delnet, W.; Proux, O.; Kieffer, I.; Basset, J.-M.; Takanabe, K.; Hazemann, J.-L. *The Review of scientific instruments* **2018**, *89* (3), 35109. DOI: 10.1063/1.4998929.

(291) Hosono, N.; Terashima, A.; Kusaka, S.; Matsuda, R.; Kitagawa, S. *Nature chemistry* **2019**, *11* (2), 109–116. DOI: 10.1038/s41557-018-0170-0.

(292) Foo, M. L.; Matsuda, R.; Hijikata, Y.; Krishna, R.; Sato, H.; Horike, S.; Hori, A.; Duan, J.; Sato, Y.; Kubota, Y.; Takata, M.; Kitagawa, S. *J. Am. Chem. Soc.* **2016**, *138* (9), 3022–3030. DOI: 10.1021/jacs.5b10491.

(293) Li, L.; Lin, R.-B.; Krishna, R.; Wang, X.; Li, B.; Wu, H.; Li, J.; Zhou, W.; Chen, B. *J. Am. Chem. Soc.* **2017**, *139* (23), 7733–7736. DOI: 10.1021/jacs.7b04268.

(294) Knebel, A.; Geppert, B.; Volgmann, K.; Kolokolov, D. I.; Stepanov, A. G.; Twiefel, J.; Heitjans, P.; Volkmer, D.; Caro, J. *Science* **2017**, *358* (6361), 347–351. DOI: 10.1126/science.aal2456.

(295) Yuan, S.; Zou, L.; Li, H.; Chen, Y.-P.; Qin, J.; Zhang, Q.; Lu, W.; Hall, M. B.; Zhou, H.-C. *Angew. Chem. Int. Ed.* **2016**, *55* (36), 10776–10780. DOI: 10.1002/anie.201604313.

(296) Nguyen Thi, H. P.; Ninh, H. D.; van Tran, C.; Le, B. T.; Bhosale, S. V.; La, D. D. *ChemistrySelect* **2019**, *4* (8), 2333–2338. DOI: 10.1002/slct.201803887.

(297) Huang, W.; Pan, F.; Liu, Y.; Huang, S.; Li, Y.; Yong, J.; Li, Y.; Kirillov, A. M.; Wu, D. *Inorg. Chem.* **2017**, *56* (11), 6362–6370. DOI: 10.1021/acs.inorgchem.7b00457.

(298) Freund, P.; Senkovska, I.; Kaskel, S. *ACS applied materials & interfaces* **2017**, *9* (50), 43782–43789. DOI: 10.1021/acsami.7b13924.

(299) Troyano, J.; Carné-Sánchez, A.; Pérez-Carvajal, J.; León-Reina, L.; Imaz, I.; Cabeza, A.; Maspoch, D. *Angew. Chem. Int. Ed.* **2018**, *57* (47), 15420–15424. DOI: 10.1002/anie.201808433.

(300) Evans, J. D.; Garai, B.; Reinsch, H.; Li, W.; Dissegna, S.; Bon, V.; Senkovska, I.; Fischer, R. A.; Kaskel, S.; Janiak, C.; Stock, N.; Volkmer, D. *Coordination Chemistry Reviews* **2019**, *380*, 378–418. DOI: 10.1016/j.ccr.2018.10.002.

(301) Elsaidi, S. K.; Mohamed, M. H.; Banerjee, D.; Thallapally, P. K. *Coordination Chemistry Reviews* **2018**, *358*, 125–152. DOI: 10.1016/j.ccr.2017.11.022.

(302) Chen, L.; Zhan, W.; Fang, H.; Cao, Z.; Yuan, C.; Xie, Z.; Kuang, Q.; Zheng, L. *Chemistry* **2017**, *23* (47), 11397–11403. DOI: 10.1002/chem.201702103.

(303) Takashi Ohhashi; Takaaki Tsuruoka; Kohei Inoue; Yohei Takashima; Satoshi Horike; Kensuke Akamatsu. *Microporous and Mesoporous Materials* **2017**, *245*, 104–108.

(304) Buso, D.; Nairn, K. M.; Gimona, M.; Hill, A. J.; Falcaro, P. *Chemistry of Materials* **2011**, *23* (4), 929–934. DOI: 10.1021/cm101519s.

(305) S Sutono, S L BR Ginting, M F Wicaksono, K R Tembo. *IOP Conf. Ser.: Mater. Sci. Eng.* **2019**, *662*, 1–7.

(306) Wang, K.; Ren, H.; Li, N.; Tan, X.; Dang, F. *Talanta* **2018**, *188*, 708–713. DOI: 10.1016/j.talanta.2018.06.019.

(307) Lu, G.; Li, S.; Guo, Z.; Farha, O. K.; Hauser, B. G.; Qi, X.; Wang, Y.; Wang, X.; Han, S.; Liu, X.; DuChene, J. S.; Zhang, H.; Zhang, Q.; Chen, X.; Ma, J.; Loo, S. C. J.; Wei, W. D.; Yang, Y.; Hupp, J. T.; Huo, F. *Nature chemistry* **2012**, *4* (4), 310–316. DOI: 10.1038/nchem.1272.

(308) Wang, X.; Li, M.; Cao, C.; Liu, C.; Liu, J.; Zhu, Y.; Zhang, S.; Song, W. *ChemCatChem* **2016**, *8* (20), 3224–3228. DOI: 10.1002/cctc.201600846.

(309) Wang, S.; Fan, Y.; Teng, J.; Fan, Y.-Z.; Jiang, J.-J.; Wang, H.-P.; Grützmacher, H.; Wang, D.; Su, C.-Y. *Small* **2016**, *12* (41), 5702–5709. DOI: 10.1002/smll.201601873.

(310) Lee, H. J.; Cho, W.; Oh, M. *Chemical communications* **2012**, *48* (2), 221–223. DOI: 10.1039/c1cc16213f.

(311) Bugaev, A. L.; Guda, A. A.; Lomachenko, K. A.; Kamyshova, E. G.; Soldatov, M. A.; Kaur, G.; Øien-Ødegaard, S.; Braglia, L.; Lazzarini, A.; Manzoli, M.; Bordiga, S.; Olsbye, U.; Lillerud, K. P.; Soldatov, A. V.; Lamberti, C. *Faraday discussions* **2018**, *208* (0), 287–306. DOI: 10.1039/c7fd00224f.

(312) Meng, F.; Zhang, S.; Ma, L.; Zhang, W.; Li, M.; Wu, T.; Li, H.; Zhang, T.; Lu, X.; Huo, F.; Lu, J. *Advanced materials* **2018**, *30* (49), e1803263. DOI: 10.1002/adma.201803263.

(313) Zheng, G.; Marchi, S. de; López-Puente, V.; Sentosun, K.; Polavarapu, L.; Pérez-Juste, I.; Hill, E. H.; Bals, S.; Liz-Marzán, L. M.; Pastoriza-Santos, I.; Pérez-Juste, J. *Small* **2016**, *12* (29), 3935–3943. DOI: 10.1002/smll.201600947.

(314) Chen, L.; Chen, H.; Luque, R.; Li, Y. *Chemical science* **2014**, *5* (10), 3708–3714. DOI: 10.1039/C4SC01847H.

(315) Chen, L.; Chen, X.; Liu, H.; Bai, C.; Li, Y. *J. Mater. Chem. A* **2015**, *3* (29), 15259–15264. DOI: 10.1039/C5TA02860D.

(316) Li, X.; Zhang, Z.; Xiao, W.; Deng, S.; Chen, C.; Zhang, N. *J. Mater. Chem. A* **2019**, *7* (24), 14504–14509. DOI: 10.1039/C9TA03578H.

(317) Tsumori, N.; Chen, L.; Wang, Q.; Zhu, Q.-L.; Kitta, M.; Xu, Q. *Chem* **2018**, *4* (4), 845–856. DOI: 10.1016/j.chempr.2018.03.009.

(318) Liu, T.; Feng, J.; Wan, Y.; Zheng, S.; Yang, L. *Chemosphere* **2018**, *210*, 907–916. DOI: 10.1016/j.chemosphere.2018.07.085.

(319) Xie, L.; Yang, Z.; Xiong, W.; Zhou, Y.; Cao, J.; Peng, Y.; Li, X.; Zhou, C.; Xu, R.; Zhang, Y. *Applied Surface Science* **2019**, *465*, 103–115. DOI: 10.1016/j.apsusc.2018.09.144.

(320) Wang, Q.; Wang, X.-S.; Chen, C.-H.; Yang, X.; Huang, Y.-B.; Cao, R. *Chemical communications* **2018**, *54* (64), 8822–8825. DOI: 10.1039/C8CC04485F.

(321) Liang, L.; Liu, L.; Jiang, F.; Liu, C.; Yuan, D.; Chen, Q.; Wu, D.; Jiang, H.-L.; Hong, M. *Inorganic chemistry* **2018**, *57* (9), 4891–4897. DOI: 10.1021/acs.inorgchem.7b03076.

(322) Wu, Y.-L.; Yang, G.-P.; Cheng, S.; Qian, J.; Fan, D.; Wang, Y.-Y. *ACS applied materials & interfaces* **2019**, *11* (50), 47437–47445. DOI: 10.1021/acsami.9b17348.

(323) Kamsuwan, T.; Jongsomjit, B. *Journal of oleo science* **2018**, *67* (8), 1005–1014. DOI: 10.5650/jos.ess18001.

(324) Shang, N.; Gao, S.; Zhou, X.; Feng, C.; Wang, Z.; Wang, C. *RSC Adv* **2014**, *4* (97), 54487–54493. DOI: 10.1039/C4RA10065D.

(325) Zhu, Q.-L.; Li, J.; Xu, Q. *Journal of the American Chemical Society* **2013**, *135* (28), 10210–10213. DOI: 10.1021/ja403330m.

(326) Bennett, T. D.; Cheetham, A. K.; Fuchs, A. H.; Coudert, F.-X. *Nature chemistry* **2016**, *9* (1), 11–16. DOI: 10.1038/nchem.2691.

(327) Bennett, T. D.; Cheetham, A. K.; Fuchs, A. H.; Coudert, F.-X. *Nature chemistry* **2016**, *9* (1), 11–16. DOI: 10.1038/nchem.2691.

(328) Xiang, W.; Zhang, Y.; Lin, H.; Liu, C.-J. *Molecules* **2017**, *22* (12). DOI: 10.3390/molecules22122103.

(329) Rösler, C.; Fischer, R. A. *CrystEngComm* **2015**, *17* (2), 199–217. DOI: 10.1039/C4CE01251H.

(330) Hermes, S.; Schröter, M.-K.; Schmid, R.; Khodeir, L.; Muhler, M.; Tissler, A.; Fischer, R. W.; Fischer, R. A. *Angew. Chem. Int. Ed.* **2005**, *44* (38), 6237–6241. DOI: 10.1002/anie.200462515.

(331) Schröder, F.; Esken, D.; Cokoja, M.; van den Berg, M. W. E.; Lebedev, O. I.; van Tendeloo, G.; Walaszek, B.; Buntkowsky, G.; Limbach, H.-H.; Chaudret, B.; Fischer, R. A. *J. Am. Chem. Soc.* **2008**, *130* (19), 6119–6130. DOI: 10.1021/ja078231u.

(332) Jiang, H.-L.; Akita, T.; Ishida, T.; Haruta, M.; Xu, Q. *J. Am. Chem. Soc.* **2011**, *133* (5), 1304–1306. DOI: 10.1021/ja1099006.

(333) Moon, H. R.; Kim, J. H.; Suh, M. P. *Angew. Chem. Int. Ed.* **2005**, *44* (8), 1261–1265. DOI: 10.1002/anie.200461408.

(334) Aijaz, A.; Karkamkar, A.; Choi, Y. J.; Tsumori, N.; Rönnebro, E.; Autrey, T.; Shioyama, H.; Xu, Q. *J. Am. Chem. Soc.* **2012**, *134* (34), 13926–13929. DOI: 10.1021/ja3043905.

(335) Jiang, H.-L.; Liu, B.; Akita, T.; Haruta, M.; Sakurai, H.; Xu, Q. *J. Am. Chem. Soc.* **2009**, *131* (32), 11302–11303. DOI: 10.1021/ja9047653.

(336) Yang, Q.; Liu, W.; Wang, B.; Zhang, W.; Zeng, X.; Zhang, C.; Qin, Y.; Sun, X.; Wu, T.; Liu, J.; Huo, F.; Lu, J. *Nature communications* **2017**, *8*, 14429. DOI: 10.1038/ncomms14429.

(337) Li, B.; Ma, J.-G.; Cheng, P. *Angew. Chem. Int. Ed.* **2018**, *57* (23), 6834–6837. DOI: 10.1002/anie.201801588.

(338) Zhao, M.; Yuan, K.; Wang, Y.; Li, G.; Guo, J.; Gu, L.; Hu, W.; Zhao, H.; Tang, Z. *Nature* **2016**, *539* (7627), 76–80. DOI: 10.1038/nature19763.

(339) He, L.; Liu, Y.; Liu, J.; Xiong, Y.; Zheng, J.; Liu, Y.; Tang, Z. *Angew. Chem. Int. Ed.* **2013**, *52* (13), 3741–3745. DOI: 10.1002/anie.201209903.

(340) Sato, H.; Matsuda, R.; Sugimoto, K.; Takata, M.; Kitagawa, S. *Nature materials* **2010**, *9* (8), 661–666. DOI: 10.1038/nmat2808.

(341) Modrow, A.; Zargarani, D.; Herges, R.; Stock, N. *Dalton Transactions* **2011**, *40* (16), 4217–4222. DOI: 10.1039/c0dt01629b.

(342) Sato, O. *Nature chemistry* **2016**, *8* (7), 644–656. DOI: 10.1038/nchem.2547.

(343) Henke, S.; Schneemann, A.; Wütscher, A.; Fischer, R. A. *J. Am. Chem. Soc.* **2012**, *134* (22), 9464–9474. DOI: 10.1021/ja302991b.

(344) Wharmby, M. T.; Henke, S.; Bennett, T. D.; Bajpe, S. R.; Schwedler, I.; Thompson, S. P.; Gozzo, F.; Simoncic, P.; Mellot-Draznieks, C.; Tao, H.; Yue, Y.; Cheetham, A. K. *Angew. Chem. Int. Ed.* **2015**, *54* (22), 6447–6451. DOI: 10.1002/anie.201410167.

(345) Pallach, R.; Keupp, J.; Terlinden, K.; Frentzel-Beyme, L.; Kloß, M.; Machalica, A.; Kotschy, J.; Vasa, S. K.; Chater, P. A.; Sternemann, C.; Wharmby, M. T.; Linser, R.; Schmid, R.; Henke, S. *Nature communications* **2021**, *12* (1), 4097. DOI: 10.1038/s41467-021-24188-4.

(346) Bennett, T. D.; Cheetham, A. K. *Accounts of Chemical Research* **2014**, *47* (5), 1555–1562. DOI: 10.1021/ar5000314.

(347) Bennett, T. D.; Horike, S. *Nature Reviews Materials* **2018**, *3* (11), 431–440. DOI: 10.1038/s41578-018-0054-3.

(348) Yang, L.; Zhou, W.; Li, H.; Alsalme, A.; Jia, L.; Yang, J.; Li, J.; Li, L.; Chen, B. *Chinese journal of chemical engineering* **2020**, *28* (2). DOI: 10.1016/j.cjche.2019.09.005.

(349) Wang, X.; Jia, Y.; Mao, X.; Liu, D.; He, W.; Li, J.; Liu, J.; Yan, X.; Chen, J.; Song, L.; Du, A.; Yao, X. *Advanced materials* **2020**, *32* (16), e2000966. DOI: 10.1002/adma.202000966.

(350) Mukherjee, S.; He, Y.; Franz, D.; Wang, S.-Q.; Xian, W.-R.; Bezrukov, A. A.; Space, B.; Xu, Z.; He, J.; Zaworotko, M. J. *Chemistry* **2020**, *26* (22), 4923–4929. DOI: 10.1002/chem.202000008.

(351) Schneemann, A.; Bloch, E. D.; Henke, S.; Llewellyn, P. L.; Long, J. R.; Fischer, R. A. *Chemistry* **2015**, *21* (51), 18764–18769. DOI: 10.1002/chem.201503685.

(352) Clearfield, A. *Dalton Transactions* **2016**, *45* (10), 4100–4112. DOI: 10.1039/c5dt03228h.

(353) Krause, S.; Hosono, N.; Kitagawa, S. *Angew. Chem. Int. Ed.* **2020**, *59* (36), 15325–15341. DOI: 10.1002/anie.202004535.

(354) Henke, S.; Schneemann, A.; Fischer, R. A. *Adv. Funct. Mater.* **2013**, *23* (48), 5990–5996. DOI: 10.1002/adfm.201301256.

(355) Broom, D. P.; Webb, C. J.; Fanourgakis, G. S.; Froudakis, G. E.; Trikalitis, P. N.; Hirscher, M. *International Journal of Hydrogen Energy* **2019**, *44* (15), 7768–7779. DOI: 10.1016/j.ijhydene.2019.01.224.

(356) Kapelewski, M. T.; Runčevski, T.; Tarver, J. D.; Jiang, H. Z. H.; Hurst, K. E.; Parilla, P. A.; Ayala, A.; Gennett, T.; FitzGerald, S. A.; Brown, C. M.; Long, J. R. *Chemistry of Materials* **2018**, *30* (22). DOI: 10.1021/acs.chemmater.8b03276.

(357) Hu, Z.; Wang, Y.; Shah, B. B.; Zhao, D. *Advanced Sustainable Systems* **2019**, *3* (1), 1800080. DOI: 10.1002/adsu.201800080.

(358) Milner, P. J.; Martell, J. D.; Siegelman, R. L.; Gygi, D.; Weston, S. C.; Long, J. R. *Chemical science* **2018**, *9* (1), 160–174. DOI: 10.1039/c7sc04266c.

(359) Herm, Z. R.; Bloch, E. D.; Long, J. R. *Chemistry of Materials* **2014**, *26* (1), 323–338. DOI: 10.1021/cm402897c.

(360) Cmarik, G. E.; Kim, M.; Cohen, S. M.; Walton, K. S. *Langmuir : the ACS journal of surfaces and colloids* **2012**, *28* (44), 15606–15613. DOI: 10.1021/la3035352.

(361) Shyam Biswas, Pascal Van Der Voort. *Eur. J. Inorg. Chem.* **2013**, *2013* (12), 2154–2160. DOI: 10.1002/ejic.201201228.

(362) Luo, X.-L.; Yin, Z.; Zeng, M.-H.; Kurmoo, M. *Inorg. Chem. Front.* **2016**, *3* (10), 1208–1226. DOI: 10.1039/C6QI00181E.

(363) Dybtsev, D. N.; Chun, H.; Kim, K. *Angew. Chem. Int. Ed.* **2004**, *43* (38), 5033–5036. DOI: 10.1002/anie.200460712.

(364) Maji, T. K.; Uemura, K.; Chang, H.-C.; Matsuda, R.; Kitagawa, S. *Angewandte Chemie* **2004**, *116* (25), 3331–3334. DOI: 10.1002/ange.200453923.

(365) Sebastian Henke. Metal-Organic Frameworks with Additional Flexible Substituents:Modulating Responsiveness, Gas Sorption Selectivity & Network Topologies. PhD, Ruhr-University Bochum, Bochum, 2011.

(366) Schneemann, A.; Rudolf, R.; Baxter, S. J.; Vervoorts, P.; Hante, I.; Khaletskaya, K.; Henke, S.; Kieslich, G.; Fischer, R. A. *Dalton Transactions* **2019**, *48* (19), 6564–6570. DOI: 10.1039/c9dt01105f.

(367) Schneemann, A.; Vervoorts, P.; Hante, I.; Tu, M.; Wannapaiboon, S.; Sternemann, C.; Paulus, M.; Wieland, D. F.; Henke, S.; Fischer, R. A. *Chemistry of Materials* **2018**, *30* (5), 1667–1676. DOI: 10.1021/acs.chemmater.7b05052.

(368) Alaghemandi, M.; Schmid, R. *J. Phys. Chem. C* **2016**, *120* (12), 6835–6841. DOI: 10.1021/acs.jpcc.5b12331.

(369) Griffiths, K.; Halcovitch, N. R.; Griffin, J. M. *Inorg. Chem.* **2021**, *60* (17), 12950–12960. DOI: 10.1021/acs.inorgchem.1c01364.

(370) Schwedler, I.; Henke, S.; Wharmby, M. T.; Bajpe, S. R.; Cheetham, A. K.; Fischer, R. A. *Dalton Transactions* **2016**, *45* (10), 4230–4241. DOI: 10.1039/c5dt03825a.

(371) Chen, B.; Liang, C.; Yang, J.; Contreras, D. S.; Clancy, Y. L.; Lobkovsky, E. B.; Yaghi, O. M.; Dai, S. *Angew. Chem. Int. Ed.* **2006**, *45* (9), 1390–1393. DOI: 10.1002/anie.200502844.

(372) Kitagawa, S.; Uemura, K. *Chemical Society reviews* **2005**, *34* (2), 109–119. DOI: 10.1039/b313997m.

(373) Tanaka, S.; Fujita, K.; Miyake, Y.; Miyamoto, M.; Hasegawa, Y.; Makino, T.; van der Perre, S.; Cousin Saint Remi, J.; van Assche, T.; Baron, G. V.; Denayer, J. F. M. *J. Phys. Chem. C* **2015**, *119* (51), 28430–28439. DOI: 10.1021/acs.jpcc.5b09520.

(374) Bennett, T. D.; Cao, S.; Tan, J. C.; Keen, D. A.; Bithell, E. G.; Beldon, P. J.; Friscic, T.; Cheetham, A. K. *J. Am. Chem. Soc.* **2011**, *133* (37), 14546–14549. DOI: 10.1021/ja206082s.

(375) Bennett, T. D.; Keen, D. A.; Tan, J.-C.; Barney, E. R.; Goodwin, A. L.; Cheetham, A. K. *Angew. Chem. Int. Ed.* **2011**, *50* (13), 3067–3071. DOI: 10.1002/anie.201007303.

(376) Cao, S.; Bennett, T. D.; Keen, D. A.; Goodwin, A. L.; Cheetham, A. K. *Chemical communications* **2012**, *48* (63), 7805–7807. DOI: 10.1039/c2cc33773h.

(377) Chapman, K. W.; Sava, D. F.; Halder, G. J.; Chupas, P. J.; Nenoff, T. M. *J. Am. Chem. Soc.* **2011**, *133* (46), 18583–18585. DOI: 10.1021/ja2085096.

(378) Xin, Z.; Chen, X.; Wang, Q.; Chen, Q.; Zhang, Q. *Microporous and Mesoporous Materials* **2013**, *169*, 218–221. DOI: 10.1016/j.micromeso.2012.11.003.

(379) Masciocchi, N.; Ardizzoia, G. A.; LaMonica, G.; Maspero, A.; Galli, S.; Sironi, A. *Inorg. Chem.* **2001**, *40* (27), 6983–6989. DOI: 10.1021/ic010585d.

(380) Hu, Y. H.; Zhang, L. *Phys. Rev. B* **2010**, *81* (17). DOI: 10.1103/PhysRevB.81.174103.

(381) Zhou, Y.; Liu, C.-J. *Plasma Chem Plasma Process* **2011**, *31* (3), 499–506. DOI: 10.1007/s11090-011-9290-7.

(382) Henke, S.; Fischer, R. A. *J. Am. Chem. Soc.* **2011**, *133* (7), 2064–2067. DOI: 10.1021/ja109317e.

(383) Zacharia, R.; Cossement, D.; Lafi, L.; Chahine, R. *J. Mater. Chem.* **2010**, *20* (11), 2145. DOI: 10.1039/b922991d.

(384) Lapidus, S. H.; Halder, G. J.; Chupas, P. J.; Chapman, K. W. *J. Am. Chem. Soc.* **2013**, *135* (20), 7621–7628. DOI: 10.1021/ja4012707.

(385) Ohara, K.; Martí-Rujas, J.; Haneda, T.; Kawano, M.; Hashizume, D.; Izumi, F.; Fujita, M. *J. Am. Chem. Soc.* **2009**, *131* (11), 3860–3861. DOI: 10.1021/ja9005145.

(386) Mart-Rujas, J.; Islam, N.; Hashizume, D.; Izumi, F.; Fujita, M.; Kawano, M. *J. Am. Chem. Soc.* **2011**, *133* (15), 5853–5860. DOI: 10.1021/ja109160a.

(387) Lohe, M. R.; Rose, M.; Kaskel, S. *Chemical communications* **2009** (40), 6056–6058. DOI: 10.1039/b910175f.

(388) Bueken, B.; Vermoortele, F.; Cliffe, M. J.; Wharmby, M. T.; Foucher, D.; Wieme, J.; Vanduyfhuys, L.; Martineau, C.; Stock, N.; Taulelle, F.; van Speybroeck, V.; Goodwin, A. L.; Vos, D. de. *Chemistry* **2016**, *22* (10), 3264–3267. DOI: 10.1002/chem.201600330.

(389) Yanai, N.; Kaneko, W.; Yoneda, K.; Ohba, M.; Kitagawa, S. *J. Am. Chem. Soc.* **2007**, *129* (12), 3496–3497. DOI: 10.1021/ja069166b.

(390) Xiu, J.-W.; Wang, G.-E.; Yao, M.-S.; Yang, C.-C.; Lin, C.-H.; Xu, G. *Chemical communications* **2017**, *53* (16), 2479–2482. DOI: 10.1039/c6cc09310h.

(391) Uemura, K.; Kitagawa, S.; Fukui, K.; Saito, K. *J. Am. Chem. Soc.* **2004**, *126* (12), 3817–3828. DOI: 10.1021/ja039914m.

(392) Vismara, R.; Galli, S.; Terruzzi, S.; Colombo, V. *Dataset CH-6073* **2021.** DOI: 10.15151/ESRF-ES-517791935.

(393) Le Bail, A. *Powder Diffraction* **2005**, *20* (4), 316–326. DOI: 10.1154/1.2135315.

(394) Coelho, A. A. *J Appl Crystallogr* **2000**, *33* (3), 899–908. DOI: 10.1107/S002188980000248X.

(395) Rietveld, H. M. *J Appl Crystallogr* **1969**, *2* (2), 65–71. DOI: 10.1107/S0021889869006558.

(396) Coelho Software. *TOPAS-Academic, www.topas-academic.net.*

(397) micromod Partikeltechnologie GmbH. *Sicastar®-redF, red fluorescent silica particles, www.micromod.de*.

(398) Willcott, M. R. *J. Am. Chem. Soc.* **2009**, *131* (36), 13180. DOI: 10.1021/ja906709t.

(399) Coelho, A. A. *J Appl Crystallogr* **2018**, *51* (1), 210–218. DOI: 10.1107/S1600576718000183.

(400) Brunelli, M.; Fitch, A. N. *Journal of synchrotron radiation* **2003**, *10* (Pt 4), 337–339. DOI: 10.1107/s0909049503007969.

(401) Cheary, R. W.; Coelho, A. A. *J Appl Crystallogr* **1998**, *31* (6), 851–861. DOI: 10.1107/S0021889898006876.

(402) Her, J. H.; Stephens, P. W.; Gao, Y.; Soloveichik, G. L.; Rijssenbeek, J.; Andrus, M.; Zhao, J. C. *Acta crystallographica. Section B, Structural science* **2007**, *63* (Pt 4), 561–568. DOI: 10.1107/S0108768107022665.